

JOURNAL OF THE ELECTROCHEMICAL SOCIETY

ELECTROCHEMICAL
SCIENCE AND TECHNOLOGY

SOLID-STATE
SCIENCE AND TECHNOLOGY

REVIEWS AND NEWS



VOL. 119, NO. 5

MAY 1972

นักสังคม กรรมการศาสตร์

JESOAN 119 (5) 551-654, 143C-158C (1972)

FUTURE MEETINGS

Of The Electrochemical Society



MIAMI BEACH, FLORIDA—OCTOBER 8, 9, 10, 11, 12 & 13, 1972

Headquarters at the Fontainebleau Hotel

Planned symposia for the Miami Beach Meeting include the following Divisions and subjects:

Battery—Load Leveling and Standby Power, General Sessions; **Corrosion**—Effects of Metallurgical Substrates on Fundamental Corrosion Processes, General Session; **Dielectrics and Insulation**—Electrets Charge Storage and Transport in Dielectrics, Oxide-Electrolyte Interfaces, General Session; **Electrodeposition**—General Session; **Electrodeposition and Electronics**—Electrodeposition Processes in the Electronics Industry; **Electronics**—Semiconductor General Session, Chemistry and Physics of Compound Semiconductor Surfaces, General Electronics (Molecular Beam Epitaxy); **Electro-Organic**—General Session; **Electrothermics and Metallurgy**—Trace Elements; **New Technology Committee with the Battery, Corrosion, Electro-Organic, and Electrothermics and Metallurgy Divisions**—Marine Electrochemistry.

CHICAGO, ILLINOIS—MAY 13, 14, 15, 16, 17 & 18, 1973

Headquarters at the Sheraton-Chicago Hotel

The following Divisions are planning symposia:

Dielectrics and Insulation; Electronics (Semiconductor, General, Luminescence); Electro-Organic; Electrothermics and Metallurgy; Industrial Electrolytic; Physical Electrochemistry; New Technology Committee—Electrochemical Aspects of Bio-Engineering.

BOSTON, MASSACHUSETTS—OCTOBER 7, 8, 9, 10, 11 & 12, 1973

Headquarters at the Sheraton-Boston Hotel

The following divisions are planning symposia:

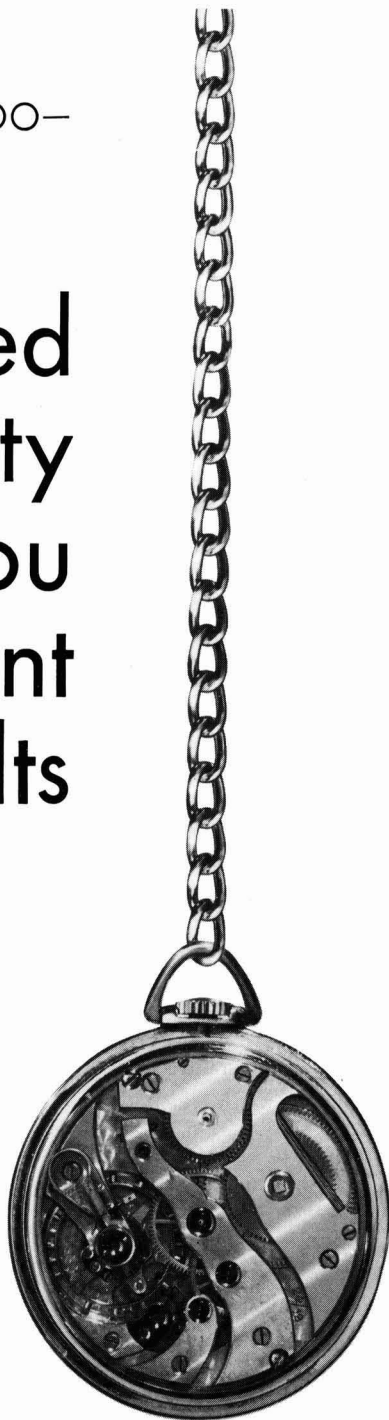
Battery; Corrosion; Dielectrics and Insulation; Electrodeposition; Electronics; Electrothermics and Metallurgy; New Technology Committee—Electrochemical Control of the Environment.

In GLC ANODES too—

time-tested
uniformity
gives you
consistent
results

In cell after cell after cell, the records of leading chlor-alkali producers show that time-tested GLC Anodes are made from longer-lasting graphite.

Give time-tested GLC Anodes innovative operational dimensions. Make them produce more, for less. Make them make new records for you.



GREAT LAKES CARBON CORPORATION

GRAPHITE PRODUCTS DIVISION
Offices and Agents Around the World

299 Park Avenue, New York, N. Y. 10017

One of the world's largest manufacturers of graphite for electrothermic and electrochemical processes—and for aerospace, nuclear, metallurgical and other industrial uses.

MAY 1972

EDITOR

Norman Hackerman

DIVISIONAL EDITORS

BATTERY

R. J. Brodd
Elton J. Cairns

L. W. Niedrach
J. L. Weininger

CORROSION

Theodore R. Beck
Richard C. Carlston
J. W. Faust, Jr.
Z. A. Foroulis

Jerome Kruger
Ken Nobe
Earl S. Snively, Jr.
J. Bruce Wagner

DIELECTRICS AND INSULATION

Robert S. Alwitt
Newton Schwartz

Donald M. Smyth
Lawrence Young

ELECTRODEPOSITION

Seymour Senderoff

ELECTRONICS

Ephraim Banks
Charles M. Chapman
George R. Cronin
Simon Larach
I. Arnold Lesk
Ernest Paskell

Jerome Prener
Bertram Schwartz
Alan J. Strauss
P. Wang
J. M. Woodall

ELECTRO-ORGANIC

Manuel M. Balzer

Stanley Wawzonek

ELECTROTHERMICS AND METALLURGY

Joan B. Berkowitz
J. M. Blocher, Jr.

W. E. Kuhn
W. W. Smeltzer

INDUSTRIAL ELECTROLYTIC

P. A. Danna

Scott Lynn

PHYSICAL ELECTROCHEMISTRY

Allen J. Bard
M. W. Breiter
A. J. de Bethune

R. M. Hurd
Royce J. Murray
C. W. Tobias

EDITORIAL STAFF

Nancy Gay Stewart, Assistant to the Editor
Julius Klierer, Book Review Editor

PUBLICATION STAFF

Sarah A. Kilfoyle, Publication Editor
Beverly M. Bruns, Assistant Publication Editor

PUBLICATION COMMITTEE

Newton Schwartz, Chairman
Elton Cairns
Robert T. Foley
Frederick Fowkes
Norman Hackerman
Earl S. Snively, Jr.
Fred Strieter
Dennis R. Turner

ADVERTISING OFFICE

P.O. Box 2071
Princeton, N. J. 08540



ELECTROCHEMICAL SCIENCE AND TECHNOLOGY

TECHNICAL PAPERS

M. C. B. Hotz
R. C. Kerby
T. R. Ingraham
... 551

Galvanic Cells in Molten Sodium Bisulfate

K. D. South
J. L. Sudworth
J. G. Gibson
... 554

Electrode Processes in Sodium Polysulfide Melts

K. F. Blurton
P. Greenberg
H. G. Oswin
D. R. Rutt
... 559

The Electrochemical Activity of Dispersed Platinum

E. J. McHenry
P. Hubbauer
... 564

Hermetic Compression Seals for Alkaline Batteries

R. F. Amlie
E. Y. Weissman
C. K. Morehouse
N. M. Qureshi
... 568

A New Water-Activated Lead-Acid Battery Concept

C. M. Shepherd
S. Schuldiner
... 572

Effect of Chloride Ion on Iron Corrosion in NaOH Solution

J. W. Johnson
H. W. Jiang
S. B. Hanna
W. J. James
... 574

Anodic Oxidation of Ethylenediaminetetraacetic Acid on Pt in Acid Sulfate Solutions

ELECTROCHEMICAL SOCIETY

Vol. 119 • No. 5

B. S. Hobbs
A. C. C. Tseung
... 580

The Anodic Oxidation of Hydrogen on Platinized Tungsten Oxides
I. Composition of Tungsten Blue in Platinized WO_3 Hydrogen Electrocatalyst

P. C. Wayner, Jr.
... 584

The Effect of Viscous Shear on a Meniscus in an Electrochemical System

BRIEF COMMUNICATION

R. N. O'Brien
... 589

Low Current Density Microcell Diffusion Layer Thickness at Shallow Vertical Electrodes

SOLID-STATE SCIENCE AND TECHNOLOGY

TECHNICAL PAPERS

C. M. Osburn
D. W. Ormond
... 591

Dielectric Breakdown in Silicon Dioxide Films on Silicon
I. Measurement and Interpretation

C. M. Osburn
D. W. Ormond
... 597

Dielectric Breakdown in Silicon Dioxide Films on Silicon
II. Influence of Processing and Materials

C. M. Osburn
E. J. Weitzman
... 603

Electrical Conduction and Dielectric Breakdown in Silicon Dioxide Films on Silicon

S. G. Parker
R. E. Johnson
... 610

Preparation of $(Y,Yb,Er)F_3$ Phosphors for Green-Light Emission

M. Bleicher
... 613

Thermodynamic Calculations for $GaAs_{1-x}P_x$ Vapor Growth

DIVISION OFFICERS

Battery Division

Alvin J. Salkind, Chairman
Ralph J. Brodd, Vice-Chairman
Howard R. Karas, Secretary-Treasurer
General Battery Corp.
P. O. Box 1262
Reading, Pa. 19603

Corrosion Division

Z. A. Foroulis, Chairman
J. P. Pemsler, Vice-Chairman
Roger Stashie, Secretary-Treasurer
Ohio State University
Dept. of Metallurgical Engineering
116 West 19th Avenue
Columbus, Ohio 43210

Dielectrics and Insulation Division

Dieter Gerstenberg, Chairman
Lawrence V. Gregor, Vice-Chairman
Frederick Vratny, Treasurer
Lyon Mandelcorn, Secretary
Westinghouse Research Laboratory
Pittsburgh, Pennsylvania 15200

Electrodeposition Division

Rolf Weil, Acting Chairman
John L. Griffin, Secretary-Treasurer
Research Laboratories
General Motors Corporation
12 Mile and Mound Roads
Warren, Michigan 48090

Electronics Division

Erik Peli, Chairman
I. Arnold Lesk, Vice-Chairman (Semiconductors)
William A. McAllister, Vice-Chairman (Luminescence)
Ian M. Croll, Vice-Chairman (General)
Jerry M. Woodall, Secretary-Treasurer
Thomas J. Watson Research Center
IBM Corporation
Yorktown Heights, New York 10598

Electro-Organic Division

Allen J. Bard, Chairman
Manuel M. Balzer, Vice-Chairman
Charles K. Mann, Secretary-Treasurer
Department of Chemistry
Florida State University
Tallahassee, Florida 32306

Electrothermics and Metallurgy Division

Joan B. Berkowitz, Chairman
Walter W. Smeltzer, Senior Vice-Chairman
Robert Bakish, Junior Vice-Chairman
John M. Blocher, Jr., Secretary-Treasurer
Battelle Memorial Institute
Columbus, Ohio 43200

Industrial Electrolytic Division

Luther Vaaler, Chairman
Noian E. Richards, Vice-Chairman
D. N. Goets, Secretary-Treasurer
Route 2, Box 714
Golden, Colorado 80401

Physical Electrochemistry Division

Robert E. Meredith, Chairman
Manfred W. Breiter, Vice-Chairman
James D. E. McIntyre, Secretary-Treasurer
Bell Telephone Laboratories, Inc.
IE-439
Murray Hill, New Jersey 07974

SOCIETY OFFICERS AND STAFF

Cecil V. King, President
American Gas & Chemicals, Inc.
511 East 72 St.
New York, N. Y. 10021

Theodore D. McKinley, Vice-President
E. I. du Pont de Nemours & Co. Inc.
Pigments Department
Experimental Station
Wilmington, Del. 19898

N. Bruce Hannay, Vice-President
Bell Telephone Laboratories, Inc.
Murray Hill, N. J. 07971

David A. Vermilyea, Vice-President
General Electric Research Laboratories
Building K01, Room 3A45
Schenectady, N. Y. 12301

Dennis R. Turner, Secretary
Bell Telephone Laboratories, Inc.
Room 1E-245
Murray Hill, N. J. 07971

R. Homer Cherry, Treasurer
2350 Huntingdon Road
Huntingdon Valley, Pa. 19006

Ernest G. Enck, Executive Secretary
The Electrochemical Society, Inc.
P.O. Box 2071
Princeton, N. J. 08540

V. H. Branneky, Assistant Executive Secretary
The Electrochemical Society, Inc.
P.O. Box 2071
Princeton, N. J. 08540

Marie Falloon, Financial Secretary
The Electrochemical Society, Inc.
P.O. Box 2071
Princeton, N. J. 08540

Manuscripts submitted to the Journal should be sent, in triplicate, to the Editorial Office at P. O. Box 2071, Princeton, N. J. 08540. They should conform to the revised "Instructions to Authors" available from Society Headquarters. Manuscripts so submitted, as well as papers presented before a National technical meeting, become the property of the Society and may not be published elsewhere in whole or in part without written permission of the Society. Address such requests to the Editor.

The Electrochemical Society does not maintain a supply of reprints of papers appearing in its Journal. A photoprint copy of any particular paper may be obtained from University Microfilms, 300 North Zeeb Road, Ann Arbor, Michigan 48106.

Inquiries regarding positive microfilm copies of volumes should be addressed to University Microfilms, Inc., 300 N. Zeeb St., Ann Arbor, Mich. 48106.

Walter J. Johnson, Inc., 111 Fifth Ave., New York, N. Y., 10003, have reprint rights to out-of-print volumes of the Journal, and also have available for sale back volumes and single issues, with the exception of the current calendar year. Anyone interested in securing back copies should correspond directly with them.

Published monthly by The Electrochemical Society, Inc., at 215 Canal St., Manchester, N. H.; Executive Offices, Editorial Office, and Circulation Dept., and Advertising Office at P. O. Box 2071, Princeton, N. J. 08540, combining the JOURNAL and TRANSACTIONS OF THE ELECTROCHEMICAL SOCIETY. Statements and Opinions given in articles and papers in the JOURNAL OF THE ELECTROCHEMICAL SOCIETY are those of the contributors, and The Electrochemical Society assumes no responsibility for them.

Claims for missing numbers will not be allowed if received more than 60 days from date of mailing plus time normally required for postal delivery of JOURNAL and claim. No claims allowed because of failure to notify the Circulation Dept., The Electrochemical Society, P. O. Box 2071, Princeton, N. J., 08540, of a change of address, or because copy is "missing from files." Subscription to members as part of membership service; subscription to non-members \$40.00 plus \$3.00 for postage outside U.S. and Canada. Single copies \$2.50 to members, \$4.00 to nonmembers. © 1972 by The Electrochemical Society, Inc. Second Class Postage Paid at Princeton, New Jersey, and at additional mailing offices. Printed in U.S.A.

SOLID STATE SCIENCE (Cont.)

S. Kishino
M. Ogirima
K. Kurata
... 617

A Cross-Hatch Pattern in $\text{GaAs}_{1-x}\text{P}_x$ Epitaxially Grown on GaAs Substrate

C. D. Thurmond
R. A. Logan
... 622

The Equilibrium Pressure of N_2 over GaN

P. Mayer
W. W. Smeltzer
... 626

Kinetics of Manganese-Wustite Scale Formation on Iron-Manganese Alloys

A. K. Garbee
S. N. Flengas
... 631

Electrical and Structural Properties of Metal Sulfides in Chloride Melts
The Systems $\text{Cu}_2\text{S-CuCl}$ and FeS-FeCl_2

H. W. Pickering
... 641

On the Transition from Internal to External Oxidation in Ternary Alloys

TECHNICAL NOTES

N. Ramasubramanian
... 649

Electrical Switching in Anodic Oxide Films on Zircaloy-2

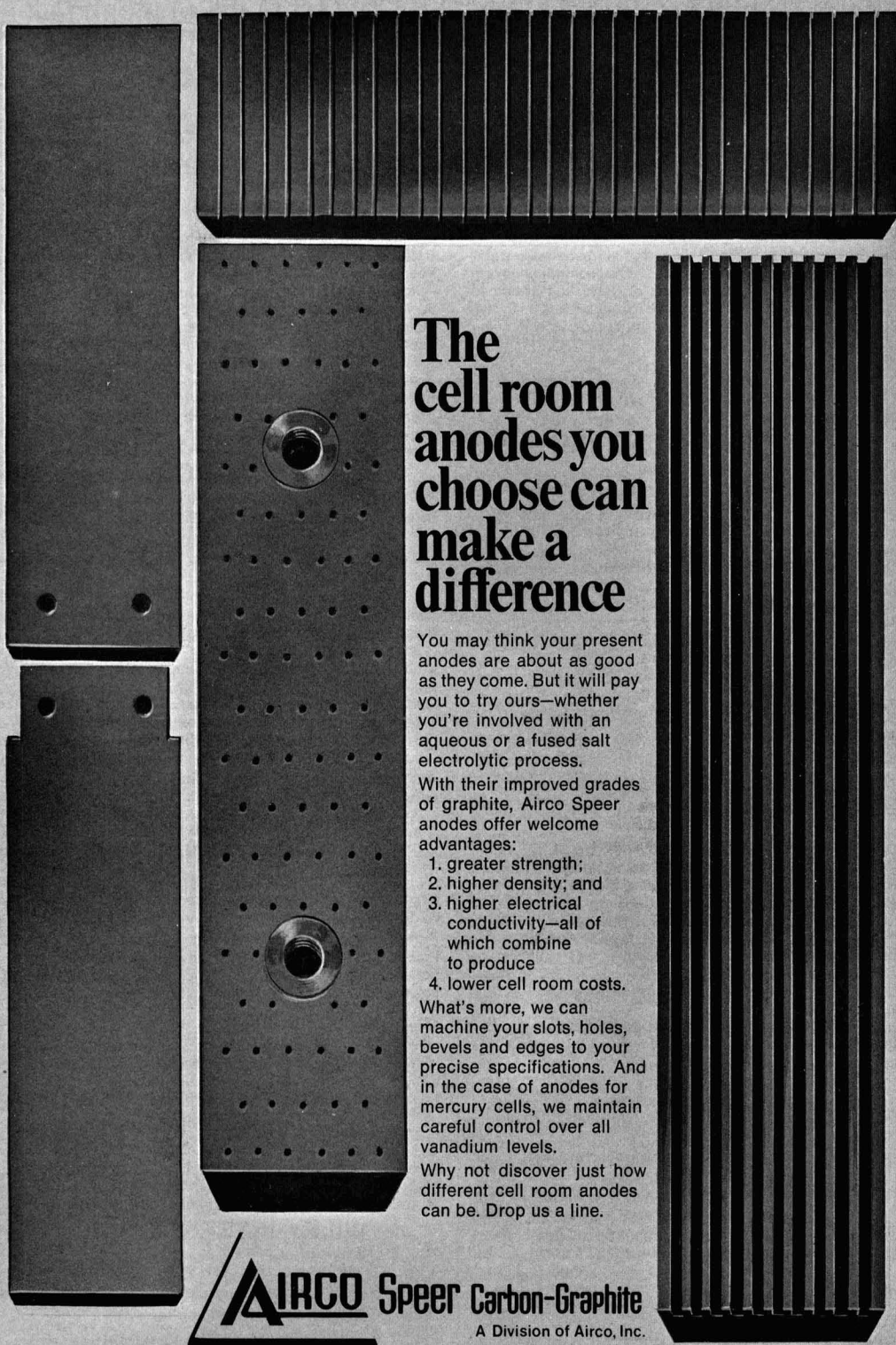
W. G. Rado
W. J. Johnson
R. L. Crawley
... 652

The Composition of $\text{Ga}_{1-x}\text{Al}_x\text{As}$ Grown from Ga-Rich Solutions as a Function of Growth Temperature and Solution Composition

REVIEWS AND NEWS

NEWS

... 149C



The cell room anodes you choose can make a difference

You may think your present anodes are about as good as they come. But it will pay you to try ours—whether you're involved with an aqueous or a fused salt electrolytic process.

With their improved grades of graphite, Airco Speer anodes offer welcome advantages:

1. greater strength;
2. higher density; and
3. higher electrical conductivity—all of which combine to produce
4. lower cell room costs.

What's more, we can machine your slots, holes, bevels and edges to your precise specifications. And in the case of anodes for mercury cells, we maintain careful control over all vanadium levels.

Why not discover just how different cell room anodes can be. Drop us a line.

AIRCO Speer Carbon-Graphite
A Division of Airco, Inc.
ST. MARYS, PENNSYLVANIA 15857

A new series designed with the specialist in mind—

TECHNIQUES IN ELECTROCHEMISTRY

Volume One

Edited by **Ernest Yeager**, Case Western Reserve University
and **Alvin J. Salkind**, ESB Incorporated Research Center

Volume One launches a new series specifically designed to enhance the *practical* ability of electrochemists working with measurement techniques. The contributions are authoritative, complete treatments of basic and advanced practices, augmented by a wealth of illustrative material. Volume One, devoted to *electrode processes*, is scheduled to contain—

Measurement of Reversible Electrode Potentials—**Roger G. Bates**; The Study of the Ionic Double Layer and Adsorption Phenomena—**Richard Payne**; Overpotential Measurements—**Jaroslav Kuta** and **Ernest Yeager**; The Measurement of Surface Area and Porosity—**Alvin J. Salkind**; Special Techniques in the Study of Electrode Processes and Electrochemical Adsorption—**B. E. Conway**; Index.

1972 173 illus. 464 pages (approx.) \$24.95 (tent.)

The first comprehensive book on primary batteries to appear in twenty years—

THE PRIMARY BATTERY

Volume One

Edited by **George W. Heise** and **N. Corey Cahoon**
both Consultants

A Volume in the Electrochemical Society Series

Whether in academics or industry, electrochemists know that for size, capacity, temperature tolerance, and applicability, the primary battery is still the outstanding means for direct conversion of chemical to electrical energy. In *The Primary Battery*, experts now have a contemporary, authoritative exploration of the theoretical and practical evolution of this uniquely versatile instrument.

1971 238 illus. 500 pages \$24.95

From the theoreticians and experimentalists breaking new ground in materials and technology—

ZINC-SILVER OXIDE BATTERIES

Edited by **Arthur Fleischer**, Consulting Chemist and **John J. Lander**, Air Force Aero Propulsion Laboratory

A Volume in the Electrochemical Society Series

This collection of 36 papers from the symposium on zinc-silver oxide batteries sponsored by the Electrochemical Society is a valuable sourcebook for every worker in the field. The contributing authors have brought together a wealth of up-to-date information, providing state-of-the-art material on everything from electrokinetic theory to battery construction processes.

1971 210 illus. 544 pages \$27.95

"...the most comprehensive description yet available of the technology of fuel cells."

—*Journal of the Electrochemical Society*

FUEL CELLS

Modern Processes for the Electrochemical Production of Energy

By **Wolf Vielstich**, Institut für Physikalische Chemie der Universität Bonn

Translated from the German by **D. J. G. Ives**

This comprehensive monograph offers a wealth of factual information on the highly topical direct conversion of heat, chemical and nuclear energy into electrical energy.

"Anyone working in the area of fuel cells will find this book of great value." —*Journal of the Electrochemical Society*

1970 291 illus. 501 pages \$25.00

Established fundamentals and new advances are blended into the new Second Edition of—

CORROSION AND CORROSION CONTROL

An Introduction to Corrosion Science and Engineering By **Herbert H. Uhlig**, Massachusetts Institute of Technology

"... an effective bridge between theory, recent research findings, and modern corrosion control methods. The book is excellent. . . ." —*from a review of the first edition in Chemical and Engineering News*

Topics featured in the new Second Edition include—

- detailed descriptions of critical pitting potentials and stress corrosion cracking
- new data on corrosion fatigue and passivity
- new material on the intergranular corrosion of nonsensitized stainless steels and related alloys
- an elementary account of Pourbaix diagrams

1971 165 illus. 419 pages \$14.95

A complete compendium of concepts and research results—

CORROSION IN NUCLEAR APPLICATIONS

By **Warren E. Berry**, Battelle Memorial Institute

A Volume in The Corrosion Monograph Series, edited by R. T. Foley, N. Hackerman, C. V. King, F. L. LaQue, and Z. A. Foroulis

Practical use of atomic energy principles uncovered an important factor for practitioners in the field: optimizing nuclear power depends on maximizing corrosion control. In this introduction to and survey of the field, the author concentrates on the corrosion problems associated with specific types and subtypes of reactors. Every practical aspect is covered, from corrosion processes in mining nuclear fuels through problems encountered in reactors using fluid (molten and aqueous) fuels.

1971 140 illus. 572 pages \$24.95

wiley

Available at your bookstore or from Dept. 092

WILEY-INTERSCIENCE

a division of JOHN WILEY & SONS, Inc.
605 Third Avenue, New York, N.Y. 10016

In Canada: 22 Worcester Road, Rexdale, Ontario

Prices subject to change without notice.



Galvanic Cells in Molten Sodium Bisulfate

M. C. B. Hotz*

Hydrologic Sciences Division, Inland Waters Branch, Department of the Environment, Ottawa, Ontario, Canada

and R. C. Kerby, and T. R. Ingraham

Extraction Metallurgy Research Section, Mines Branch,
Department of Energy, Mines, and Resources, Ottawa, Ontario, Canada

ABSTRACT

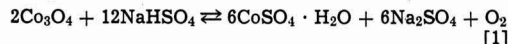
Study of the cells $\text{Pt}, \text{H}_2|\text{NaHSO}_4|\text{H}_2, \text{Pt}$ and $\text{Pt}, \text{H}_2|\text{NaHSO}_4||\text{Ag}_2\text{SO}_4, \text{NaHSO}_4|\text{Ag}$ shows that the hydrogen electrode behaves reversibly in molten sodium bisulfate. Emf's of the cell $\text{Pt}, \text{H}_2|\text{CoSO}_4(m_2), \text{NaHSO}_4||\text{CoSO}_4(m_1), \text{NaHSO}_4|\text{Co}$ in the range 200°–270°C have been used to calculate thermodynamic data for the reaction



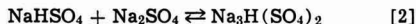
A plot of emf against $\log m_1/m_2$ is linear, but the slope is steeper than predicted.

In previous papers (1,2), we have shown that molten sodium bisulfate and sodium pyrosulfate are the sulfating agents in the sulfate-catalyzed roasting of sulfide ores containing cobalt and nickel. More recently, we have published data on the stability and the thermodynamics of decomposition of these compounds, and a partial phase diagram for the sodium pyrosulfate-water system, in which sodium bisulfate appears as a constituent (3, 4).

The sodium bisulfate roasting cycle includes two reactions that occur simultaneously at temperatures between the melting point of NaHSO_4 (187°C) and 250°C



and



so that it is difficult to obtain thermodynamic and kinetic data for the commercially significant reaction [1]. A possible approach seemed to be through the development of satisfactory nickel and cobalt electrodes in molten sodium bisulfate, and this paper describes attempts to examine the behavior of a cobalt electrode in this environment with respect to a hydrogen electrode.

The literature contains very few papers on the electrochemistry of solutions in molten bisulfates. Tajima, Soda, Mori, and Baba (5) showed that hydrogen and oxygen were obtained in a molar ratio of 2:1 when KHSO_4 was electrolyzed with platinum electrodes, and Shams El Din (6) studied overpotentials in the same system. Le Ber (7) briefly considered the $\text{H}_2|\text{H}^+$ system, but had some difficulty in achieving reversibility. Arvia and his co-workers appear to be the first to have considered the hydrogen electrode as the basis of an electrochemical series in a bisulfate melt (8–10). They found the electrode reaction to be reversible and determined its potential against a silver/silver sulfate refer-

ence electrode. Their attempt to establish an electrochemical series was based on corrosion potentials of a number of metals.

The only other studies of equilibrium systems involving bisulfates are those of Seward and Miller (11) on the $\text{Hg}|\text{Hg}^{2+}$ and $\text{Ag}|\text{Ag}^+$ electrodes in NaHSO_4 and Le Ber (7) on the $\text{Ag}|\text{Ag}^+$ electrode in $\text{KHSO}_4|\text{NaHSO}_4$ eutectic.

The decomposition of molten bisulfate to pyrosulfate poses a major problem in maintaining the purity levels of the bisulfate melts, and those used in many of the investigations quoted were likely contaminated by pyrosulfates, as well as water and sulfuric acid.

Our study of the stability of sodium bisulfate at temperatures between 100° and 400°C showed that sodium bisulfate starts to lose water at temperatures just below the melting point (187°C) to form sodium pyrosulfate. In order to effectively prevent pyrosulfate formation in our sodium bisulfate melts, we used a closed system in the present investigation.

Experimental

Preparation of materials.—Sodium bisulfate was prepared by adding stoichiometric amounts of water to sodium pyrosulfate that had been made by direct reaction between sodium sulfate and sulfur trioxide (4).

Cobalt sulfate was made by heating Fisher Certified $\text{CoSO}_4 \cdot 7\text{H}_2\text{O}$ at 400°C for 8 hr, crushing the product, and reheating for a further 8 hr (1).

Johnson, Matthey and Mallory cobalt wire and platinum foil were washed with acetone and distilled water, and oven-dried before use.

Linde hydrogen was purified by passage through a Deoxo tube, and then over copper mesh at 500°C.

Fisher Certified sodium sulfate was oven-dried at 200°C before use.

The double salt $\text{Na}_2\text{Co}(\text{SO}_4)_2$ was prepared by precipitation of its tetrahydrate from a mixed solution of the two sulfates, followed by dehydration at 400°C for 8 hr.

* Electrochemical Society Active Member.

Key words: galvanic, galvanic cells, molten, sodium bisulfate.

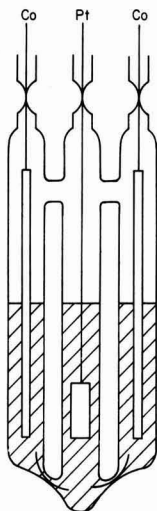


Fig. 1. Cell vessel

Apparatus and procedure: Emf's were measured with a L&N Type K2 potentiometer, using a Pye nanoammeter as a null detector. Readings were steady within 1 mV over periods of several hours.

The cell vessels were made of Pyrex glass; junctions between the half-cell containers were made with asbestos fibers (12). In such dilute solutions the activities would not differ significantly on either side of the junction, and transport should be almost exclusively by the predominating sodium and bisulfate ions. A diagram of the cell is shown in Fig. 1. The outer compartments contained cobalt electrodes and solutions of cobalt sulfate in molten sodium bisulfate. The electrodes were 1.3 mm diameter lengths of cobalt wire welded to 0.4 mm diameter support wires. A piece of bright platinum foil 1 cm² in cross-section was welded to 0.4 mm platinum wire to form the reference electrode in the center compartment. This arrangement permitted two series of measurements to be made simultaneously. The cells were sealed to prevent decomposition of sodium bisulfate, and their construction ensured that all three compartments were at the same pressure during the measurement.

The vessels used for the study of hydrogen electrodes were similar in that junctions were made through asbestos fibers, but some cells were designed to permit bubbling of hydrogen, while others had half cells in which the platinum electrodes were isolated completely from gaseous hydrogen. Various combinations of these half cells were used to check for zero emf between isolated and bubbling electrodes. Reversible behavior of the hydrogen electrodes was also established with respect to a silver/silver sulfate electrode.

The cells were packed in alumina powder in a Pyrex tube that fitted closely into a cylindrical brass block furnace heated by four GE 150W Type 186 H cartridge heaters. The block was insulated by layers of glass wool, firebrick, and transite. Temperatures were controlled by a Honeywell Pulse-Pyrovan unit, and cell temperatures were measured on the K2 potentiometer with a platinum-10% rhodium platinum thermocouple in conjunction with a Kaye Ice-point Reference Standard. Temperature control was within $\pm 0.2^\circ\text{C}$.

Apparatus used for the associated differential thermal analysis and x-ray powder diffraction analysis were described in an earlier paper (2).

Results and Discussion

Differential thermal analyses on mixtures of cobalt powder and sodium bisulfate were done at a programmed temperature increase of $2^\circ\text{C}/\text{min}$ between

Table I.
Pt, H₂ | NaHSO₄ || NaHSO₄ | H₂, Pt

Cells	Emf, V	Flow rate, cc/min	Temperature, °C
Pt:Pt, H ₂ (g _{ss})	0.0003	5.0	233
Pt:Pt	0.0006	—	233
$\text{Ag} \left \text{Ag}_2\text{SO}_4(m) \right \left \text{NaHSO}_4 \right \text{Pt, H}_2$			
Concentration (m)	Emf, V	Temperature, °C	
0.184	-0.183	214.0	
0.184	-0.182	215.0	
0.184	-0.194	240.0	
0.184	-0.200	240.3	
0.184	-0.211	270.0	

room temperature and 500°C . The sodium bisulfate fusion endotherm at 187°C was followed immediately by a large exothermic peak. X-ray powder diffraction analysis identified the products of this reaction as cobalt sulfate and sodium sulfate when the reaction was allowed to proceed at temperatures below 250°C , and the double salt $\text{Na}_2\text{Co}(\text{SO}_4)_2$ when the reaction proceeded above this temperature. Other endothermic peaks appearing at 455° and 470°C were identified as phase transitions of the system $\text{CoSO}_4\text{-Na}_2\text{SO}_4$ (13). Hydrogen was also produced by the above reaction. The suggested stoichiometry is



This is apparently the reaction for the galvanic cell Pt, H₂|NaHSO₄, CoSO₄(m₂)||NaHSO₄, CoSO₄(m₁)|Co. Measurement of the emf's of such a cell in which $m_1 = m_2$ should provide thermodynamic data for reaction [3], if the cobalt and hydrogen electrodes operate reversibly in a bisulfate melt.

In order to demonstrate that a reversible hydrogen electrode is formed in molten sodium bisulfate, the cells Pt, H₂|NaHSO₄||NaHSO₄|H₂, Pt and Pt, H₂|NaHSO₄||NaHSO₄, Ag₂SO₄|Ag were examined, and the results are shown in Table I.

The potential of the platinum/hydrogen electrode is shown to be independent of the gaseous hydrogen partial pressure, implying that the melt is saturated with respect to hydrogen and that the activity of the hydrogen in the melt is constant. Arvia (9) has demonstrated that a reversible hydrogen electrode is formed in potassium bisulfate melts, and that once the platinum electrode was saturated with hydrogen from the cathodic reaction, bubbling hydrogen over its surface did not change the emf. In the present case, it would appear that the platinum surface has become saturated with hydrogen without the necessity of a prior electrolysis to saturate the surface; alternatively, mere adjustment of the potentiometer balance may have sufficed to saturate the surface.

The emf of the cell, H₂, Pt|NaHSO₄||NaHSO₄, Ag₂SO₄|Ag varies linearly with temperature and is reversible (Table I). The hydrogen electrode has also been found to be reversible with respect to a silver/silver sulfate electrode in the systems KHSO₄ (9), KHSO₄|NaHSO₄ eutectic (7), and NH₄HSO₄ (11). Because the potential of the hydrogen electrode does not vary with the partial pressure of hydrogen gas, melt decomposition to pyrosulfate can be prevented by using platinum immersed in the melt in a sealed system as a reversible hydrogen electrode. This also prevents contamination with atmospheric moisture; sealed vessels were therefore used in the experiments involving the cobalt electrode.

The range of molalities in which a cobalt electrode will function reversibly is restricted by the corrosion of the metal by sodium bisulfate, and by the solubility of cobalt sulfate in the melt. In experiments using the cell Pt, H₂|CoSO₄(m₂)||NaHSO₄|CoSO₄(m₁)|NaHSO₄|Co, for the determination of the thermodynamic data

Table II.

Emf of the cell $\text{H}_2 | \text{CoSO}_4(m_2), \text{NaHSO}_4 || \text{CoSO}_4(m_1), \text{NaHSO}_4 | \text{Co}$
(0.0350m) (0.0350m)
and thermodynamic data for the reaction
 $\frac{1}{2}\text{Co} + \text{NaHSO}_4 = \frac{1}{2}\text{Na}_2\text{SO}_4 + \frac{1}{2}\text{CoSO}_4 + \frac{1}{2}\text{H}_2$

Temperature, °K	Emf, V	$-\Delta G$, cal	Equilibrium constant	$-\Delta H$, kcal
475.2	-0.3314	7644	3270.0	34.0
496.4	-0.2761	6369	636.0	34.4
501.2	-0.2707	6245	528.0	34.5
518.9	-0.2305	5316	173.0	34.6
542.0	-0.1671	3853	35.8	34.4
543.0	-0.1645	3794	33.7	34.4

Table III.

Emf of the cell $\text{H}_2 | \text{CoSO}_4(m_2), \text{NaHSO}_4 || \text{CoSO}_4(m_1), \text{NaHSO}_4 | \text{Co}$
at 511.2°K. $m_1 = 0.0350\text{m}$

m_2 , mole kg ⁻¹	Emf, V
0.0177	-0.2668
0.0350	-0.2425
0.0530	-0.2301
0.0750	-0.2152

for reaction [3], the molalities m_1 and m_2 were set at 0.0350m. Effective inhibition of corrosion by the solute at this concentration was indicated by the absence of observable attack on the cobalt electrode during the course of an experiment. Emf's were measured at temperatures between 200° and 270°C, and were found to vary linearly with temperature. The measured emf's were constant within 1 mV for several hours. This excludes the possibility of mixed potentials due to continuing corrosion of the cobalt electrode, which would change the cobalt ion activity in the melt and alter the emf.

The measured emf's and the calculated free energies, enthalpies, and equilibrium constants for reaction [3] are shown in Table II. The entropy change for the corrosion of cobalt by molten sodium bisulfate is $\Delta S = 56.4 \pm 1.4$ eu. Using standard entropy values for aqueous solutions for a comparison

$$\Delta S = \frac{1}{2}S^\circ_{\text{H}_2(\text{g})} + \frac{1}{2}S^\circ_{\text{Na}_2\text{SO}_4(\text{aq})} + \frac{1}{2}S^\circ_{\text{CoSO}_4(\text{aq})} - \frac{1}{2}S^\circ_{\text{Co(s)}} - S^\circ_{\text{NaHSO}_4(\text{l})} \quad [4]$$

provides an entropy change of $\Delta S^\circ = 51.9$ eu at 500°K. Application of the van't Hoff isochore to the equilibrium constant data leads to an enthalpy at 500°K of $\Delta H = -34.5$ kcal · mole⁻¹, in good agreement with values calculated from the Gibbs-Helmholtz equation, providing further justification for the validity of the data.

Addition of an equivalent molar amount of sodium sulfate to the cobalt electrode vessel did not change

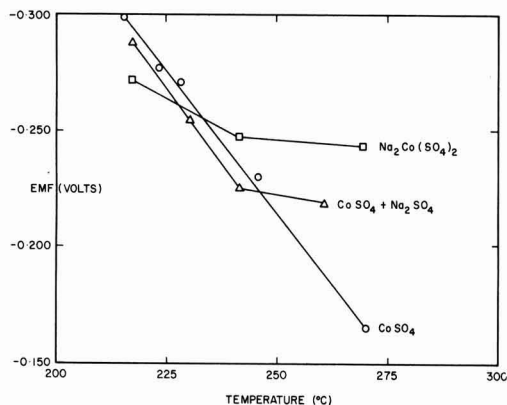


Fig. 2. Effect of addition of Na_2SO_4 and $\text{Na}_2\text{Co}(\text{SO}_4)_2$ on the emf of $\text{Pt}, \text{H}_2 | \text{CoSO}_4(m_2), \text{NaHSO}_4 || \text{CoSO}_4(m_1), \text{NaHSO}_4 | \text{Co}$.

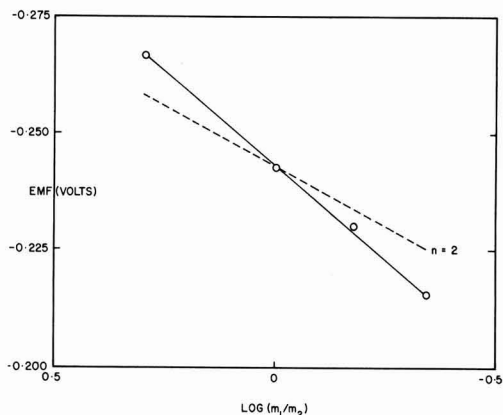


Fig. 3. Theoretical (---) and observed (—) Nernst plots for $\text{Pt}, \text{H}_2 | \text{CoSO}_4(m_2), \text{NaHSO}_4 || \text{CoSO}_4(m_1), \text{NaHSO}_4 | \text{Co}$.

the slope of the emf-temperature relationship below 240°C, but the measured emf's were about 10 mV lower. Above 250°C, however, there is a marked change in slope, the new slope approximating that found when cobalt sulfate and sodium sulfate are replaced by an equal amount of the double salt $\text{Na}_2\text{Co}(\text{SO}_4)_2$. These effects are shown in Fig. 2. Seward and Miller (11) observed that the addition of sulfate ion to their cell lowered the emf, implying an increase in the activity of the silver ion. In spite of viscosity studies that indicated structural changes in the melt, they were unable to explain the increase in silver ion activity. The same effect occurs in the present work with the cobalt electrode, an increase in cobalt ion activity occurring on addition of sodium sulfate. Sodium bisulfate forms highly structured melts (14), with extensive hydrogen bonding (15), and it seems likely that the added sulfate ions would be incorporated into this structure. This would reduce association of the divalent sulfate ion with the cobalt ion, thereby increasing its activity. At higher temperatures, where the hydrogen bonding breaks down, this trend should be reversed, as is evidenced by the behavior of the cells on sulfate addition at temperatures above 250°C.

A series of experiments were done with the cell $\text{Pt}, \text{H}_2 | \text{CoSO}_4(m_2), \text{NaHSO}_4 || \text{CoSO}_4(m_1), \text{NaHSO}_4 | \text{Co}$ in which the molality m_1 was maintained at 0.0350m, and m_2 varied between 0.0177 and 0.0750m. Emf's measured at 238°C are shown in Table III; the cells usually reached equilibrium within 6-7 hr. A plot of emf against the logarithm of the ratio of the molalities is linear but the slope is about 55% steeper than that predicted by the Nernst equation (Fig. 3).

Although the Nernst slope indicates that the behavior of the cobalt ion in a bisulfate melt is complex, this effect may be qualitatively explained by reasoning similar to that used for the addition of sodium sulfate, that is, the incorporation of sulfate ion into the melt structure effectively increases the cobalt activity.

Acknowledgment

The authors are grateful to M. R. Hughson for the x-ray power diffraction analyses.

Manuscript submitted Aug. 25, 1969; revised manuscript received July 21, 1971. This was Paper 284 presented at the Boston Meeting of the Society, May 5-9, 1968.

Any discussion of this paper will appear in a Discussion Section to be published in the December 1972 JOURNAL.

REFERENCES

1. M. C. B. Hotz and T. R. Ingraham, *Can. Met. Quart.*, **4**, 295 (1965).

2. M. C. B. Hotz and T. R. Ingraham, *ibid.*, **5**, 237 (1966).
3. T. R. Ingraham and M. C. B. Hotz, *ibid.*, **7**, 139 (1968).
4. M. C. B. Hotz and T. R. Ingraham, *ibid.*, **7**, 147 (1968).
5. S. Tajima, M. Soda, T. Mori, and N. Baba, *Electrochim. Acta*, **4**, 205 (1959).
6. A. M. Shams El Din, *ibid.*, **7**, 613 (1962).
7. F. Le Ber, Commissariat à l'Energie Atomique. Rapport CEA-R-2567 (1964).
8. H. A. Videla and A. J. Arvia, *Electrochim. Acta*, **10**, 21 (1965).
9. A. J. Arvia, A. J. Callandra, and H. A. Videla, *ibid.*, **10**, 33 (1965).
10. A. J. Arvia and H. A. Videla, *ibid.*, **11**, 537 (1966).
11. R. P. Seward and J. P. Miller, *J. Phys. Chem.*, **69**, 3156 (1965).
12. S. N. Flengas and T. R. Ingraham, *Can. J. Chem.*, **35**, 1139 (1957).
13. K. A. Bolshakov and P. I. Federov, *Zh. Obshch. Khim.*, **26**, 348 (1956).
14. S. E. Rogers and A. R. Ubbelohde, *Trans. Faraday Soc.*, **46**, 1051 (1950).
15. M. C. B. Hotz and N. J. Ramey, Extended Abstracts Electrochem. Soc. (Industrial Electrolytic Div.), **5**, 501 (1969).

Electrode Processes in Sodium Polysulfide Melts

K. D. South, J. L. Sudworth, and J. G. Gibson

British Railways Research Department, Derby, England

ABSTRACT

Results are reported of three-electrode measurements in sodium polysulfide melts. The composition range covered was Na_2S_3 - Na_2S_5 and the temperature range 300°-400°C. The electrode material used was vitreous carbon. Voltammetric, chronopotentiometric, and current interruption techniques were used to investigate cathodic and anodic processes. Evidence is produced that sulfide films are formed at the cathode and that these result in limiting currents. The lowest value of limiting current density was 28 $\text{mA} \cdot \text{cm}^{-2}$ obtained for Na_2S_3 at 350°C. At the anode the current appears to be limited by accumulation of liquid sulfur. The value of the limiting current density in Na_2S_5 was 100 $\text{mA} \cdot \text{cm}^{-2}$ at 350°C. A reaction scheme which best fits our results is suggested.

Interest in the electrochemistry of sodium polysulfides has recently been stimulated by the development of the sodium/sulfur battery (1-3), in which the overall process at the cathode is the reduction of sulfur to sulfide ions. In order to gain a further understanding of the electrode processes we decided to study the behavior of a nonporous carbon electrode in three different polysulfide melts. Vitreous carbon was deemed a suitable material for this purpose.

Following a suggestion (4) that lithium polysulfides might exhibit electronic conductivity, we decided to investigate the electronic conductivity of sodium polysulfides. Although this work is not yet complete, preliminary results indicate that the electronic contribution to the conduction in these melts is very small, and in the interpretation of our results we have assumed electronic conductivity in these melts to be negligible.

The phase diagram for the system $\text{Na}_2\text{S}/\text{S}$ has been constructed by Pearson and Robinson (5) and revised by others (6,7). At 350°C, if precipitation of solids is to be avoided, the sodium content of the melt must not exceed 40 atomic per cent (a/o) (Na_2S_3). Experience in our laboratory indicates that polarization of the sulfur electrode is most severe in the one-phase region (Na_2S_3 - Na_2S_5). We therefore decided to study three different compositions corresponding to melts in this region, viz., $\text{Na}_2\text{S}_{3.5}$ (two-phase, Na_2S_3 + sulfur), Na_2S_4 , and Na_2S_5 . Results in $\text{Na}_2\text{S}_{3.5}$ refer to the sulfide-rich phase (Na_2S_3).

Very little work has been reported on the electrochemistry of the alkali metal polysulfides, but recently, mass transfer effects in molten $\text{Na}_2\text{S}/\text{S}$ mixtures were investigated by Selis (8). He used voltammetric sweeps to distinguish between the electrode behavior in the two liquids present in the two-phase region. Results in the sulfide-rich phase indicated that the current maxi-

mum was associated with an irreversible oxidation process. At cathodic potentials a current maximum followed by a current surge was observed. In a recent paper by Bodewig and Plambeck (9) concerning the S^{2-}/S^0 electrode in molten LiCl-KCl , a voltammetric curve was shown for the reduction of S^0 to S^{2-} at a graphite electrode. Only one current surge was evident.

In this work we have used voltammetric sweeps, current interruption experiments, and chronopotentiometry in an attempt to determine the electrode reactions.

Experimental

Apparatus.—Voltammetry experiments were performed with a Wenking 61 RH Potentiostat coupled to a Wenking SMP 61 sweep unit (max rate 50 $\text{mV} \cdot \text{sec}^{-1}$). A few faster cyclic voltammetric sweeps were performed with the potentiostat coupled to a Hewlett-Packard 3310A function generator. Voltammetric curves were recorded on a Bryans 26000 Series XY plotter. Chronopotentiometric experiments were carried out with the aid of a 5A max constant current unit in conjunction with a mercury-wetted relay switch. Both pieces of equipment were built in the laboratory. Chronopotentiograms were recorded on the Bryans XY plotter set in the Y/t mode. Electrode potentials were measured with a Vibron electrometer backed-off with a Pye portable potentiometer. A Techne fluidized sand bath was used to maintain the temperature at 300°-400°C. A molten salt bath would have allowed better temperature control, but was not used for safety reasons. Temperature control was by "Cal" proportional controller unit, which maintained the temperature to $\pm 3^\circ\text{C}$.

The experimental cell is shown diagrammatically in Fig. 1. The side arm containing a porous sinter was incorporated to enable melt to be filtered *in situ* into the electrochemical compartment. Ground-glass joints were greased with Apiezon T compound.

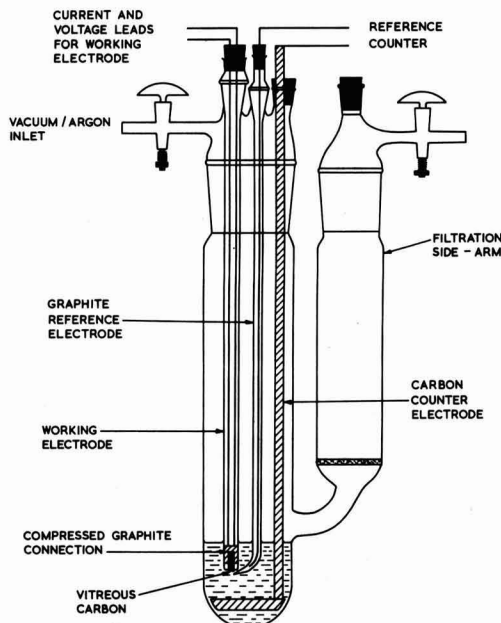


Fig. 1. Electrochemical cell assembly

Electrodes.—A conventional three-electrode assembly was used. The working electrode material, vitreous carbon, was supplied in the form of 0.32 cm diameter rod. A short length was sealed into a Pyrex tube and faced off to expose a disk of area 0.08 cm². The electrode was polished to 0.25 μ surface finish. The sealing of vitreous carbon rod into Pyrex was carried out by the Allen Clarke Research Centre, Towcester, following several unsuccessful attempts in our laboratory to obtain a leakproof seal. The counterelectrode consisted of a large carbon disk attached to a threaded carbon rod; both pieces were spectrographic grade porous carbon. Electrode potentials were measured using a carbon/sodium polysulfide reference electrode. This electrode, which consisted of a strip of flexible graphite sheet ("Grafoil," Union Carbide Corporation) immersed in a melt of the same composition as the bulk melt, was contained in a Luggin capillary. The potential of this carbon/polysulfide reference electrode which has been shown to be reversible (10), was consequently dependent upon the composition of the melt under investigation. All electrode potentials have therefore been corrected to the carbon/Na₂S₅/S electrode, using the potential/composition relationship for the cell Na/ β alumina/Na₂S_x/carbon (where $x = 3-5$), determined independently by Gupta and Tischer (7) and Davies (10).

Melt.—Sodium polysulfide (Na₂S₃) was prepared electrochemically in a specially designed sodium/sulfur cell. Special care was taken in handling the sodium trisulfide which was removed from the preparation cell in the molten state using a large argon-purged pipette. This was allowed to cool, transferred to a glove box and removed from the pipette by breaking the glass. A dry argon atmosphere was maintained at all times in the glove box, where the trisulfide was stored until required. Higher polysulfides were obtained from the trisulfide by mutually melting with the appropriate amount of sulfur.

Procedure.—The introduction of electrolyte into the filtration side arm of the cell was done in the glove box. The electrolyte was filtered into the cell through a porosity 4 sinter under an argon atmosphere.

On completion of the filtration, rest potentials of both counter and working electrodes were measured. The cell impedance was also determined using an a-c bridge (automatic Wayne Kerr B641). These measurements were repeated at intervals of 1-2 days as a check on the condition of the cell and electrodes. Experiments were continued on any one melt for a maximum of 10 days.

Voltammetric curves were obtained at different sweep rates at both positive and negative potentials. In each case the start of the sweep corresponded to the initial rest potential of the electrode which was 2-3 mV, wrt the graphite reference electrode described previously. After each run the electrode was allowed to attain its rest potential before proceeding with further measurements.

The interruption experiments were performed by holding the electrode at a given potential with the potentiostat for 1 min, opening the circuit with a high speed switch and simultaneously recording the subsequent behavior of the electrode potential with time on an oscilloscope (Hewlett Packard 141) or an XY recorder. The rise times of the switch and the oscilloscope were less than 1 μ sec.

The procedure for chronopotentiometric measurements was straightforward using the equipment already described. The same cell and electrode geometry were employed.

Results

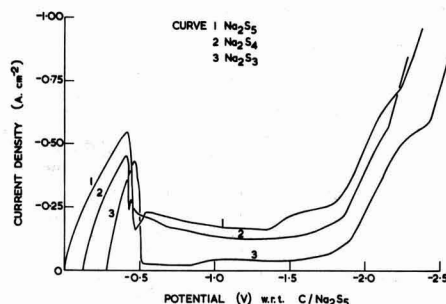
Voltammetry.—Cathodic voltammetric curves at 350°C are shown in Fig. 2. Salient features are a current maximum followed by a sharp drop in the current, a region of limiting current and a final current surge at about -1.7 to -1.8V. The height of the current peak was proportional to the square root of the sweep rate, in accordance with the equation for peak voltammetry (11).

$$i_p = K n^{3/2} D^{1/2} C v^{1/2} \quad [1]$$

where i_p = peak current density; K = Randles-Sevcik constant, n = number of electrons transferred, D = diffusion coefficient, C = bulk concentration of reducible species, and v = potential sweep rate.

Values of the slope of the plot i_p vs. $v^{1/2}$ which was a good straight line, were 1.9 - 2.1 A \cdot V^{-1/2} \cdot cm⁻² \cdot sec^{1/2} and showed no significant variation with melt composition. Peak potentials were displaced in the cathodic direction with increasing sweep rates suggesting uncompensated IR effects due to the large currents obtained. In successive runs at lower sweep rates, a second, more complex peak appeared on the curves (Fig. 3). The height of this peak was virtually constant below sweep rates of 16 mV \cdot sec⁻¹.

Values of the limiting current were determined in each melt at sweep rates at which they became constant (less than 10 mV \cdot s⁻¹). Actual values at 350°C were 28 mA \cdot cm⁻² in Na₂S₃; 45 mA \cdot cm⁻² in Na₂S₄; and 100 mA \cdot cm⁻² in Na₂S₅. The temperature dependence of limiting current density in Na₂S₃ is shown in Fig. 4.

Fig. 2. Cathodic voltammetric curves for different melt compositions at 350°C. Sweep rate v , 50 mV \cdot sec⁻¹.

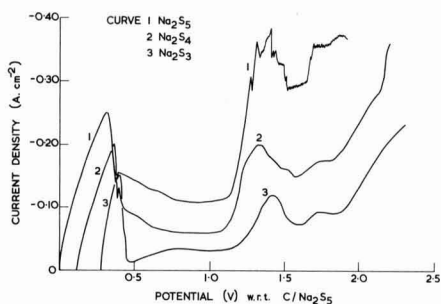


Fig. 3. Cathodic voltammetric curves for different melt compositions at 350°C showing the second current maxima. Sweep rate v , 8.33 $\text{mV} \cdot \text{sec}^{-1}$.

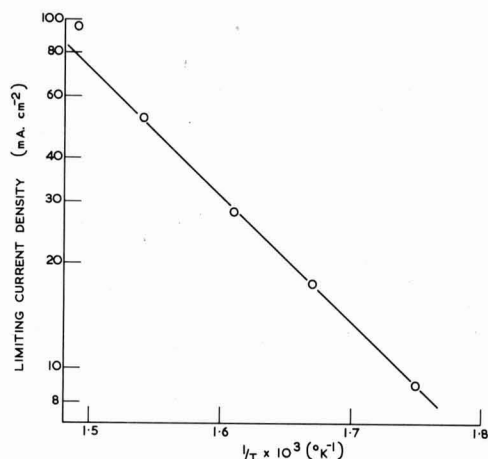


Fig. 4. Temperature dependence of the limiting current density for the composition Na_2S_3 .

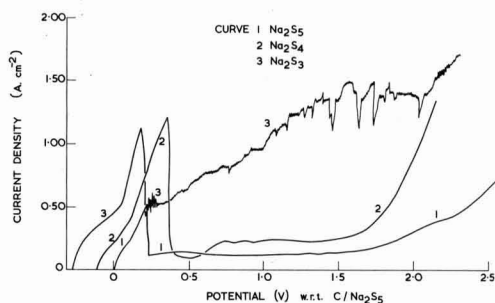


Fig. 5. Anodic voltammetric curves for different melt compositions at 350°C. Sweep rate v , 50 $\text{mV} \cdot \text{sec}^{-1}$.

Results of anodic voltammetric sweeps are shown in Fig. 5. These curves were less reproducible than the corresponding cathodic ones. This was particularly so in the case of the Na_2S_3 melt composition. In this melt the curve rarely showed a current maximum. The current continued to increase up to a value corresponding to the maximum capability of the potentiostat. When a current peak was obtained in this melt as in Fig. 5, it was followed by a region of oscillating current. In the other two melt compositions the current maximum was followed by a limiting current region. The value of the limiting current in Na_2S_5 was about $100 \text{ mA} \cdot \text{cm}^{-2}$. Again the height of the current density peak was proportional to the square root of the sweep rate. In Na_2S_4 the value of the slope,

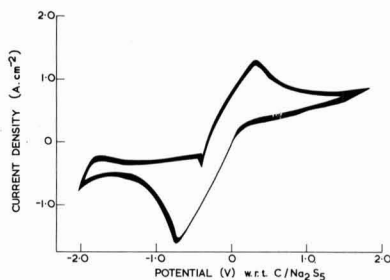


Fig. 6. Cyclic voltammogram pattern for the composition Na_2S_4 at 350°C. Sweep rate v , 0.4 $\text{V} \cdot \text{sec}^{-1}$.

$5.5 \text{ A} \cdot \text{V}^{-1/2} \cdot \text{cm}^{-2} \cdot \text{sec}^{1/2}$, was more than twice the value obtained from the cathodic results. However, in Na_2S_5 the value of slope of $0.8 \text{ A} \cdot \text{V}^{-1/2} \cdot \text{cm}^{-2} \cdot \text{sec}^{1/2}$ was less than half the corresponding cathodic value.

An example of a cyclic voltammogram is shown in Fig. 6. Noteworthy features are the peak separation of a 1.04V, and the greater height of the cathodic current maximum. The peak separation is very much greater than the value expected at 350°C for a reversible couple (11).

In the single sweeps the anodic current maximum was higher than the cathodic one in this composition, yet this situation is reversed in the cyclic sweep.

Interruption experiments.—These experiments were conducted in two different melts and the results for Na_2S_3 are given in Table I. Results for Na_2S_5 showed a similar trend although values of R were generally lower. Anodic experiments were not conducted above 120 mV in Na_2S_3 as the current exceeded the maximum control capability of the potentiostat. An initial sharp drop, ΔE , in the potential was noted. This was ascribed to IR drop and found to occur in less than 1 μsec . From the knowledge of I , the current flowing prior to switch off, a value for the electrode resistance, R , was obtained. Both sets of results showed an increase in the electrode resistance up to approximately -1.1V , thereafter the resistance showed a decreasing trend. Another significant feature was the sharp increase in the resistance at cathodic potentials which approximately correspond to the initial current density maxima on the voltammetric curves. Two stable potentials were evident on the cathodic decay curves, one at -340 mV and the other at about -1.9V .

Chronopotentiometry.—All measurements were made with a vitreous carbon disk electrode of geometric area 0.08 cm^2 . Figure 7 shows a chronopotentiogram for Na_2S_3 together with the potential decay curve

Table I. Results of interruption experiments in Na_2S_3 at 350°C
Geometric electrode area = 0.08 cm^2

Potentiostated potential (mV) wrt C/Na ₂ S ₃	Current, I (mA)	E (mV)	Resistance R (ohm)	Potential following interruption (mV) wrt C/Na ₂ S ₃
120	60	130	2.2	-10
20	30	70	2.3	-50
-80	5.8	12	2.1	-95
-180	3.0	16	2.0	-190
-330	1.9	4	2.1	-326
-380	3.8	8	2.1	-372
-430	2.5	86	34	-340
-480	2.4	140	58	-340
-680	2.4	230	96	-340
-880	2.4	430	180	Arrest at -450
-1080	2.4	640	266	Arrest at -450
-1280	5.6	940	168	Arrest at -450
-1480	8.8	1140	130	-340
-1680	6.2	200	32	-346
-1880	3.3	40	12	Arrest at -1480 & -450
-2280	8.8	350	40	-1840
-2680	220	770	3.5	-1930
				-1910

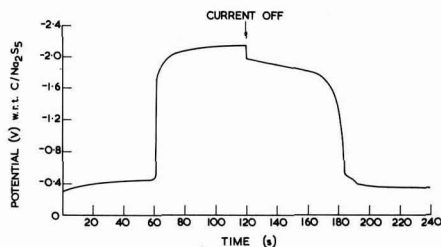


Fig. 7. Chronopotentiogram for the composition Na_2S_3 at 350°C , showing the potential decay pattern after switching off the current. Current density, $80 \text{ mA} \cdot \text{cm}^{-2}$.

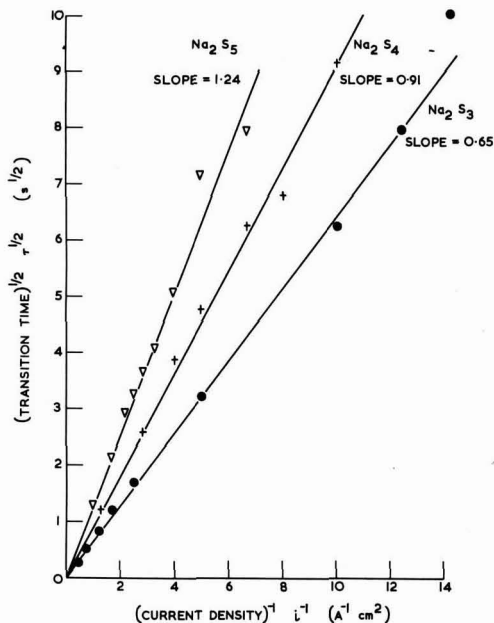


Fig. 8. Chronopotentiometric results. Dependence of $\tau^{1/2}$ on i^{-1} for different melt compositions at 350°C .

following the opening of the circuit. The chronopotentiograms obtained in Na_2S_4 and Na_2S_5 were similar.

For cathodically impressed currents the observed transition time, τ , is proportional to the reciprocal of the current density. Results are shown in Fig. 8 and suggest that the process is controlled by diffusion in accordance with the Sand equation

$$i\tau^{1/2} = \frac{1}{2}\pi^{1/2}nFCD^{1/2} \quad [2]$$

where symbols have their usual significance and i is the current density.

Anodic chronopotentiograms were only recorded for Na_2S_5 . The traces were again characterized by very sharp end points. The observed transition times, however, were not in accordance with the Sand equation since the plot of $\tau^{1/2}$ vs. i^{-1} was nonlinear.

Discussion

The linear dependence of both i_p and $\tau^{1/2}$ on $v^{1/2}$ and i^{-1} respectively suggests that the electroactive species are transported predominantly by a diffusion process. Simultaneous solution of the voltammetric and chronopotentiometric equations gave a value of K , the Randles-Sevcik constant, which was dependent on melt composition, viz., 1.95×10^{-5} in Na_2S_3 , 1.3×10^{-5} in Na_2S_4 , and 1.0×10^{-5} in Na_2S_5 . The theoretical value of the constant at 350°C for a reversible process

is 1.88×10^{-5} (13). Experimental values are therefore in fair agreement with the theoretical value particularly in the Na_2S_3 melt where the agreement is within 5%. This suggests that under these experimental conditions effects other than those due to diffusion can be neglected. This is somewhat surprising in view of the fact that no supporting electrolyte was used.

From the shape of the cathodic voltammetric curves it is evident that several processes are occurring at the electrode. Unfortunately, lack of experimental data on the species present in sodium polysulfide melts makes interpretation of our results rather difficult. Recently, however, some data (10) on the activity of sulfur in the melts have become available. Values obtained were 0.9 in Na_2S_5 , 0.2 in Na_2S_4 , and 0.04 in Na_2S_3 . In the light of these results we are inclined to ascribe the first current maximum in all melts to the reduction of a polysulfide ion rather than elemental sulfur. This step appears to be diffusion-controlled as indicated by the linear dependence of i_p on $v^{1/2}$. The chronopotentiometric results also confirm diffusion-control, and further imply that the diffusing species is not the same in all melts. Analysis of the current maxima over a range of sweep rates yields horizontal straight line plots of $i_E/v^{1/2}$ vs. $v^{1/2}$, (where i_E is the current density at a potential, E , less cathodic than E_p) suggesting a fast, reversible electron-transfer process. Further analysis of the current maxima indicates the occurrence of a following chemical reaction, thus the plot of $i_p/v^{1/2}$ vs. $v^{1/2}$ which should be a horizontal straight line for an uncomplicated electron-transfer step shows a positive deviation from linearity at low sweep rates in accordance with the diagnostic criteria for a chemical reaction following the initial electrochemical step (12). This is found in Na_2S_5 and Na_2S_4 melts but not in Na_2S_3 as seen in Fig. 9. We therefore conclude that this chemical step involves elemental sulfur.

The sharp drop in the current following the initial maximum could be associated with the formation of a film of Na_2S_2 . The fact that this sharp drop is observed even at very low sweep rates ($0.6 \text{ mV} \cdot \text{min}^{-1}$) tends to support the formation of a film. The sharpness of the transitions in the chronopotentiograms are also indicative of film formation. The reduction of a higher polysulfide ion could give rise to S_2^{2-} ions which would precipitate in accordance with the phase diagram. Other S_2^{2-} ions could diffuse away into the bulk melt and recombine with sulfur to form the original polysulfide ion. This step would constitute the chemical step observed in Na_2S_5 and Na_2S_4 melts. The fact that the following chemical reaction is faster in Na_2S_5 (see Fig. 9) which is the melt having the highest sulfur activity lends support to the above explanation.

In Na_2S_5 and Na_2S_4 there is evidence of a small current peak immediately following the initial peak (Fig. 2 and 3). This could be associated with the re-

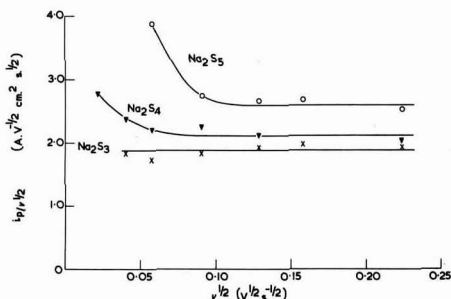


Fig. 9. Dependence of the voltammetric function $i_p/v^{1/2}$ on $v^{1/2}$ for cathodic sweeps in different melt compositions at 350°C showing the effect of a following chemical reaction at lower sweep rates [Ref. (12)].

duction of either elemental sulfur or a different polysulfide ion.

In the region of limiting current, the resistance ascribed to the film of Na_2S_2 continues to increase to a maximum at about -1.1V . In Na_2S_3 , where the activity of sulfur is very low, we might expect a more stable film since the rate of reaction of the film with sulfur to form higher polysulfides will be much slower. This is in fact the case, as indicated by the high values of electrode resistance obtained in this melt.

The second current maximum, which is observed at about -1.3V , we believe to be associated with the reduction of the Na_2S_2 film to Na_2S . At this potential, however, the value of the electrode resistance began to decrease (Table I). This may be interpreted as the faster rate of dissolution of Na_2S than Na_2S_2 in the bulk melt. Alternatively, the film of Na_2S may assume some degree of electronic conductivity although there does not appear to be any independent evidence for this.

We believe the final current surge to be associated with the production of metallic sodium. This is contrary to the suggestion put forward by Selis that this surge is due to the formation of sulfide ions. Our opinion is substantiated by the agreement between the corresponding potential, about -1.8V , and the free energy of formation of sodium polysulfides (7). Maintaining the electrode at potentials more cathodic than -1.9V resulted in a potential of about -1.9V persisting for several minutes after the current had been switched off. The existence of metallic sodium at the electrode in such a reactive medium could be explained by a thin sodium ion conducting film of Na_2S protecting the metal from the melt.

The shape of the anodic current maximum suggests the occurrence of two different electrochemical steps. The first process could be the oxidation of a lower polysulfide ion to form a higher species. As the potential is increased the higher polysulfide is then itself oxidized, and the current increases until the point is reached when the electrode becomes covered by a film of liquid sulfur. The current therefore drops sharply and is subsequently limited by this film. This situation would be accentuated in melts containing sulfur at a higher activity, which was found to be the case. Conversely, the electrochemically produced sulfur could react quite rapidly with Na_2S_3 and this would explain the rarity of a limiting current in this melt.

The final current surge at around 1.8V on the voltammetric curves is difficult to explain. One explanation could be interference by the products of a cath-

odic process at the counterelectrode, although the high current reached renders this view somewhat doubtful.

Conclusions

At the carbon cathode the first step in the reduction of sodium polysulfide appears to be the reversible formation of a lower polysulfide species. In Na_2S_4 and Na_2S_5 melts this is followed by a chemical reaction involving sulfur. Available evidence suggests that the current becomes limited by the formation of sodium sulfide films at the electrode. At higher potentials, -1.7 to -1.8V , metallic sodium is formed.

At the anode the current is limited by the formation of a film of liquid sulfur and this limitation is greatest in the Na_2S_5 melt.

Acknowledgments

The authors express thanks to the British Railways Board for permission to publish this paper and acknowledge the helpful discussions with Dr. B. Cleaver of Southampton University.

Manuscript submitted Oct. 7, 1971; revised manuscript received ca. Dec. 21, 1971.

Any discussion of this paper will appear in a Discussion Section to be published in the December 1972 JOURNAL.

REFERENCES

1. J. K. Kummer and N. A. Weber, Society of Automotive Engineers, Automotive Engineering Congress, Detroit, Mich., January (1967).
2. L. J. Miles and I. Wynn Jones, "Proceedings of the 6th International Power Sources Symposium Brighton 1970."
3. J. L. Sudworth and M. D. Hames, "Proceedings of the 6th Power Sources Symposium, Brighton, 1970."
4. E. J. Cairns, Private communication (1970).
5. T. G. Pearson and P. L. Robinson, *J. Chem. Soc.*, **132**, 1473 (1930).
6. M. D. Hames, Thesis, University of Southampton (1970).
7. N. K. Gupta and R. P. Tischer, Abs. 344, p. 769, Electrochem. Soc. Extended Abstracts, Spring Meeting, Los Angeles, May 10-15, 1970.
8. S. M. Selis, *Electrochim. Acta*, **15**, 1285 (1970).
9. F. G. Bodewig and J. A. Plambeck, *This Journal*, **116**, 607 (1969).
10. A. Davies, Private communication.
11. R. N. Adams, "Electrochemistry at Solid Electrodes," Chap. 5, Marcel Dekker, Inc., New York (1969).
12. R. S. Nicholson and I. Shain, *Anal. Chem.*, **36**, 706 (1964).
13. P. Delahay, "New Instrumental Methods in Electrochemistry," p. 119, Interscience, New York (1954).

The Electrochemical Activity of Dispersed Platinum

K. F. Blurton,* P. Greenberg, H. G. Oswin,* and D. R. Rutt

Energetics Science Inc., New York, New York 10470

ABSTRACT

A highly dispersed platinum catalyst (platinum crystallite size less than 15Å) on a conductive carbon support was prepared. These doped carbons were made into Teflon-bonded fuel cell electrodes and the platinum surface area and the dispersed platinum specific activity (i.e., the activity per unit area of platinum) for oxygen electroreduction in acid electrolyte was determined. The specific activity of the dispersed platinum was found to be approximately twenty times less than that of crystalline platinum black. The lower activity of this catalyst compared with that of platinum black may be due either to the difference in the platinum crystallite sizes, or to the influence of the support on the platinum activity, or to a combination of both these factors.

To build low cost acid electrolyte fuel cells with platinum as the cathode catalyst, it is desirable to utilize Pt with the maximum activity and one method of achieving this is to use Pt with the maximum surface area. High degrees of dispersion of Pt (defined as the ratio of surface metal atoms to total number of atoms) have been prepared by supporting the platinum on a porous, conducting substrate. However a basic question which must be answered before using these supported Pt catalysts is whether the support and/or Pt crystallite size affects the platinum specific activity (i.e., the activity per unit area of Pt).

Many dispersed metal catalysts supported on non-metallic substrates have been prepared (1, 2) and in some cases the ultimate goal of an atomic dispersion of the metal has been claimed (3, 4). These dispersed metal catalysts have been used in many studies with gas reactants. The reactions have been divided into two classes: structure insensitive or facile reactions and structure sensitive or demanding reactions. Examples of the former are the dehydrogenation of cyclohexane (5), the hydrogenation of ethylene (6), and the hydrogenation of cyclopropane (7). Examples of demanding (1) reactions are propane cracking (8), the hydrogenation of benzene (9), ethane hydrogenolysis (10), and the isomerization of neopentane (11).

To relate the specific activity of metals and supported metals to the metal crystallite size, the catalyst activity free of mass transfer limitations and the catalyst area must be measured. Zeliger (12) showed that the specific activity of Pt supported on asbestos for the electroreduction of oxygen was constant for Pt crystallites in the range of 50-100Å. Bett *et al.* (13) extended this observation and showed that the specific activity of unsupported Pt for the same reaction was independent of the Pt crystallite size in the range of 100-400Å. Thus it would appear that this reaction was facile. However these observations may not be applicable to smaller Pt crystallites since the influence of the crystallite size on the specific activity of a metal is expected (1) to be much more significant for crystallites smaller than 40Å.

In the present paper we describe the preparation of a highly dispersed platinum catalyst (platinum crystallite size less than 15Å) on a conductive carbon support and the specific activity of this dispersed Pt for oxygen electroreduction. Polarization curves for oxygen reduction on Teflon-bonded diffusion electrodes prepared from these catalysts were determined in oxygen-saturated 20% H_2SO_4 solution at 70°C and the Pt area of the catalyst was measured by the electrochemical oxidation of adsorbed hydrogen and of adsorbed carbon monoxide. We have shown that the specific activity of this highly dispersed Pt for the

electroreduction of oxygen is approximately twenty times less than that of crystalline Pt black.

High dispersions of Pt on nonconducting supports have been prepared either by localizing metal ions at specific sites by ion exchange prior to reduction with hydrogen (4, 14) or by using a low Pt concentration [less than 1 weight per cent (w/o)] (3, 6). The limitation of the latter method is that, at these low Pt concentrations, the minimum Pt crystallite size which can be detected by x-ray diffraction is approximately 50Å (15). Thus we prepared the highly dispersed platinum catalysts on a conducting substrate by localizing the platinum ions through exchange with ions in a commercial ion exchange resin and subsequently reducing the metal ions by resin pyrolysis in an inert atmosphere. Thus the initial stage fixes the platinum ions at specific sites while in the second stage a conducting substrate is produced and the metal ions are reduced. We have termed this material a Pt-doped carbon in order to differentiate it from the material prepared by the reduction of chloroplatinic acid adsorbed on a preformed carbon.

Experimental

Preparation of the highly dispersed platinum.—The procedure used to prepare the highly dispersed platinum was similar to that used by Pohl (16) and by Pohl and Rosen (17) in the preparation of metal-doped, semiconductor, polymer carbons.

Cation exchange resins were received in the free acid form and they were converted into the calcium form with calcium hydroxide solution. The platinum solution consisted of 3 g/liter of diamminoplatinum (II) dinitrate dissolved in a calcium hydroxide solution of pH 9. Fifty milliliters of the calcium form of the resin [measured in $Ca(OH)_2$ solution] was stirred in 500 ml of the hot platinum solution for 3 hr. The resin was doped with platinum ions in this way to ensure uniform distribution of the ions throughout the resin. The resin was decanted from the platinum solution, washed with water, dried at 110°C for 24 hr and then at 200°C for 24 hr. It was then pyrolyzed in an inert atmosphere at a temperature in the range 700°-900°C for 24 hr. The pyrolyzed material was washed thoroughly with dilute nitric acid and then water to remove the calcium salt and finally dried at 110°C in a vacuum oven.

Highly dispersed platinum was formed in the platinum-doped carbon only with weak acid cationic resins which were neutralized with calcium hydroxide solution (18). The two commercial weak acid cation exchange resins used in this work were: Amberlite IRC 50 (Rohm & Haas Company) which is based on methacrylic acid and has a particle size of 16-50 mesh and Amberlite CG50 (Rohm & Haas Company) which has a similar structure but a particle size of 200-400 mesh.

The noncombustible gases are listed in Table I and the pyrolysis time was 24 hr for all samples.

* Electrochemical Society Active Member.

Key words: catalytic activity, dispersed platinum, oxygen cathodes, fuel cells.

Table I. The preparation conditions of Pt-doped carbons containing highly dispersed Pt^a

Sample No.	Pyrolysis temperature	Furnace atmosphere	Weight ^b % Pt
1	700	N ₂	6.1
2 ^c	700	N ₂	6.1
3	700	N ₂	6.2
4	700	N ₂	7.3
5	700	N ₂	7.8
6	700	N ₂	12.2
7	700	10% CO, 90% N ₂	8.1
8	700	50% CO, 50% N ₂	9.7
9	700	10% C ₂ H ₄ , 90% N ₂	8.0
10	800	N ₂	8.4

^a These samples contained no detectable Pt crystallites.

^b The ratio of the weight of Pt to the total weight of Pt and carbon.

^c Sample 2 was prepared from Amberlite CG50 resin, the remainder were prepared from Amberlite IRC50 resin.

Characterization of the highly dispersed platinum.—The particle sizes of the Pt-doped carbons were in the range 0.4–12 μ and it was possible to prepare Teflon-bonded diffusion electrodes from all these catalysts. Clearly it was essential to prepare reproducible electrodes and this was achieved by using the same procedure as that of Vogel and Lundquist (19). As a check on the electrode preparation technique, electrodes were also prepared from commercial Pt black (Engelhard Industries) and 5% Pt supported on graphite. The latter catalyst was prepared by the reduction of chloroplatinic acid adsorbed on graphite.

The polarization curves for oxygen reduction were determined galvanostatically in oxygen saturated 20% H₂SO₄ solution at 70°C using the floating electrode technique (20). The cell was a 500 ml round-bottom flask, and its temperature was maintained by placing in a heating mantle. The electrodes were inserted through ground glass joints in the flask. The working electrode was supported in a gold foil spring, and it was floated on the surface of the electrolyte. Current collection from the gold foil to the external circuit was made via a platinum wire. The counterelectrode was a platinum gauze on which platinum was electrodeposited. The reference electrode was a reversible hydrogen electrode which was placed in a Luggin capillary and immersed in the test electrolyte. The IR drop between the floating electrode and the tip of the Luggin capillary was determined using an interrupter technique. All potentials given in this paper refer to the reversible hydrogen electrode in the same electrolyte and are corrected for IR drop.

The available Pt area of the electrodes was measured by determining the charge due to the oxidation of adsorbed H₂ and of adsorbed CO in N₂ purged 1M H₂SO₄ solution at 30°C using the periodic triangular voltage sweep technique. These sweeps were made using an Electroscan 30 (Beckman Instrument Company).

The platinum concentrations in the doped carbons were determined by measuring the weight loss after heating in a muffle furnace at 900°C. These concentrations were checked in selected doped carbons by dissolving the platinum in aqua regia and measuring the absorbance of the stannous chloride complex (21). The size of the platinum crystallites in the Pt-doped carbons was determined from the broadening of the x-ray diffraction line from the (111) plane using a Norelco diffractometer.

Results

Preparation of highly dispersed platinum catalysts.—The minimum Pt crystallite size which can be detected depends on the Pt concentration (15). Preliminary experiments showed that 15Å or bigger Pt crystallites were detected by x-ray diffraction providing the Pt concentration was greater than 5 w/o. Thus the samples with greater than 5 w/o Pt in which Pt could not be detected by x-ray diffraction contained highly dispersed platinum. It is not known whether the Pt was monatomically dispersed or whether it existed as

small crystallites but the average crystallite size was less than 15Å.

Table I lists the preparation conditions of platinum-doped carbons containing highly dispersed Pt (samples 1–10). All these samples had greater than 5 w/o Pt and Pt crystallites could not be detected by x-ray diffraction. The concentration of the highly dispersed Pt in the doped carbon could not be increased above 12.2 w/o (18) (Table I).

In the preparation of the highly dispersed platinum it was important to ensure that all the platinum ions were ion exchanged and that no platinum salt was precipitated in the resin pores. This was achieved by doping the resin in a hot platinum solution. When the resin doping solution was at room temperature, platinum crystallites were detected in the doped carbons after pyrolysis and it was presumed that these crystallites were formed by platinum salt precipitated in the resin pores. Highly dispersed Pt was formed when either of the resins was used as the starting material and when any of the gases was used as the furnace atmosphere.

To compare the electrochemical activity of crystalline and subcrystalline platinum, three platinum-doped carbons were prepared containing platinum crystallites. These platinum crystallites were formed in the doped carbons either by precipitating platinum salt in the resin pores and pyrolyzing at 700°C (samples 12 and 13), or by doping the resin in a hot platinum solution and pyrolyzing at 900°C (Table II).

The specific resistance of several Pt-doped carbons was measured (18). The values of the materials prepared by resin pyrolysis at 700°C were approximately 0.01 ohm-cm and this is in agreement with the values determined by Pohl (16). This resistance was sufficiently low for there to be no ohmic drop in the electrode at the low experimental current densities.

Platinum surface areas.—The platinum surface areas of the doped carbons were measured by determining the charge associated with the electrochemical oxidation of adsorbed hydrogen and of adsorbed carbon monoxide. This was carried out by measuring the current/potential curve during the application of a periodic triangular potential sweep to the electrode in nitrogen-purged 1M H₂SO₄ solution at 30°C at a sweep rate of 10 mV/sec. This sweep rate was chosen since faster rates gave ill-defined oxidation peaks in the current/potential curves.

In agreement with the work of Giner *et al.* (22) we found that it was not possible to obtain reproducible values for the charge associated with the oxidation of adsorbed hydrogen (Q_H) with a floating electrode due to hydrogen evolution at potentials cathodic to approximately 0.3V. Also it was not possible to determine the charge due to the reduction of chemisorbed oxygen (Q_{PO}) by galvanostatic stripping since there was no arrest in the potential/time curve due to chemisorbed oxygen reduction. Thus Q_H was determined on a submerged electrode.

Figures 1, 2, and 3 show the current/potential curves determined on the application of a potential sweep in the range 0.05–1.45V to electrodes prepared from sample 5, Pt black and Pt supported on graphite, respectively. Similar current/potential curves to Fig. 1 were observed with all the electrodes prepared from the Pt-

Table II. Preparation of platinum-doped carbons containing Pt crystallites

Ion exchange resin: Amberlite IRC50; pyrolysis atmosphere: N₂

Sample No.	Pyrolysis temperature (°C)	Weight % Pt	Pt crystallite diameter (Å) (from x-ray diffraction data)
11	900	9.4	55
12	700 ^a	11.0	40
13	700 ^a	6.7	25

^a The Pt crystallites were formed by precipitating the Pt salt in the resin pores prior to pyrolysis.

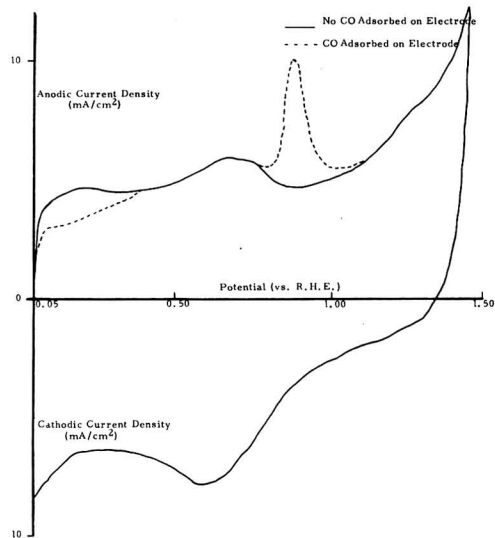


Fig. 1. Potential sweeps on electrodes prepared from sample 5. Pt loading 0.6 mg/cm^2 , $1 \text{M H}_2\text{SO}_4$ solution at 30°C .

doped carbons containing dispersed Pt (samples 1-10) and with those containing crystalline Pt (samples 11-13).

The current/potential curves obtained with Pt black (Fig. 2) and Pt/graphite (Fig. 3) electrodes are the same as those obtained with Pt foil electrodes (23). The unusual characteristics of the current/potential curves with Pt-doped carbon (Fig. 1) were: (i) it had a large capacity current in the potential range of 0.05-0.40V which interfered with the measurement of Q_H on Pt, (ii) it had no peak due to the reduction of chemisorbed oxygen, and (iii) it had an anodic peak at 0.71V and a cathodic peak at 0.68V.

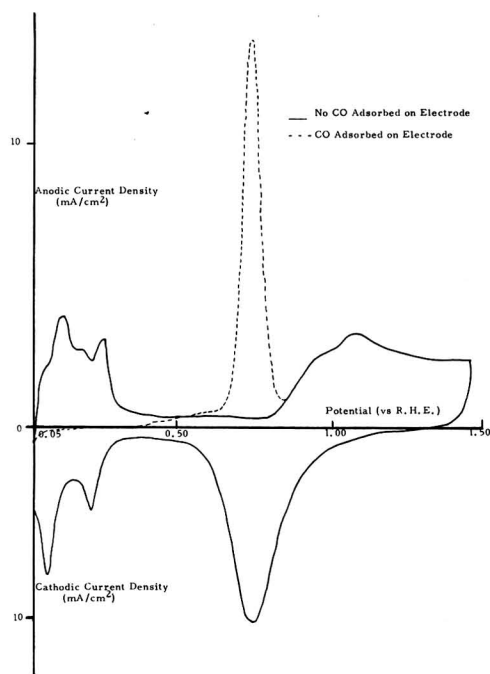


Fig. 2. Potential sweeps on Pt black electrodes. Pt loading 9.2 mg/cm^2 , $1 \text{M H}_2\text{SO}_4$ solution at 30°C .

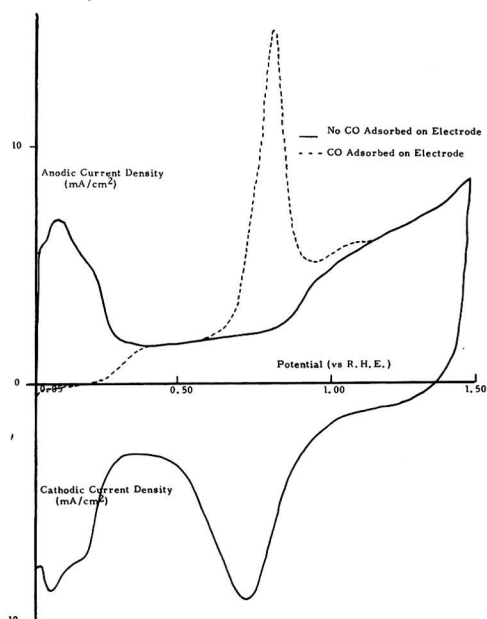


Fig. 3. Potential sweeps on 5% Pt/graphite electrode. Pt loading 0.7 mg/cm^2 , $1 \text{M H}_2\text{SO}_4$ solution at 30°C .

Since Q_H could not be determined on the Pt-doped carbon electrodes from the potential sweeps in nitrogen-purged electrolyte, it was determined by comparing the potential sweeps with and without carbon monoxide adsorbed on the electrode surface. The same measurements were also made with the Pt black and the Pt/graphite electrodes.

Figures 1, 2, and 3 show the current/potential curves determined by the application of a potential sweep with (dashed line) and without (solid line) carbon monoxide adsorbed on electrodes prepared from sample 5 (Fig. 1), Pt black (Fig. 2), and Pt supported on graphite (Fig. 3), respectively, in N_2 -purged $1 \text{M H}_2\text{SO}_4$ at 30°C . These measurements were made by first performing the potential sweep on the electrode in nitrogen-purged electrolyte (solid lines, Fig. 1-3). The electrolyte was then purged with CO for 1 min while the electrode was on open circuit (approximately 0.20V) and then with N_2 for 5 min to remove dissolved CO. The cyclic voltammetric sweep on the electrode was then repeated in the N_2 -purged electrolyte (dashed) lines (Fig. 1-3). The difference in the shape of the two curves in the potential region 0.05-0.45V is due to the adsorption of CO on the electrode and in the potential region 0.60-0.80V it is due to the oxidation of CO. Preliminary experiments indicated that a 5 min N_2 purge was sufficient to remove all the dissolved CO from the electrolyte with minimal desorption of carbon monoxide from the electrode surface.

Figure 4 shows the potential sweeps in nitrogen-purged electrolyte on an electrode prepared from a carbon. This carbon was prepared by the pyrolysis at 700°C of the calcium form of Amberlite IRC50 ion exchange resin but similar current/potential curves were also observed with graphite electrodes. There is no peak due to the oxidation of adsorbed hydrogen or of adsorbed carbon monoxide on carbon (Fig. 4) and hence the values of Q_H and Q_{CO} calculated from Fig. 1 and 3 are due solely to reactions occurring on Pt. Also Fig. 4 indicates that the anodic and cathodic peaks at 0.71 and 0.68V, respectively, Fig. 1, are due to the oxidation and reduction of surface groups on the carbon.

Pt-doped carbons prepared by resin pyrolysis at 500° and 600°C also contained highly dispersed Pt (18).

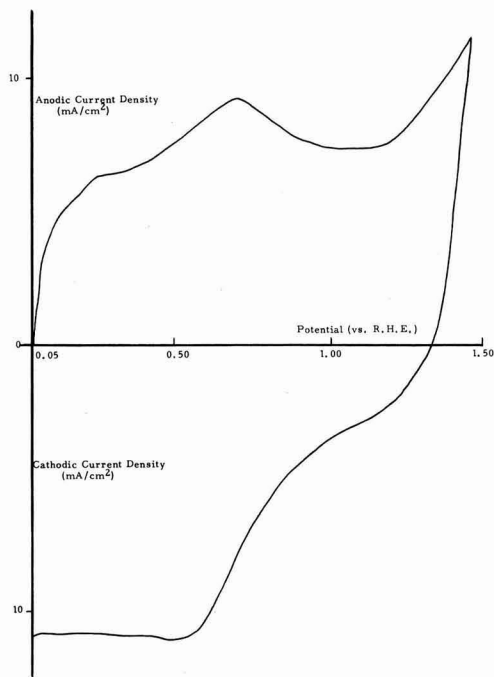


Fig. 4. Potential sweep on carbon electrode 1M H_2SO_4 solution at 30°C.

However no well-defined peaks in the current/potential curves were obtained with these materials and no further studies were made with them since it was not possible to measure their Pt areas.

For the Pt-doped carbons (samples 1-13), the ratio of Q_{CO} to Q_{H} was in the range 1.5-2.0 to 1. The slightly low value of Q_{CO} is probably caused by CO desorption during the N_2 purge. The values of Q_{H} and Q_{CO} of selected Pt-doped carbons were measured in 20% H_2SO_4 solution at 70°C as well as in 1M H_2SO_4 solution at 30°C and the same values were obtained in each of two electrolytes. With Pt black and Pt supported on graphite, the ratio of $Q_{\text{H}}:Q_{\text{PtO}}:Q_{\text{CO}}$ was 1:2:2 within $\pm 10\%$. Thus the oxidation of CO was a 2 electron process on dispersed and on crystalline Pt.

The values of the Pt areas (expressed as m^2/g) of the Pt-doped carbons (samples 1-13), Pt black, and Pt supported on graphite are given in Table III. They were calculated from the experimental values of Q_{H} and the Pt loading on the electrode by assuming that the average density of Pt atoms is 1.12×10^{15} atoms/ cm^2 (3). The values of the Pt area reported in Table III are average values obtained with 3 electrodes and the Pt area of these electrodes agreed within $\pm 10\%$. The area of the Pt black (Table III) agreed with other data with Engelhard Pt black (19).

The Pt areas calculated from the CO oxidation data are not included in Table III. However these values were the same as those calculated from Q_{H} since the ratio of $Q_{\text{H}}:Q_{\text{CO}}$ was 1:2.

The calculated areas of a monatomic Pt dispersion and of a 14Å Pt crystallite are (3) 276 m^2/g and 167 m^2/g , respectively. The experimental values of the areas of highly dispersed platinum (samples 1-10) are less than the calculated values for a 14Å crystal indicating that a significant fraction of the platinum is buried inside the carbon during the resin pyrolysis and is therefore not wetted by the electrolyte.

Thus the x-ray diffraction measurements (Table I) show that there are no platinum crystallites in samples 1 through 10 greater than 14Å and the surface area data (Table III) indicates the Pt available for

Table III. Values of the available Pt surface areas of the activity of Pt of Pt-doped carbons, Pt black, and Pt supported on graphite

Sample No.	Pt surface area (m^2/g of Pt) (from H_2 oxidation data)	Activity of Pt	
		mA at 0.9V/ mg of Pt ^a	mA at 0.9V/ mC H_2 oxidation ^{b,c}
1	132	1.5	0.007
2	54	0.7	0.007
3	108	0.9	0.007
4	58	0.6	0.005
5	102	1.6	0.008
6	143	1.0	0.004
7	84	0.3	0.002
8	22	0.1	0.002
9	69	0.3	0.002
10	84	0.4	0.003
11	39	1.3	0.030
12	49	3.0	0.041
13	84	8.1	0.063
Pt black	24	2.5	0.071
5% Pt/graphite	50	6.3	0.101

^a The current was calculated by extrapolating the Tafel plot to 0.9V.

^b This is the specific activity (i.e., the activity per unit area) of the Pt.

^c The average value of the specific activity of highly dispersed Pt catalysts (samples 1-10) was 0.004.

the electrochemical reaction. The "burying" of Pt makes it impossible to calculate the actual degree of dispersion of Pt.

The relatively low platinum area of sample 8 (Table III) indicates that a particularly large fraction of platinum was buried during resin pyrolysis in the N_2/CO (50% CO) furnace atmosphere. This is substantiated by the fact that calcium was detected in this sample by x-ray diffraction and it was not possible to wash it out. Hence it appears that the furnace atmosphere does influence the pyrolysis reaction but it does not measurably affect the size of the platinum crystallites (18).

Activity of highly dispersed platinum.—Figure 5 shows the steady-state polarization curves for oxygen

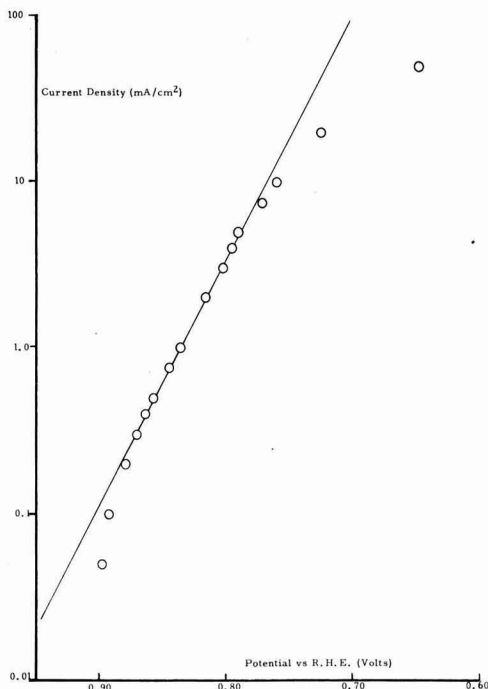


Fig. 5. Cathode performance on oxygen. Sample 4, Pt loading 0.2 mg/cm^2 , 20% H_2SO_4 at 70°C.

reduction in oxygen-saturated 20% H_2SO_4 solution at 70°C on an electrode prepared from sample 4. The data obtained with the other electrodes followed the same general pattern and the slopes of the semi-logarithmic plots were equal to 70 ± 5 mV. These plots were linear over $1\frac{1}{2}$ decades of current for electrodes prepared from the platinum-doped carbons (samples 1-13) and from Pt supported on graphite and over 3 decades of current for those prepared from Pt black. Since these plots are linear over a large current density range, it is possible to obtain the activation polarization for oxygen reduction on the electrodes.

In the potential range of the oxygen reduction measurements (i.e., 0.9-0.6V), there was no significant current (approximately $1 \mu\text{A}/\text{cm}^2$) due to oxygen reduction on carbon and on the Au electrode holder and there was no current due to carbon corrosion in N_2 -saturated 20% H_2SO_4 solution at 70°C. Thus the experimental polarization curves represent oxygen reduction on Pt.

The activity of Pt in Table III is expressed in two ways: (i) the ratio of the current at 0.9V to the weight of Pt on the electrode (mA at 0.9 V/mg of Pt) and (ii) the ratio of the current at 0.9V to mC for H_2 oxidation. The value of the current at 0.9V was obtained by extrapolating the semilogarithmic plot to 0.9V and hence these values of the Pt activity are free of mass transfer effects.

The first method of expressing the Pt activity (mA at 0.9 V/mg of Pt) is of practical importance since it allows the calculation of the activation polarization per unit weight of Pt. The second method (mA at 0.9 V/mC for H_2 oxidation) is used in the theoretical discussion since it is a measure of the specific activity (i.e., the activity per unit Pt area) of Pt for oxygen reduction.

The average value of the specific activity of the highly dispersed Pt was 0.004 and it was apparently independent of its preparation conditions (furnace atmosphere and ion exchange resin particle size). The values of the specific activity of Pt black and of Pt supported on graphite were in excellent agreement with the value calculated from other Pt black data (19).

It can be seen from Table III that the specific activity of highly dispersed Pt is significantly lower than that of Pt-doped carbons containing crystallites, Pt black, and Pt supported on graphite. This low value was not due to an experimental artifact. Thus the high activity of Pt-doped carbons containing crystallites demonstrated that the low activity of dispersed Pt was not due to catalyst inhibition during resin pyrolysis, large carbon corrosion currents in oxygen-saturated electrolyte, and high ohmic losses between the catalyst and current collector; and the high activity of samples 11-13, Pt black and Pt supported on graphite demonstrated that it was not caused by inadequate electrode structures.

Discussion

The x-ray diffraction data indicate that a highly dispersed Pt catalyst was prepared. It was not possible from the Pt surface area data to determine whether a monatomic dispersion of Pt was prepared but the average Pt crystallite size in the samples was less than 15Å.

It was shown (24), from measurements of the rate of hydrogen chemisorption on platinized carbon from the gas phase, that hydrogen was initially adsorbed on the metal and it then migrated over the carbon surface. This process was termed hydrogen spillover (1), and it has resulted (1, 4, 24, 25) in anomalously high Pt areas for platinum supported on carbon, zeolites, and tungsten oxide.

Carbon monoxide spillover onto a support has not been reported in the literature. Thus hydrogen spillover onto the support did not occur in the present work since the ratio of $Q_{\text{H}}:Q_{\text{CO}}$ was 1:2. Hence the Pt areas (Table III) are not anomalously high and the specific activities of Pt (Table III) are correct values.

Table IV. Elemental analysis of Pt-doped carbons

Sample No.	Atomic per cent			
	C	H	O	Pt
4	77.4	13.9	8.4	0.4
6	65.0	22.1	12.0	0.9
7	73.0	20.5	5.8	0.5
9	77.3	15.5	6.7	0.5

The specific activity of the highly dispersed Pt for O_2 electroreduction in acid electrolyte was considerably lower than that of crystalline Pt (Table III). The specific activity of Pt foil has not been measured. However the current/potential curve in the Tafel region is the same in concentrated phosphoric and sulfuric acid solutions (19) and thus using data in H_3PO_4 (26) solution and assuming $0.21 \text{ mC}/\text{cm}^2$ for H_2 oxidation, the specific activity of Pt foil at 76°C is 0.02. This value is significantly lower than those of Pt black and Pt supported on graphite but greater than that of dispersed Pt.

The lower activity of the dispersed Pt catalysts may be due either to the difference in the Pt crystallite sizes, or to the influence of the support on the Pt activity, or to a combination of both these factors. It is not possible from the present data to determine which has the major influence.

The influence of Pt crystallite size on the activity of Pt arises since the coordination number of the surface atoms depends on the crystallite size. For example, Poltorak and Boronin (27) have shown that in a 14Å crystal only 33% of the surface atoms have the coordination number of atoms in an infinite, ideal face, whereas in a 50Å crystal 85% of the surface atoms have the coordination number of atoms in an infinite face. It is clear that the Pt crystallite size distribution may also affect the Pt activity.

Evidence for an interaction between Pt and the support was obtained by Nicolau, Thom, and Pobitschka (28) and by Hillenbrand and Lacksonen (29, 30). Nicolau, Thom, and Pobitschka (28) found that the sample prepared by the reduction of chloroplatinic acid adsorbed on charcoal exhibited strong paramagnetic resonance absorption but that the paramagnetic resonance absorption was weaker when Pt was mixed with the charcoal. Hillenbrand and Lacksonen (29, 30) found that adsorption of Pt on carbon altered the number of unpaired electrons in the carbon and this modification depended on the pretreatment of the carbon. There are no measurements of the interaction between the metal and the support as a function of metal crystallite size but it is expected that this interaction will be greater for the smaller metal crystallites.

The catalysts prepared by the pyrolysis of an ion exchange resin at 700°C do not consist solely of Pt and carbon, and selected doped-carbons were analyzed¹ to determine the fraction of hydrogen and oxygen atoms in each support. These results are reported in Table IV.

It can be seen from Table IV that the supports contained significant fractions of hydrogen and oxygen. Comparison of the analysis results (Table IV) with the Pt specific activity data (Table III) indicates that small changes in the composition of the support does not change the activity of Pt for oxygen reduction, but this does not prove that the support is not influencing the activity of platinum. Further work aimed at larger variations in support composition is required to extend the present study.

This work demonstrates that the activity for oxygen reduction of highly dispersed Pt on a support prepared by the pyrolysis of an ion exchange resin is less than that of crystalline Pt. This may not hold true for all dispersed Pt catalysts but it may only be applicable to the Pt dispersion prepared by this particular method.

¹ Analyses were made by Schwarzkopf Microanalytical Laboratories, New York, New York.

In addition the low activity of dispersed Pt catalyst may be applicable only to the electroreduction of oxygen and the relative activity of highly dispersed and crystalline platinum will probably depend on the nature of the reactant and even of the electrolyte. For example, Poltorak and Boronin (31) using highly dispersed Pt on silica gel found that many hydrogenation, dehydrogenation, and hydrogenolysis reactions were independent of the platinum crystallite sizes. However when the same catalysts were used for reactions involving oxygen species (e.g., hydrogen peroxide decomposition, methanol and ethanol oxidation, and acetaldehyde oxidation) their activity was at least one order of magnitude lower than that of Pt black. It was claimed (31) that in the latter reactions the platinum was completely covered with oxygen and consequently it lost its metallic character.

The highly dispersed Pt catalyst prepared by the pyrolysis of an ion exchange resin in which Pt ions were adsorbed is not suitable as cathode catalysts in acid fuel cells since the increase in Pt area is more than outweighed by the decrease in Pt specific activity.

Manuscript submitted Aug. 13, 1971; revised manuscript received ca. Jan. 7, 1972.

Any discussion of this paper will appear in a Discussion Section to be published in the December 1972 JOURNAL.

REFERENCES

1. M. Boudart, in "Advances in Catalysis," Vol. 20, p. 153, D. D. Eley, H. Pines, and P. B. Weisz, Editors, Academic Press (1969).
2. E. I. Gildebrand, *Intern. Chem. Eng.*, **6**, 449 (1966).
3. L. Spenadel and M. Boudart, *J. Phys. Chem.*, **64**, 204 (1960).
4. J. A. Rabo, V. Schomaker, and P. E. Pickert, "Proc. 3rd Intern. Congr. Catalysis, Amsterdam, 1964," Vol. 2, p. 1277, North-Holland Pub., Amsterdam (1965).
5. J. A. Cusumano, G. W. Dembinski, and J. H. Sinfelt, *J. Catalysis*, **5**, 471 (1966).
6. T. A. Dorling, M. J. Eastlake, and R. L. Moss, *ibid.*, **14**, 23 (1969).

7. G. K. Boreskov and V. S. Chesalova, *Zh. Fiz. Khim.*, **30**, 2560 (1956).
8. D. W. McKee, *J. Phys. Chem.*, **67**, 841 (1963).
9. T. A. Dorling and R. L. Moss, *J. Catalysis*, **5**, 111 (1966).
10. D. J. C. Yates and J. H. Sinfelt, *ibid.*, **8**, 348 (1967).
11. M. Boudart, A. W. Aldag, L. D. Ptak, and J. E. Benson, *ibid.*, **11**, 35 (1968).
12. H. I. Zeliger, *This Journal*, **114**, 144 (1967).
13. J. A. S. Bett, E. Washington, and K. Routsis, Paper 285 presented at the Electrochem. Soc. Meeting, Los Angeles, May 10-15, 1970.
14. H. A. Benesi, R. M. Curtis, and H. P. Studer, *J. Catalysis*, **10**, 328 (1968).
15. R. A. Van Nordstrand, A. J. Lincoln, and A. Carnevale, *Anal. Chem.*, **36**, 819 (1964).
16. H. A. Pohl, "Proc. 4th Carbon Conference," p. 241, Pergamon Press (1960).
17. H. A. Pohl and S. L. Rosen, "Proc. 5th Carbon Conference," p. 113, Pergamon Press (1962).
18. K. F. Blurton, *Carbon*, Accepted for publication.
19. W. M. Vogel and J. T. Lundquist, *This Journal*, **117**, 1512 (1970).
20. J. Giner and S. Smith, *Electrochem. Technol.*, **5**, 61 (1967).
21. W. M. MacNevin and W. B. Crummett, *Anal. Chem.*, **25**, 1628 (1953).
22. J. Giner, J. M. Parry, S. Smith, and M. Turchan, *This Journal*, **116**, 1692 (1969).
23. S. Gilman, "Electroanalytical Chemistry," Vol. 2, p. 112, A. J. Bard, Editor, Marcel Dekker, New York (1967).
24. A. J. Robell, E. V. Ballou, and M. Boudart, *J. Phys. Chem.*, **68**, 2748 (1964).
25. J. E. Benson, H. W. Kohn, and M. Boudart, *J. Catalysis*, **5**, 307 (1966).
26. A. J. Appleby, *This Journal*, **117**, 328 (1970).
27. O. M. Poltorak and V. S. Boronin, *Intern. Chem. Eng.*, **7**, 452 (1967).
28. C. S. Nicolau, H. G. Thom, and E. Pobitschka, *Trans. Faraday Soc.*, **55**, 1430 (1959).
29. L. J. Hillenbrand and J. W. Lacksonen, *This Journal*, **112**, 245 (1965).
30. L. J. Hillenbrand and J. W. Lacksonen, *ibid.*, **112**, 249 (1965).
31. O. M. Poltorak and V. S. Boronin, *Zh. Fiz. Khim.*, **40**, 2671 (1966).

Hermetic Compression Seals for Alkaline Batteries

E. J. McHenry* and P. Hubbauer

Bell Telephone Laboratories, Incorporated, Murray Hill, New Jersey 07974

ABSTRACT

An accelerated thermal cycle test is described which has been used to evaluate the long-term reliability of seals for nickel-cadmium batteries in Bell System use. Results of this test correlate well with life test results on long-term overcharge. Two new types of seal have been developed for use in nickel-cadmium or other alkaline batteries. The first is a simple modification of the seal developed by A. W. Ziegler for submarine cable use. It entails substitution of an injection molded nylon bushing for the machined Kel-F bushing used by Ziegler, thus eliminating a costly machining operation and greatly simplifying fabrication of the seal. The second is a design employing the same principles as the Ziegler seal but is simpler and can be made in smaller sizes than the Ziegler seal. Both designs have been subjected to accelerated thermal cycle tests and found to be superior to the seals used on commercial alkaline cells.

The maintenance-free rechargeable nickel-cadmium cell depends on a proper balance among oxygen pressure, state-of-charge of the electrodes, electrolyte content, and positive-to-negative capacity in order to function dependably. This balance can be maintained only as long as there is no material transport across the walls of the container. A leakage rate of as little as

10 std cm³ of oxygen per month (4×10^{-6} std cm³/sec) would result in an increase of 480 mA-hr in negative state-of-charge in one year. This represents approximately one third of the excess negative capacity in a typical D (4 A-hr) cell and would result in cell failure within three years.

Leakage is a problem which seriously limits the life of nickel-cadmium batteries in Bell System service. These batteries contain conventional commercial cells

* Electrochemical Society Active Member.
Key words: injection molding, terminal seals.

in which economic and size limitations usually dictate the use of a seal based on a compressed plastic gasket. Aerospace cells, having no such economic limitations, have traditionally used ceramic-to-metal and glass-to-metal seals in an attempt to achieve long life. However, NASA data (1) indicate that despite their high cost, leakage occurred in 33% of the cells tested containing ceramic-to-metal seals and 53% of the cells tested containing glass-to-metal seals. In addition to the fact that glass and ceramic seals are expensive, inherently fragile, and subject to chemical degradation, previous work in the laboratory (see section on Ziegler seal) has shown better results with properly designed compression seals. Therefore, this work was directed toward improvement of the compression seal.

Experimental

Theory and accelerated testing.—The basic principle of the compression seal is shown in Fig. 1. In its simplest form the seal is composed of a plastic gasket, 1, compressed between the negative terminal, 2, and the positive terminal, 3, sealing leakage paths, A. Provided there is continuous contact between the metal and gasket surfaces and sufficient pressure is maintained on the gasket, this seal will effectively prevent leakage. When metal-to-plastic contact is not continuous or contact pressure is not maintained above a critical point, failure occurs. Failure of compression seals may be the result of any one or combination of the following:

1. Improper construction (misaligned gasket, feathered edges, burrs, etc.).
2. Poor design.
3. Chemical or thermal degradation of the gasket.
4. Thermal or mechanical fatigue of the gasket.

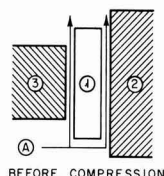
Chemical or thermal degradation of the gasket is normally not encountered at room temperature or below but may be serious at higher temperatures. Diffusion of gas or liquid through the gasket occurs at an appreciable rate only at high temperature or pressure. Seal failures are normally due to poor design, improper construction, or gasket fatigue, all of which result in insufficient contact pressure between the gasket and metal surfaces.

Fatigue results from pressure fluctuations inside the cell or from stress variations caused by thermal cycle of components with large differences in thermal expansion coefficients. The internal gas pressure of a sealed Ni-Cd cell varies with the state of charge and rate of overcharging. This differential may be as great as 5 atm between the end of charge and the end of discharge. In conventional cells the area of the cover acted on by the internal pressure is considerably

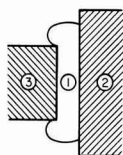
greater than the bearing (contact) surface between the cover and the gasket. Thus the resulting stress in the gasket is of the order of 10 times the internal gas pressure. Normal operation also entails thermal cycle (daily temperature variation superimposed on a seasonal temperature cycle) which causes expansion and contraction of the seal components. Gasket materials generally have thermal expansion coefficients ten times that of metal container materials so that expansion of the gasket is restricted by the container. Heating and cooling cause a fluctuating stress on the gasket which eventually results in fatigue failure. Thus rapid, broad range thermal cycling would be expected to greatly accelerate seal failures which would result from any of the causes listed above. This test would rapidly provide comparative data on seal quality which might otherwise take months or years to accumulate.

The temperature profile that was used in our experiments is shown in Fig. 2. It consisted of cycling between -40°F and $+160^{\circ}\text{F}$, one full cycle every 2 hr. The lag time required for the chamber to come to the set temperature was approximately 20 min on both rise and fall. Thermal cycling was continuous seven days a week with no rest period until failure of the seal. Failure was determined by applying wet multi-range pH paper to the seal and observing color change after 5 min. If the paper indicated a pH of 9 or greater, the seal was considered failed. Leak checks were made every day during the first week of testing and every week thereafter.

Experimental evidence of the correlation between thermal cycle and overcharge tests is shown in Fig. 3. The upper graph is a conglomerate of leakage data on 60 commercial D cells of four manufacturers which were tested at 20°F , 32°F , and room temperature at 200 mA constant overcharge (2). The lower graph shows results of thermal cycle tests on 20 additional D cells taken from the same lots. As can be seen, there is one-to-one correspondence in relative seal quality exhibited in the two types of tests. Thus, the thermal



BEFORE COMPRESSION



AFTER COMPRESSION

Fig. 1. Compression seal principles

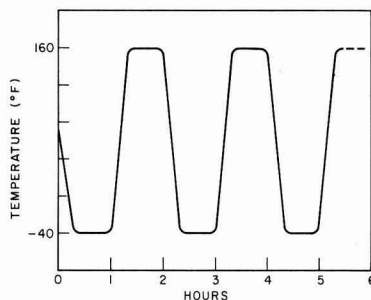


Fig. 2. Thermal cycle test temperature profile

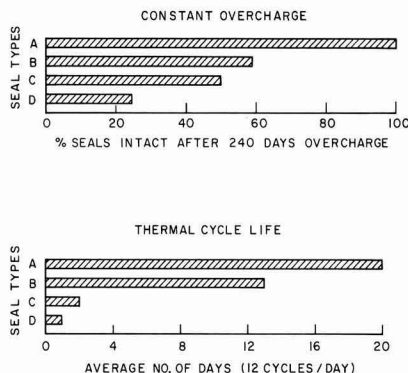


Fig. 3. Commercial battery seal performance

Table I. Leakage tests, TELSTAR® battery seals

Type of seal	No. of seals	% Failed after 4 yr Overcharge at C/100	% Failed after 5 yr Additional O.C. stand
Glass-to-metal	50	100	100
Ceramic-to-metal	400	50	100
Ziegler	50	0	0

cycle test is established as a valid accelerated test of relative quality of compression seals.

Ziegler seal.—Among the seals developed for use with nickel-cadmium batteries for TELSTAR® (3) was a plastic compression seal designed by Ziegler (4) originally for use in submarine cable repeaters. Although the reliability of the seal design was not established in time for the TELSTAR® flights, long-term experiments carried out subsequently showed them to be superior to glass and ceramic seals as seen in Table I. More important, they show it to be capable of eliminating the leakage problem in long-term service.

A diagram of the Ziegler seal used in these experiments is shown in Fig. 4. The threaded metal barrel is first brazed into the lid of a cell. The Kel-F bushing is then screwed into the barrel and the central lead wire inserted through the bushing. Radial compression is then applied to reduce the barrel diameter from 0.250 to 0.234 in.

In order to insure continuous uniform compression of the threaded Kel-F bushing, a 0.156-32 Whitworth thread is used. The important feature of this thread is the rounded roots and crests. Normal threads with sharp roots and crests are very difficult to match by a machining operation so that a helical leakage path along the sharp root is a primary failure mode. High precision is required in machining the threads to prevent burrs which would mar the Kel-F during assembly. This construction is referred to as the standard Ziegler seal.

Injection molded Ziegler seal.—Although the Ziegler seal is very effective, the precision machining required is time-consuming and expensive. Of the possible fabrication techniques available, injection molding appeared most suitable for our design objectives of simplicity and economy. This technique is rapid, economical, and faithfully reproduces the surface characteristics of the threaded barrel. It has the added advantage of eliminating the assembly operation since the bushing is formed *in situ*.

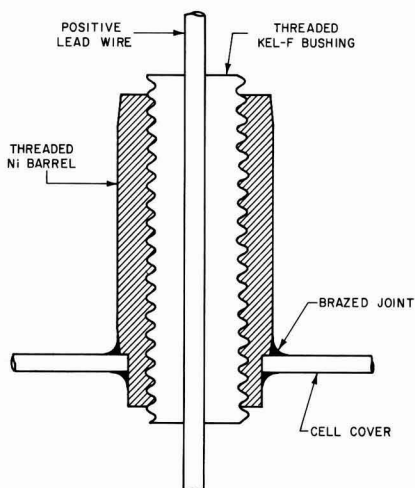


Fig. 4. Construction of Ziegler seal

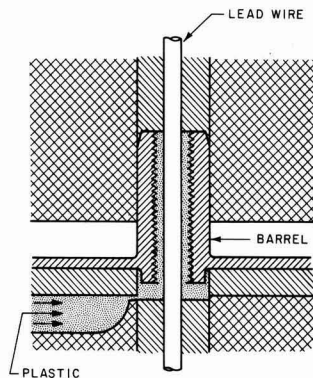


Fig. 5. Injection mold for Ziegler seal

Starting with the basic Ziegler design, a modified seal was fabricated by injection molding a nylon 6-6 bushing into a nickel barrel. The barrel was identical to the standard Ziegler barrel (shown in Fig. 4) with the exception of the thread which was cut with a standard 8-32 tap. Threaded barrels were brazed into covers made to fit a standard D cell can. The cover and lead wire were placed in a mold (Fig. 5) and plastic material was injected into the cavity to form a bushing. Molding conditions are shown in Table II. A cylindrical electrode core taken from a standard commercial D cell was then placed in a can and the cover with the injection molded seal was welded onto the can. The barrel was then crimped in the same manner as the standard Ziegler seal. At this point the cells were pressurized with 60 psig of helium and placed on a mass spectrometer leak detection device. This instrument is capable of detecting a leak rate of 2×10^{-10} std cm³/sec or 0.0063 std cm³/yr. No leakage was detected on any of the cells. Approximately 18 ml of electrolyte was then added to the cell through a fill tube on the bottom of the can. The cells were placed on thermal cycle at 50 mA overcharge. Results of these tests are presented in Table III.

As can be seen, these seals are equally as effective as the standard Ziegler seal. A major difference between the two types of seal is the quality of workmanship required in their fabrication. To illustrate this

Table II. Operating conditions for injection molding Ziegler seals using a one-half ounce-12 ton Unex jet molding machine

	Nylon 6-6	Nylon 6-10	Nylon 12
Die temperature, °F	170	170	170
Cylinder temperature, °F	600	500	510
Injection time, sec	12	12	12
Clamp closing time, sec	30	30	30
Over-all time, sec	60	60	60
Injection pressure, psi	6000	5000	6000
Feed, in.	1¼	1¼	1¼

Nylon was dried for 16 hr at 72°C prior to molding.

Table III. Thermal cycle performance of Ziegler seals

No. of seals	Plastic material	Assembly method	No. of thermal cycles	No. of seals failed
5	Nylon 12	Injection mold	1236	0
5	Nylon 6-6	Injection mold	1236	0
5*	Nylon 6-6	Injection mold	1236	0
4	Nylon 6-10	Injection mold	1101	0
5**	Nylon 6-6	Injection mold	3410	0
5	Kel-F	Standard	1101	0

* Heat and oxidation stabilized.

** 304L stainless steel barrel was used in place of nickel.

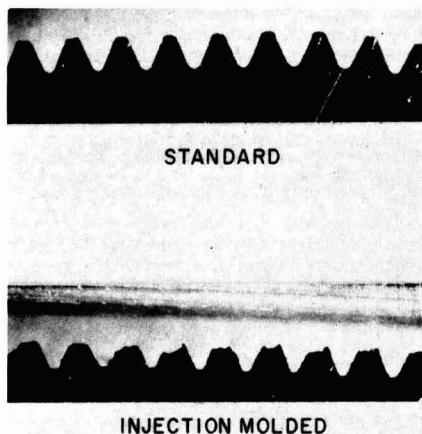


Fig. 6. Thread design for Ziegler seals

point, seals were constructed using a worn 8-32 tap to produce deliberately poor thread quality. Figure 6 shows a comparison between the threads of the standard and these injection molded seals. Both of the seals shown have withstood over 1000 thermal cycles without any indication of leakage.

Multiple crimp seal.—The proportionally large increase in over-all cell height accompanying the use of the Ziegler seal on small cylindrical cells is a major disadvantage. For this reason another design (5) operating on principles similar to that of the Ziegler seal was developed in which the seal is inverted and extends into the central void of the cylindrically wound core of the cell as shown in Fig. 7.

It consists of a metal tube containing a coaxial plastic tube and a central metal lead wire. The lead wire is normally nickel and serves as the positive terminal of the cell. The outer metal tubing is brazed into the cell cover, and the plastic tubing and wire are inserted into it. Multiple crimps compress the plastic tubing between the outer metal tubing and the central lead wire, thus effecting a seal. A 0.125 in. OD by 0.062 in. ID nickel tubing was employed in all of these seals with a 0.060 in. OD by 0.031 in. ID plastic tubing. The central wire was drawn to approximately 0.001 in. less than the plastic tubing ID. In all cases the crimping operation reduced the outside metal tubing diameter

by approximately 0.017 in. Each crimp was $\frac{1}{8}$ in. long, and the space between crimps was $\frac{1}{8}$ in. Two groups of seals were made 2 in. long with seven crimps, and two groups were made with two crimps and a length of $\frac{3}{8}$ in.

Injection molding was also applied to the crimp seal in order to simplify construction and avoid assembly errors. A larger tubing measuring 0.187 in. OD by 0.125 in. ID by 1 in. long was used with a 0.060 in. diameter nickel lead wire. Plastic material was injected into the annulus between the wire and the metal tubing. The tubing was crimped in four equally spaced sections of $\frac{1}{8}$ in. length. Crimping reduced the tubing OD from 0.187 to 0.176 in. on the crimped portion.

Since this type of seal extends into the cell it is not possible to crimp after the welding operation. Therefore, adequate heat sinking is required to prevent the seal from being heated above 200°F during welding. Helium leak check and electrolyte addition were performed in the same manner described for the Ziegler seals. Thermal cycle performance of the new seals is presented in Table IV.

Discussion

Values of gas diffusion rates through plastic bodies comparable in size to the Ziegler seal have been calculated. These values are presented in Table V for $\frac{1}{4}$ in. diameter by $\frac{1}{2}$ in. long bodies of nylon 6 and Kel-F and are based on diffusion rates reported in the literature (6) and a 1 atm pressure differential at room temperature. Leakage of helium through the standard and injection molded Ziegler seals as well as the crimp seal has been measured as less than 6.3×10^{-3} std cm³/year (2×10^{-10} std cm³/sec). This value is of the same order as the calculated gas diffusion rates shown in Table V. Thus gas diffusion is not considered to be a life-limiting factor. Accelerated thermal cycle tests indicate that fatigue failure may also be eliminated as a failure mode in a five to ten year life. All available evidence suggests that leakage is no longer a problem in any application where the Ziegler or crimp seals can be employed.

A major advantage of the new seals over the standard Ziegler or ceramic seals is the simplicity and expected economy in their fabrication techniques. Costly precision machining has been eliminated and replaced by punching, drawing, stamping, and welding operations. It is expected that relatively unskilled workers can assemble these seals quickly with very low in-

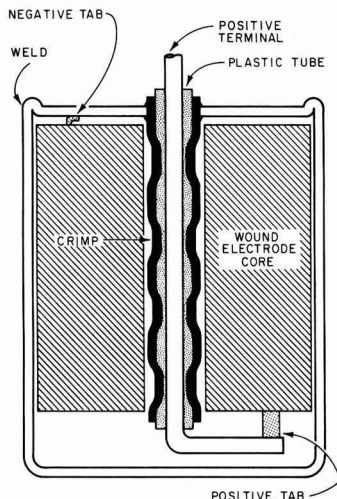


Fig. 7. Diagram of crimp seal

Table IV. Thermal cycle performance of multiple crimp seals with nylon 6-6 bushings

No. of seals	Seal OD, in.	No. of crimps	No. of thermal cycles	No. of seals failed
3	0.125	7	2070	0
5	0.125	7	1596	0
2	0.125	2	996	0
7	0.125	2	558	0
5*	0.187	4	744	0

* Injection molded.

Table V. Diffusion rates of gases through $\frac{1}{4}$ in. diameter $\frac{1}{2}$ in. long plastic bodies

Component	Nylon		KEL-F	
	g/yr	std cm ³ /yr	g/yr	std cm ³ /yr
N ₂	4×10^{-7}	3×10^{-4}	2×10^{-7}	2×10^{-4}
O ₂	2×10^{-6}	1×10^{-3}	2×10^{-8}	1×10^{-4}
CO ₂	2×10^{-7}	1×10^{-4}	5×10^{-7}	3×10^{-4}
H ₂	2×10^{-7}	2×10^{-3}	5×10^{-9}	5×10^{-5}
H ₂ O	2×10^{-4}	0.2	4×10^{-7}	4×10^{-4}

Calculations based on 1 atm pressure differential at room temperature.

cidence of rejects. The new seals have the added advantage of flexibility in design change. That is, the seal dimensions need not be changed at all unless a gross change is made in the cell design. Thus exactly the same seal design can be used in the size range from "sub C" to D cell without any change in any dimension of the seal. It is conceivable that in small quantities of special cells it may be cheaper to use the Ziegler or crimp seal rather than the ordinary commercial seal.

All of the seals studied in this work employed a nylon insulating bushing. Ease of fabrication, prior experience with nylon in Ni-Cd cells, and physical and chemical properties were the main reasons for this choice. Other materials such as polypropylene, FEP Teflon, Kel-F, and Kynar appear to be suitable for use in these types of seals. Some of these materials were used in preliminary experiments, and results indicate that with proper control, they will be equally suitable in these designs. Further work is planned to investigate other plastic materials and to develop a seal which will withstand sterilization at 135°C for 72 hr.

Conclusions

The injection molded Ziegler seal and the multiple crimp seal perform far better on accelerated thermal

cycle testing than do ordinary commercial seals and are expected to perform satisfactorily for five to ten years of normal operation. These seals are simple in construction and can be produced at a cost considerably below that for ceramic seals, which they will outperform under most conditions.

Manuscript submitted Oct. 14, 1971; revised manuscript received Jan. 10, 1972. This was Paper 72 presented at the Atlantic City Meeting of the Society, Oct. 4-8, 1970.

Any discussion of this paper will appear in a Discussion Section to be published in the December 1972 JOURNAL.

REFERENCES

1. "Evaluation Program for Secondary Spacecraft Cells—Fifth Annual Report of Cycle Life Test," QEL Report QE/C 69-244, April 7, 1969.
2. M. L. Cassotta, Unpublished work.
3. D. C. Bomberger and L. F. Moose, *Bell System Tech. J.*, **42**, 1687 (1963).
4. A. W. Ziegler, U.S. Pat. 3, 109, 055.
5. E. J. McHenry, U.S. Pat. 3, 510, 353.
6. J. Brandrup and E. H. Immergut, "Polymer Handbook," Interscience Publishers, Inc., New York (1967).

A New Water-Activated Lead-Acid Battery Concept

R. F. Amlie,* E. Y. Weissman,* C. K. Morehouse,* and N. M. Qureshi

Globe-Union, Inc., Milwaukee, Wisconsin 53201

ABSTRACT

A discussion is presented of a reserve lead-acid battery concept based on water-soluble sulfuric acid gels. The gels consist primarily of 100% sulfuric acid plus small amounts of boric and phosphoric acids. These gels exhibit excellent mechanical and thermal stability characteristics when prepared with a relatively large molar excess of boric acid with respect to phosphoric acid. The rate of water activation of a battery containing this gel is controllable, and no solid residues are left after the activation has been completed. Performance, life, and electrolyte composition aspects are covered in this discussion, with a view to defining the advantages and limitations of the system and its future possibilities.

The development of a satisfactory water-activated dry-charged lead-acid battery is of particular interest since it would fill a definite need that exists in military and possibly also commercial applications for a reserve system. A water-activated battery would have several advantages over the widely accepted acid-activated battery in that no separate acid volume is required and shipment, storage, and activation are inherently less costly, safer, and simpler. A satisfactory water-activated concept requires the internal storage of concentrated sulfuric acid (or its precursor) in a mechanically and thermally stable form which will produce sufficient sulfuric acid electrolyte in a safe yet sufficiently rapid manner upon addition of water. Other characteristics for a practical concept require that the acid concentrate occupy essentially a minimal volume, since internal free space is greatly limited in conventional batteries, and that it produce no degradation of cell components. Further, performance should be comparable to that of a conventional battery of the same external dimensions.

Various concepts for water-activated lead-acid batteries are described primarily in the patent literature

and have appeared at an increasing rate in recent years following a feasibility study reported in 1965 (1). Briefly, these concepts could be described as involving the immobilization of concentrated sulfuric acid by mechanical encasement of the liquid (2-4), physical sorption (5-9), chemical reaction (10), and gelation (11-17), although this classification may not always be completely rigorous.

Stable Boron Phosphate Gels

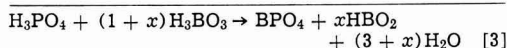
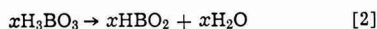
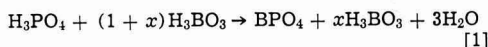
This paper presents a water-activated lead-acid battery concept based on the use of stable "boron phosphate" gels of concentrated sulfuric acid. Gelation of concentrated sulfuric acid and oleum by the addition of essentially equimolecular amounts of boric and phosphoric acids was described by Leicester in 1948 (18). Leicester suggested that gelation is due to the formation of a boron phosphate, (BPO₄), structure which may be isomorphous with a silicic acid gel of sulfuric acid in which the silicon atoms are alternately replaced by boron and phosphorus atoms. He describes general properties of these gels including the observation that, "Equimolecular proportions of the two acids (H₃BO₃ and H₃PO₄) gave the best gels, but the quantities could be varied within wide limits (±30%) with-

* Electrochemical Society Active Member.

Key words: gelled sulfuric acid, boron phosphate gels, water-activated battery, lead-acid battery, dry-charged battery.

out seriously affecting gel formation for the 1/100 (mole ratio $\text{BPO}_4/\text{H}_2\text{SO}_4$) and more concentrated gels." Other properties listed included: (a) increased firmness with concentration, (b) faint to strong opalescence, (c) slight syneresis (separation of liquid phase due to gel contraction) with little indication of thixotropic properties, (d) readily broken down and dissolved by the addition of water, (e) good thermal stability at 100°C , and (f) good room temperature stability for several months. Leicester also shows that gelation time decreased rapidly with increasing water content and moderately with increased BPO_4 content.

We found these gels to be easily prepared starting with boric acid crystals, 85% orthophosphoric acid, concentrated sulfuric and oleum solutions. Since the composition of the sulfuric acid component (or $\text{H}_2\text{O}/\text{SO}_3$ ratio) of the mixture greatly influences gel stability, we assumed the gelation reactions shown below in order to define a calculated $\text{H}_2\text{O}-\text{SO}_3$ composition



In addition to the water introduced in the gelation process, the 85% phosphoric acid and the concentrated sulfuric acid ingredients also introduce water into the system. This water is effectively removed by the addition of oleum (free SO_3) and the resulting H_2SO_4 and H_2O , or SO_3 contents were calculated according to the above assumptions. Laborious material balance equations involving different ingredient concentrations and gel compositions were avoided by use of a FORTRAN program in our computer facility.

In actual practice, it was found that gel preparation can be readily monitored by measuring the electrolyte solution conductivity which is very sensitive to concentration in the range of interest. Specific conductance values of liquid gelling mixtures with an acid mole ratio of $2\text{H}_3\text{PO}_4/5\text{H}_3\text{BO}_3/100\text{H}_2\text{SO}_4$ are plotted in Fig. 1 as a function of the weight per cent (w/o) H_2SO_4 . The weight per cent H_2SO_4 calculated for each solution is based on the total SO_3 content, and H_2O which was both added and assumed to be derived from gelation and dehydration. Gel compositions with this 2/5/100 mole ratio exhibit excellent stabilities in the calculated H_2SO_4 concentration range from about 99 to 101%, above which SO_3 fuming becomes progressively evident. The specific conductance curve of a pure sulfuric acid solution with a minimum at 99.7 w/o H_2SO_4 (19) is also included in Fig. 1. It is evident that the minimum, as calculated for the gelling solution, exceeds that of pure H_2SO_4 by approximately 1 w/o. This would indicate that the assumed gelation reaction [3] does not provide a complete description of this complex system which may involve interaction of acid species. A systematic study of the boron phosphate-sulfuric acid system is required to clarify these results.

Gels prepared in our laboratory using Leicester's formulations did not exhibit satisfactory thermal and storage stabilities toward syneresis as deemed necessary for a water-activated battery application. The hygroscopic gels were stored in tightly capped glass bottles at temperatures up to 100°C . In agreement with Leicester, it was found that gel stability was improved by decreasing the water content and increasing the BPO_4 content, but neither the equimolar gels nor gels containing up to 30% excess of boric or phosphoric acid were sufficiently stable.

Gel stabilities were found to be greatly improved when a relatively large molar excess of boric acid relative to phosphoric acid is used (16). Table I summarizes the optimum ranges of acid mole ratios necessary to produce battery-stable gels. An approximate stability-composition domain for gels containing a 99-

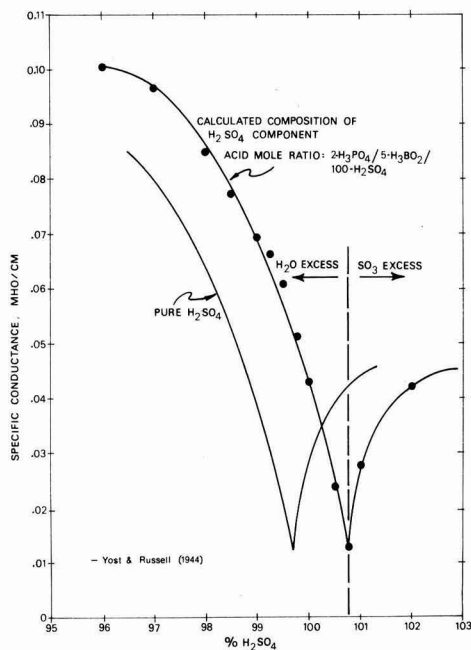


Fig. 1. Specific conductance vs. per cent H_2SO_4 at 30°C

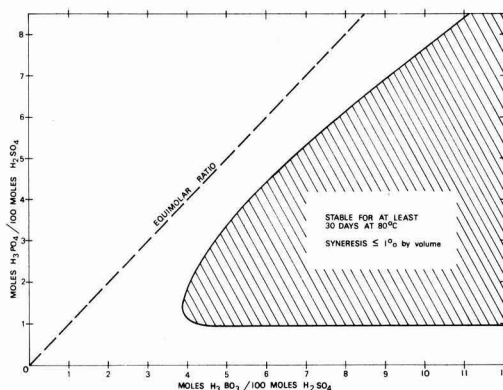


Fig. 2. Approximate stability composition domain for $\text{H}_3\text{PO}_4/\text{H}_3\text{BO}_3/\text{H}_2\text{SO}_4$ gels containing 99-100% calculated H_2SO_4 .

100% calculated (aqueous) H_2SO_4 component, wherein syneresis was less than 1% by volume after 30 days' storage at 80°C , is shown in Fig. 2. Acid composition of the gels is given in moles of phosphoric and boric acid per 100 moles of calculated (100%) sulfuric acid. Stabilities of these gels were generally best in the lower portion of the composition domain where the H_3PO_4 content exceeded 1 mole per 100 moles H_2SO_4 and the maximum $\text{H}_3\text{BO}_3/\text{H}_3\text{PO}_4$ mole ratios were attained. The more stable gels exhibited no evidence of syneresis or breakdown after 100 days' storage at 100°C

Table I. Optimum acid ingredient mole ratios for stable $\text{BPO}_4\text{-H}_2\text{SO}_4$ gels

$\text{H}_3\text{BO}_3/\text{H}_3\text{PO}_4 > 1.3$ and, preferably > 1.5
$3.5 \leq \text{H}_3\text{BO}_3/100 \text{ moles } \text{H}_2\text{SO}_4 \leq 12$
$1 \leq \text{H}_3\text{PO}_4/100 \text{ moles } \text{H}_2\text{SO}_4 \leq 5$



Fig. 3. Photograph of a water-clear gel

at which time the tests were discontinued. Attempts to liquify the most stable gels at even higher temperatures produced instead a surface decomposition with gradual reduction of the gel body size.

Gel appearance varied from strongly opalescent to water-clear and was found to be dependent on the $\text{H}_3\text{PO}_4/\text{H}_3\text{BO}_3$ ratio, the water content, and the setting temperature. Water-clear gels generally exhibited the greatest stability and were obtained only with an excess of boric acid and minimal (or no) calculated water content. A photograph of a water-clear gel sample is shown in Fig. 3.

A particular advantage with this gel is that it can be combined rapidly with water without the hazard encountered with concentrated sulfuric acid liquid.

Having established that gels could be prepared with excellent mechanical, thermal, and storage stabilities, effort in this development was devoted to determining the effect of gel-prepared electrolytes on battery performance.

Water-Activated Battery Performance

Electrochemical phenomena arising from the use of solutions prepared from gelled acids rather than pure sulfuric acid are primarily due to the presence of orthophosphoric acid. Furthermore, our measurements and observations support Leicester's view that the addition of water (at least 10-15% by volume of gel) readily hydrolyzes the gels to the constituent acids yielding a clear solution (18).

The addition of phosphoric acid to the lead-acid battery has been rather extensively tried (20) and will not be reviewed here. Definitive conclusions have often been dependent on the materials, design, and test mode or service employed. While the earliest patents claimed such general improvements as "the elimination of harmful sulfation" (21), it is now generally accepted that phosphoric acid additions are of particular benefit in improving the cycle life of nonantimonial grid batteries (22, 23). More fundamental investigations of the reactions of phosphoric acid with the lead dioxide electrode have also been reported (23-27) and we have carried out measurements on the electroanalytical determination of Pb(IV) phosphate species in solution (28). Nevertheless, a more comprehensive understanding of the incorporation of phosphoric acid in the positive plate and the changes it produces is definitely needed.

Activation of Prototype Batteries

Initial 20-min activation performances of prototype water-activated batteries are superior to comparable commercial acid-activated batteries owing to the heat of dilution of the concentrated sulfuric acid gel. This advantage is illustrated in Fig. 4 wherein discharges are plotted for 12V-60 A-hr batteries activated and discharged according to the standard SAE $\sim 0^\circ\text{C}$ (30°F)-150A discharge test specification. These batteries were assembled with production dry-charged 60

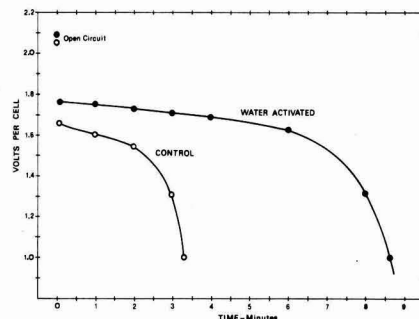


Fig. 4. Performance of 12V-60 A-hr water-activated batteries on the SAE 20-min activation test at -1°C (30°F), 150A.

A-hr elements in polypropylene containers (and covers). The water-activated batteries contained 210 cc (388g) of gel mounted above each cell element (16). Prior to activation, the batteries and the (1.270 sp. gr.) sulfuric acid solution had been cooled to $\sim 0^\circ\text{C}$ (30°F) and the water to $+1^\circ\text{C}$. These water-activated batteries were designed to dissolve the gel body in about 20 min after the addition of water and the dissolution occurred with no emission of liquid from the filling ports. The 150A discharge was started 20 min after filling, at which time the average temperatures of the commercial acid-activated and water-activated batteries were 3.5° and 69.5°C , respectively.

Short and Long Term Results

Only a brief summary of available storage, cycle-life, overcharge, and field service results for one gelled electrolyte composition will be given at this time. A more detailed presentation of design and performance characteristics will be given elsewhere (29).

Standard production dry-charged 12V-60 A-hr batteries with 6% antimonial-lead grid alloy have frequently been used to compare the performance of solutions prepared from gelled acids with the standard sulfuric acid solutions. No effort was made to optimize or alter the batteries for this application. To make this extensive comparison, gel with an acid mole ratio of $2\text{H}_3\text{PO}_4/5\text{H}_3\text{BO}_3/100\text{H}_2\text{SO}_4$ was selected based on initial laboratory test results. The acid concentrations of a solution prepared from this gel are typically 9, 14, and 455g per liter of phosphoric, boric, and sulfuric acid, respectively. The solution prepared by the addition of 480g of a 2/5/100 gel containing 0.5 w/o "excess" water to 802g of water has a specific gravity of 1.282 at 21°C . The control batteries were filled with 1.270 sp. gr. sulfuric acid (460 g/liter).

The most significant available results can be summarized as follows:

1. The 60 A-hr sealed, dry-charged, SLI-type batteries with gel mounted above the plate elements continue to show satisfactory storage after more than six months in a 60°C -100% relative humidity environment.
2. Gel prepared electrolyte capacities on the 20-hr (3A) discharge at 27°C (80°F) have shown an average reduction of 6% relative to their respective controls.
3. At low temperatures (0 to -29°C) and high discharge rates (150 and 300A), the 2/5/100 gel prepared electrolyte solution has exhibited increased 5 sec voltages¹ of 3 to 6% and reduced discharge times ranging from 5 to 33% relative to the control.
4. When cycled according to the SAE cycle-life specification (30), the 60 A-hr SLI batteries with the 2/5/100 composition electrolyte have averaged only 2/3 of the control cycles. On the other hand, Edison Cycle Life Test (see Appendix) results average about 10% higher for the experimental batteries. Field test results are still inconclusive but seem to suggest a detrimental effect on life in hot climate use.

¹ Voltage measured after 5 sec of discharge at the given rate.

5. Overcharge life test comparisons for 60 A-hr batteries on the standard SAE overcharge test (30) routine have shown the same performance for the 2/5/100 acid solution and the sulfuric acid control.

6. There appears to be a structure-dependent scale effect when evaluating experimental and control batteries so much so that certain types of low-capacity batteries (not of the SLI variety) have not exhibited the above-mentioned performance differences. This aspect will be discussed at a later date.

7. Gel prepared electrolyte solutions used in batteries fabricated with nonantimonial lead alloy grids are expected to improve positive paste adherence. Fortunately, a practical phosphoric acid concentration for typical nonantimonial systems (e.g., lead-acid batteries having lead-calcium grids), namely 10 g/liter of solution, corresponds to what results from the utilization of the gelled acids described in this paper.

Conclusions

The technical feasibility of a water-activated, dry-charged lead-acid battery based on stable boron phosphate-concentrated sulfuric acid gels has been demonstrated. Properly formulated gels have been developed which exhibit superior mechanical, thermal, and shelf stabilities when stored out of contact with moisture. The low-temperature activation performance of prototype SLI batteries is excellent due to the H_2SO_4 heat of dilution released. Laboratory cycle life, and field testing of SLI prototype batteries indicate that the gelled acid may reduce the performance of standard batteries in certain SLI applications, although optimization of the system to compensate for the modified electrolyte effects is possible.

Finally, while this discussion addresses itself to the SLI type of battery, it should be obvious that the water-activation principle described here is adaptable to any battery system utilizing a sulfuric acid electrolyte.

Manuscript submitted Nov. 1, 1972; revised manuscript received Dec. 20, 1971. This was presented at the Cleveland Meeting of the Society, Oct. 3-8, 1971.

Any discussion of this paper will appear in a Discussion Section to be published in the December 1972 JOURNAL.

APPENDIX

Edison Cycle Life Test for Lead-Acid SLI Batteries

Temperature:	38°-43°C in air environment	
Cycle time:	10 min; 1000 cycles/week	
Charge	— 6 min, 27 sec at 5-6A	} 10 min
Discharge	— 10 sec at 150A	
Rest	— 3 min, 23 sec	
Capacity test:	150A to 7.2V (1.2 V/cell)	

Specified minimums:

Capacity — > 0.5 min to 7.2V
Life — 10 weeks (10,000 cycles)
for 60 A-hr battery

REFERENCES

1. G. L. Simmons, R. W. Adler, W. E. Elliott, and W. L. Towle, "Immobilized Electrolyte Feasibility Study," U.S. Army Tank Automotive Center, Contract DA-11-022-AMC-2236 (T), Dec. 21, 1965, AD 678594.
2. T. Yeoman, U.S. Pat. 2,773,927 (1956).
3. A. Sam, U.S. Pat. 3,304,202 (1963).
4. J. T. Redmon, U.S. Pat. 3,525,639 (1970).
5. G. W. Vinal, "Storage Batteries," John Wiley & Sons, Inc., New York (1955).
6. R. G. Robinson, Brit. Pat. 785,848 (1957).
7. K. Parker and J. L. Brosilow, U.S. Pat. 3,408,233 (1968).
8. J. P. Badger and H. A. Bernholtz, U.S. Pat. 3,540,939 (1970).
9. H. A. Bernholtz and J. P. Badger, U.S. Pat. 3,591,422 (1971).
10. L. E. Solomon, U.S. Pat. 3,067,275 (1962).
11. H. H. Roth, U.S. Pat. 2,596,046 (1952).
12. J. T. Rivers, U.S. Pat. 2,684,950 (1954).
13. D. L. Douglas, R. E. Biddick, and J. B. Ockerman, "Power Sources 2" (1968), p. 93, D. H. Collins, Editor, Pergamon Press, Inc., New York.
14. D. L. Douglas and H. J. Banas, U.S. Pat. 3,556,850 (1971) and 3,556,851 (1971).
15. M. H. Little, U.S. Pat. 3,530,002 (1970).
16. R. F. Amlie, U.S. Pat. 3,556,860 (1971).
17. H. Lauck, U.S. Pat. 3,586,539 (1971).
18. J. Leicester, *J. Soc. Chem. Ind. (London)*, 67 433 (1948).
19. D. M. Yost and H. Russell, Jr., "Systematic Inorganic Chemistry of the Fifth and Sixth Group Non-Metallic Elements," p. 340, Prentice-Hall Inc., Englewood Cliffs, N. J. (1944).
20. C. Drotschmann, "Bleiakkumulatoren," p. 160, Verlag Chemie, GmbH, Weinheim (1951).
21. M. Kugel, U.S. Pat. 1,748,485 (1930).
22. S. Tudor, A. Weissstuch, and S. H. Davang, *Electrochim. Technol.*, 3, 90 (1965); 4, 406 (1966); 5, 21 (1967).
23. K. Eberts, "Power Sources 2" (1968), p. 61, D. H. Collins, Editor, Pergamon Press Inc., New York.
24. E. Voss, "Proceedings of the 2nd International Symposium on Batteries," Bournemouth (1960), Paper No. 16.
25. H. Bode and E. Voss, *Electrochim. Acta*, 6, 11 (1962).
26. P. Ness, *ibid.*, 12, 161 (1967).
27. F. Huber and M. S. A. El-Meligy, *Z. Anorg. Allgem. Chem.*, 367, 154 (1969).
28. R. F. Amlie and T. A. Berger, To be published in *Journal Electroanalytical Chemistry, Interfacial Electrochemistry*.
29. R. F. Amlie, E. Y. Weissman, and N. M. Qureshi, "Proceedings of the Twenty-Fifth Power Sources Symposium, Atlantic City, May 23-25, 1972," To be published.
30. "The Storage Battery Manufacturing Industry—1970 Yearbook," Battery Council International, Burlingame, California.

Effect of Chloride Ion on Iron Corrosion in NaOH Solution

Clarence M. Shepherd* and Sigmund Schuldiner*

Naval Research Laboratory, Electrochemistry Branch, Washington, D. C. 20390

ABSTRACT

Potentiostatic polarization curves for the system Fe-NaOH, in which the level of detectable impurities had been reduced to 10^{-6} ppm, showed that Fe did not corrode and that the Fe behavior was similar to Pt. Introduction of chloride ion changed the potentiostatic polarization behavior and at Cl^- concentrations $\geq 2 \mu\text{g/cc}$ Fe corrosion occurred. Chloride ion also caused the development of a pronounced active dissolution region in the anodic polarization curves. At $0.2 \mu\text{g/cc}$ of chloride ion, the changes in the polarization curve were small. At $2 \mu\text{g/cc}$ of chloride ion a typical pattern had developed which showed a definite corrosion region, followed by "passivity" as the potential was increased. At $2000 \mu\text{g/cc}$ of chloride ion corrosion was marked, even in the "passive" region.

The present work extends our previous (1) study of the effects of chloride ion on the potentiostatic behavior of iron in oxygen-free ($<10^{-6}$ ppm) NaOH solution. Mayne, Mentor, and Pryor (2) showed that in oxygen-free solution chloride ion concentrations from 3.5 to $35 \mu\text{g/cc}$ will cause iron to corrode, however no corrosion occurred when oxygen was present. The chloride ion concentration in our high-purity 0.2M NaOH was approximately $0.01 \mu\text{g/cc}$ so that we were able, under O_2 -free conditions, to determine the effects of chloride ion at considerably lower levels than previously had been investigated.

Experimental

The electrode was a high purity Fe wire immersed in 0.2M NaOH under an atmosphere of helium at 25°C . The closed system and measuring equipment have been previously described (1, 3, 4). The 20 mm diameter Fe wire was fabricated from 3 pass electron beam zone refined iron which was reported by the supplier to contain less than 4 ppm metallic impurities. The NaOH electrolyte was prepared by dissolving high purity sodium from a glass capsule inside the closed cell (1). Final purification was by electrolysis to remove traces of heavy metals and organic material. A point on the curves shown was determined by potentiostating the Fe electrode until a constant current was reached. The potential was then increased and another steady-state current was obtained. The process was repeated until the potential was well up into the O_2 generating region after which the potential was decreased stepwise until well into the H_2 generating region. The potential was then increased stepwise back to its original value, thus completing a cycle. Repeated cycling gave essentially the same results.

Results and Discussion

The results for the highly purified system, Fe/ 0.2M NaOH containing about $0.01 \mu\text{g/cc}$ Cl^- (from NaCl) as an impurity, are shown in Fig. 1 where the constant value of the apparent current density is plotted against the potential measured against the normal hydrogen electrode (NHE). This curve is used as a standard for comparison with the results that were obtained when small known amounts of Cl^- were added to the pure system. No visual corrosion or changes in the Fe were observed under low power microscopy nor was Fe found in the analyzed solution.

When Cl^- is added to the system the potentiostatic polarization curve of Fig. 1 is affected. The results are shown in Fig. 2-5 for concentrations of Cl^- from $0.2 \mu\text{g/cc}$ to $2000 \mu\text{g/cc}$. The concentration of O_2 in these systems was less than 10^{-6} ppm (4).

When the chloride ion concentration reached $2 \mu\text{g/cc}$ (Fig. 3-5), one observes a large increase in the anodic

current density, particularly in the region of the loop where the potential is being increased from point C through K to L. This increase in current is accompanied by corrosion. This confirms the Mayne, Mentor, and Pryor (2) finding of iron corrosion in O_2 -free solution containing 3.5 to $35 \mu\text{g/cc}$ of Cl^- . Under conditions in which no chloride has been added to the electrolyte the iron remains bright and shiny over repeated cyclings. After 2 cycles in the solution containing $2000 \mu\text{g/cc}$ of chloride ion, the iron electrode was pitted appreciably. Considerable amounts of dark brown corrosion products were observed, particularly in the

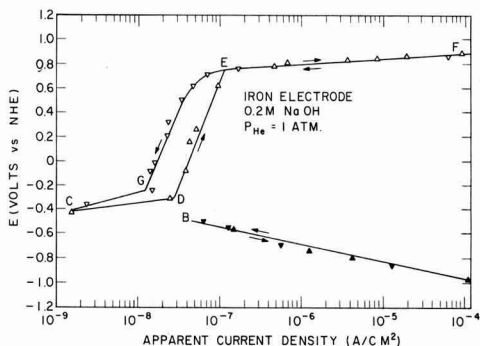


Fig. 1. Fe potentiostatic polarization curves in 0.2M NaOH at 25°C . Δ anodic current, increasing potential; ∇ anodic current, decreasing potential; \blacktriangle cathodic current, increasing potential; \blacktriangledown cathodic current, decreasing potential.

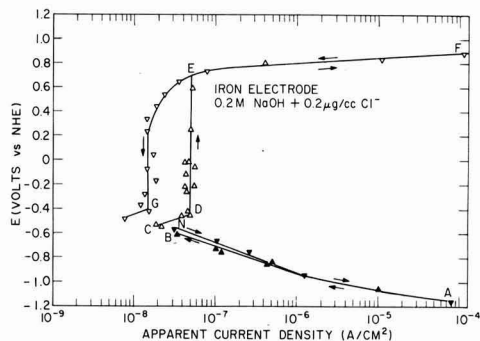


Fig. 2. Effect of addition of $0.2 \mu\text{g/cc}$ of Cl^- ion on Fe potentiostatic polarization curves in 0.2M NaOH at 25°C and $P_{\text{H}_2} = 1\text{ atm}$. See Fig. 1 for symbols.

* Electrochemical Society Active Member.

Key words: corrosion, iron, chloride ion, passivity, polarization, potentiostatic, high purity.

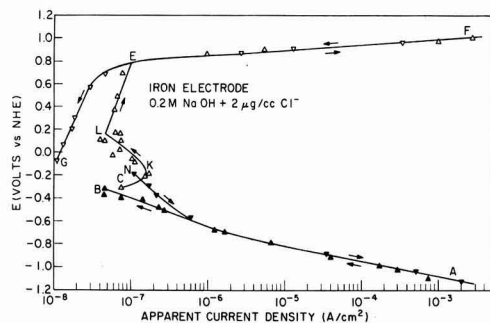


Fig. 3. Effect of addition of 2 $\mu\text{g/cc}$ of Cl^- ion on Fe potentiostatic polarization curves in 0.2M NaOH at 25°C and $P_{\text{He}} = 1$ atm. See Fig. 1 for symbols.

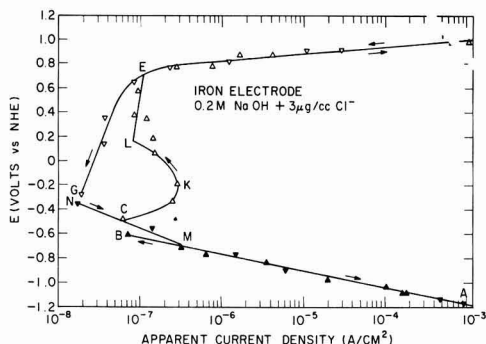


Fig. 4. Effect of addition of 3 $\mu\text{g/cc}$ of Cl^- ion on Fe potentiostatic polarization curves in 0.2M NaOH at 25°C and $P_{\text{He}} = 1$ atm. See Fig. 1 for symbols.

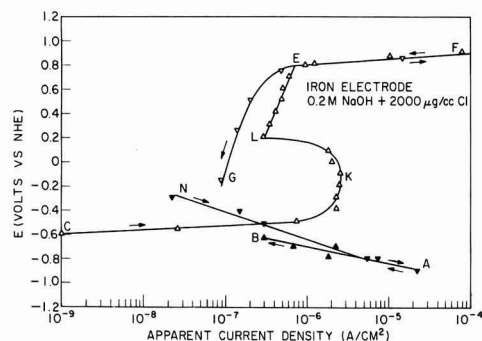


Fig. 5. Effect of addition of 2000 $\mu\text{g/cc}$ of Cl^- ion on Fe potentiostatic polarization curves in 0.2M NaOH at 25°C and $P_{\text{He}} = 1$ atm. See Fig. 1 for symbols.

pits. These pits were not randomly distributed but tended to occur in clusters.

In Fig. 3-5 the Fe electrode is exhibiting normal passive behavior. At a potential in the neighborhood of C, a reaction is initiated involving the oxidation of iron. The current reaches a maximum at the point K, declines, and enters the passive region along line L-E. As the amount of chloride ion increases, the nature of the passive region changes as is evident by the higher current densities. The current density at 2000 $\mu\text{g/cc}$ of chloride ion is several times that at low concentrations of chloride. If the reactions that take place in the system shown in Fig. 1 take place at the same rate in the systems shown in Fig. 3-5, their current density in the passive region is being masked by a reaction or

reactions, whose current density is several hundred per cent higher. If this latter reaction or reactions involve the oxidation of iron, then an appreciable amount of corrosion is being experienced in the so-called "passive" region. Around point K in Fig. 5 the current densities are 100 times higher than found in Fig. 1. As the potential moves upward from E toward F (the transpassive region), the current density involved in the production of O_2 becomes so high that it completely masks out the effect of the impurities. Consequently, this portion of the potentiostatic polarization curve was not affected by change in chloride content.

As the potential was decreased the current went from anodic to cathodic at about -0.22V in the presence of 2000 $\mu\text{g/cc}$ of Cl^- . When the potential was increased the current went from cathodic to anodic at about -0.61V . The difference between these two potentials, ΔE , is 0.39V. This difference in changeover potentials is characteristic of impure systems and decreases monotonically as the amount of impurity decreases, as can be seen in Fig. 6 where ΔE is plotted as a function of the chloride content of the electrolyte. As the chloride content is increased, the value of ΔE appears to be leveling off in the neighborhood of a value of 0.4V. As the chloride value is decreased ΔE approaches zero in value (1). Similar results have been observed qualitatively with other impurities.

In Fig. 3-5 it can be seen in each case that the potential at point K remains fairly constant at -0.2V , whereas the potential at point C decreases appreciably with increase in chloride content.

The maximum current, i_M , is a good measure of the extent of corrosion in the system. In Fig. 7, the current density at the potential of -0.2V has been plotted as a function of the chloride content. This is the potential that gives the maximum current density at point K in those cases where the chloride content is sufficiently high to show a corrosion loop. The relationship is

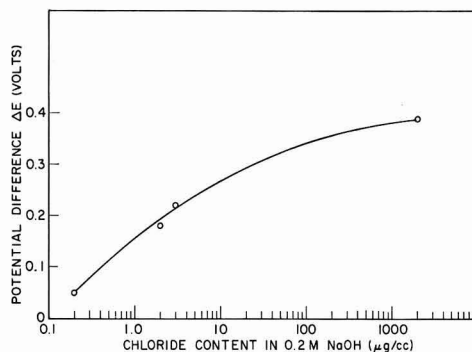


Fig. 6. The effect of Cl^- ion content on ΔE , the potential at which the current changes from anodic to cathodic minus the potential at which the current changes from cathodic to anodic.

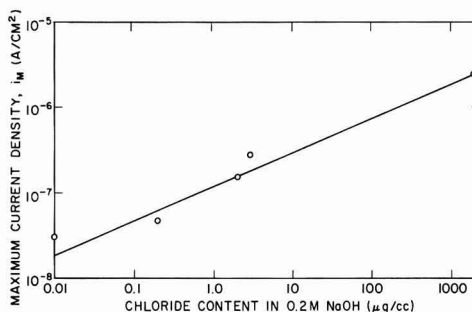


Fig. 7. The effect of Cl^- ion on the maximum corrosion current (current density measured at -0.2V).

logarithmic and can be expressed as the equation

$$i_M = 1.2 \times 10^{-7} C^{0.4}$$

where C is the concentration of chloride ion in $\mu\text{g/cc}$ and i_M is the current density at -0.2V vs. the normal hydrogen electrode (NHE) and is measured on the increasing potential curve. In the standard system, where impurity effects have been minimized, there is no visible corrosion and the potential-current relationships, as shown in Fig. 1, are essentially straight lines, it seems quite likely that the low chloride content of approximately $0.01 \mu\text{g/cc}$ neither causes Fe corrosion nor typical passive behavior. At a level of $0.2 \mu\text{g/cc}$ of chloride ion in the electrolyte (Fig. 2), definite changes have occurred in the potentiostatic polarization curve, and at $2 \mu\text{g/cc}$ of Cl^- (Fig. 3), there is the first evidence of an active dissolution region. This indicates that a concentration of 10^{-1} to $1 \mu\text{g/cc}$ of chloride ion must be present to initiate corrosion or the steps that lead to corrosion.

The variation in results obtained using two successive cycles in a given purified electrolyte is not large, in most cases, and is much less than the variation in results obtained between separately prepared and purified electrolytes unless the chloride content is high. At $2000 \mu\text{g/cc}$ of chloride ion the iron is corroding and pitting rapidly, thus causing a rapid increase in the surface area which resulted in an increase of 50% in the current density in going from one cycle to the next. The data in Fig. 1-5, as well as each of the points plotted in Fig. 6 and 7 were obtained from separate solutions. The variation between results would probably have been much less for low chloride contents if the data had been taken on a single solution for each of the successively added increments of chloride ion.

It has been observed that a silver or a silver-silver oxide anode would under certain conditions remove Cl^- from a 15% KOH solution as AgCl on the electrode. The optimum conditions were not determined nor is it known to how low a level the Cl^- can be reduced. It does suggest the possibility that the Cl^- content of existing purified electrolytes could be lowered even more in this manner. The silver introduced into the system could be removed by electrodeposition.

This technique might also be useful commercially in keeping the Cl^- content low enough to inhibit appreciably metallic corrosion in a system.

Techniques of this sort might lead the way to the possibility of efficiently removing unreactable impurities. For a given electrolyte containing a given unreactable ionic impurity, a suitable electrode material, temperature, potential, etc., might be found which would make it possible for this ion to react with the electrode and form an insoluble film which then could be removed from the system by removing the electrode.

Highly porous metallic electrodes can be prepared (5) which have surface areas so large that the formation of even a fraction of a monomolecular layer would remove relatively large amounts of a given ionic impurity. This would thus open up the possibility of removing nearly all of the impurities in an electrolyte down to levels that in many cases might approach the approximately 10^{-6} ppm that is now being obtained with reactable impurities. Under these conditions it would be possible to prepare a wide range of reagents whose impurity levels would be several orders of magnitude less than can be achieved with current techniques.

Acknowledgment

This research was supported by the Advanced Research Projects Agency of the Department of Defense, ARPA Order No. 878, under Problem No. M04-08.

Manuscript submitted July 23, 1971; revised manuscript received ca. Dec. 7, 1971.

Any discussion of this paper will appear in a Discussion Section to be published in the December 1972 JOURNAL.

REFERENCES

1. C. M. Shepherd and S. Schuldiner, *This Journal*, **115**, 1124 (1968).
2. J. E. O. Mayne, J. W. Mentor, and M. J. Pryor, *J. Chem. Soc.*, **1950**, 3229.
3. S. Schuldiner and R. M. Roe, *This Journal*, **110**, 332 (1963).
4. S. Schuldiner, T. B. Warner, and B. J. Piersma, *ibid.*, **114**, 343 (1967).
5. C. M. Shepherd and H. C. Langelan, *ibid.*, **109**, 657 (1962).

Anodic Oxidation of Ethylenediaminetetraacetic Acid on Pt in Acid Sulfate Solutions

J. W. Johnson,* H. W. Jiang, S. B. Hanna, and W. J. James*

Departments of Chemical Engineering and Chemistry and the Graduate Center for Materials Research, University of Missouri-Rolla, Rolla, Missouri 65401

ABSTRACT

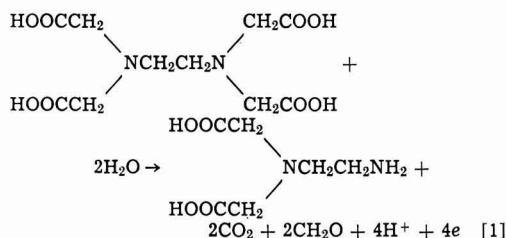
The anodic oxidation of EDTA was studied in acid sulfate solutions on platinized-Pt at 25°C . Polarization relationships were obtained for the EDTA concentration range 3.42×10^{-5} to $3.42 \times 10^{-3}\text{M}$ and pH range 0.35 to 3.80. Numerous reaction products were identified that indicated a sequential removal of acetate groups from the EDTA, each by an initial decarboxylation followed by a reverse Schiff-type reaction, that produced formaldehyde and the corresponding amine. A reaction sequence which correlated the experimental data involved Frumkin-type adsorption of the EDTA species through an un-ionized acetate group followed by a rate-determining electrochemical decarboxylation.

Ethylenediaminetetraacetic acid, commonly abbreviated "EDTA," forms very stable, water-soluble complexes with many metal ions. Because of this, studies

* Electrochemical Society Active Member.
Key words: ethylenediaminetetraacetic acid, anodic oxidation, decarboxylation.

involving EDTA have dealt mainly with complex formation and associated analytical and industrial applications. A few reports have been concerned with electrochemical aspects. One, a polarographic investigation of the products of the anodic oxidation of EDTA on Pt in alkaline solutions, was made by Kopek'a (1).

The over-all anodic reaction proposed was



In another, Reishakhrit *et al.* (2) studied the oxidation of EDTA on a Pt rotating-disk anode and found increases in the limiting currents with pH. Shifts in the polarization curves with pH were attributed to shifts in the dissociation equilibrium. With carbon paste indicator electrodes, Kitagawa and Tsushima (3) reported a single anodic wave for EDTA in acidic media with $E_{p/2} = 0.93\text{V}$ (vs. SCE).

The presence of EDTA during electrochemical processes (e.g., corrosion, metal dissolution, metal deposition, etc.) is not uncommon. Thus, it is of interest to know if EDTA itself is reactive. The purpose of this investigation was to determine if it could be oxidized on platinized platinum, and if so, to obtain information about the electrochemical reaction kinetics. The investigation included polarization measurements in acid sulfate solutions of various pH, the determination of reaction products and coulombic efficiency for CO_2 production, and the effect of temperature on the reaction rate.

Experimental

The electrolyses were carried out in the usual H-cell (400 ml capacity). All solutions employed analytical grade chemicals and conductivity water. Prepurified nitrogen was bubbled through the electrolyte to provide an inert atmosphere and for stirring. A constant flow rate (50 cm^3/min STP) was maintained through the anode compartment. The electrodes consisted of 52-mesh Pt gauze folded on Pt wire frames for support. They were platinized using a platinum chloride solution to which a trace of lead acetate had been added. The anode had a geometric surface area of 11.5 cm^2 . It was activated in 1.0N H_2SO_4 before each experiment as described previously (4).

The electrolytes for the studies were H_2SO_4 + Na_2SO_4 solutions (pH 0.35–4.0) in which the sulfate concentration was kept constant at unit normality. The EDTA concentration was varied from 3.42×10^{-5} to $3.42 \times 10^{-3}\text{M}$. The polarization measurements were made potentiostatically. A $\text{Hg}/\text{Hg}_2\text{SO}_4$ (1N H_2SO_4) reference electrode was used in conjunction with a salt bridge of the same electrolyte as in the cell. The potentials are reported vs. the standard hydrogen electrode (SHE) at 25°C. Reaction products were determined by standard qualitative analyses and paper electrophoresis. All studies were carried out at 25°C except as noted.

Results

Polarization measurements.—The rest potentials, Tafel slopes, and limiting currents from the polarization studies are summarized in Table I. The rest potentials and limiting currents were affected by the N_2 bubbling rate (the rest potentials decreased and limiting currents increased with increasing bubbling rate). There was no effect on currents in the linear Tafel region. All reported data were taken with the constant N_2 bubbling rate mentioned above. Steady currents at a given potential were obtained within about 25 min and remained quite stable for hours. Individual points were reproducible within $\pm 10\%$.

Semilogarithmic plots of the polarization curves are shown in Fig. 1. There are linear sections in the potential regions slightly above the rest potentials, with

Table I. Rest potentials, Tafel slopes, and limiting currents for the anodic oxidation of EDTA in acid sulfate solutions on Pt at 25°C

Electrolyte concentration				Rest potential V (SHE)	Tafel slope, V	Limiting current, $\text{A}/\text{cm}^2 \times 10^5$
EDTA, $\text{M} \times 10^4$	H_2SO_4 , N	Na_2SO_4 , N	pH			
3.42	1.00	—	0.35	0.803	0.125	1.9
1.027	1.00	—	0.35	0.842	0.130	1.1
0.342	1.00	—	0.35	0.889	0.120	0.65
3.42	0.100	0.900	1.78	0.680	0.130	8.7
1.027	0.100	0.900	1.78	0.698	0.130	2.0
13.7	0.010	0.990	2.74	0.650	0.115	13
3.42	0.010	0.990	2.78	0.679	0.110	3.7
1.027	0.010	0.990	2.80	0.700	0.110	1.9
0.342	0.010	0.990	2.72	0.730	0.120	0.96
34.2	0.001	0.999	2.93	0.623	0.120	30
13.7	0.001	0.999	3.10	0.652	0.105	20
3.42	0.001	0.999	3.59	0.648	0.110	3.4
1.027	0.001	0.999	3.72	0.645	0.110	1.7
0.342	0.001	0.999	3.80	0.665	0.120	0.65

slopes varying from 105 to 130 mV. The limiting current region was reached at potentials of about 0.95V (SHE). No pronounced passivation regions were found.

Two basic solutions, 3.42×10^{-2} and $1.028 \times 10^{-1}\text{M}$ EDTA in 1N NaOH, were also investigated. The polarization curves are shown in Fig. 2. Very small limiting currents were reached at potentials immediately above the rest potentials. Visible oxygen evolution occurred at potentials above 0.78V.

Reaction products.—Qualitative analyses showed the anodic oxidation products of EDTA to be quite numerous. A positive test for CO_2 was obtained by passing the N_2 purge through a saturated $\text{Ba}(\text{OH})_2$ solu-

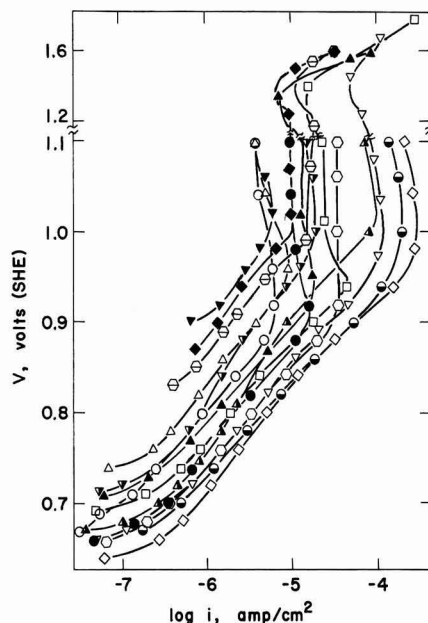


Fig. 1. Polarization curves for EDTA oxidation on Pt in acidic sulfate solutions at 25°C. \ominus , $3.42 \times 10^{-4}\text{M}$ EDTA in 1N H_2SO_4 ; \blacklozenge , $1.027 \times 10^{-4}\text{M}$ EDTA in 1N H_2SO_4 ; \blacktriangledown , $3.42 \times 10^{-5}\text{M}$ EDTA in 1N H_2SO_4 ; \blacktriangle , $3.42 \times 10^{-4}\text{M}$ EDTA in 0.1N H_2SO_4 + 0.9N Na_2SO_4 ; \blacktriangledown , $1.027 \times 10^{-4}\text{M}$ EDTA in 0.1N H_2SO_4 + 0.9N Na_2SO_4 ; \blacktriangledown , $1.37 \times 10^{-3}\text{M}$ EDTA in 0.01N H_2SO_4 + 0.99N Na_2SO_4 ; \square , $3.42 \times 10^{-4}\text{M}$ EDTA in 0.01N H_2SO_4 + 0.99N Na_2SO_4 ; \blacktriangle , $1.027 \times 10^{-4}\text{M}$ EDTA in 0.01N H_2SO_4 + 0.99N Na_2SO_4 ; \triangle , $3.42 \times 10^{-5}\text{M}$ EDTA in 0.01N H_2SO_4 + 0.99N Na_2SO_4 ; \diamond , $3.42 \times 10^{-3}\text{M}$ EDTA in 0.001N H_2SO_4 + 0.999N Na_2SO_4 ; \circ , $1.37 \times 10^{-3}\text{M}$ EDTA in 0.001N H_2SO_4 + 0.999N Na_2SO_4 ; \ominus , $3.42 \times 10^{-4}\text{M}$ EDTA in 0.001N H_2SO_4 + 0.999N Na_2SO_4 ; \blacklozenge , $1.027 \times 10^{-4}\text{M}$ EDTA in 0.001N H_2SO_4 + 0.999N Na_2SO_4 ; \blacktriangledown , $3.42 \times 10^{-5}\text{M}$ EDTA in 0.001N H_2SO_4 + 0.999N Na_2SO_4 .

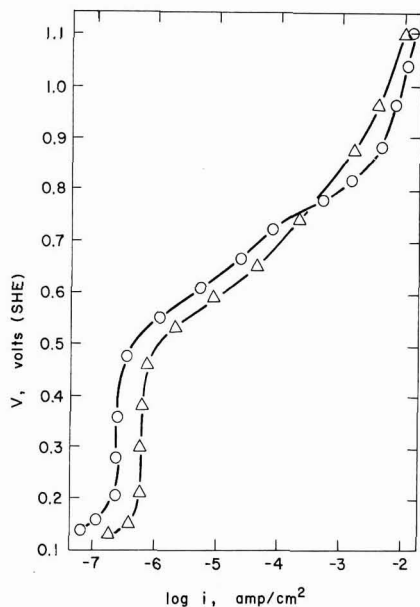


Fig. 2. Polarization curves for EDTA oxidation on Pt in basic solutions at 25°C. ○, 3.42×10^{-2} M EDTA in 1N NaOH; Δ, 1.027×10^{-1} M EDTA in 1N NaOH.

tion where a white precipitate (BaCO_3) was formed (5). Formaldehyde was detected by determining the melting point of a yellow precipitate formed on addition of a saturated solution of 2,4-dinitrophenylhydrazine (6). Other products in the electrolyte were identified by paper electrophoresis (7), the results of which are shown schematically in Fig. 3. Quantitative measurements of CO_2 production were made galvanostatically for 3.42×10^{-3} M EDTA in 10^{-3} N H_2SO_4 + 0.999 N Na_2SO_4 at potentials in the linear Tafel region. The average efficiency based on Eq. [1] was $124 \pm 6\%$.

Temperature dependence.—Arrhenius plots of current vs. temperature for 3.42×10^{-3} M EDTA in 10^{-3} N H_2SO_4 + 0.999 N Na_2SO_4 are shown in Fig. 4 for poten-

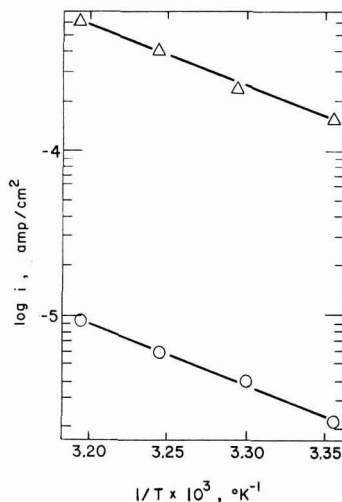
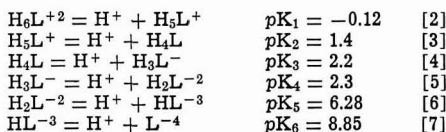


Fig. 4. Effect of temperature on current for oxidation of 3.42×10^{-3} M EDTA in 0.001N H_2SO_4 + 0.999N Na_2SO_4 on Pt. ○, 0.76V; Δ, 0.86V.

tials of 0.76 and 0.86V (SHE). The slopes of the two straight lines yielded activation energies of 18.4 and 17.0 kcal, respectively. These further give an effect of potential on the activation energy, $\partial E_a/\partial V$, of ca. -14 kcal/V which is consistent with the Tafel slopes.

Discussion

Limiting currents.—An initial consideration of the limiting (potential-independent) currents, i_L , from the polarization curves indicated them to be of the same order of magnitude as diffusion currents. However, the expected first-order dependence between current and concentration (8) was not found when the total EDTA concentration was used. This, together with the absence of reaction prior to oxygen evolution in basic solutions, suggested that some EDTA species may be preferentially participating. It is well known that EDTA engages in various equilibria with hydrogen ions with reported species covering the complete spectrum from H_6L^{+2} to L^{-4} .¹ Constants for these equilibria have been reported and are given in Eq. [2]–[7].



There is a considerable variation in the values of these constants reported by various investigators. All the values in Eq. [2]–[7] were from a single source, those reported by Anderegg (9). The concentrations of the EDTA species in all the electrolytes were calculated and are shown in Table II. The hydrogen ion activities used in the calculations were evaluated directly from the measured pH. For all other species, the activities and concentrations were assumed equal.

A comparison of the limiting currents with concentrations of the individual species (Tables I and II) shows that no single species can account for the reaction over the entire region studied. Various combinations of species were tried and the one most successful in correlating the data was the summation of the concentrations of the species H_5L^+ , H_4L , H_3L^- , H_2L^{2-} , and HL^{-3} . A log-log plot of i_L vs. C_x ² is shown in Fig. 5 with a straight line of unit slope drawn through the

¹ With this symbolic representation, H_4L = un-ionized EDTA.

² Sum of the concentrations of species H_5L^+ through HL^{-3} .

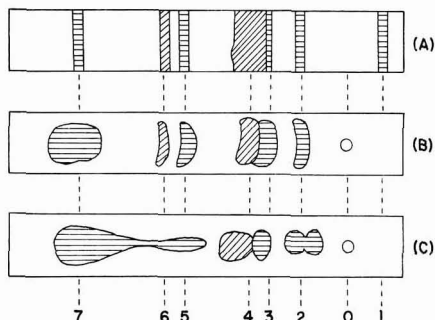


Fig. 3. Products of EDTA oxidation on Pt in acidic sulfate solutions at 25°C. (A) Standard tape. (B) 3.42×10^{-4} M EDTA in 1N H_2SO_4 , polarized at 1.2×10^{-4} A for 83 hr. (C) 3.42×10^{-4} M EDTA in 0.01N H_2SO_4 , polarized at 1.1×10^{-3} A for 75 hr. Electrophoretic separation in 1M acetic acid at 5 mA for 45 min, color developed with ninhydrin: horizontal hatch, purple bands; diagonal hatch, yellow bands. Bands: 1. IMDA and ED3A (iminodiacetic acid and ethylenedinitrilotriacetic acid), 2. S-EDDA and U-EDDA (N,N'-ethylenediglycine and N,N'-ethylenediglycine), 3. GL (glycine), 4. S-KP (2-oxo-1-piperazineacetic acid), 5. EDMA (N-(2-aminoethyl)glycine), 6. 2-KP (2-oxopiperazine), 7. EDA (ethylene-diamine).

Table II. Concentrations of EDTA species in acid sulfate solutions at 25°C

pH	a_{H^+}	$[H_4L], M$	$[H_3L^{+2}], M$	$[H_2L^{+3}], M$	$[HL], M$	$[H_2L^{-2}], M$	$[HL^{-3}], M$	$[L^{-4}], M$
0.35	0.447	3.422×10^{-4}	8.112×10^{-4}	2.394×10^{-4}	2.134×10^{-5}	3.014×10^{-7}	3.382×10^{-9}	3.973×10^{-15}
0.35	0.447	1.027×10^{-4}	2.434×10^{-5}	7.182×10^{-5}	6.401×10^{-5}	9.042×10^{-8}	1.018×10^{-9}	1.192×10^{-15}
0.35	0.447	3.422×10^{-5}	8.112×10^{-6}	2.394×10^{-5}	2.134×10^{-5}	3.014×10^{-8}	3.382×10^{-10}	3.973×10^{-16}
1.78	1.660×10^{-2}	3.422×10^{-4}	9.367×10^{-7}	7.440×10^{-5}	1.785×10^{-4}	6.786×10^{-5}	2.049×10^{-5}	6.480×10^{-10}
1.78	1.660×10^{-2}	1.027×10^{-4}	2.810×10^{-7}	2.232×10^{-5}	5.354×10^{-5}	2.036×10^{-5}	6.148×10^{-6}	1.944×10^{-10}
2.74	1.820×10^{-3}	1.369×10^{-3}	6.140×10^{-9}	4.448×10^{-6}	9.732×10^{-4}	3.374×10^{-4}	9.293×10^{-4}	2.680×10^{-7}
2.78	1.660×10^{-3}	3.422×10^{-4}	1.100×10^{-9}	8.736×10^{-7}	2.096×10^{-5}	7.967×10^{-5}	2.406×10^{-5}	7.608×10^{-8}
2.80	1.585×10^{-3}	1.027×10^{-4}	2.769×10^{-10}	2.320×10^{-7}	5.828×10^{-6}	2.337×10^{-5}	7.337×10^{-5}	2.429×10^{-8}
2.72	1.908×10^{-3}	3.422×10^{-5}	1.811×10^{-10}	1.253×10^{-7}	2.618×10^{-6}	8.668×10^{-6}	2.280×10^{-5}	6.280×10^{-9}
2.93	1.175×10^{-3}	3.422×10^{-5}	3.070×10^{-10}	3.444×10^{-6}	1.167×10^{-6}	6.268×10^{-6}	2.674×10^{-5}	1.194×10^{-9}
3.10	7.943×10^{-4}	1.369×10^{-3}	2.784×10^{-10}	4.620×10^{-7}	2.315×10^{-5}	1.839×10^{-4}	1.160×10^{-3}	7.667×10^{-7}
3.59	2.570×10^{-4}	3.422×10^{-4}	8.528×10^{-13}	4.373×10^{-9}	6.774×10^{-7}	1.663×10^{-5}	3.242×10^{-4}	6.619×10^{-7}
3.72	1.906×10^{-4}	1.027×10^{-4}	7.826×10^{-14}	5.414×10^{-10}	1.131×10^{-7}	3.746×10^{-6}	8.852×10^{-5}	2.714×10^{-7}
3.80	1.585×10^{-4}	3.422×10^{-5}	1.256×10^{-14}	1.045×10^{-10}	2.624×10^{-8}	1.045×10^{-6}	3.304×10^{-5}	1.094×10^{-7}

points. Although there is a great deal of scatter, the trend is correct and covers the entire concentration range. A least squares analysis of the data gives a slope of 0.8 ± 0.1 .

Product analyses.—The product analyses suggest that the oxidation of EDTA proceeds along at least two

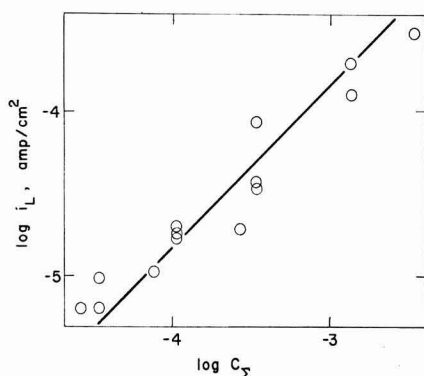


Fig. 5. Limiting currents for EDTA oxidation on Pt in acidic sulfate solutions at 25°C.

paths. Such a reaction scheme is shown in Fig. 6 for which all the species were identified with the exception of ED3A. The paper-electrophoresis method used was not sensitive to the latter three, and according to Doran (7), the cyclization of ED3A to 3-KP is so extensive in acid solutions that ED3A cannot be detected. Separate studies have indicated that equilibria are reached in the other cyclization reactions ($U-KP \rightleftharpoons U-EDDA$, $S-KP \rightleftharpoons S-EDDA$, and $2-KP \rightleftharpoons EDMA$) in which appreciable quantities of both species exist (10). From the product distribution, it appears that each decarboxylation step is a separate electrochemical reaction that gives a desorbed product capable of further similar reactions as long as acetate groups are available. This indicates adsorption through the carboxylate group with a Hofer-Moest-type reaction (11) occurring which involves the loss of two electrons, decarboxylation, and a reaction with water (not necessarily in that order) to form an alcohol. The two most common sequences offered to explain such reactions involve free-radical and/or carbonion ion intermediates. In both sequences, the first electron transfer is thought to form a free radical which leads to decarboxylation, i.e.

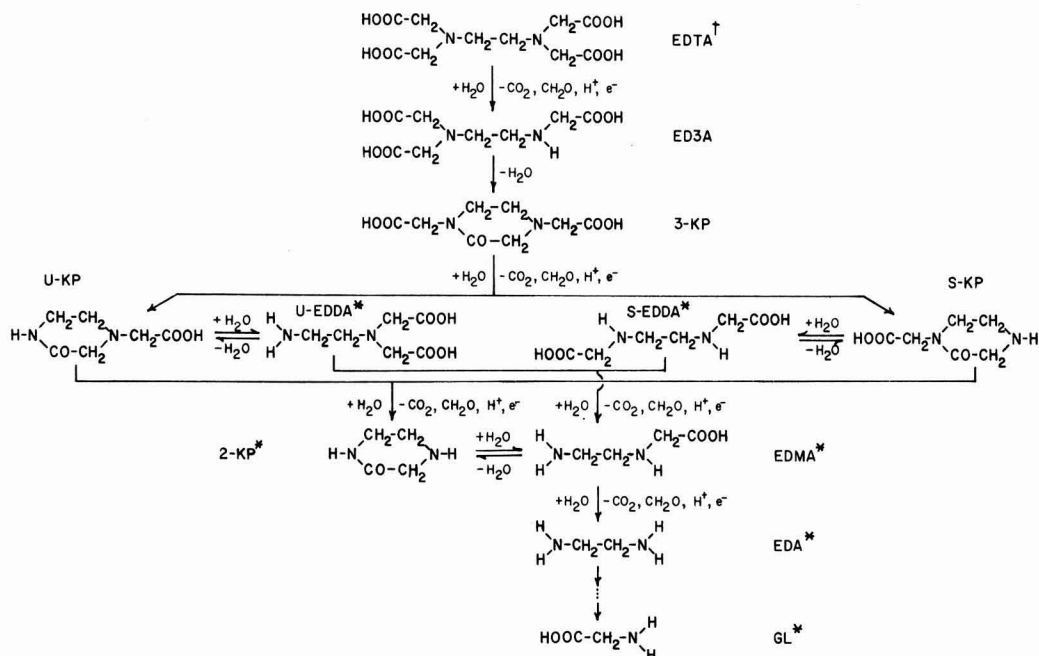
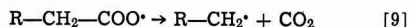
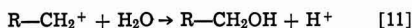
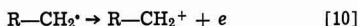
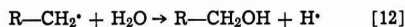


Fig. 6. Suggested reaction scheme for EDTA oxidation on Pt in acidic sulfate solutions at 25°C. †, Representative of any of the reactive species; *, species identified by paper electrophoresis, bands shown in Fig. 3.

At this point the sequences diverge with $R-CH_2^*$ either forming a carbonium ion by the second electron transfer or reacting to form another intermediate that may or may not involve an electron transfer. These can be represented by



and

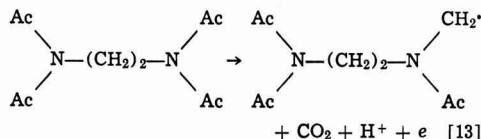


In either case with EDTA, the group $-N-CH_2OH$ is formed which is unstable and produces formaldehyde

through a reverse Schiff-type reaction, leaving $-NH$ (12). A feature that might allow one to distinguish between these two possibilities is the opportunity for different coulombic efficiencies for CO_2 production. In the first case (Eq. [10] and [11]), the carbonium ion is believed to be formed by electron transfer to the anode (13) which gives 1 mole of CO_2 per 2F of charge as shown in Eq. [1]. (Also implied here is the continued adsorption of the reacting species until after formation of the carbonium ion.) In the second case, it is possible that the radical $R-CH_2^*$ may have been desorbed during decarboxylation and that Eq. [12] represents a homogeneous reaction. (This is consistent with adsorption through the carboxylate group as mentioned above.) The H^* produced in this manner could be oxidized at the anode which would again give $1CO_2/2F$, but there is also opportunity for it to participate in some homogeneous reaction which would lead to $1CO_2/F$. If this latter reaction should occur, CO_2 efficiencies (based on Eq. [1]) greater than 100% would be observed. As seen above, efficiencies greater than 100% were found experimentally, thus favoring the sequence of Eq. [8], [9], and [12].

If adsorption had occurred through bonding with the nitrogen (as opposed to adsorption through the carboxylate), one would expect both the acetate groups to be removed before desorption with only U-EDDA and EDA as products as well as a $1CO_2/2F$ coulombic efficiency.

Rest potentials.—According to the reaction scheme shown in Fig. 6 and discussed in the above section, the initial electrochemical reaction is between EDTA and the precursor to ED3A and involves only one electron. (The preceding reactions will become significant only when sufficient current has passed so that appreciable quantities of the subsequent reactants are produced.) Thus, the measured rest potentials may reflect the reaction



Although the CO_2 and ED3A precursor (R^*) concentrations are not known and their standard free energies of formation are not available to allow a comparison of the rest and calculated potentials, the Nernst equation will allow a test of the effect of EDTA concentration and pH on the potential. At 25°C, the relation for Eq. [13] is

$$E = E_{13} - 0.0591 \log(a_{\text{EDTA}})/(a_{R^*})(a_{\text{CO}_2})(a_{\text{H}^+}) \quad [14]$$

Assuming a_{R^*} and a_{CO_2} constant and $a_{\text{EDTA}} = C_{\Sigma}$ gives

$$E = E_{13} - 0.0591 \log(C_{\Sigma}/a_{\text{H}^+}) \quad [15]$$

(C_{Σ} is the concentration of the species as mentioned previously.) A plot of E_{rest} vs. $\log(C_{\Sigma}/a_{\text{H}^+})$ is shown in Fig. 7. The relationship is linear and has a slope

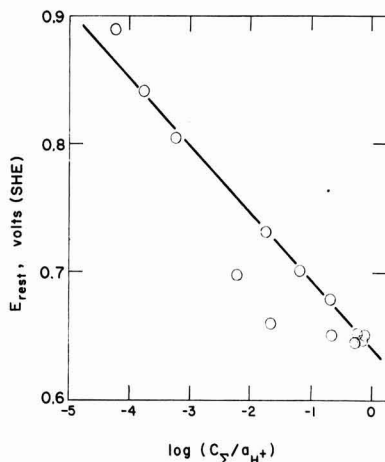


Fig. 7. Rest potentials for EDTA on Pt in acidic sulfate solutions at 25°C.

of 55 mV, in good agreement with that predicted by Eq. [15].

Polarization curves.—The oxidation of EDTA is seen to occur at potentials somewhat more positive than those for other organic compounds where CO_2 is produced (exclusive of Kolbe-type syntheses). For example in 1N H_2SO_4 , ethylene (4) oxidizes in the potential region from ca. 0.35 to 0.75V; formic acid (14), 0.15 to 0.45V; oxalic acid (15), 0.5 to 0.8V; and maleic acid (16), 0.35 to 0.60V. Acetic acid has been reported not to be reactive (17). In the majority of these cases, adsorption of the organic species was thought to involve the formation of bonds between C and Pt atoms, and passivation was observed between the upper potential limit for the organic oxidation and that for the commencement of oxygen evolution. The passivation ordinarily occurred in the region where EDTA has been found to be oxidized. This absence of passivation with EDTA indicates a different type of adsorption bonding that can presumably take place on an oxide-covered surface. Considering the apparent step-wise decarboxylation, the adsorption reaction thus appears to involve the carboxylate group and the electrode surface.

The Tafel slopes of ca. 120 mV or $2(2.3RT/F)$, are ones frequently encountered in electrochemical kinetic studies and normally associated with first-electron-transfer rate determining steps. The concentration and pH effects were unusual in that they were both fractional and approximately equal. The EDTA concentration effect (reaction order) was fairly well defined as 0.36 from the experiments in 1N H_2SO_4 where the pH was constant. It should be noted from Table I for 1N H_2SO_4 that the fraction of EDTA forming any of the individual species is independent of the initial EDTA concentration. Thus, the same reaction order (~ 0.36) would be found for any individual or combination of EDTA species. By a trial and error procedure, it was found that a pH effect also of 0.36 in conjunction with the concentration of EDTA species, C_{Σ} , best correlated the data. A log-log plot of i vs. $(C_{\Sigma}/a_{\text{H}^+})^{0.36}$ is shown in Fig. 8 for the entire EDTA concentration and pH region of the study. The line of unit slope drawn through the points show the data to be reasonably well correlated. This gives an empirical expression for the current as

$$i = nFk(C_{\Sigma}/a_{\text{H}^+})^{0.36} \exp(\alpha FV/RT) \quad [16]$$

Reaction mechanism.—From the preceding, several qualitative conclusions can be drawn about the reaction mechanism:

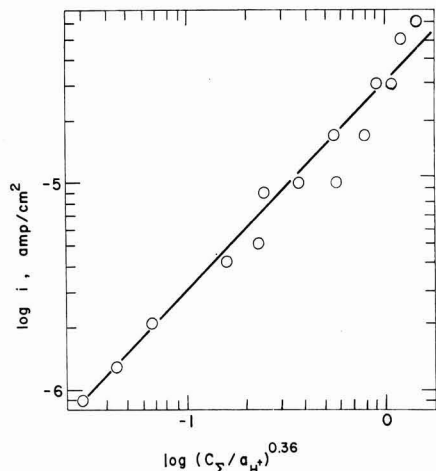


Fig. 8. Effect of concentration and pH on current for EDTA oxidation on Pt in acidic sulfate solutions at 25°C.

1. The rds (rate determining step) involves EDTA species or species derived therefrom since the concentration effect is positive.

2. The fractional concentration effect indicates that the EDTA species are adsorbed and that significant, although not complete, coverages are involved.

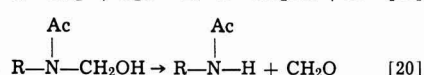
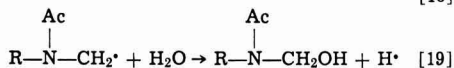
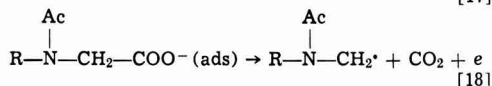
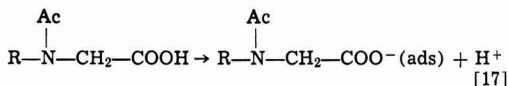
3. The positive pH effect indicates OH^- as a reactant or H^+ as a product during or prior to the rds. Since the OH^- concentration is very small, the latter case would be the most probable and would necessarily occur in an equilibrium step prior to the rds.

4. From the product analyses, there appears to be separate step-wise over-all reactions involving the acetate groups on EDTA, each of which yields CO_2 and CH_2O . From the rest potential and CO_2 efficiency studies, it further appears that only one electron is transferred to the faradaic circuit during the reaction that directly involves CO_2 production from the acetate group of the EDTA species.

5. From the concentration correlations for both the current and rest potentials, the pH effect, and the absence of reaction in basic solutions where L^{-4} is the predominant species, it appears that an un-ionized carboxyl group may be initially involved in the reaction sequence.

6. The occurrence of the reaction in a potential region where the anodic oxidation of ethylene, acetylene, etc. is passivated indicates that water discharge is not involved.

With these considerations, the initial electrochemical sequence ($\text{EDTA} \rightarrow \text{ED3A}$, Fig. 6) can be represented as follows³



The atomic hydrogen produced by reaction [19] can be oxidized at the anode and contribute to the faradaic

³ Species shown in these reactions are nonadsorbed unless otherwise indicated.

process or be removed by some nonelectrochemical reaction causing the CO_2 efficiency (based on Eq. [1]) to be increased. The ED3A thus produced can participate further in the sequence as shown in Fig. 6.

The type of adsorption (e.g., Langmuir, Temkin, etc.) as well as the nature and position of the rds in a reaction sequence can affect the associated kinetic parameters. For Langmuir-type adsorption, a first electron transfer rds is normally associated with the Tafel slope of 120 mV. For this case (reaction [18]), an EDTA concentration effect either close to zero or unity should be observed for conditions where this type adsorption is applicable, i.e., either high or low coverages. This does not appear to be the case.

The Temkin isotherm is often assumed for intermediate coverages when lateral interactions between adsorbed species are appreciable. For EDTA with the same rds (reaction [18]), Temkin-type adsorption gives a Tafel slope of 120 mV and concentration dependences $(a_{\text{EDTA}}/a_{\text{H}^+})^{0.5}$. These concentration effects are reasonably close to the observed values although 0.5 gives a poorer correlation than the value of 0.36 illustrated in Fig. 8. The use of the Frumkin isotherm allows a better correlation, primarily due to the added adjustable parameter associated with the variation of free energy of adsorption with coverage (18). This isotherm takes into account long-range interactions between adsorbed species which may be especially applicable due to the geometry of the EDTA molecule. Its application to the present case is as follows:

From reaction [17]

$$r_{17} = k_{17} a_{\text{EDTA}} \theta_v \exp(-\beta\theta/RT) - k_{-17} \theta_{\text{R}} \cdot a_{\text{H}^+} \exp[(f-\beta)\theta/RT] \quad [21]^4$$

Assuming quasi-equilibrium and the effect of coverage to be predominately controlled by the exponential terms gives

$$f\theta/RT = \ln(K_{17} a_{\text{EDTA}}/a_{\text{H}^+}) \quad [22]$$

From the rate determining step, reaction [18]

$$i = nFk_{18} \theta_{\text{R}} \cdot \exp(\alpha FV/RT) \exp(\beta\theta/RT) \quad [23]^4$$

Again assuming the exponential term to dominate the effect of coverage and substituting Eq. [22] into Eq. [23]

$$i = nFk' (a_{\text{EDTA}}/a_{\text{H}^+})^{\beta/f} \exp(\alpha FV/RT) \quad [24]$$

The term β/f can be made equal to 0.36 by assigning the appropriate value to the adjustable parameter f , thus making Eq. [24] correspond to the empirical rate expression, Eq. [16]. For the present case, f would equal 1.4 (assuming $\beta = 0.5$).

Acknowledgments

This paper is based on a thesis submitted by one of us (H.W.J.) for the M.S. degree in Chemical Engineering at the University of Missouri-Rolla. It is Contribution No. 131 from the Graduate Center for Materials Research, UMR.

Manuscript submitted July 6, 1971; revised manuscript received Dec. 18, 1971.

Any discussion of this paper will appear in a Discussion Section to be published in the December 1972 JOURNAL.

⁴ The symbols θ_v and θ_{R} refer to the fractions of the reaction surface that are available for reaction and covered by R^* , respectively.

REFERENCES

1. L. Kopeck'a, *Chem. Listy*, **50**, 1085 (1956).
2. L. S. Reishakhrit, V. N. Martynova, and Z. I. Tikhonova, *Ser. Fiz. Khim.*, **1**, 146 (1965).
3. T. Kitagawa and S. Tsushima, *Bull. Chem. Soc. Japan*, **39**, 636 (1966).
4. H. Wroblowa, B. J. Piersma, and J. O'M. Bockris, *J. Electroanal. Chem.*, **6**, 401 (1963).
5. R. K. McAlpine and B. A. Soule, "Qualitative Chemical Analysis," p. 448, D. Van Nostrand Co., New York (1933).

6. N. D. Cheronis and J. B. Entrikin, "Identification of Organic Compounds," p. 137, John Wiley & Sons Inc., New York (1967).
7. M. A. Doran, *Anal. Chem.*, **33**, 1752 (1961).
8. E. C. Potter, "Electrochemistry," p. 144, MacMillan Co., New York (1961).
9. G. Anderegg, *Helv. Chim. Acta*, **50**, 2333 (1967).
10. S. B. Hanna, Private communication.
11. B. J. Piersma and E. Gileadi, "Modern Aspects of Electrochemistry," Vol. 4, p. 52, J. O'M. Bockris, Editor, Plenum Press, New York (1966).
12. R. Q. Brewster, "Organic Chemistry," p. 271, Prentice-Hall, Inc., New York (1948).
13. A. K. Vijh and B. E. Conway, *Chem. Rev.*, **623** (1967).
14. S. B. Brummer and A. C. Makrides, *J. Phys. Chem.*, **68**, 1448 (1964); C. W. Fleischmann, G. K. Johnson, and A. T. Kuhn, *This Journal*, **111**, 602 (1964); M. H. Gottlieb, *This Journal*, **111**, 465 (1964).
15. J. W. Johnson, H. Wroblowa, and J. O'M. Bockris, *Electrochim. Acta*, **9**, 639 (1964).
16. J. W. Johnson and L. D. Gilmartin, *J. Electroanal. Chem.*, **15**, 231 (1967).
17. B. J. Piersma and E. Gileadi, "Modern Aspects of Electrochemistry," Vol. 4, p. 118, J. O'M. Bockris, Editor, Plenum Press, New York (1966).
18. E. Gileadi, "Electrosorption," p. 12, Plenum Press, New York (1967).

The Anodic Oxidation of Hydrogen on Platinized Tungsten Oxides

I. Composition of Tungsten Blue in Platinized WO₃

Hydrogen Electrocatalyst

B. S. Hobbs¹ and A. C. C. Tseung

Department of Chemistry, The City University, St. John Street, London EC1V 4PB, England

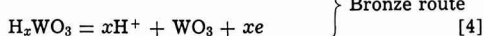
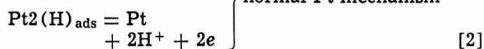
ABSTRACT

A synergistic effect is apparent when Pt/WO₃ catalysts are used in hydrogen electrodes. The exact mechanism of this effect depends on the composition and mode of formation of a reduced intermediate tungsten oxide. Chemical analysis and x-ray studies confirmed that this intermediate oxide consists of blue tungsten bronzes. The influence of Pt loading, platinizing technique, temperature, and pH on the bronze composition was investigated. The maximum reduction (H_{0.44}WO₃) was obtained using WO₃ impregnated with 0.8 weight per cent (w/o) Pt in acidic solution between 25° and 100°C.

When platinum is admixed with WO₃, it undergoes an apparent enhancement in its ability to catalyze the anodic oxidation of hydrogen in acid solution (1-3). WO₃ alone has no activity towards H₂-oxidation. Past workers have been unable to make definite conclusions on the origin of this effect owing to difficulties encountered in eliminating electrode structural effects from their results. Thus, the higher activity observed with WO₃ electrodes compared to other platinized substrates [e.g., graphite or TaC (2, 3)] could have arisen from differences in Pt morphology or physical electrode parameters such as wetting, permeability, etc. However, an alternative explanation has been proposed in which WO₃, in physical contact with Pt, participates in the electrode reaction via formation of hydrogen tungsten bronzes (2).

Hydrogen tungsten bronzes belong to a general class of nonstoichiometric mixed oxides (4) of general formula A_xM_yO_z; where M is a transition metal, M_yO_z its highest binary oxide, A is some other metal or hydrogen, and x is a variable, usually 0 < x < 1. Formation of blue hydrogen tungsten bronzes generally occurs whenever WO₃ is exposed to reducing conditions, e.g., gaseous atomic hydrogen (5-10), treatment of aqueous suspensions of WO₃ with reducing agents (11-14) (viz. Zn/HCl, SnCl₂, etc.), but of special interest to this study is their appearance in mixtures of platinized WO₃ when exposed to H₂, particularly in the presence of water vapor (15, 16). According to Benson *et al.*, gaseous H₂ dissociatively chemisorbs on the Pt then

migrates across the metal/oxide interface to form bronzes. The migration is considerably aided by the presence of an adsorbed water layer when an exchange mechanism operates and the WO₃ particles are rapidly reduced in depth. Bronze oxides are characteristically chemically inert, metallic conductors of electricity and the H-compounds are typical group members, except that they are sensitive towards oxidizing conditions which reconvert them to the parent oxide (13), e.g., air, hydrogen peroxide, oxidizing ions such as Fe³⁺ and Ce⁴⁺, and presumably anodic potentials. Thus a reaction scheme can be formulated for the H₂-electrode to include the WO₃ support, namely



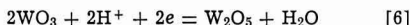
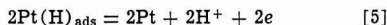
By means of the bronze route the reaction zone can be extended and the Pt appears to increase its activity. No such possibility exists for graphite or TaC which can be termed "passive" catalyst supports, WO₃ being an "active" support.

Both moist Pt/WO₃ powders, and suspensions in acidic solutions, rapidly turn blue when exposed to H₂, indicating partial reduction of the oxide. However, this "tungsten blue" may consist of either, or both, of two classes of compound, namely the lower tungsten oxides (17, 18) (WO_x, where 2 < x < 3) or hydrogen

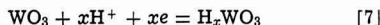
¹ Present address: Electrical Research Association, Cleeve Road, Leatherhead, Surrey, England.

Key words: hydrogen, oxidation, platinized tungsten oxides, tungsten bronzes, tungsten blue, chemical analysis, x-ray studies, H₂ uptake, crystal structure.

bronzes. Although direct reduction of WO_3 to lower oxides by H_2 at room temperature does not occur (19), they could form by local cell action between the hydrogenated Pt surface and WO_3



Although the reduction of WO_3 to W_2O_5 (or $\text{WO}_{2.5}$) is not thermodynamically favored at normal H_2 anode potentials [$E^\circ \text{WO}_3/\text{W}_2\text{O}_5 = -0.03\text{V}$ (20)], reduction might occur through the formation of nonstoichiometric WO_3 [$\text{WO}_{3.00-2.95}$ (18)], the stable intermediate phase $\text{W}_{20}\text{O}_{58}$ (17, 18) or solid solutions of lower oxide phases, for which no thermodynamic data could be found. Bronze formation is also possible by local cell action and again no thermodynamic data is available for such reactions



In any system whereby local cells are the sole means of WO_3 reduction, e.g., via the lower oxides of tungsten, no net contribution to the steady state anodic current is possible since all the anodic current will be cancelled by the cathodic reducing current (reactions [6] and [7] above). The oxide will equilibrate at any given working potential and the local cells will merely provide a mechanism for electron conduction between the Pt particles and current collector.

Benson *et al.* (15, 16) have studied tungsten blue formation in a vacuum system and shown it to consist exclusively of bronzes formed by chemical reduction (reaction [3]). However, in view of the importance of the nature and mode of formation of the reduction product to the electrochemical oxidation of H_2 , it is necessary to confirm this finding under conditions closer to those in a fuel electrode, viz. Pt/ WO_3 slurries in 5N H_2SO_4 between ambient temperature and 80°C and 1 atm of bubbling H_2 .

Experimental

Using x-ray diffraction and analytical techniques, the tungsten blue composition was determined as a function of: (i) platinizing method, viz. mechanical mixing and impregnation—this has been shown to exert considerable influence on both the rate of tungsten blue formation (15) and the electrochemical performance (2); (ii) Pt content; (iii) pH of slurry; and (iv) temperature.

Due to the extreme sensitivity of tungsten blue to air, all preparations and analyses were carried out in completely O_2 -free conditions.

Materials.—(i) Impregnation of WO_3 —to ensure a high, uniform and intimate dispersion of Pt on the oxide, a freeze drying technique was employed for the impregnation (21, 22): A slurry of WO_3 powder, suspended in chloroplatinic acid solution, was quickly frozen by pouring into liquid nitrogen. The water was then removed by vacuum sublimation and the Pt-salt reduced to metal in a warm H_2 stream (50°C) below its melting point (60°C). Complete decomposition was checked by weighing before and after reduction.

The Pt content was analyzed by extracting the WO_3 with warm NaOH solution and weighing the washed and dried Pt residue. This residue was also used for surface area determination by "BET nitrogen adsorption." Blank Pt black samples were measured for surface area before and after NaOH treatment to ensure that the area remained unaltered during the extraction procedure. Specific surface areas of extracted Pt residues were all around $35 \text{ m}^2/\text{g}$.

(ii) WO_3 and chloroplatinic acid—Hopkin and Williams laboratory reagent grade chemicals were used without further purification. The measured specific surface area of WO_3 was $8 \text{ m}^2/\text{g}$.

(iii) Pt-black used in mechanical mixtures—Johnson Matthey Company fuel cell grade, specific surface area $30 \text{ m}^2/\text{g}$.

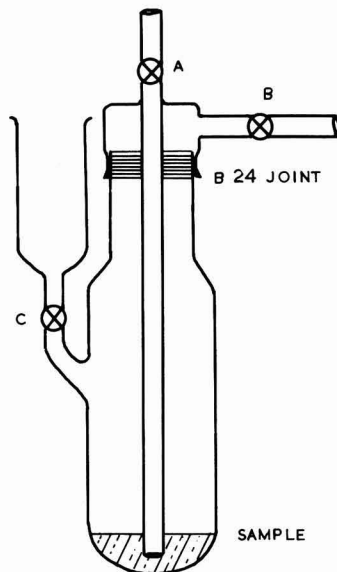


Fig. 1. Apparatus for tungsten blue analysis

(iv) 5N sulfuric acid was prepared from ANALAR grade concentrated acid and distilled/deionized water.
(v) White spot H_2 , purified with a palladium diffuser, was used throughout.

H_2 -uptake experiments.—Before carrying out the tungsten blue preparations, the time required to reach equilibrium was determined using a conventional volumetric apparatus at 1 atm pressure and ambient temperature. With impregnated powders the H_2 -uptake volume reached a limiting value after about 1 hr corresponding to a tungsten blue composition of $\text{H}_{0.44}\text{WO}_3$ or $\text{WO}_{2.78}$. The time taken to reach this value is almost certainly controlled by H_2 mass transfer through the slurry. In practical fuel electrodes the conditions are designed to achieve high transfer rates and the oxide composition will change much more rapidly.

In all experiments involving tungsten blue preparation a standard H_2 -contact time of 2 hr was used.

Analysis of tungsten blue.—Tungsten blue was prepared and analyzed in the apparatus shown in Fig. 1 as follows: Tap A was connected to N_2 (O_2 -free) and H_2 supplies. After N_2 purging, H_2 was bubbled from A through a weighed platinized WO_3 sample suspended in 5N H_2SO_4 . The H_2 was turned off after 2 hr and a measured volume of standard potassium dichromate solution admitted through tap C. The vessel contents were heated to ca. 60°C , when the blue color changed to yellow indicating complete oxidation. The cooled vessel contents were transferred to a beaker and the excess dichromate back-titrated with standardized ferrous ammonium sulfate solution. The end point was determined potentiometrically using a platinized wire indicator electrode with a glass standard electrode. In all cases a small correction was made to the titre to allow for reaction with H_2 adsorbed on the Pt surface.

Preparation of tungsten blue for x-ray diffraction.—The apparatus, shown schematically in Fig. 2, is a modified version of that described by Glemser and Naumann (13). Taps A_1 , A_2 , and A_3 were connected to N_2 (O_2 -free) and H_2 supplies. The flask contained distilled water, freed of O_2 by boiling during the passage of N_2 from A_2 and out the pressure release valve. After purging with N_2 and sealing the capillary, H_2 was bubbled through the sample suspended in H_2SO_4 , from A_2 and out B_2 , for 2 hr. The tungsten blue formed

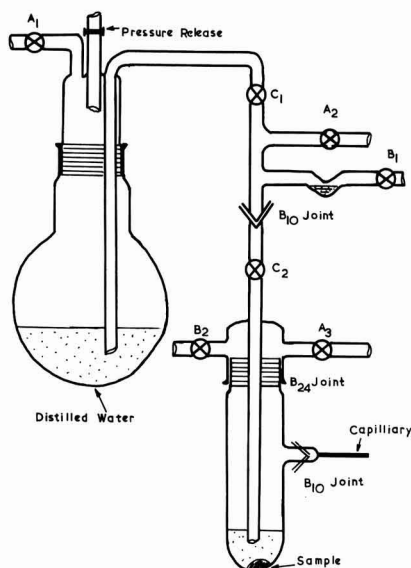


Fig. 2. Preparation of tungsten blue for x-ray examination

was washed by decantation—pressurized H_2 from A_3 forced the supernatant liquor from the settled suspension through C_2 and out B_1 . Water from the flask was forced onto the sample by pressurizing at A_1 . This procedure was repeated until the washings were neutral (pH 7.0). After the final wash all taps were closed and the apparatus below the B_{10} joint (between C_1 and C_2) detached and fused into a high vacuum line ($< 10^{-5}$ Torr) at the B_2 outlet. The product was dried by evacuation through B_2 , then after closing B_2 and detaching from the vacuum line, a sample of powder was sealed into the capillary by lying the vessel on its side, gently vibrating the powder, then when sufficiently full, applying a spot flame to remove and seal the capillary without releasing the vacuum.

X-ray powder photographs were taken of the samples using an 11.4 cm Phillips camera, copper $K\alpha$ radiation and exposure times of 8 hr. Lattice d-spacings were calculated from the patterns to within $\pm 0.005\text{\AA}$ from the Bragg equation.

In order to simplify the glassblowing of the apparatus, Pyrex capillaries were used instead of the usual Lindemann glass. Diffraction photographs of WO_3 using both materials showed no differences.

Results and Discussion

Analytical results.—The analytical results are summarized in Table I. The reproducibilities of the quoted values agreed closely with the estimated limits of experimental error which were as follows: tungsten oxi-

Table I. Analytical data for platinized WO_3

Powder	Plat-inum (wt %)	Tem-per-ature ($^{\circ}\text{C}$)	pH	W ox-idation state	Equiv-alent bronze	Equiv-alent oxide
Pt/ WO_3 mech. mixt.	2	25	-0.3	5.86	$H_{0.14}WO_3$	$WO_{2.83}$
Pt/ WO_3 mech. mixt.	2	25	-0.3	5.86	$H_{0.14}WO_3$	$WO_{2.83}$
Pt/ WO_3 mech. mixt.	2	25	7.0	5.99	$H_{0.01}WO_3$	$WO_{2.905}$
Pt/ WO_3 mech. mixt.	2	25	2.0	5.86	$H_{0.11}WO_3$	$WO_{2.83}$
Pt/ WO_3 mech. mixt.	2	25	0.5	5.86	$H_{0.11}WO_3$	$WO_{2.83}$
Pt/ WO_3 mech. mixt.	10	25	-0.3	5.73	$H_{0.27}WO_3$	$WO_{2.87}$
Pt/ WO_3 mech. mixt.	10	25	-0.3	5.77	$H_{0.28}WO_3$	$WO_{2.89}$
Pt/ WO_3 impreg.	0.8	25	-0.3	5.56	$H_{0.44}WO_3$	$WO_{2.78}$
Pt/ WO_3 impreg.	0.8	25	-0.3	5.56	$H_{0.44}WO_3$	$WO_{2.78}$
Pt/ WO_3 impreg.	0.8	25	-0.3	5.58	$H_{0.42}WO_3$	$WO_{2.79}$
Pt/ WO_3 impreg.	0.8	72	-0.3	5.82	$H_{0.39}WO_3$	$WO_{2.81}$
Pt/ WO_3 impreg.	0.8	100	-0.3	5.82	$H_{0.39}WO_3$	$WO_{2.81}$
Pt/ WO_3 impreg.	10	25	-0.3	5.88	$H_{0.30}WO_3$	$WO_{2.84}$
Pt/ WO_3 impreg.	0.1	25	-0.3	5.88	$H_{0.13}WO_3$	$WO_{2.84}$

dation state $\pm 0.2\%$, tungsten oxide composition $\pm 0.2\%$, and bronze composition $\pm 7\%$.

The most notable result in Table I is the considerably higher extent of reduction achieved by impregnation methods over straight mechanical mixtures. This result parallels previous findings (2, 15), and is certainly due to the higher dispersion of the Pt and intimacy of contact with the oxide.

The analytical result for a 0.8 w/o Pt impregnated powder in 5N H_2SO_4 agreed with the H_2 -uptake value of $H_{0.44}WO_3$ or $WO_{2.78}$.

The Pt content of impregnated powders had little effect on the oxide composition above 0.8 w/o, but when reduced to 0.1 w/o a drastic fall in the degree of reduction occurred. This effect is explained in Part II dealing with the electrochemistry of the Pt/ WO_3 system. The small decrease in the reduction of the 10 w/o powder could have arisen from greater uncertainties in the correction applied for H adsorbed on the Pt.

With mechanical mixtures, reduction was significantly increased by changing the Pt content from 2 to 10 w/o. Even at 10 w/o Pt however, the reduction was still only about half that achieved with 0.8 w/o impregnated powders.

As long as the solution remained acidic the extent of reduction remained independent of pH. In neutral solutions however, blue formation was severely restricted.

Increasing the temperature to 100°C resulted in a slight decrease in reduction of an impregnated powder.

X-ray diffraction results.—Measured d-spacings (within $\pm 0.005\text{\AA}$) and relative line intensities are recorded in Table II for diffraction patterns obtained from a 2 w/o Pt/ WO_3 mechanical mixture and 0.8 w/o Pt impregnation. Both patterns exhibited line broadening at high diffraction angles due to small particle size (23), but the lines were sharp enough for accurate measurements of angles corresponding to d-spacings above 1.2\AA .

Comparison of the d-spacings with the A.S.T.M. index values for the possible species showed no evidence for the presence of lower tungsten oxides and interpretation could be made entirely in terms of the bronze phases, $H_{0.1}WO_3$, $H_{0.33}WO_3$, and $H_{0.5}WO_3$ (13). The Pt concentration was below the detection limits for any diffraction lines to be discernible.

The mechanically mixed powder had a complex pattern which proved difficult to index. Most lines were attributable to $H_{0.1}WO_3$ and $H_{0.33}WO_3$, or solid solutions of these phases—as evidenced by lines having intermediate values between those quoted for the separate phases. This conclusion was supported by the empirical formula $H_{0.14}WO_3$ obtained by analysis. Some

Table II. Experimental x-ray data for tungsten blues

2% Pt mechanical mixture		0.8% Pt impregnation		
d (Å)	Intensity	d (Å)	Intensity	h k l
3.840	f	3.745	vs	001
3.713	vs	2.651	s	110
3.645	vs	2.168	m	111
3.087	f	1.883	m	002
2.650	vs	1.866	f	200
2.591	m	1.681	s	210
2.157	f	1.678	vf	102
1.993	f	1.533	f	112, 211
1.933	f	1.329	f	022, 220
1.884	f	1.252	m	122, 221
1.836	f			
1.809	f	1.19		
1.709	vf	1.18		
1.682	m	1.134		
1.664	m	1.129		
1.644	m	1.09		
1.533	m	1.045		
1.515	m	1.039		
1.486	f	1.005		
1.330	vff			
1.253	vs			

Intensity key: vs = very strong, s = strong, m = medium, f = faint, vf = very faint.

lines remained which were best interpreted as being due to unreacted WO_3 , possibly in solid solution with the bronzes.

The impregnated powder had a far simpler pattern and evidently consisted of a solid solution of $\text{H}_{0.33}\text{WO}_3$ and $\text{H}_{0.5}\text{WO}_3$ (cf. data in Tables II and III). Using a Bunn Chart (24), the "blue" was shown to possess a tetragonal unit cell and assigned the hkl values given in Table II. The unit cell parameters a_0 and c_0 were calculated from the relationship (24)

$$d_{\text{tetragonal}} = \frac{1}{\sqrt{\frac{h^2 + k^2}{a_0^2} + \frac{l^2}{c_0^2}}}$$

using d -spacings of the 110 and 002 planes respectively. The choice of these planes gave maximum accuracy and ease of calculation. Closer spacings and secondary reflections at higher diffraction angles (e.g., 220, 003, etc.) had diffuse lines due to particle size effects, and the sharp 001 lines had a high inherent error due to the finite specimen thickness (25).

The a_0 and c_0 values are compared with those quoted for $\text{H}_{0.5}\text{WO}_3$ and $\text{H}_{0.33}\text{WO}_3$ (13) in Table IV. Differences in a_0 were too small to draw any conclusions as to the composition of the solid solution, but the c_0 -axis for the tungsten blue had an intermediate value between $\text{H}_{0.5}\text{WO}_3$ and $\text{H}_{0.33}\text{WO}_3$. Assuming that as H_2 progressively enters the tetragonal $\text{H}_{0.33}\text{WO}_3$ lattice, the c_0 -axis linearly decreases until the system becomes cubic at $\text{H}_{0.5}\text{WO}_3$, then an empirical formula can be calculated for the "blue" of $\text{H}_{0.42} \pm 0.06\text{WO}_3$. This is in good agreement with the analytical result of $\text{H}_{0.44} \pm 0.03\text{WO}_3$.

Final confirmation of the composition of the impregnated powder was obtained by reducing some plain WO_3 with zinc and hydrochloric acid to the same reduction state—previously determined by analysis of various Zn/WO_3 mixtures. This method which is definitely known to form bronzes (13, 26), produced an identical diffraction pattern.

Table III. A.S.T.M. d -spacings for hydrogen bronzes (13)

$\text{H}_{0.1}\text{WO}_3$		$\text{H}_{0.33}\text{WO}_3$		$\text{H}_{0.5}\text{WO}_3$	
d (Å)	Intensity	d (Å)	Intensity	d (Å)	Intensity
4.00	10	3.79	80	3.68	50
3.84	60	2.69	80	2.63	50
3.64	100	2.19	10	2.16	10
3.11	10	1.91	20	1.87	30
2.87	60	1.87	10	1.68	100
2.61	20	1.69	100	1.53	80
2.16	10	1.68	20	1.33	80
2.00	10	1.55	100	1.25	80
1.92	10	1.34	10	1.19	30
1.84	40	1.26	100	1.13	30
1.82	40	1.20	10	1.09	10
1.71	10	1.185	10	1.05	50
1.66	20	1.14	10	1.01	80
1.64	20	1.13	10		
1.58	5	1.09	10		
1.54	5	1.05	10		
1.51	20	1.04	10		
1.485	20	1.01	50		
		1.01	50		

Table IV. Unit cell dimensions for impregnated WO_3 powders and hydrogen bronzes prepared by other authors (13)

	Experimental values	$\text{H}_{0.33}\text{WO}_3$ (13)	$\text{H}_{0.5}\text{WO}_3$ (13)
a_0 (Å)	3.750 ± 0.006 ($\sqrt{2}d_{110}$)	3.751 ± 0.006	3.755 ± 0.006
c_0 (Å)	3.77 ± 0.01 ($\sqrt{2}d_{002}$)	3.796 ± 0.006	3.755 ± 0.006

Conclusions

Hydrogen tungsten bronzes (H_xWO_3) are formed in platinized WO_3 under the prevailing conditions in a fuel cell hydrogen electrode. The highest degree of reduction $\text{H}_{0.44}\text{WO}_3$, was obtained at 25°C using an impregnation technique for platinizing with 0.8 w/o Pt. Mechanical mixtures do not produce very intimate mixing, resulting in slower, incomplete reduction which can be improved by increasing the Pt loading. So long as the electrolyte is acidic, pH has no effect on the reduction.

Although bronzes are the major product when platinized WO_3 is reduced in acid slurries by H_2 , it is not apparent whether they form by chemical reduction or by local cell action. Whether or not the bronzes contribute to the net anodic current of a H_2 -anode will depend on which of these mechanisms predominates, as well as the relative rates of bronze formation and anodic oxidation. Part II describes work aimed at answering these questions.

Acknowledgment

This work was supported by the Ministry of Defence.

Manuscript submitted Nov. 1, 1971; revised manuscript received Dec. 21, 1971.

Any discussion of this paper will appear in a Discussion Section to be published in the December 1972 JOURNAL.

REFERENCES

1. L. W. Niedrach and I. B. Weinstock, *Electrochem. Technol.*, **3**, 270 (1965).
2. B. S. Hobbs and A. C. C. Tseung, *Nature*, **222**, 556 (1969).
3. A. C. C. Tseung and B. S. Hobbs, *Platinum Metals Rev.*, **13**, 14 (1970).
4. P. G. Dickens and M. S. Whittingham, *Quart. Rev. (London)*, **30** (1968).
5. T. H. Johnson, *J. Franklin Inst.*, **207**, 629 (1929).
6. D. Brennan and P. C. Fletcher, *Nature*, **183**, 249 (1959).
7. J. R. Arthur, **164**, 537 (1949).
8. J. C. Robb and H. W. Melville, *Discussions Faraday Soc.*, **2**, 132 (1947).
9. J. C. Robb and H. W. Melville, *Proc. Roy. Soc. (London)*, **A196**, 445 (1949).
10. O. Glemser, U. Hauschild, and G. Lutz, *Z. Anorg. Allgem. Chem.*, **269**, 93 (1952).
11. O. Glemser and H. Sauer, *Z. Anorg. Chem.*, **252**, 144 (1943).
12. O. Glemser, J. Weidelt, and F. Freund, *Z. Anorg. Allgem. Chem.*, **332**, 299 (1964).
13. O. Glemser and C. Naumann, *Z. Anorg. Chem.*, **265**, 288 (1951).
14. O. Glemser and G. Lutz, *ibid.*, **264**, 17 (1951).
15. J. E. Benson, H. W. Kohn, and M. Boudart, *J. Catalysis*, **5**, 307 (1966).
16. M. Boudart, M. A. Vannice, and J. E. Benson, *Z. Physik. Chem. Neue Folge*, **64**, 171 (1969).
17. A. E. Vol, in "Handbook of Binary Metallic Systems," Israel Program Sci. Trans., N. V. Ageev, Editor, 727 (1966).
18. K. C. Li and C. Y. Wang, "Tungsten," Reinhold Press (1955).
19. A. J. Hegedus, T. Millner, J. Neugebauer, and K. Sasvari, *Z. Anorg. Allgem. Chem.*, **281**, 64 (1955).
20. W. M. Latimer, "Oxidation Potentials," p. 254, Prentice Hall Inc., Englewood Cliffs, N. J. (1952).
21. A. C. C. Tseung and H. L. Bevan, *J. Mater. Sci.*, **5**, 604 (1970).
22. L. Wong, M. Phil Thesis, The City University, London (1969).
23. C. W. Bunn, "Chemical Crystallography," p. 107, Oxford Press (1961).
24. C. W. Bunn, *ibid.*, p. 144.
25. C. W. Bunn, *ibid.*, p. 127.
26. P. G. Dickens and R. J. Hurditch, *Nature*, **215**, 1266 (1967).

The Effect of Viscous Shear on a Meniscus in an Electrochemical System

P. C. Wayner, Jr.

Fluid, Chemical, and Thermal Processes Division, Rensselaer Polytechnic Institute, Troy, New York 12181

ABSTRACT

Fluid flow in the evaporating meniscus of an electrode-gas-electrolyte reacting system has been studied to examine the effect of viscous shear on the meniscus profile. The evaporating meniscus profile, the pressure derivative profile, and the curvature profile for various assumed evaporation profiles were calculated for 1N H_2SO_4 . Due to the thinness of the meniscus profile in the interline region, large pressure gradients were needed to balance the viscous shear stress. The resulting evaporating meniscus profile was significantly different from the static profile. Depending on the evaporation rate the interline radius of curvature could be micron size for a large meniscus. Heat and mass transfer rates would also be significantly effected by these changes during an electrochemical reaction. Therefore, the effect of viscous shear should not be neglected in analyzing electrochemical processes in a "finite contact angle" meniscus.

The triple interline region of a meniscus formed on an immersed solid surface has been the subject of considerable research. In part, this derives from interest in the potentially high heat and mass transfer rates associated with a large surface area covered by a thin liquid film in the form of a myriad of menisci (porous fuel cell electrodes are of particular interest herein). The study of electrochemical processes on wetted metallic surfaces partially immersed in an electrolyte could be classified according to whether or not a thin film extends above the intrinsic meniscus. The obvious and significant characteristic of a meniscus without a thin film ["finite contact angle meniscus" (1)] is that the diffusion path length across the liquid film approaches zero at the interline. This study is particularly concerned with the outstanding work of Bockris and Cahan (1) which discusses the effect of a finite contact angle meniscus on kinetics in porous electrode systems. Conversely, various other authors (2-4) considered models and systems that included a thin film above the intrinsic meniscus. Due to the large number of experimental variables, the complete set of conditions that insure the presence of a particular type of meniscus is still questionable.

The following three of many conclusions concerning electrochemical kinetics in a meniscus presented by Bockris and Cahan (1) are of particular interest herein: (i) "most of the current is produced in the first 1% of the meniscus;" (ii) "the extreme concentration of current density into this small area can produce local heating and create a dynamic situation in the physical location of the meniscus;" and (iii) "the local geometry of the meniscus, particularly in the three-phase region, dominates the behavior of porous electrodes." They also state that some of the heat is readily removed by evaporation. In their analysis of this extremely complex system, the geometry of the meniscus is represented by the equation for a cylindrical surface, thereby neglecting the effect of viscous flow of the evaporating liquid on the meniscus profile. The major effect of this shear stress would be in the thinnest and most important region of the meniscus. Recently, a procedure to evaluate the effect of viscous flow on the profile has been developed (5). Although it is not the present objective to completely reanalyze the very complex transport processes occurring in an active electrochemical meniscus, the results presented below demonstrate that it is very instructive to examine the effect of viscous flow in a few selected and related cases.

Synopsis of Reference (1)

In Ref. (1) a 1N, H_2SO_4 meniscus was formed between two parallel optical glass flats. One glass surface of the resulting slot was coated with Pt to serve as an electrode. Optical measurements of the resulting meniscus were made through the other glass surface. Using reflectometric techniques, the slope was determined as a function of distance from the interline at intervals of approximately 12.7μ . Interferometrically, fringes of the same kind reoccurred at film thickness differences of 2945Å. Simultaneously, the steady-state total current-potential behavior of the system was also measured for both H_2 and O_2 dissolution in the electrolyte. Within the accuracy of the experiments, the results indicated that the most stable meniscus configuration was one with a finite contact angle between 1° and 3° , and that it could be represented by the surface of a cylinder with a diameter equal to the slot width. On the basis of the experimental measurements, a detailed second-order nonlinear nonhomogeneous differential equation describing the reaction zone was derived and solved numerically. The microscopic description of the reaction zone was a strong function of the meniscus profile. The calculated relationship between the total current and potential which depended on many variables agreed well with the experimental results.

Qualitative Description of an Evaporating Meniscus

Consideration is given herein to an evaporating meniscus formed on a vertical flat plate immersed in a pool of liquid. The pressure gradient for fluid flow from the pool to the zone of evaporation results from a change in the meniscus profile (curvature). Relative to the isothermal case, the interline of the evaporating meniscus has migrated down the plate so that the profile can accommodate the increased pressure gradient needed to balance the viscous stresses of fluid flow. Assuming that the contact angle remains constant, the average curvature of the evaporating meniscus is larger than that of the isothermal meniscus and varies with heat flux. The present analysis only evaluates the effect of capillary pressure given by σ/R and does not include the additional effects of a disjoining pressure, surface tension variation, and surface viscosity. Insufficient data are presently available to include these additional factors. Therefore, bulk fluid properties and Newtonian flow are assumed applicable in the interline region. The effect of surface tension variation on thin supermeniscus electrolyte films of a uniform thickness has been analyzed by Lightfoot and Ludviksson (6). Comparable effects would be present in that portion of a finite contact angle meniscus where

* Key words: meniscus profile, capillarity, porous gas electrode, planar electrode.

evaporated in the meniscus above that level. Using Euler's method the above process can now be continued until either the heat flux becomes negligible or the wedge angle equals ninety degrees. In the present case, the effect of evaporation on the meniscus profile is significant only at small angles. However, continuing the analysis until $\theta = 90^\circ$, allows the use of the boundary condition at the base of the meniscus ($K = 1/R_b$, $\theta = 90^\circ$) to select the initial curvature.

Evaporation in H_2SO_4 Meniscus

The above analysis is now applied to three arbitrarily selected evaporation rates, water vapor equivalent of 8, 24, and 72 W/cm^2 , which are assumed to occur over the top 250Å of a 1N, H_2SO_4 meniscus. Although these flux profiles are not intended as a definitive description of the evaporation zone described in Ref. (1), which is beyond the scope of this work, the results based on their use significantly improve the understanding of the transport process occurring in a reacting system. Alternatively, considering the large IR drop and polarizations calculated for the finite contact angle meniscus in Ref. (1), these evaporation rates are possible in the interline region. Since we are only investigating the general effect of viscous flow, the size of the evaporation region is purposely limited. As a result of the thinness of the interline region, the effect of the same evaporation occurring further down the meniscus would be substantially less. In this model, the generated vapor could easily diffuse away under a vapor pressure gradient and condense on a surface at a lower temperature. Even with an enlarged zone of evaporation, the total power dissipation would remain small in the finite contact angle model because the upper limit on the zone is very small. In this analysis, Δy was equal to 250Å for the initial five intervals, 625Å for the next ten intervals, 1.25×10^{-4} cm for the next 380 steps, and 6×10^{-3} cm for the remaining distance. The radius of curvature at the base of the meniscus is assumed to be 0.5 mm (one half the slot width), and the fluid properties are assumed constant and evaluated at 25°C.

Results

The calculated meniscus thickness at 250Å below the interline and the meniscus heights for the assumed heat fluxes and contact angles are presented in Table I. Comparing the isothermal and evaporating cases, these results demonstrate that the meniscus interline migrates a small, though measurable distance as a result of viscous shear. There is a possible +6% error in the calculated meniscus height due to the use of only the boundary condition for curvature at the base of the meniscus instead of both the meniscus thickness and curvature. Since the approximate size and sign of the error is the same in all cases, the error in the migration distance is less than 6%. Auxiliary work (not presented herein), in which a fixed height at $\theta = 90^\circ$ was used as a boundary condition, demonstrated that the meniscus profile in the interline region is not significantly different from the results presented herein. However, the profile at the base of the meniscus

is significantly different. The average radius of curvature for the fixed height boundary value analysis is approximately 5% less. Previous work (5) demonstrated that the error due to step size is small. It is interesting to note that for the cases studied the evaporating meniscus height is not strongly affected by the initial contact angle and that the height for the larger contact angle is slightly larger. This results from the slightly larger pressure gradient (curvature change) in the initial portion of the meniscus with a zero contact angle where the film is thinner.

Comparing the film thicknesses for the various cases at a point 250Å below the interline demonstrates the following: (i) the film thickness of an evaporating meniscus is substantially larger than the film thickness of an isothermal meniscus with the same contact angle; (ii) the film thickness of an evaporating meniscus with a 0° contact angle is larger than the film thickness of an isothermal meniscus with a contact angle of 2° (however, the 0° contact angle meniscus must start smaller in the interline region); (iii) the film thickness for the present isothermal model and the cylindrical surface model are approximately the same; and (iv) an increase in the heat flux and/or the contact angle results in a larger film thickness. These substantial changes in the film thickness due to viscous shear would have a correspondingly large effect on the transport processes occurring in this region of potentially high current densities.

The liquid-vapor interfacial height and the logarithm of the reciprocal of the distance from the interline are plotted vs. the logarithm of the meniscus thickness in Fig. 2. The curves for the reciprocal distance from the interline start at $y = 125$ Å. These curves show the substantial effect of evaporation on the meniscus profile. At a given distance from the interline (for $y > 175$ Å) the evaporating meniscus with a zero contact angle for the heat fluxes analyzed is always thicker than the isothermal meniscus with a contact angle equal to 2°. Previous analysis (1) indicated that 90% of the current is produced in the region $y < 10^{-4}$ – 10^{-5} cm, with the largest current density in the immediate vicinity of the interline. These results were partly based on diffused interferences fringes that reoccurred every 2.9×10^{-5} cm. The interaction of these results indicates that it is theoretically possible to define an evaporating meniscus with a contact angle equal to 0° that is indistinguishable from an isothermal meniscus with a 3° contact angle

Table I. Meniscus thickness at 250Å below the interline and over-all meniscus height

Conditions	Meniscus thickness, Å, at $y = 250$ Å	Meniscus height, cm
$\theta_c = 0^\circ$ isothermal	Less than mono layer	0.0558
$\theta_c = 2^\circ$ isothermal	8.75	0.0546
$\theta_c = 0^\circ$, $q = 8$ W/cm ²	11.4	0.0532
$\theta_c = 0^\circ$, $q = 24$ W/cm ²	15.1	0.0521
$\theta_c = 0^\circ$, $q = 72$ W/cm ²	19.8	0.0507
$\theta_c = 2^\circ$, $q = 72$ W/cm ²	20.2	0.0508
$\theta_c = 2^\circ$ cylindrical surface	8.73	0.0483

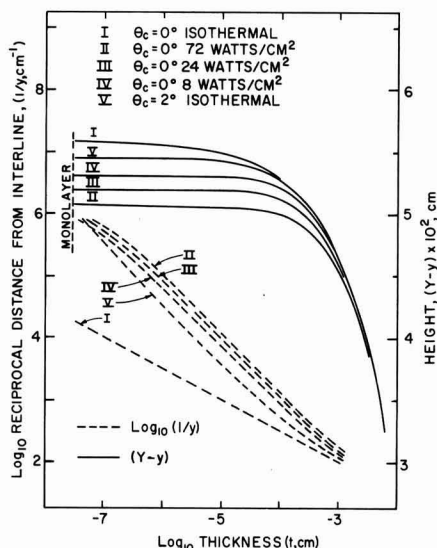


Fig. 2. Calculated meniscus profiles

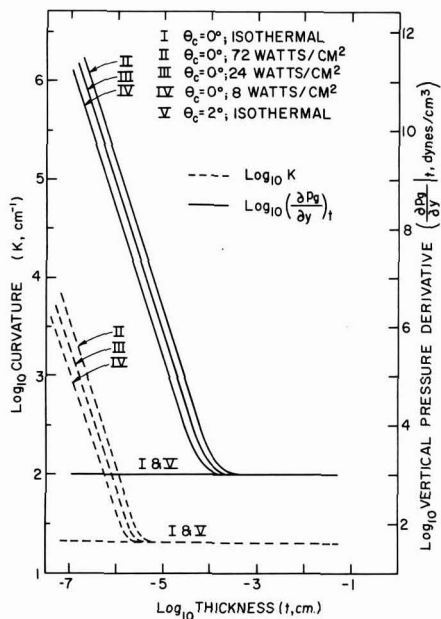


Fig. 3. Calculated vertical pressure derivative and curvature vs. the calculated meniscus thickness.

within the accuracy of the described experimental data and theoretical analysis. Considering this conclusion and the current understanding of transport processes in the critical interline region, considerable additional study of this area is needed to properly model the electrochemical reaction zone.

The logarithm of the meniscus curvature and the vertical pressure derivative are plotted vs. the logarithm of the film thickness for the upper portion of the meniscus in Fig. 3. These results demonstrate that there are orders-of-magnitude increases in the pressure gradient to balance the effect of viscous flow. The horizontal solid line near the bottom of the figure is the weight density of the fluid. The effect of viscous shear becomes negligible before the wedge angle is equal to 10° . The absolute value of the approximate wall shear stress can be calculated using

$$|\tau_s| = \left(\frac{\partial p_0}{\partial y} \right)_{z=t} - \rho g \quad [12]$$

In this analysis the integrated product of the local wall shear stress and the area would be equal to the decrease in weight of the meniscus. These results also indicate that there are orders-of-magnitude increases in the radius of curvature near the interline. The average radius of curvature in the first interval for run No. 4 in Fig. 3 is 2.5μ vs. 479μ for the isothermal meniscus. Therefore, the meniscus profile in the interline region more closely resembles the meniscus found in a pore than that found on an immersed flat plate.

Discussion

Curve IV presented in Fig. 2 and 3 represents a system with an evaporative heat flux of 8 W/cm^2 which is assumed to occur over only the top 250\AA of the meniscus. This is 30% of the average thermal energy generated in the top 250\AA of the meniscus presented in Fig. 24e of Ref. (1), and a small per cent of the total heat generated. A substantial flow profile change occurs when the evaporating fluid flow results from a curvature change, which gives a plausible mechanism for the flow. This particular evaporating meniscus profile starts with a zero contact angle but resembles an isothermal meniscus with a 4° contact

angle for a large portion of the main reaction region. Curve III (72 W/cm^2 over 250\AA , 0° contact angle) corresponds closely to an isothermal curve with a 6° contact angle in a large portion of the main reaction region. If a reliable method of predicting the relative percentage of the thermal energy removed by evaporation were available, the method described herein could be used to improve the results of Bockris and Cahan. At present, these results give a good estimate of the effect of contact angle on the current vs. overpotential curve if the apparent contact angle is used. For example, in Fig. 17 of Ref. (1), the per cent decrease in the current at an overpotential of one volt for a change in the apparent contact angle from 1° to 4° is 26%. Additional results are presented in Ref. (10). The same change would occur if the profile change was due to fluid flow instead of the contact angle. This supports the model of an evaporative heat sink by giving a plausible mechanism for fluid flow. The large predicted increase in evaporative heat flux required to go from an apparent contact angle of 4° to 6° indicates that sufficient fluid flow is available for even the highest thermal fluxes. A similar effect could be expected to occur in porous electrodes.

In the complete system, conduction in the electrode would also remove some of the thermal energy. Therefore, it is instructive to make an order-of-magnitude calculation of the unit thermal conductance in a porous solid (k_{eff}/L) and compare it to a "mass conductance" in the pores. The unit thermal solid conductance ($L = 1\mu$) is $1400 \text{ cal/sec-cm}^2\text{-K}^\circ$ in nickel, 100 in carbon, 31 in quartz, and 5.6 in Teflon. The conduction path in Ref. (1) was quartz with a thin surface film of sputtered Pt. The unit thermal conductance in a porous media is much lower than this and is a strong function of the manufacturing process. For example, the conductance in strongly consolidated sintered metals is an order-of-magnitude less than the solid conductance and could be a factor of 100 less in poorly sintered specimens. For unconsolidated packed material, the ratio of the two conductances could be 1000. Therefore, thermal conductance in a porous electrode is a strong function of the material, the manufacturing process, and the meniscus location (relative to the junction between two particles).

Assuming that molecular diffusion through a stagnant gas occurs in a uniform pore, the conductance of the vapor space for water can be estimated to be (in equivalent thermal units) $7 \text{ cal/cm}^2\text{-sec-K}^\circ$ at 25°C . This is obtained using Eq. [13] with $T = 298^\circ\text{K}$, $L = 1\mu$, $p = 1 \text{ atm}$, $D_{\text{H}_2\text{O-H}_2} = 0.825 \text{ cm}^2/\text{sec}$, and a water vapor pressure difference corresponding to a temperature difference of 1°C

$$N_A = \frac{p D_{AB}}{RTL} \ln \left(1 + \frac{\Delta p_B}{p_B} \right) \quad [13]$$

This is larger at higher temperatures since the rate of change of vapor pressure with temperature and the diffusivity increase with temperature. Like the thermal conductance, the effective mass conductance in a porous material is a function of its manufacturing process. These calculations indicate that the evaporative heat flux in porous electrodes made from carbon and Teflon is relatively large. Alternately, the solid heat conduction process is much more effective than evaporation in well-sintered metal electrodes. However, in both cases, the evaporation-condensation mechanism could cause meniscus migration but at different velocities. In addition, if vaporization occurred at a surface with a large radius of curvature and condensation occurred in a crevice with a small radius of curvature, vapor transport would be enhanced. Theoretically, once the ideal electrochemical meniscus is completely described, the porous electrode design can be optimized.

The above analysis is based on the premise that a fully developed wedge flow model can be used in the meniscus. A partial feeling for the correct velocity

distribution can be obtained from a boundary layer calculation of the distance required for the boundary layer thickness for flow over a flat plate to be equal to 1×10^{-3} cm. This is the approximate thickness of the meniscus in the region where viscous effects become negligible. A simple form of the boundary layer equation is

$$x = \frac{t^2 u_\infty}{30\nu} \quad [14]$$

Using the interfacial velocity at $t = 1 \times 10^{-3}$ cm for u_∞ , the calculated distance is negligible compared to the distance from the bottom of the plate to this point. In fact the velocity is so low and thickness so small, that the use of the simple form of the boundary layer equation is not justified. However, the large difference between these two distances definitely indicates that the accelerating velocity profile is well developed in and above this region. In addition, since the angle θ_1 is still small in this region, θ -direction flow has a small effect on the meniscus profile. These two results demonstrate that the wedge flow model is a good approximation to the flow field in the upper portion of the meniscus. Since viscous effects become negligible below this region, the continued use of the model does not effect the validity of the rest of the profile.

The thermocapillary shear stress at the liquid-vapor interface is assumed to be negligible in the present analysis. This assumption is based on the results of Ref. (5) which demonstrated that the thermocapillary effect in the upper portion of the meniscus was small compared to the curvature effect. Thermocapillary flow would have an effect on the profile in the lower and less important portion of the meniscus. Further, inclusion of this effect requires *a priori* knowledge of the temperature gradient. Since this gradient is unknown, its inclusion would require an additional set of iterations which is beyond the scope of the present study.

Conclusions

Fluid flow in the evaporating meniscus of an electrode-gas-electrolyte reacting system was modeled and analyzed. The meniscus profile, the curvature profile, and pressure derivative profile were calculated for 1N H_2SO_4 using various assumed evaporation profiles. The results demonstrate that: (I) A sufficiently large capillary force was available to supply the required fluid flow for a large evaporative heat sink. (II) Due to the thinness of the meniscus profile in the interline region large pressure gradients were needed to balance the viscous shear stress. (III) The change in curvature due to viscous flow had a significant effect on the meniscus profile in the critical interline region. (IV) Depending on the evaporation rate, the interline radius of curvature could be micron size for a large meniscus. (V) This change in meniscus profile would have an equally significant effect on the transport and kinetic processes occurring. (VI) The effect of viscous shear on the meniscus profile should not be neglected in analyzing electrochemical processes in a finite contact angle meniscus. (VII) Currently used optical techniques are not sufficiently accurate to measure the meniscus profile in the critical region.

SYMBOLS

D	molecular diffusivity, cm^2/sec
g	gravitational acceleration, cm/sec^2
k	thermal conductivity, $cal/cm \cdot ^\circ K$
K	curvature, cm^{-1}

L	conductance path length, cm
N	mass flux, moles/ cm^2 -sec
P	modified pressure, $p_a - \rho g(Y - y)$, dynes/ cm^2
p	pressure, dynes/ cm^2 ; partial pressure
q	heat flux, W/ cm^2
Re	Reynolds number, $(2u\bar{r}/\nu)$
R	radius of curvature, cm; gas constant, cm^3 -atm/ $moles \cdot K^\circ$
r	radial direction (see Fig. 1), cm
s	arc length (see Fig. 1), cm
S	arc length (see Fig. 1), cm
t	meniscus thickness, cm
u	velocity, cm/sec
V	specific volume of vapor, cm^3/g
x	x coordinate
Y	interline distance from meniscus base, cm
y	y coordinate distance from interline, cm
z	distance (see Fig. 1), cm
Δ	difference
ϵ	velocity weighting factor [Ref. (6)]
θ	angle (see Fig. 1), radians
λ	function of Re and θ , see Eq. [7]
ν	kinematic viscosity, cm^2/sec
ξ	$= (\phi/\theta_1)$
ρ	density, g/cm^3
σ	surface tension, dynes/cm
ϕ	coordinate angle (see Fig. 2), radians

Subscripts

A	component A
B	component B
a	atmospheric
c	contact
eff	effective
f	liquid surface
g	gauge
i	location "i" (see Fig. 1)
R	R coordinate surface or direction
r	r coordinate surface or direction
s	solid surface
t	liquid vapor interface
v	vapor
1	initial interval

Acknowledgment

This research was supported by the Department of the Army Contract No. DAA B07-69-c 0063 entitled "Electrochemical Power Sources."

The computational assistance of M. Potash is gratefully acknowledged.

Manuscript submitted Jan. 27, 1971; revised manuscript received ca. Sept. 4, 1971.

Any discussion of this paper will appear in a Discussion Section to be published in the December 1972 JOURNAL.

REFERENCES

1. J. O'M. Bockris and B. D. Cahan, *J. Chem. Phys.*, **50**, 1307 (1969).
2. F. G. Will, *This Journal*, **110**, 145, 152 (1963).
3. R. P. Iczkowski, *ibid.*, **111**, 1078 (1964).
4. D. N. Bennion and C. W. Tobias, *ibid.*, **113**, 589 (1966).
5. P. C. Wayner, Jr. and M. Potash, Jr., Preprint No. 30b, 63rd Annual Meeting A.I.Ch.E., Chicago (1970); To be published.
6. E. N. Lightfoot and V. Ludviksson, *This Journal*, **113**, 1325 (1966).
7. Yu. A. Chizmadzhev and V. S. Markin, *Electrokhimiya*, **2**, 1360 (1966).
8. Yu. G. Chirkov, V. S. Markin, and V. S. Chesnokov, *ibid.*, **6**, 889 (1970).
9. E. M. Sparrow and J. B. Starr, *J. App. Mech.*, **32E**, 684 (1965).
10. B. D. Cahan, Ph.D. Thesis, University of Pennsylvania, Philadelphia (1968).

Low Current Density Microcell Diffusion Layer Thickness at Shallow Vertical Electrodes

R. N. O'Brien

Chemistry Department, University of Victoria, Victoria, British Columbia, Canada

Use of microcell interferometry techniques which have been well reported (1-4) permit detailed analysis of the limiting effect of natural convection at vertical electrodes. A number of authors (5-9) have evolved equations to describe natural or free convection at vertical electrodes. Only that evolved by Wilke, Eisenberg, and Tobias (10) has been tested for microcells and found satisfactory (11, 12). Since the testing of this expression by conventional means, interferometric data has become available and is presented here. Microcells are for the purposes of this work defined as those with electrolyte volumes of 0.5 ml or less. Those used also had electrode area to electrolyte volume ratios of about 10^4 in contrast with conventional cells which have ratios usually in the range of 10^{-2} cm^{-1} .

The cell used was very similar to that reported in Ref. (1). The electrodes were 0.31 cm apart and were 0.191 cm thick, of high purity microcrystalline copper carefully prepared and polished to give a vertical edge to avoid shadowing. The experiments were done at room temperature (22°C).

The limitation of the extent of the diffusion layer by natural convection is shown in Fig. 1. Fig. 1(a) shows the concentration gradients for horizontal electrodes with the cathode over the anode (C/A) previously published in Ref. (3), and Fig. 1(b) shows them for shallow vertical (S/V) electrodes in the cell Cu/CuSO₄/Cu at the natural pH of 4.3 of 0.05M CuSO₄ at a nominal 1 mA/cm² C. D. (0.902 mA/cm²). For short periods of electrolysis, irregularities of the surface of horizontal electrodes, small departures from the truly horizontal position, and inequalities of electrode areas in activity have usually not produced detectable convection.

The differences between the convecting system and the nonconvecting system are that the diffusion layer constantly expands for the horizontal C/A system and is limited after about 15 sec by convection in the S/V arrangement of electrodes to about 0.025 cm. The differences under these conditions are more easily seen in Fig. 2(a) and (b) where the concentration at a given distance out from the electrode is plotted at various times. An idea of the uncertainty of the measurements is given by the scatter of points shown in Fig. 2(b) at times less than 10 sec.

Contrasting Fig. 2(b) with 2(a) convection appears to have begun at the anode first and is detectable as an undulation in the curve at 10-15 sec after electrolysis was begun. The first irregularity in the cathode side occurred farther out from the electrode at just over 20 sec and was more severe, the slope of the concentration contour actually reversing. Close to the electrode, the anode exhibited 3 anomalous changes in concentration contour until settling down at about 45

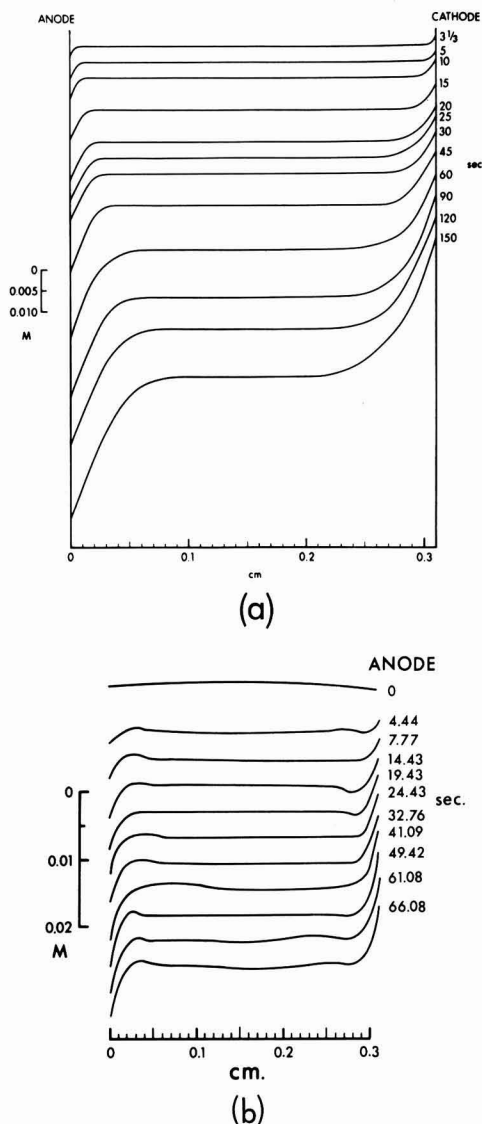


Fig. 1. Reproductions of interferograms: (a) no convection, cathode over anode and (b) shallow vertical electrodes, natural convection occurring, limiting the diffusion layer to about 0.03 cm.

* Electrochemical Society Active Member.
Key words: diffusion layer thickness, natural convection, interferometry.

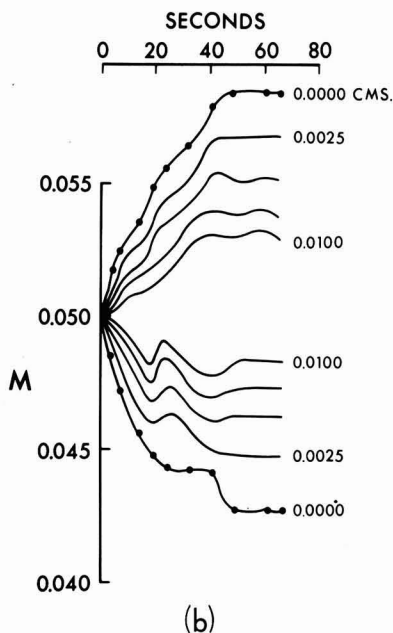
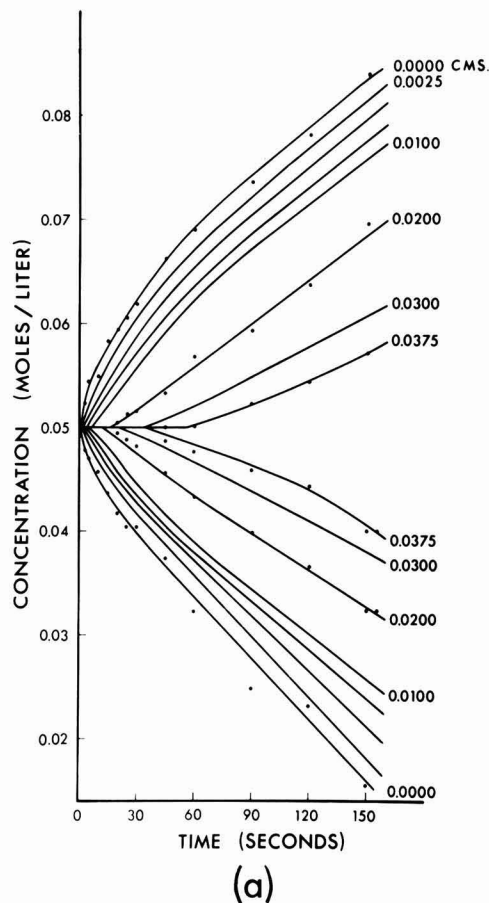


Fig. 2. Concentration changes at various times of electrolysis at various distances from the electrodes: (a) no convection and (b) natural convection limiting the diffusion layer.

sec to a constant concentration value and a pseudo-steady state. At 0.01 cm out from the anode small changes in concentration were still occurring at 60 sec. At the cathode, stability at the electrode and at 0.01 cm from it occurred at the same time, about 50 sec, and only two major perturbations to the smooth curve occurred. Two convective vortices were set up by 50 sec with overflow and underflow between them as described previously (4).

The characteristics shown in this experiment are generally true, that is, although the number of changes of slope to the pseudo-steady state is not constant, the anode region has the most, and they begin and end there first. The initial 10 sec has a smooth concentration change form similar to that of a convectionless system and like it, gives a linear plot of ΔC vs. \sqrt{t} , but the plot does not go through the origin. Higher current densities produce noticeable convection a little sooner and have less extensive diffusion layers as shown in a recent paper by Tvarusko and Watkins (13). Ibl and Bohm (12) have found a similar instability in a redox system when similar heights and separations of electrodes were used. Optical errors calculated according to Ibl (14) are negligibly small, of the order of 1% for these concentrations and current densities.

Manuscript submitted Sept. 27, 1971; revised manuscript received ca. Jan. 18, 1972.

Any discussion of this paper will appear in a Discussion Section to be published in the December 1972 JOURNAL.

REFERENCES

1. R. N. O'Brien, *Rev. Sci. Instr.*, **35**, 803 (1964).
2. R. N. O'Brien, *This Journal*, **111**, 1300 (1964).
3. R. N. O'Brien, *ibid.*, **113**, 389 (1966).
4. R. N. O'Brien, *Nature*, **201**, 74 (1964).
5. B. Levich, *Acta Physicochim. U.R.S.S.*, **19**, 117 (1944).
6. C. Wagner, *J. (and Trans.) Electrochem. Soc.*, **95**, 161 (1949).
7. G. H. Keulegan, *J. Res. Nat. Bur. Std.*, **47**, 156 (1951).
8. J. N. Agar, *Discussions Faraday Soc.*, **26**, 1937.
9. J. R. Selman and John Newman, *This Journal*, **118**, 1070 (1971).
10. C. R. Wilke, M. Eisenberg, and C. W. Tobias, *ibid.*, **100**, 513 (1953).
11. R. N. O'Brien and L. M. Mikherjee, *ibid.*, **111**, 1358 (1964).
12. Ursula Bohm and N. Ibl, *Electrochim. Acta*, **13**, 891 (1968).
13. A. Tvarusko and L. S. Watkins, *ibid.*, **14**, 1969.
14. N. Ibl, *Proceedings of the 7th Meeting C.I.T.C.E.*, Lindau, Butterworths, London (1955).



Dielectric Breakdown in Silicon Dioxide Films on Silicon

I. Measurement and Interpretation

C. M. Osburn* and D. W. Ormond

IBM Thomas J. Watson Research Center, Yorktown Heights, New York 10598

ABSTRACT

Depending on how one measures the dielectric breakdown strength of thermally grown SiO_2 films in the thickness range useful for MOSFET applications, different results may be obtained. These results are shown not to be an intrinsic property of the SiO_2 but rather are artifacts dependent on metallurgical contact thickness, oxide thickness, capacitor area, applied bias voltage, instrument impedance, and time constant. These parameters lead to phenomena commonly referred to as self-healing (or nonshorting) breakdowns which represent a voltage collapse followed by thermal processes that vaporize the shorting electrode metal allowing the capacitor to break down repeatedly at higher fields. Statistical distributions of breakdown fields for the initial breakdown event point to a continuum of oxide defects having different breakdown fields in contrast to prior work showing specific defect types. Measurements of the final shorting voltage (after self-healing breakdown events no longer occurred) are useful in determining the maximum dielectric strength of a defect-free film. A ramp-rate dependence of the breakdown field is observed for slow ramps, and a time instability is seen in the high-field conduction which leads to breakdown.

The dielectric strength of SiO_2 films on silicon is important to the performance of MOSFET devices. Both the initial yield and the reliability of these devices during operation can be related, at least in part, to the breakdown characteristics of the SiO_2 gate dielectric.

Dielectric breakdown in materials has been of interest for many years, particularly as related to high-voltage insulators and capacitors. More recently, growing interest in the large-scale integration of transistors and other thin-film components has shifted attention to breakdown in very thin films, and, consequently, breakdown strengths have been measured for films of many different materials. Unfortunately, only a limited amount of work has been done to relate materials and processing parameters to the breakdown characteristics in SiO_2 , in order to both improve the oxide integrity as well as to determine the major breakdown mechanisms.

Several ways of describing the dielectric strength of thin insulating films have been developed and refined in recent years (1). The following three methods have received special attention: (i) measuring one capacitor sample having thin metal electrodes in order to allow self-healing breakdowns (2) to take place by vaporizing the metalization over the failed or weak spot in the dielectric, thereby eliminating the weak spots; (ii) constructing a statistical distribution of breakdown values by using a large number of test specimens (3-4); and (iii) determining the current-voltage characteristics of a capacitor, just prior to the breakdown event (5). Each method has certain advantages and disadvantages, and the choice is important. For in-

stance, the first method permits the taking of a large amount of data from a single capacitor structure, but its usefulness is usually restricted to studying the so-called primary, or high-field, breakdown strength; as such, it tells little about the low-field breakdown strength which is important for device applications, and it does not reveal the effect of materials and processing parameters on the number of oxide defects. The statistical approach (ii) gives perhaps the best indication of when an actual MOSFET device might fail during loading, but it does not shed as much light as the former technique on the nature of the breakdown mechanism. While current-voltage measurements (iii) provide additional information on the breakdown mechanism, their usefulness is restricted mainly to observing primary-type breakdowns; furthermore, the measurements can be very tedious and difficult to interpret when other time-dependent components (e.g., from ionic displacements) appear in the total current.

When measuring breakdown in MOS capacitors, the statistical approach is often employed because it is probably most directly related to device reliability. It has the additional advantage of being the most sensitive measure of the effect of materials and processing parameter changes. However, it will be shown that the procedure used in measuring statistical distributions does affect the results obtained and that care must be taken in interpreting data. In this paper, the results of an attempt by the authors to interrelate various materials and measuring parameters to the dielectric breakdown characteristics of thermally grown SiO_2 films are reported. The interactions of such variables as oxide thickness, metal electrode area and thickness (here, aluminum), time response, and impedance of the electrical measuring circuit, as well as testing ramp rate

* Electrochemical Society Active Member.

Key words: dielectric breakdown, silicon dioxide films, metal-oxide-semiconductor (MOS), self-healing breakdown, conduction.

and polarity, are discussed. In addition, certain implications of the current-voltage characteristics are considered since they suggest a likely breakdown mechanism.

Experimental Procedure

Metal-oxide-semiconductor capacitors were fabricated on 2 ohm-cm, p- and n-type <100>-oriented silicon wafers. The wafers were ultrasonically cleaned using $\text{NH}_4\text{OH}-\text{H}_2\text{O}_2$, $\text{HCl}-\text{H}_2\text{O}_2$, and HF solutions, while the quartz glassware was etched with HNO_3 -HF; oxides from 200 to 2000 Å thick were then grown in dry oxygen at 1000°C. By using all reasonable precautions to insure pure SiO_2 films, mobile Na^+ ion concentrations on the order of $5 \times 10^{10}/\text{cm}^2$ were obtained as determined by the flatband voltage shift technique (6). One hundred aluminum electrode dots were electron-gun evaporated through metal masks onto each wafer in a clean evaporation system, and the wafers were then given a 5-min anneal at 500°C in dry nitrogen.

Measurements were made with the circuit shown in Fig. 1, wherein a ramp voltage (i.e., increasing linearly with time) was applied to the MOS sample. Breakdown was accompanied by a rapid voltage drop across the MOS capacitor which was sensed by a special triggering circuit that would record the breakdown voltage on a voltmeter. Often, particularly if the aluminum electrode was thin, the MOS capacitor would not short out but would recover and continue increasing in voltage as the ramp voltage increased until another breakdown event occurred. This process of recovering is the well-known phenomenon of self-healing whereby the capacitor discharges through the breakdown path and vaporizes the metalization over the path leaving a nonshorted capacitor containing a small, burned-out area. Up to several hundred of these self-healing events could take place before the sample would short permanently. The voltage at which this shorting, or final, destructive breakdown, took place was recorded on a second, peak-reading voltmeter. Thus only the initial, self-healing breakdown voltage and the final, destructive breakdown voltage were recorded and the intermediate breakdown events were ignored. When the aluminum was thick and self-healing did not occur, both breakdown values were the same. After all the capacitor specimens on a wafer were tested, histograms giving the percentage of capacitors that broke down vs. the voltage of breakdown for the initial and the final breakdown were constructed. From a practical point of view, only the initial breakdown distribution was important; from the point of view of understanding breakdown processes in defect-free SiO_2 , the final one was important. This measuring procedure combined methods (i) and (ii) described earlier in that (a) statistical distributions were constructed in order to study low-field breakdown events, and (b) self-healing events were allowed in order to measure the intrinsic breakdown strength of SiO_2 . Intermediate-field breakdown events gave no additional information since the use of statistical distributions made it possible to determine the probability of breakdown at any given field.

The voltage ramp was obtained by charging a fixed capacitor by means of a constant current generator,

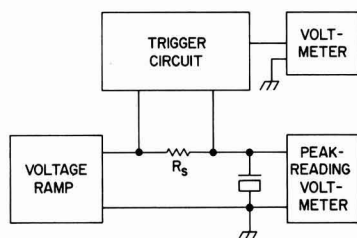


Fig. 1. Diagram of the breakdown measuring circuit

and its speed was varied by adjusting the current. The value of the series resistor (R_s) ranged from 10 ohms to 100 kilohms. The triggering circuit was basically the nanoampere sensing arrangement described elsewhere (7) with the input impedance reduced in order to speed the response time to under 1 μsec . The circuit would trip a relay when a 1-volt, 1- μsec pulse appeared across R_s . With a large series resistor, the time constant for recharging the MOS after a self-healing event was larger than 1 μsec so that the circuit would detect all of the self-healing events in which the capacitor voltage dropped by one volt or more; later considerations show that the chances of self-healing occurring with less than a one-volt drop are quite remote.

Results and Discussion

Measurement of statistical distributions.—When the series resistor was 100 ohms or less, the initial and final breakdown distributions were identical, and visual inspection at 100 magnifications showed that no self-healing breakdowns had occurred. For larger R_s values (>10 kilohms) self-healing breakdowns occurred which were later observed as small black specks on the aluminum electrodes under this magnification. Accordingly a 100-kilohms series resistor was used subsequently to permit self-healing so that the maximum breakdown strength of each sample could be evaluated. Figure 2 compares the initial and final breakdown distributions for a typical wafer with the metal biased negatively. It was found that the initial breakdown values were continuously distributed over the entire field range from 0 to 10 MV/cm and did not show distinct peaks in general. More careful preparation of the SiO_2 films did, however, reduce the frequency of breakdowns occurring below 2 MV/cm. The final (i.e., destructive) distribution, on the other hand, consisted of distinct peaks similar to those observed earlier by Fritzsche (3) as well as by Chou and Eldridge (4). The measuring circuit of Chou and Eldridge was identical to the one used here for measuring the final breakdown voltage except that their series resistor was even larger (250 kilohms); furthermore, visual inspection did show that their samples experienced self-healing which was undetected by their slower responding (~ 0.1 sec) testing circuitry; hence, their data are probably more representative of the final breakdown phenomena. The presence of a low-field peak in the final breakdown distribution can be explained simply by the lack of sufficient energy stored in the MOS capacitor to promote self-healing at low fields. At low fields, breakdowns are shorting giving rise to a low-field peak while at intermediate fields breakdowns are self-healing. This behavior is explained more fully later. The occurrence of this peak in the final break-

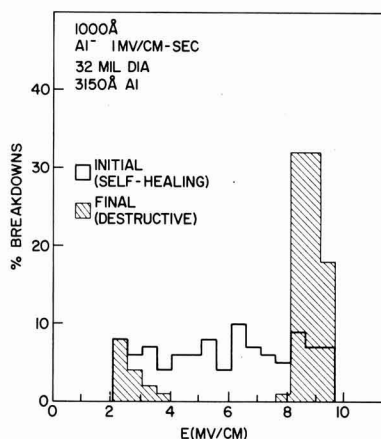


Fig. 2. Initial and final breakdown distributions

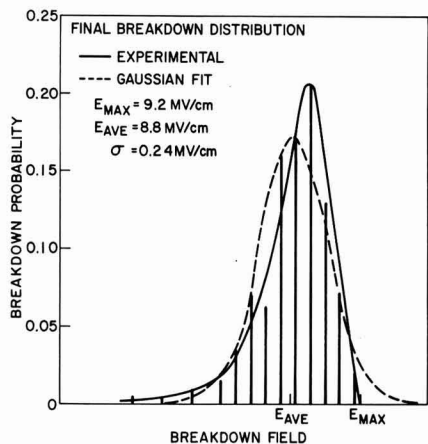


Fig. 3. Shape of typical final breakdown distribution

down distribution does not reflect any property of the SiO_2 film but is rather a consequence of measuring conditions. The wide distribution of breakdown fields across a wafer, as determined from the initial self-healing breakdown events, indicates either a distribution of weak spot sizes or several breakdown mechanisms. Both initial and final distributions were dependent on the electrode area since the frequency of low-field breakdown events increased with increasing electrode area.

A more expanded plot of a typical final breakdown distribution, as used to determine the maximum dielectric strength (see Fig. 3), shows that the high-field curve is not Gaussian but rather is skewed at low fields and has a sharp cutoff at the upper end (E_{max}). Furthermore, the peak of the experimental distribution occurs at a field that is greater than the average field. The variance of the distribution in most cases is two to five times larger than would be expected from thickness fluctuations over the wafer and must be explained in terms of other mechanisms, possibly large numbers of very small defects. The shape of the final distribution is largely independent of measuring temperature. The variance of the distribution remains about 4% of the average field down to 400 Å thick films. Distributions for thinner oxides have larger standard deviations which can be attributed to the lack of self-healing.

A correlation has been observed between the initial and the final breakdown strength of a particular capacitor. Those which had a low initial, self-healing breakdown also had low final breakdown voltages; conversely high final breakdown usually followed high initial breakdown voltages. It has not been possible to determine whether the process of self-healing weakens the remainder of the film or whether both breakdowns are associated with a generally defective film. Destructive breakdown usually involves a series of propagating breakdowns in a cluster until the breakdown area is so large that insufficient energy is stored to sustain further clearing of shorted regions.

Polarity.—When the aluminum is biased negatively in p-type MOS capacitors, the silicon surface is in accumulation and the entire applied voltage appears across the oxide. When the aluminum is positive, however, the surface can be either depleted or inverted, depending on the field applied and the minority carrier generation rate. In the equilibrium case, the maximum voltage across the silicon is equal to the maximum amount of band bending allowed or about 1 volt; this is a small correction factor for samples that break down at roughly 50V or more. On the other hand, when the carrier generation rate is slow compared to the measuring ramp, deep depletion can occur, and

most of the applied field can be in the silicon. Avalanche in the silicon could possibly trigger the breakdown in this case. Because of this potential difficulty, most of the measurements in this study were made with the aluminum negative; a comparison was made with the aluminum positive, however. Under room lighting and with a ramp rate of 1 MV/cm-sec, the distribution for the aluminum positive was spread out over a very large range. The maximum breakdown voltage ranged up to 150V for 1000 Å films and went over 80V for 200 Å films (15 and 40 MV/cm, respectively, if the entire voltage were across the oxide). This compares with maximum breakdown strengths of 92 and 25.8V for 1000 and 200 Å films (9.2 and 12.9 MV/cm, respectively) with the aluminum negative. As expected, the Al(+) distribution results were very light sensitive since light increases the carrier generation rate and gives faster equilibration; strong illumination reduced the maximum breakdown voltage in a 200 Å film from over 80 to 19.4V and from 150 to 89V in a 1000 Å film. Comparisons of breakdown distributions measured under strong illumination with both polarities gave identical results for the most part. The maximum dielectric strength for Si(+) is about 0.4 MV/cm less than for Si(−) however. Occasionally a capacitor withstood an abnormally high voltage with depletion bias even under illumination. Subsequent examination showed that these capacitors exhibited a high leakage current through the oxide. The authors attributed the high breakdown voltage in this case to the high oxide leakage prohibiting the formation of an inversion layer in the silicon and not to superior breakdown strength. Thus care must be taken to insure that equilibrium occurs if meaningful breakdown measurements are to be made with the silicon depleted. Many measurements were made on n-type Si wafers with the aluminum biased positively. The behavior observed was the same as that with Al(−) on p-type wafers. Apparently the measuring polarity is not an important factor in itself but rather the condition of the silicon surface (i.e., accumulated or depleted).

The tendency for self-healing was found to be very polarity dependent; viz., self-healing breakdowns would occur for both polarities but were much less frequent when the aluminum was biased positively. For a sample to self-heal with positive aluminum, thinner aluminum, larger capacitor area, or thicker oxide was required than for Al(−). Klein (2) found that for p-type samples of 0.3 and 9 ohm-cm the resistance of the discharge path was an order of magnitude greater for Al(+) than for Al(−) so that the initial current surge through the discharge path was an order of magnitude greater for negative aluminum. It could be argued that the high-current, Al(−) breakdown could vaporize the discharge path more effectively (and, hence, self-heal) while the low-current, Al(+) breakdown could not. In an actual device, only the first breakdown event is important, of course, and is not affected by self-healing and hence is not affected by polarity.

Ramp rate.—If the breakdown mechanism in SiO_2 is thermal in nature, one would expect to find a ramp-rate dependence of the maximum breakdown strength. In this study, the ramp rate was varied from 0.05 to 10^5 MV/cm-sec with only subtle changes in breakdown strength. For Al(−) the high-field, or primary, breakdown peak was observed to shift to higher field values by about 7% when the ramp rate was increased from 0.05 to 2 MV/cm-sec, as shown in Fig. 4. No statistically significant changes in the lower field breakdowns could be discerned. Breakdown measurements on a single sample using the self-healing technique (2) showed that the breakdown strength was constant for ramp rate over 2 MV/cm-sec (see Fig. 5). These results extend the work of Fritzsche (3) who found no pulse duration effect from 8 to 400 μsec . With the silicon depleted in room light, the faster ramp in-

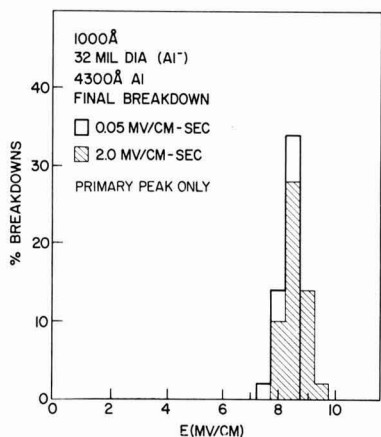


Fig. 4. Ramp-rate dependence of breakdown distributions

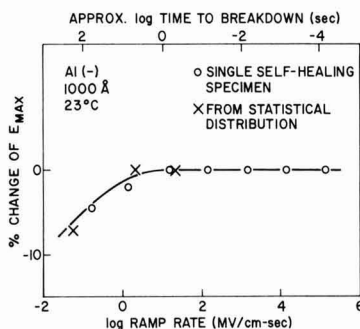


Fig. 5. Ramp-rate dependence of maximum dielectric strength

creased the low-field breakdowns but had no real discernable effect at high fields. It should be noted that even in room light, many samples withstood voltages that would create fields in the oxide greater than 10 MV/cm for over 5 min (this anomalously high voltage is divided between the oxide and the silicon and results from a low minority carrier generation rate as compared to the rate of loss of carriers through oxide conduction). Previous studies of low-frequency C-V characteristics (8, 9) also found very slow carrier generation rates.

Effect of material parameters on breakdown distributions.—Oxide thickness.—One significant finding here where the breakdown distributions were determined for various oxide thicknesses is that fewer self-healing breakdowns occur in thinner SiO₂ samples. Thus, for thin films (e.g., 200 Å), the initial and the final breakdown distributions are almost identical while they are quite different for much thicker SiO₂ layers. One qualitative explanation for this behavior is apparent; namely, the energy (W) stored in a capacitor of area F and oxide thickness d is

$$W \propto F \cdot d \cdot E^2 \quad [1]$$

where E is the electric field strength applied across the oxide. For a given field and area, thinner oxide samples store proportionately less energy that can be subsequently released for volatilizing a portion of the metal, thereby resulting in a self-healing event. The implications of this observation are important when it is realized that several breakdown studies in the past have measured the final breakdown only. The final breakdown voltage in a thick film is usually much higher than the initial breakdown because the MOS capacitor can self-heal; in contrast, the final break-

down in a thinner film is identical to the initial breakdown. Hence, a determination of only the final breakdown distributions can make the apparent intrinsic breakdown strength and the apparent high-field breakdown frequency decrease with decreasing SiO₂ thickness; these observations are artifacts of the measurement and do not represent the properties of the film itself.

Aluminum thickness.—The electrode area dependence of the fraction of capacitors having final breakdown strengths within the range of the high-field, or primary, breakdown peak (i.e., the high-field peak of the final breakdown distribution in Fig. 2) has been used to characterize a defect density of the oxide film. For example, Chou and Eldridge reported defect densities for several oxide thicknesses wherein the mobile Na⁺ concentration was $\sim 2 \times 10^{11}/\text{cm}^2$ and the immobile sodium was not determined. Since self-healing breakdowns were present but undetected in their samples, it was necessary to determine the extent of any interaction between their measurements and results. Accordingly, the aluminum thickness was varied, and, as expected, those samples having thicker aluminum contacts showed fewer self-healing breakdowns and therefore more low-field, final shorting breakdowns; however, some self-healing events were observed with over 10,000 Å of aluminum thicknesses. The electrode area dependence of the fraction of high-field breakdowns is shown in Fig. 6 for several thicknesses of aluminum; the oxide defect density, ρ , can be determined from this figure using the relation

$$-\ln P = \rho F \quad [2]$$

where F is the electrode area and P is the probability of a primary breakdown. Since ρ , as computed from final breakdown distributions, is a function of aluminum thickness (see Fig. 7), it is not a true measure of a density of defects in the oxide but is apparently a more complicated indicator of the defect density coupled with the aluminum thickness. The occurrence of undetected self-healing events can greatly distort results obtained for defect densities. The initial breakdown distribution, on the other hand, was independent of aluminum thickness to first order at least; although the wafer dependence precluded an exact comparison of wafers having different thicknesses of metal, no statistically significant difference was ever observed.

Capacitor area and defect density.—In examining the initial and final breakdown distributions, one observes a more or less definite threshold field (V_t) below which no self-healing breakdowns occur. In practice, it was found that most samples with initial breakdown above this threshold do self-heal but no samples self-heal below the threshold. This threshold voltage varied with the capacitor area, F, as

$$K = \frac{kF}{2d} (V_t^2 - V_r^2) \quad [3]$$

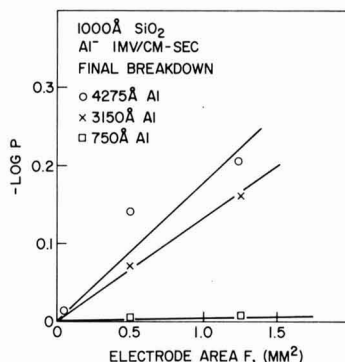


Fig. 6. Electrode area dependence of breakdown

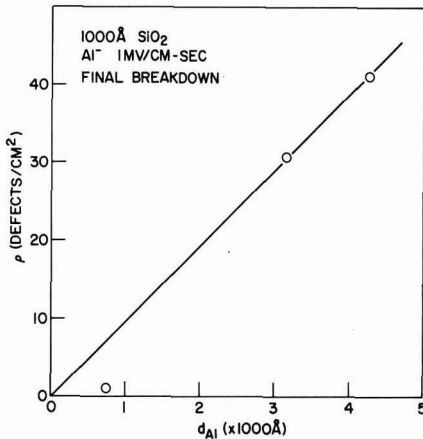


Fig. 7. Aluminum thickness dependence of breakdown

where V_r is associated with the minimum voltage remaining across the capacitor during a self-healing breakdown event; d is the thickness of the oxide having dielectric constant k ; and K represents the minimum energy required to vaporize the discharge path for self-healing and is dependent on aluminum thickness. A value of V_r about 23V gave the best fit to the experimental data for the present films. By comparison, Klein (2) found that the theoretical lower limit of V_r should be 12.2V for SiO₂ films; this value is considered to be the minimum voltage needed to support a gas discharge and is composed of the aluminum work function plus the silicon ionization potential. High-speed oscilloscope traces showing the voltage across the capacitor during a self-healing breakdown event with the wafers used in this study further verified the minimum value of V_r as 22-24V; Klein found an experimental value of 16V for V_r by using oscilloscope traces.

Since the fraction of the final, secondary breakdown events varies with aluminum thickness and since the self-healing threshold voltage of the secondary breakdown varies with capacitor area, it becomes necessary to re-examine the defect density, ρ , as used first by Fritzsche and then by Chou and Eldridge. The past work has made the assumption of a single type of defect responsible for the secondary breakdown peak; this study finds the absence of a well-defined secondary peak for the initial breakdown distribution. Instead the breakdowns are distributed over a wide range of fields. The probability, $p_F(E)$, that a capacitor of area F will break down between E and $E + dE$ can be determined from the initial breakdown histograms. Typical distributions of the breakdown probability for three different capacitor diameters are given in Fig. 8. In the most general case, three regions can be discerned: (i) high fields ($0.8 E_{\max}$ to E_{\max}) where $p_F(E)$ does not depend on the area F and can be associated with the intrinsic breakdown of the film, (ii) low fields (0 to $0.8 E_{\max}$) where $p_F(E)$ can be expressed as $F \times \rho(E)$, and $\rho(E)$ can be considered as the density of defects having breakdown E , and (iii) moderately high fields ($0.6 E_{\max}$ to E_{\max}) where $p_F(E)$ increases with increasing area but not linearly and appears to be a transition between the intrinsic breakdown region and the defect-related breakdown region. It should be noted that the range of each region varied from one sample to another. The use of the defect densities as a function of field was a very sensitive indicator of the variability in breakdown properties of different wafers. Some wafers did show a distinct peak in the defect density at lower fields indicating a high incidence of a single type of defect in those particular wafers. Most wafers, however, showed a continuum of defect sizes or properties. As expected the

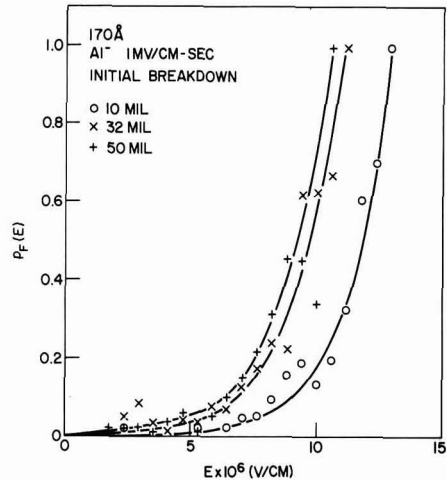


Fig. 8. Breakdown probability as a function of field

probability of a defect being present increases as the defect size decreases. No significant variations in the defect densities have been observed as a function of oxide thickness beyond normal wafer to wafer differences.

The mathematical treatment of a distributed defect density is only slightly more complicated than for the discrete defect case. In the defect-related breakdown region, if we let $P(E)$ be the probability that a capacitor of area F has a defect with breakdown less than or equal to E , then

$$P(E) = \int_0^E F \rho(\xi) [1 - P(\xi)] d\xi \quad [4]$$

Solving gives

$$P(E) = 1 - \exp \left\{ - \int_0^E F \rho(\xi) d\xi \right\} \quad [5]$$

If $P'(E)$ is the probability that the capacitor has breakdown greater than E , then

$$P'(E) = \exp \left\{ - \int_0^E F \rho(\xi) d\xi \right\} \quad [6]$$

or

$$-\ln P'(E) = F \int_0^E \rho(\xi) d\xi \quad [7]$$

which is the same as Eq. [2] with an integral replaced for a discrete density. It should be noted that the data of Fig. 8 fit Eq. [7] at all oxide thicknesses for $E = 0.8 E_{\max}$ with

$$\int_0^{0.8 E_{\max}} \rho(\xi) d\xi \simeq 120/\text{cm}^2 \quad [8]$$

Measurement of current-voltage characteristics.—Figure 9 gives the steady-state I-V curves for a 1300 Å oxide film at room temperature. The data were taken after the field had been applied for a few hours to drive the mobile ions to one electrode or the other. The data are quite similar to those of Lenzlinger and Snow (10) showing Fowler-Nordheim tunneling. In the present case Al(+) gives higher current at a given field than Al(−) which is opposite of their result indicating different barrier heights. There is one major difference in the results: at the high fields, particularly with Al(−), the current increases with time (½ to 10 min) from its instantaneous value to a stable, equilibrium value. This change is repeatable: if the voltage is reduced, the current decreases with time to its original value at the voltage. When the voltage is increased again, both the instantaneous current and

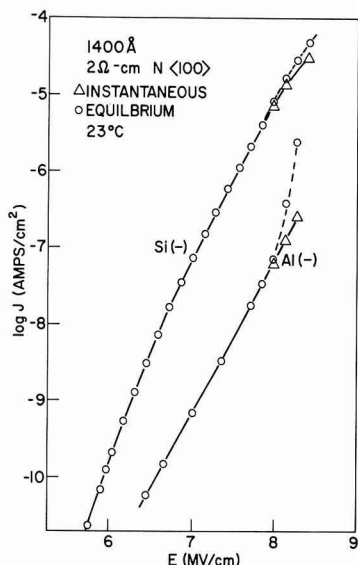


Fig. 9. Current-voltage characteristics of SiO_2

the equilibrium current are the same as they were initially. The range over which this instability could be observed was only about 4% of the entire voltage range; at any higher field the current would run away at too fast a rate to stop. Conduction measurements made on capacitor structures with a guard ring ensured that surface conduction does not affect these results. Although this instability is suggestive of joule heating in the sample, the power levels are too low to cause heating (see Appendix). Furthermore, the onset of the instability occurs at the same field for both polarities although the power levels are two to three orders of magnitude different. This field-dependent mechanism is thus more likely associated with an electronic process having a long time constant.

These steady-state I-V characteristics also shed light on the effect of breakdown measurement on the results obtained. If the breakdown voltage is defined to be the voltage at which a prescribed current flows (for example 1 μA), then the breakdown for $\text{Al}(-)$ will always be 1 to 1.5 MV/cm higher than for $\text{Al}(+)$. If the runaway point is defined as being the breakdown point, this polarity difference will be smaller since the instability occurs at the same field for both polarities.

Summary

The dielectric breakdown properties of thermally grown SiO_2 films show a wide variability. Depending on the measuring conditions, this variability may or may not be observed. Statistical breakdown distributions as determined from the initial breakdown event can be considerably different from distributions of final destructive breakdown when self-healing or non-shorting breakdowns occur. Initial breakdown distributions reveal a continuum of defects having different breakdown fields rather than distinct defect types while final distributions show a low-field peak which is an artifact of the measurement.

The initial breakdown distributions were largely independent of materials and measuring parameters. Metalization thickness, oxide thickness, capacitor area, and measuring circuit impedance did not affect the initial, self-healing results. Final distributions, on the other hand, were very strongly influenced by these parameters.

The differences in the two distributions are best explained in terms of the self-healing breakdown proc-

ess. Only when self-healing takes place is the final distribution different from the initial. The final distribution depends on the number of self-healing breakdown events while the initial distribution is not influenced by these events. For a nonshorting breakdown to occur, sufficient energy must be stored on a capacitor to vaporize the metalization over a breakdown path. The metal thickness, oxide thickness, capacitor area, and circuit impedance are merely the parameters that affect the stored energy or the energy required for self-healing and would be expected to influence the final breakdown. It should be emphasized that the phenomena of self-healing breakdowns is not related to any fundamental property of the SiO_2 film but rather is related to the measuring parameters.

Due to the interaction of the materials and measuring parameters with the final breakdown, it is concluded that the initial distribution gives the better measure of the breakdown characteristics of the SiO_2 film itself. Furthermore, since actual devices use thicker metalization which is covered with glass, self-healing does not occur readily, and the initial breakdown is destructive and is therefore the important one. Final breakdown distributions are useful, however, for determining the maximum dielectric strength of the film and the mechanism of breakdown.

Measurements of the ramp-rate dependence of the breakdown distribution, coupled with steady-state I-V characteristics, indicate that for the aluminum-biased negatively the breakdown occurs via an electronic instability.

APPENDIX

The equation governing heating in a film per unit area on silicon with no radial heat loss is

$$J \cdot V - k \frac{dT}{dx} = dC \frac{dT}{dt}$$

where T = temperature of the film, J = current density flowing through film, V = voltage across film, k = coefficient of thermal conductivity ($11 \approx 3 \times 10^{-3}$ cal $\text{cm}^{-1} \text{sec}^{-1} \text{K}^{-1}$), C = heat capacity ($11 \approx 0.4$ cal/ cm^2), d = thickness of film, x = vertical dimension, and t = time.

The highest observed current density from Fig. 9 was 10^{-5} A/ cm^2 at about 100V, thus the first term giving the heat input is about 2.5×10^{-4} cal/ $\text{cm}^2\text{-sec}$. Assuming even a minimal 1°C temperature difference across the 1000Å film gives a thermal conductance loss (second term) of 3×10^2 cal/ $\text{cm}^2\text{-sec}$ or six orders larger than the heat generated. Thermal runaway seems highly unlikely under these conditions. In 5000Å films of evaporated silicon oxide Klein and Burstein (12) observe thermal runaway when the $J \cdot V$ term is about 1 cal/ $\text{cm}^2\text{-sec}$ or four orders higher than ever attained with SiO_2 ; in addition their thermal conductance loss should be at least one order of magnitude less than for the 1000Å films here.

Acknowledgments

The authors would like to thank Dr. J. Eldridge and Dr. N. Chou for many interesting and stimulating discussions during the course of this work and for critically reviewing the results. Dr. D. Young was consulted several times and his comments are gratefully acknowledged. They would also like to thank R. Hammer for the test probe used in breakdown measurements.

Manuscript submitted Sept. 1, 1971; revised manuscript received Dec. 10, 1971.

Any discussion of this paper will appear in a Discussion Section to be published in the December 1972 JOURNAL.

REFERENCES

1. N. Klein, *Advan. Electron. Electron Phys.*, **26**, 309 (1969).
2. N. Klein, *IEEE Trans. Electron Devices*, **ED-13**, 788 (1966).

3. C. Fritzsche, *Z. Angew. Phys.*, **24**, 43 (1967).
4. N. Chou and J. Eldridge, *This Journal*, **117**, 1287 (1970).
5. N. Klein and H. Grafni, *IEEE Trans. Electron Devices*, **ED-13**, 281 (1966).
6. E. H. Snow, A. S. Grove, B. E. Deal, and C. T. Sah, *J. Appl. Phys.*, **36**, 1664 (1965).
7. General Electric Transistor Manual, p. 325, 7th Edition (1964).
8. T. Hickmott, Private communication.
9. M. Kuhn and E. H. Nicollian, *This Journal*, **118**, 370 (1971).
10. M. Lenzlinger and E. Snow, *J. Appl. Phys.*, **40**, 278 (1969).
11. D. W. Kingery, "Introduction to Ceramics," p. 446, 490, John Wiley & Sons, Inc., New York (1960).
12. N. Klein and E. Burstein, *J. Appl. Phys.*, **40**, 2728 (1969).

Dielectric Breakdown in Silicon Dioxide Films on Silicon

II. Influence of Processing and Materials

C. M. Osburn* and D. W. Ormond

IBM Thomas J. Watson Research Center, Yorktown Heights, New York 10598

ABSTRACT

The breakdown characteristics of thermally grown SiO₂ films on Si are shown to depend on oxide thickness, substrate doping concentration, sample preparation, presence of passivating layers, and testing temperatures. The maximum breakdown strength varies as [thickness]^{-0.21} below 800 Å, is essentially constant from 1000 to 2000 Å, and increases slightly (8%) with increasing testing temperature in the range -196° to +300°C. The breakdown strength is only moderately affected by the dopant-type level in the starting silicon wafer: 10²⁰ phosphorus atoms/cm³ in the silicon reduced the breakdown strength in 200 Å thick oxides by only 20%. The initial condition of the silicon wafer, cleaning procedure, oxidation temperature, passivation layer, and postmetalization anneal are important parameters in the control of defect-related, low-field breakdowns, while the oxidation ambient, substrate doping, oxide thickness, metalization, and measuring temperature have little or no influence on this process.

The fabrication of MOSFET devices requires the growth of SiO₂ films that will withstand moderate electric fields. Defects in the oxide that lead to dielectric breakdown reduce both the yield and the reliability of devices. For this reason, it is important to study processing and other material parameters that could lead to breakdown.

Low-field breakdown in SiO₂ films has previously been attributed to flaws or defects in the oxide or silicon by several investigators (1-5). Considerable work has been done to establish the conditions which reduce defect concentrations and thereby maximize the dielectric strength. The effects of oxide thickness (2, 3, 5-11), substrate doping (3, 4, 6), reactivity of the metal electrode (2), postmetalization annealing (2), passivating layers (2), and temperature (3, 9) have been examined, but, unfortunately, the results have not always been in agreement. For instance, it has been reported that SiO₂ breakdown strengths increase (2), decrease (3, 5-9), or are constant (10) as the oxide thickness is increased. One common problem of many past studies is that breakdown measuring conditions have not been well defined; as a consequence, defect-related breakdowns have obfuscated the results of investigations made to determine the thickness and temperature dependence of the maximum breakdown strength, and the occurrence of undetected self-healing events has distorted statistical breakdown characteristics. Consequently, earlier papers report breakdown strengths in the range 5-7 MV/cm, while later ones give values of 8-10 MV/cm. This study represents an attempt to systematically determine the effect of different processing and material variables on breakdown strengths through more carefully controlled, well-defined measurements.

Experimental Procedure

Metal-oxide-semiconductor capacitors were fabricated on silicon wafers using procedures previously described (1). Both p-type and n-type substrates, having from 10¹⁴ to 10²⁰ dopant atoms/cm³ of phosphorus or boron, were used in growing SiO₂ films from 50 to 2000 Å thick. Oxide thicknesses were measured ellipsometrically. Dry oxygen as well as oxygen saturated with water at 95°C were used as ambients, and oxidations were carried out from 900° to 1200°C. The standard processing involved dry oxidation at 1000°C of 2 ohm-cm material. Phosphosilicate glass layers were grown on some samples by depositing P₂O₅ onto SiO₂ at 800°C in an ambient of 91% N₂, 9% O₂, and a small amount (0.02-0.3%) of POCl₃ followed by a drive-in at 975°C. One hundred metal electrode dots were electron-gun evaporated onto each wafer through masks in a clean evaporation system, and the wafers were given a 5-min postmetalization anneal at 500°C in dry nitrogen. Aluminum, magnesium, chromium, molybdenum, gold, and platinum electrodes were added, but aluminum ones were used for most of this work. A standard metal thickness of 3000 Å was used to permit self-healing breakdown events to occur (1). Statistical breakdown distributions were measured, and care was taken to measure the voltage of the first, self-healing breakdown as well as the voltage of the final destruction (1). For device applications, only the voltage of the first breakdown event is of interest since it would render a device useless; furthermore, initial breakdown distributions are used to determine the defect density as a function of breakdown field as discussed in Part I (1). The final breakdown field is important only in studying the maximum dielectric strength of a defect-free film. The measuring polarity was selected to accumulate the silicon surface thereby minimizing the voltage drop in the wafer.

* Electrochemical Society Active Member.

Key words: dielectric breakdown, silicon dioxide films, silicon processing; MOS, silicon dioxide defects.

Results and Discussion

Oxide thickness.—When the distribution of final breakdown voltages is measured (self-healing events ignored), the fraction of high-field breakdown events increases with increasing oxide thickness as shown in Fig. 1 [the field value of $0.8 E_{\max}$ is used as the dividing line between low-field, defect-related breakdowns and high-field, intrinsic breakdown as discussed in the previous paper (1)]. This thickness behavior, first reported by Chou and Eldridge (2), occurs because low-field breakdown events are more likely to recover through self-healing if the oxide is thick (1). Thus for thick oxides, the breakdown events are self-healing until the intrinsic dielectric strength is attained; for thin oxides, all breakdown events are destructive. It therefore must be emphasized that the behavior in Fig. 1 is the result of a peculiarity in the measurement and cannot be related to any fundamental property of the oxide.

On the other hand, distributions of the initial breakdown voltages show a markedly different oxide thickness dependence. From the results in Fig. 2 for three different capacitor areas, it is evident that the fraction of high-field breakdowns is independent of oxide thickness, within experimental error. Even though each point represents an average of several wafers (or 400 to 1000 capacitors tested), the data show a large amount of scatter because the breakdown characteristics have a strong wafer dependency. The capacitor area dependence of the breakdown probability is consistent with films having 120 defects/cm². It is clear that the occurrence of high-field breakdowns does not fall off markedly, even for oxides as thin as 200 Å. Films thinner than 100 Å do show increased low-field failures, suggesting that nonuniformities in the Si/SiO₂ or SiO₂/Al interface regions have dimensions that are

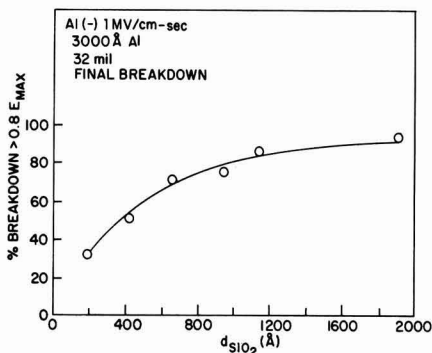


Fig. 1. Oxide thickness dependence of final breakdown distribution.

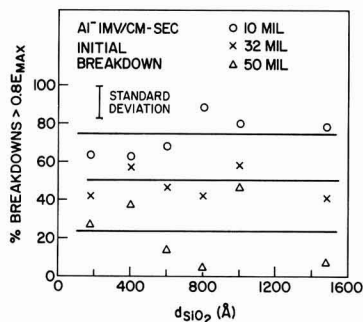


Fig. 2. Oxide thickness dependence of initial breakdown distribution for capacitors that have electrode diameters of 10, 32, and 50 mils.

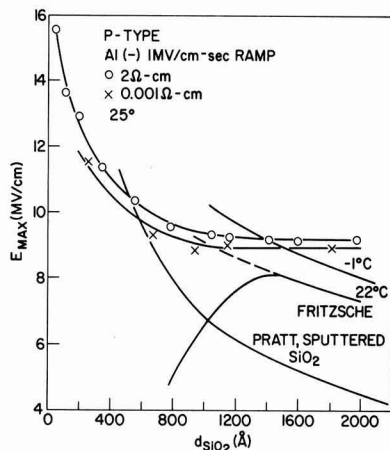


Fig. 3. Oxide thickness dependence of maximum breakdown strength.

at least a sensible fraction of ~ 100 Å. On occasion, exceptionally defect-free (~ 20 defects/cm²) oxides were grown which did seem to show a few more defects in 200–500 Å films as compared to 1000 Å thick ones. The authors observed that the initial breakdown voltage distribution provides a more sensitive measure of wafer-to-wafer defect variations than does the final breakdown one. When self-healing can occur, the final breakdown distribution reflects the maximum breakdown strength of a uniform film rather than the breakdown strength of a defective area. Initial breakdown voltages give results that can be interpreted in terms of a property of the film (such as a defect density from the data in Fig. 2) while the final breakdown voltage cannot be easily related to the quality of the film.

The oxide thickness dependence of the maximum breakdown strength shows still another type of behavior (Fig. 3). The maximum dielectric strength actually increases with decreasing thickness as observed by some previous investigations (3, 5–9, 11) and as predicted by both thermal (12–13) and electronic (13–15) breakdown models. Due to the limited range of data available, it is not possible to precisely determine the relationship between E_{\max} and d . With 2 ohm-cm Si and $d \sim 1000$ Å, the breakdown strength is constant; however, with film less than 800 Å the maximum breakdown strength varies as $d^{-0.21}$. The oxide thickness dependence is smaller for more heavily doped silicon wafers and is discussed later. This is smaller than the usual $d^{-0.50}$ dependence associated with the simplest models for electronic or avalanche breakdown but it does approximate the $d^{-0.25}$ behavior predicted by Forlani and Minnaja (15). Furthermore, O'Dwyer's (13, 16) consideration of space charge buildup due to avalanching as well as collision ionization gives breakdown strengths which do not vary with thickness as strongly as $d^{-0.50}$.

Data of Fritzsche (3) and Pratt (11) are also included in Fig. 3 for reference. Both show increasing breakdown strength with decreasing oxide thickness with the exception of Fritzsche's curve at 22°C where defects have possibly masked the intrinsic breakdown strength. Samples used in this study did not exhibit as pronounced a temperature dependence as reported by Fritzsche. In Pratt's sputtered SiO₂, $E_{\max} \propto d^{-0.66}$ for films up to 10,000 Å thick in contrast to the constant breakdown strength observed here above 1000 Å. This thickness independence of the dielectric strength for thicker films is even more surprising in view of theoretical (13) and experimental (14, 15) evidence showing a varying dielectric strength for bulk dielectric

layers of other materials. This finding suggests that the breakdown process in thin-film structures is initiated in a small region of fixed thickness, possibly near the injecting electrode.

The data in Fig. 3 also fit reasonably well to a $E_{\max}^{1/2} \propto \log(1/d)$ plot, which would indicate that the breakdown is thermal in nature. However, this alternate failure mechanism seems remote because of the low power input levels supported by the capacitor just prior to breakdown and because of the observed temperature dependence of breakdown. The high-field instability in the current-voltage characteristics prior to breakdown (1) is more likely associated with collision ionization and Fowler-Nordheim emission (16).

Substrate doping.—In the MOSFET configuration, the gate electrode extends over the diffused source and drain regions. Limited data in the literature (3, 6) (see Fig. 4) indicate that the SiO₂ breakdown strength decreases markedly as the substrate doping increases from 10^{14} to 10^{19} /cm. Extrapolation of this data, to $\sim 10^{20}$ dopant atoms/cm³ typically used in the source and drain regions of an FET device, reveals a maximum breakdown strength in the range 3-5 MV/cm, about twice that encountered in proper device operation.

The maximum breakdown fields, obtained using 100 capacitors for each condition, are shown in Fig. 4 and 5 as a function of dopant concentration for several SiO₂ thicknesses. Clearly substrate doping has a rather small influence on dielectric strength since only a 10-20% decrease in the usual strength was observed for the extreme case of 200 Å films with 10^{20} impurity atoms/cm³. The effect was even less pronounced for thicker SiO₂ films, as summarized in Fig. 3 and 6, where the thickness dependence of the maximum breakdown field for 2 and 0.001 ohm-cm wafers with boron and phosphorus doping, respectively, are plotted. It should be noted that the behavior is roughly the same for all cases: i.e., increasing breakdown strength with increasing thickness. The effect of thick-

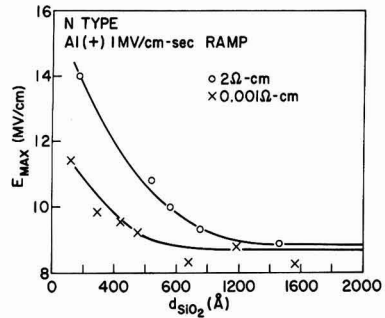


Fig. 6. Oxide thickness dependence of maximum breakdown strength with phosphorus-doped wafers.

ness is somewhat more pronounced for the more lightly doped substrate. For thicker films (over 800 Å), high substrate doping reduces the breakdown strength by a few per cent at most. The effect of doping becomes as large as 20% when the SiO₂ thickness is reduced to 200 Å. This change must be considered minor, however, in light of the more pronounced SiO₂ thickness dependence which improves oxide breakdown over both heavily and lightly doped wafers. Curiously, high phosphorus concentrations have more influence than boron does. The reverse situation might have been expected since phosphorus segregates to the silicon during the SiO₂ growth while boron moves into the oxide (17-19).

Substrate doping had no significant effect on the statistical distribution of initial breakdown events when evaluated in terms of two statistical parameters: namely, the fractions of very low-field ($<0.2E_{\max}$) and of very high-field ($>0.8E_{\max}$) initial breakdown strengths. (Neither of these parameters correlated with the doping level in the silicon.) Statistical comparison did show, however, that certain wafers exhibited substantially poorer breakdown characteristics than usual. Quite possibly, surface defects associated with a given lot of wafers can be more important than dopant concentration. Although the heavily doped wafers (0.001 ohm-cm) contained spiral rings of differing color (presumably nonuniformities introduced during growth), they exhibited typical breakdown properties. For some unknown reason, the n-type samples used here were consistently poorer than the p-type ones for all doping levels. Typically there were ~ 300 defects/cm² in n-type samples but only ~ 150 /cm² in p-type specimens, as estimated from the relationship

$$-\ln P = \rho A \quad [1]$$

where ρ is the defect density, A is the area of a capacitor dot, and P is the fraction of very high-field ($>0.8E_{\max}$) breakdown events (1). The difference might be attributed to intrinsically higher defect densities for SiO₂ film grown on n-type silicon wafers or, more likely, to the use of different oxidation furnaces for n- and p-type materials.

Steady-state current-voltage measurements were taken on MOS structures fabricated from 2 ohm-cm p-type as well as on 2 and 0.001 ohm-cm n-type Si wafers. When the capacitors were biased sufficiently long for the low-field transient to decay, the resulting I-V characteristics were essentially identical. The slight differences were well within the normal wafer-to-wafer variation and are most likely explained by minor variations in SiO₂ thicknesses across the wafers. Since conduction is limited by the barrier height of the injecting electrode (20), these measurements further support the observation (21) that the barrier height does not vary with silicon doping.

It is evident that any breakdown mechanism must explain: (i) the effect of substrate doping increases

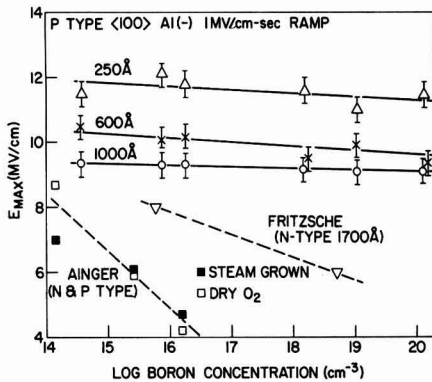


Fig. 4. Maximum breakdown strength vs. boron concentration

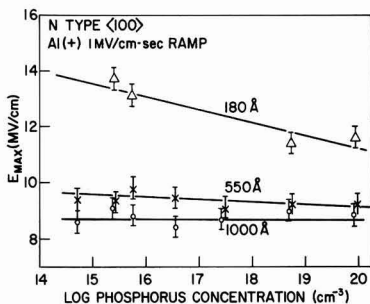


Fig. 5. Maximum breakdown strength vs. phosphorus concentration

with decreasing oxide thickness and (ii) phosphorus doping has more influence with Al(+) than boron does with Al(-). The reported segregation coefficient (17-19) for phosphorus is 10 compared to 0.1-0.3 for boron. Thus the difference between dopant concentrations in the oxide and the silicon is greater for phosphorus, but the absolute dopant concentration in the oxide is greater over the boron-doped substrates. If a certain fraction of the dopant ions in the oxide were charged (i.e., P⁺ and B⁻), the excess positive charge in the phosphorus-doped sample would enhance the electric field for the injected electrons while the negatively charged boron atoms would reduce the field. This mechanism would explain the first observation; unfortunately capacitance-voltage curves do not show any fixed charge in the oxide. In addition a charged-impurity model leading to a field enhancement would predict lower dielectric strengths for thicker films since the magnitude of the enhancement is related to the total charge in the film.

Wafer processing.—In order to determine some possible origins of defects in thermally grown SiO₂ films, specimens were prepared under various conditions including different SiO₂ growth temperatures in both O₂ and steam; the possible effects of different metal electrodes and the postmetalization anneal were also studied.

Clearly, one obvious source of oxide defects stems from surface faults (e.g., scratches, pits, bumps) in the starting silicon wafer. Chou and Eldridge (2) found that an HCl vapor polish of the silicon followed by *in-situ* oxidation using rf heating resulted in far fewer defect-related breakdowns, but apparently this reduction of defects was related more to the oxidation step than to the surface etching. A strong wafer dependency of breakdown was already noted for Fig. 2 where the data are quite scattered even though the points actually represent averages over many wafers each having 100 capacitor dots. Caines and Duffy (22) have correlated the position of breakdown in pyrolytically grown Al₂O₃ with defects or contamination of the starting silicon wafer.

In order to better understand the role of the substrate in breakdown, wafers from three suppliers were cleaned, oxidized, and metalized in the same run. Large area electrodes (50 mil diameter) were used to raise the frequency of defect-related breakdowns. The resultant defect densities (computed using Eq. [1]) were 29, 16, and 27 defects/cm² \pm 5/cm² for the three wafer sources; it thus appears that defects related to the silicon polishing can vary slightly from one lot of wafers to another. However, the defect densities that can be attributed to silicon defects here (\sim 25/cm²) are only a fraction of the defects computed from the data of Fig. 2 (i.e., 120/cm²) and from the experiments with high dopant concentrations (150-300/cm²). Thus, much of the wafer dependency of the defect density apparently arises from processing variations such as: solvent residues left on wafers during cleaning, incomplete drying, or dirty or partially devitrified furnace tubes. For instance, wafers given a cleaning sequence of trichloroethylene, isopropyl alcohol, and HF solution had 160 defects/cm² while control wafers had only 50/cm² after cleaning with NH₄OH-H₂O₂, HCl-H₂O₂, and HF. It has been also observed on many wafers that low breakdown capacitors are spacially clustered indicating the presence of either a larger defective area or a line defect. A large defect area (\lesssim 200 mil diameter) would more likely be due to processing than to wafer defects, although line defects could be due to scratches or crystallographic steps. Scratches introduced during handling have been observed to cause clustering of low-breakdown capacitors; otherwise, microscopic examination at 500 magnifications has generally failed to detect this defective area.

Laverty and Ryan (5) have previously reported an effect of the oxidation temperature on breakdown distributions. Unfortunately, their distributions were not

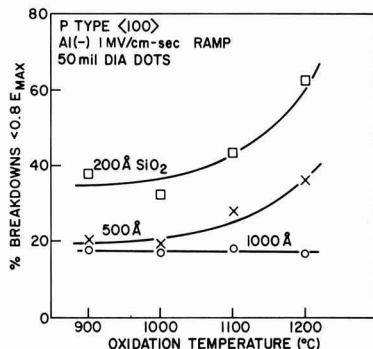


Fig. 7. Effect of oxidation temperature on breakdown distributions.

very similar in shape to those encountered in other studies (1-3); they represent very substandard oxide films. This effect, as found on oxide films typical of this study, is shown in Fig. 7 where the oxidation temperature has very little effect on films over 1000 Å thick; for thinner films higher oxidation temperatures promote defects. The effect of oxide thickness becomes more important as oxidation temperature is increased. When grown at 900° or 1000°C, the 200 Å films in this particular lot had about 15% more low-field breakdowns than 1000 Å films; when grown at 1200°C, they had 45% more low-field breakdowns.

Since oxidation temperature influences breakdown, one might expect to find a correlation of breakdown characteristics with oxidation ambient. Strangely enough it does not matter whether oxidation is done in dry O₂ or in oxygen saturated with water at 95°C. No difference in defect densities could be seen in oxides from 200 to 1000 Å thick grown under either condition at 1000° or 1200°C. These findings are in agreement with the more recent results of Fritzsche (3), but disagree with those of Ainger (6) and Deal (23), who reported much lower dielectric strengths for their samples. High-temperature annealing in nitrogen (15 min at 1000°C), following oxidation, increased defect densities by 50% in 1000 Å films and by 400% in 200 Å ones. Cleaning of the oxidation tube at 1150°C with a 6% HCl/O₂ mixture (24-25) followed by oxidation at 1150°C resulted in a 60% decrease in defect density. Other work (26) has shown that oxidation in 1% HCl/O₂ at 1000°C is likewise effective in reducing the number of defects causing dielectric breakdown. These results suggest that the improved breakdown characteristics seen with HCl vapor-polished wafers (2) may be due to the presence of HCl in the system rather than due to a better surface polish.

Several oxide films were deliberately contaminated with NaCl, during or after growth, to gain an understanding of the role contaminant ions play in defect formation and growth. Films having 10¹⁴ Na⁺/cm², evaporated onto the SiO₂ prior to electroding, showed normal breakdown behavior when the aluminum electrodes were biased negatively; for Al(+) however the peak of the breakdown distribution was shifted to a lower field as seen earlier by Raider (27). Other films were grown to half their final thickness, were contaminated with 10¹⁴/cm² sodium ions, and were then grown to the desired final thickness. These films showed 5 \times 10¹² mobile charges/cm². It was not determined if the remaining sodium evaporated during the final growth period or if it was left immobile in the film. Breakdown measurements with Al(-) showed no degradation while Al(+) slightly lowered the field at which the peak in the distribution occurred; nevertheless, the fraction of lower field or defect-related breakdowns did not increase due to the presence of the sodium.

The oxidation temperature and the nitrogen annealing dependence of the defect density support a model where a metal excess in the oxide favors increased numbers of defects. As the oxidation temperature increases or after a high-temperature N_2 anneal, the oxygen content of the oxide would be expected to be reduced; both conditions give high defect densities particularly for thin films. The rate of oxide growth is irrelevant as seen with the steam oxidation. Although crystallization was suspected, the data do not support this mechanism since both steam and NaCl should enhance recrystallization.

The choice of metallization material did not influence breakdown to any significant extent either. When biased negatively, magnesium, chromium, aluminum, molybdenum, gold, and platinum all gave similar breakdown distributions with a maximum breakdown strength of over 8 MV/cm. However, conduction measurements (28) show many orders of magnitude difference in current levels at a fixed field for injection from magnesium and for gold verifying the Fowler-Nordheim, barrier-height-limited conduction mechanism.

The postmetallization annealing treatment (5 min at 500°C in N_2) resulted in a slight improvement of oxide integrity by reducing the defect density from 32 defects/cm² to 11/cm² on 1000Å test films. This reduction of defects is believed to be due to the elimination of interface states, which if present, could create internal fields which would then enhance the applied field. Thus it appears feasible that at least some of the oxide defects are electrically charged clusters rather than structural or geometrical defects. Chou and Eldridge (2) report that a short anneal improves the shape of the final breakdown distribution and that a more protracted anneal at 500°C would induce structural defects which are responsible for shorts. Figure 8 extends the temperature range of that work down to 200°C. No measurable effect is observed after 800 hr at 200°C while at 300°C annealing doubles the defect density in only a few hundred hours. Even at 250°C only a minor change is observed after 900 hr. The degradation after prolonged annealing at 500°C in the work of Chou and Eldridge was related to the reactivity of the metal used for electrodes. Likewise with this lower temperature testing the onset of defect formation at 300°C correlates well with the onset of injection of aluminum into SiO_2 (29). Samples made with Pt electrodes do not show the pronounced deterioration at 300°C. The degradation in breakdown characteristics is dependent on oxide thickness as well as temperature; 200Å thick oxides show a high defect density after a few hundred hours at 250°C.

Oxide passivation.—Earlier work (2) has shown that a thin phosphosilicate glass layer was effective in reducing the low-field or so-called secondary breakdown events and hence in reducing the measured defect den-

Table I. Effect of phosphosilicate glass layers on defects causing dielectric breakdown in SiO_2 films

PSG thickness (Å)	P_2O_5 concentration (%)	Defect density* (cm ⁻²)
0 (starting oxide)	0	15
0 (30 min 975°C, N_2)	0	37
60	2.1	19
60	3.7	17
60	4.0	12
60	5.4	6
15	3	22
35	3	18
60	3	17

* $\pm 30\%$ as measured on 500Å SiO_2 films.

sity. Furthermore the PSG increased the resistance of undoped and Na^+ -doped wafers to extended annealing in N_2 at 500°C. The improved properties are explained by a continuous film of PSG over the underlying SiO_2 thereby filling pinholes or cracks in the film. The thickness and concentration of the passivating PSG required to eliminate defects has not been fully explored however. In this investigation PSG layers were deposited on both good (<30 defects/cm²) and poorer (>100 defects/cm²) films of SiO_2 . The substandard films were fabricated with an organic cleaning step, and oxidation was followed by a 1 hr anneal in N_2 at 1000°C; both conditions were previously shown to increase the number of defects in the film.

The results obtained with the good oxide are summarized in Table I. One immediately sees that the 30 min nitrogen drive-in at 975°C more than doubles the defect density; hence, it is not surprising that in many cases (when PSG thickness and concentration are low) the defect density is higher in glassed films than it is in the starting films. Nevertheless, the defect density does decrease with both increasing PSG thickness and P_2O_5 concentration in the glass. At least 60Å of 4% P_2O_5 glass is needed to obtain films that are substantially better than the starting films. Defect densities less than 5/cm² were never observed even with 200Å of 9% P_2O_5 glass layers. Apparently these defects (5-10/cm²) were due to defects in the wafer and could not be eliminated with PSG. We have already shown that wafers obtained from different sources result in defect densities that vary by over 10 defects/cm². It should also be emphasized that the improvement in breakdown characteristics seen with thicker PSG is very substantial particularly in eliminating low-field (<0.2 E_{max}) breakdown events. A PSG layer, 10% of the total oxide thickness, can give an 80% improvement in the breakdown strength of a capacitor. Apparently very deep pinholes or cracks in the SiO_2 layer are filled with the PSG. Since 60Å of PSG is needed to realize better films, it appears that the pinholes are of the order of 100Å in diameter.

With the poorer films (≈ 100 defects/cm²), the PSG addition markedly reduced the defect density. The defect density dropped to 60/cm² with 60Å of 2% P_2O_5 and to 40/cm² with 60Å of 5% P_2O_5 glass. Although this improvement is substantial, it is not as large fractionally as the improvement seen with good starting films. It is apparent that the effectiveness of PSG in improving breakdown characteristics is closely linked to the condition of the starting oxide films.

Temperature.—The temperature dependence of the breakdown strength is expected to be very helpful in analyzing the nature of the intrinsic breakdown mechanism. Fritzsche (3) reported that the intrinsic maximum dielectric strength decreases with increasing temperature from 0° to 80°C in much the same way as amorphous quartz. Chou and Eldridge (2) found very little change in breakdown characteristics in the 25°-150°C range. Korzo (9) on the other hand reports an increasing breakdown strength up to about 25°C followed by a slight drop at 50°C; his measurements were on oxides grown by pyrolytic decomposition of

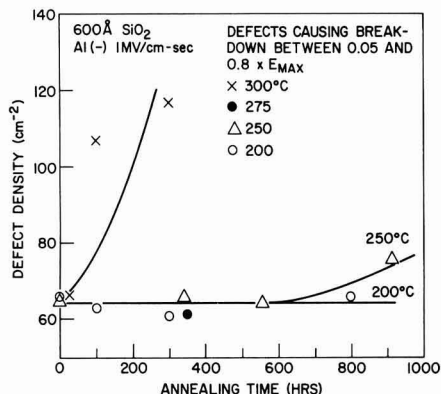


Fig. 8. Effect of extended annealing on defect densities

ethylates and had unusually low over-all breakdown strengths leading one to suspect defect-related breakdown.

To evaluate the effect of measuring temperature, a matrix of samples with 200, 400, 600, 800, 1000, and 1500 Å SiO₂ layers were tested at -30°, +25°, 70°, 130°, and 200°C; in addition, several wafers were also measured at -196° and +300°C. Figure 9 gives some typical results showing a very slight increase (≈8%) in maximum dielectric strength on going from liquid nitrogen to 300°C. Breakdown distributions were also only slightly affected by temperature. The defect density could not be correlated with measuring temperature other than by noting that the fraction of very low-field ($\leq 0.2E_{\max}$) events increased by a few per cent on going from -30° to 185°C. These results further support the conclusion that most defects are present in the MOS structures after fabrication, and, except for the lowest field breakdown, are largely unaffected by measuring temperature.

The temperature dependence of breakdown supports an electronic rather than thermal mechanism for breakdown. With thermal breakdown, models indicate that $E_{\max}^{1/2}$ should decrease linearly with increasing temperature (13), a trend that is contrary to the present data. Although it will not be dealt with in detail here, it should be remarked that the analysis of the temperature dependence of electronic breakdown is by no means complete. This dependence enters into electronic models via the temperature dependence of various ionizing processes that can take place in the oxide layer and is presumed to have a small effect on E_{\max} . Thus the behavior observed in Fig. 9 is consistent with most electronic breakdown models and inconsistent with the temperature dependence expected for thermal breakdown. A ramp-rate dependence of the breakdown distribution similar to that reported earlier (1) was observed over the entire temperature range giving further support to the electronic breakdown model. The observation of the ramp-rate dependence at liquid nitrogen temperatures suggests that a space charge redistribution in the oxide occurs and is due to electronic rather than ionic charges.

Summary

Many processing and material variables are important to the breakdown characteristics of thermally grown SiO₂ films. The condition of the starting silicon wafer, the wafer cleaning sequence, the oxidation temperature, the passivation layer, and the postmetalization anneal are important parameters in the control of defects that have low breakdown strengths. No single factor was ever responsible for all of the defect-related breakdowns although poor wafer cleaning would substantially decrease yield. A number of the defects can be associated with the wafer as determined by comparison of wafers from different sources; others can probably be associated with electrically charged clusters that are neutralized during the postmetalization anneal, and the rest can be attributed to defects introduced during growth. A 1200°C oxidation

substantially increases the defect density in 200 Å films.

Surprisingly enough, oxidation ambient (wet or dry O₂), substrate doping, oxide thickness, metalization, and temperature had little or no influence on defect-related breakdowns. High temperatures seemed to favor more low-field breakdowns although the increase was only a few per cent for a 200°C increase. Even though the maximum breakdown strength increased with decreasing oxide thickness, the number of defect-related breakdowns remained constant down to 200 Å. Below that thickness the percentage of low-field failures increased. A very strong wafer dependence was observed, however, and several lots of wafers showed poorer than average characteristics for thin samples. High oxidation temperatures did aggravate the influence of the thickness dependence on breakdown distributions.

Oxide thickness, temperature, and substrate doping influenced the maximum breakdown strength. Films grown on 2 ohm-cm p-type wafers from 60-800 Å followed the relationship $E_{\max} \propto d^{-0.21}$; above 1000 Å the dielectric strength was 9.2 MV/cm. More heavily doped wafers resulted in a less pronounced thickness dependence. The breakdown strength increased very slightly (8% over a 500°C range) with increasing temperature. This behavior points to an electronic breakdown mechanism; the observation of a high-field instability in the current voltage characteristics (1) provides experimental evidence of a space charge redistribution possibly due to internal collision ionization (13, 16). Substrate doping had only a minor (20%) effect on dielectric strength and was most noticeable for thinner films although phosphorus doping of the silicon wafers had a greater influence than boron doping.

Acknowledgments

The authors wish to thank Dr. N Chou and Dr. J. Eldridge for support and discussions during this work and for reviewing the results. The experimental work was aided by R. Hammer.

Manuscript submitted Sept. 1, 1971; revised manuscript received Dec. 10, 1971.

Any discussion of this paper will appear in a Discussion Section to be published in the December 1972 JOURNAL.

REFERENCES

1. C. M. Osburn and D. W. Ormond, Part I, *This Journal*, **119**, 591 (1972).
2. N. Chou and J. Eldridge, *ibid.*, **117**, 1287 (1970).
3. C. Fritzsche, *Z. Angew. Phys.*, **24**, 43 (1967).
4. N. Klein, *IEEE Trans. Electron Devices*, **ED-13**, 788 (1966).
5. S. J. Laverty and W. O. Ryan, *Intern. J. Electron.*, **26**, 471 (1969).
6. F. W. Ainger, *J. Mater. Sci.*, **1**, 1 (1966).
7. V. F. Korzo, *Soviet Phys.-Solid State*, **8**, 494 (1966).
8. V. F. Korzo, *ibid.*, **8**, 2003 (1967).
9. V. F. Korzo, *ibid.*, **10**, 1256 (1968).
10. F. L. Worthing, *This Journal*, **115**, 88 (1968).
11. I. H. Pratt, *Solid State Technol.*, Dec. (1969).
12. N. Klein, *Advan. Electron. Electron Phys.*, **26**, 309 (1969).
13. J. J. O'Dwyer, *This Journal*, **116**, 239 (1969).
14. J. J. O'Dwyer, *J. Phys. Chem. Solids*, **28**, 1137 (1967).
15. F. Forlani and N. Minnaja, *Phys. Status Solidi*, **4**, 311 (1964).
16. J. J. O'Dwyer, *J. Appl. Phys.*, **40**, 3887 (1969).
17. A. S. Grove, O. Leisteko, Jr., and C. T. Sah, *ibid.*, **35**, 2695 (1964).
18. B. E. Deal, A. S. Grove, E. H. Snow, and C. T. Sah, *This Journal*, **112**, 308 (1965).
19. J. S. T. Huang and L. C. Welliver, *ibid.*, **117**, 1577 (1970).
20. M. Lenzlinger and E. Snow, *J. Appl. Phys.*, **40**, 278 (1969).
21. R. Williams, *Phys. Rev.*, **140A**, 569 (1965).
22. J. E. Carnes and M. T. Duffy, *J. Appl. Phys.*, To be published.
23. B. E. Deal, *This Journal*, **110**, 527 (1963).

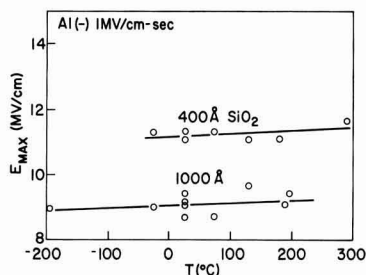


Fig. 9. Effect of measuring temperature on maximum breakdown strength.

24. P. H. Robinson and F. P. Herman, *ibid.*, **118**, 141 (1971).
 25. R. J. Kriegler, Y. C. Cheng, and D. R. Colton, *ibid.*, **118**, 73C (1971).

26. E. Terner, IBM internal communication.
 27. S. Raider, To be published.
 28. C. M. Osburn and E. Weitzman, To be published.
 29. N. J. Chou, *This Journal*, **117**, 260C (1970).

Electrical Conduction and Dielectric Breakdown in Silicon Dioxide Films on Silicon

C. M. Osburn* and E. J. Weitzman

IBM Thomas J. Watson Research Center, Yorktown Heights, New York 10598

ABSTRACT

Conduction through SiO_2 films, thermally grown on Si substrates, was found to take place via a Fowler-Nordheim (F-N) tunneling mechanism, after an initial transient current associated with trapping of charge, mobile ions, and space charge redistribution has died away. The temperature dependence of the steady-state F-N current decreases with increasing applied field and was found to be smaller in magnitude than previously reported. Typical post-metalization annealing treatments (e.g., 5 min at 500°C in dry N_2) lowers the conductivity of the MOS capacitor structures by two to three orders of magnitude, an effect that can be attributed to the elimination of either traps or fixed charge distributed throughout the oxide. For applied fields larger than 8 MV/cm, a current instability arises which can lead to dielectric breakdown. For a wide range of different electrode materials, the onset of this instability appears to correlate well with the temperature and oxide thickness dependences of breakdown, as observed earlier (10). These findings are discussed in terms of a model which suggests that carriers can be generated and re-distributed by collision ionization processes within the oxide.

Electrical conduction in SiO_2 films grown on Si substrates has been studied by several investigators (1-9) largely because of the importance of this insulator in silicon transistor technology. In particular, it is well known that metal-oxide-semiconductor FET's are operated with extremely large electric fields (e.g., 1 to 2 mV/cm) so that during testing dielectric breakdown can substantially lower the performance of these devices. As part of a continuing effort to investigate the electrical integrity of thermally grown SiO_2 films (10), prebreakdown current-voltage characteristics become important for gaining insight into the major breakdown mechanisms and for relating various materials and processing parameters to the resultant intrinsic dielectric strength.

Since several authors (11-13) have recently reviewed the various conduction mechanisms taking place in thin insulating films, this topic will not be detailed here other than to remind the reader that it is essential to distinguish between bulk-limited and electrode-limited conduction processes. In general, electronic conduction, space-charge-limited conduction, nonblocked ionic conduction, and impurity conduction are bulk limited while Fowler-Nordheim (F-N) tunneling and Schottky emission are electrode limited. Since SiO_2 is such an effective insulator, measurements of conduction in Metal/ SiO_2 /Si capacitors are highly sensitive to preparation and purity; consequently, results vary widely from one investigator to another. Earlier studies (3-5) indicated that the process was ionic in nature due to the presence of mobile impurities. Refinements in processing of MOS capacitors reduced the impurity content (notably Na^+ ions) to the point where electronic conduction could be observed, wherein the currents were believed to be space-charge-limited modified by traps (6) or space-charge-limited with tunneling at the electrodes (7). Later, multiple conduction states were observed in both

thermally grown (8) and pyrolytically deposited SiO_2 films (9), and the switching from one state to another was linked to the presence of certain impurities in the oxide. Finally, conduction through high-purity SiO_2 has been demonstrated to occur via a Fowler-Nordheim tunneling mechanism (1-2).

This paper deals with conduction through high-purity SiO_2 in MOS capacitors and its relationship to dielectric breakdown. The parameters describing F-N conduction are evaluated from experimental data, particularly the temperature and voltage dependence of the current. Finally an instability in the conduction is compared to the oxide thickness and temperature dependence of breakdown.

Experimental Procedure

Silicon wafers, 2 ohm-cm p-type as well as 2 and 0.001 ohm-cm n-type, were cleaned in solutions of NH_4OH - H_2O_2 , HCl - H_2O_2 , and HF and then oxidized in dry O_2 at 1000°C to form oxides from 200 to 1500 Å thick. An array of 100 metal electrodes, 32 mils in diameter, were electron-gun evaporated through metal masks. Aluminum, chromium, magnesium, molybdenum, gold, and platinum were deposited for this purpose since they cover a wide range of electrode work functions. The MOS samples were subsequently annealed for 5 min at 500°C in dry N_2 in order to remove radiation damage from the evaporation step (14). Capacitance-voltage tests made on electrothermally stressed capacitors indicated typical mobile ion concentrations of less than $5 \times 10^{10} \text{ cm}^{-2}$.

Current-voltage characteristics were measured with a Keithley 416 picoammeter. For measurements from room temperature to 325°C, the samples were placed on a small hot stage inside a shielded box with a dry N_2 ambient. Measurements were also made in liquid nitrogen. Care was taken to ensure that external leakage was negligible. Special measuring procedures were required to obtain repeatable results because the I-V characteristics were not at first reproducible (see Fig. 1). Note that the applied field must be cycled between

* Electrochemical Society Active Member.

Key words: dielectric breakdown, electrical conduction, silicon dioxide films, MOS, Fowler-Nordheim tunneling, electron injection, transient conduction, collision ionization.

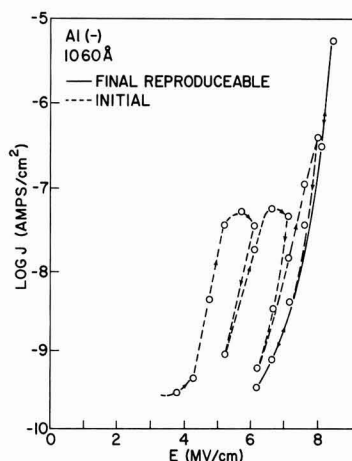


Fig. 1. Current-voltage characteristics of typical MOS capacitor showing cycling needed to achieve reproducibility.

low and high values several times before the I-V curves for increasing and decreasing fields coincide. This same degree of reproducibility could be attained by stressing the capacitor at moderately high fields ($E \approx 7$ MV/cm) for several hours while the current decreased with time to a steady-state value. Although this behavior was similar to ionic polarization effects frequently seen in other glasses, its appearance at temperatures as low as that of liquid nitrogen pointed to an electronic rather than ionic polarization in this case. No appreciable flatband voltage shift ($< 5 \times 10^{10}$ charges/cm²) was seen as a result of cycling or pre-stressing.

Using thin metalization ($< 3000\text{\AA}$) so that weak spots or flaws in the oxide would be eliminated by self-healing breakdown processes (15), it was possible to obtain on a wafer, I-V characteristics for several capacitors that were within a few per cent of one another. This high degree of reproducibility, coupled with earlier observations that the current scaled with the capacitor area (1), indicated that the measured current was distributed over the entire electrode area and not localized.

Results and Discussion

Transient conduction.—The temperature and the field dependencies of the initial current transient were studied in order to determine the origin of the decay seen here. Previous workers have reported similar transients and have attributed them to ion motion (2, 5, 17) notably sodium or protons, charge trapped or released by irradiation (18) or charge storage (4). Not surprisingly, the transient decay rate increased at higher applied voltages. The decay was not accompanied by a current transient in the opposite direction when the voltage was reduced to zero as is often seen (19) when polarization occurs. The charge levels involved in the decay, as determined by integration of current-time plots (16), were typically 10^{11} – 10^{14} /cm² and were found to increase with increasing voltage as might be expected with trapped charge and in contrast to mobile charge. It thus appears that the transient is due to trapped charges being released at high fields. The trap depth determines the field required for release. It should be noted that a current decay is observed at a high field after steady-state conduction was attained at a lower field, giving further evidence that the transient species is released by the high field. The almost linear increase in the transient charge concentration, with applied field in one sample from 3 to 7 mV/cm, indicates that the trap density must be uniformly distributed over this energy range in that

sample. The transient behavior is observed for both polarities of applied field with roughly the same amount of charge involved. Nevertheless, capacitance-voltage measurements have not been able to detect an appreciable flatband voltage shift (> 0.1 V) after the decay has occurred. Thus if traps are involved in the process, they must be located near the metal SiO₂ interface as concluded earlier (4). Calculations show that for these traps to account for 10^{14} transient charges/cm², they must be located within 0.2 Å of the metal-oxide interface for less than 0.1 V flatband voltage shift in a 1000 Å thick film. In addition, 10^{11} charges/cm² in the oxide would create fields up to 50 MV/cm. It appears more reasonable to postulate a lower number of traps (i.e., 10^{11} – 10^{12} /cm²); the field created by these trapped charges could then enhance the injected current. The transient would thus be due to two components: (i) mobile charge released from traps and (ii) injected electron current due to an internal space charge region.

The shape of the current decay curve shows a large variability although it is similar to an exponential curve. A single time constant τ in $I \propto I_0 e^{-t/\tau}$ does not satisfactorily describe the data at room temperature. Instead two different time constants must be considered. Likewise the data could be represented by $I \propto \beta_1 t^{-1/2} + \beta_2 t^{-1/2}$ as might be expected with ionic motion of different species (3, 17). The time constant for the fast decay in one sample was about 15 sec at room temperature, about twice that at -200°C and half that at 75°C , making an exponentially activated process unlikely since it would have such a low activation energy (~ 0.01 eV). These time constants are not within the range observed for sodium or proton release from traps as reported by Hofstein (17) and probably represent electronic traps. The slow decay ($\tau \approx 150$ sec at 23°C) is within the range described for ionic motion although its smaller contribution to the total current prohibited accurate temperature measurements. Likewise the complexity of this current decay made it impractical to get estimates of the distribution of trap energies. Occasionally with the metal biased positively, the current would increase with time for the first 50 sec and then decay. At this time the origin of this behavior is not known although the characteristics are similar to those involving space-charge-limited (SCL) transients (5, 17, 20) with a very long transit time. The lack of a steady-state current after the peak (rounded cusp for SCL transient) indicates trapping is important.

Conduction mechanism.—The conduction process is not affected by the oxide thickness in the 200–1500 Å range since the applied fields required to produce given current densities are independent of thickness, in accord with the earlier results reported by Lenzlinger and Snow (1) (see Fig. 2). Furthermore, to within experimental error, the currents are independent of substrate type and dopant concentration for injection from either electrode. Figure 3 shows typical I-V characteristics for various electrode metals; the curve for injection from the bulk silicon is independent of the counterelectrode material. The spread in behavior is indeed very large. For the most part, the logarithm of the current density (J) is roughly proportional to the applied field (E), although at higher fields a deviation from this behavior is observed with Mg electrodes. In addition, for high-field injection from Al, Mo, Pt, and Si (at least), another type of instability occurs in which the current increases with time until a stable value is reached within a few minutes. Figure 4 illustrates this effect in more detail for a 1400 Å-thick oxide grown on a 2 ohm-cm n-type wafer; since the same type of behavior was seen with p- and n-type substrates, it can be concluded that this particular instability is not due to minority carrier generation effects taking place in the Si depletion region. This high-field instability occurs at roughly the same field (8 MV/cm) independent of electrode

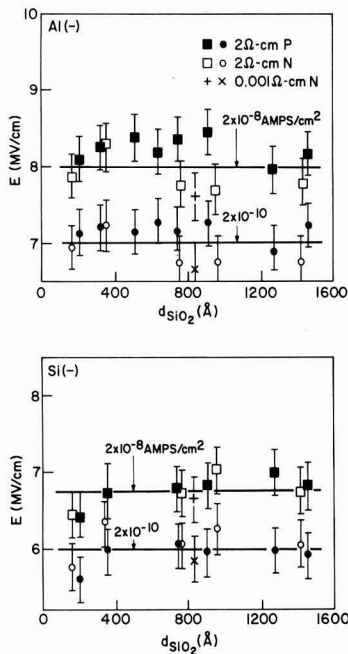


Fig. 2. Oxide thickness dependence of conduction in SiO₂ showing applied field required to produce fixed current. (a, top) Electron injection from aluminum electrode; (b, bottom) electron injection from silicon.

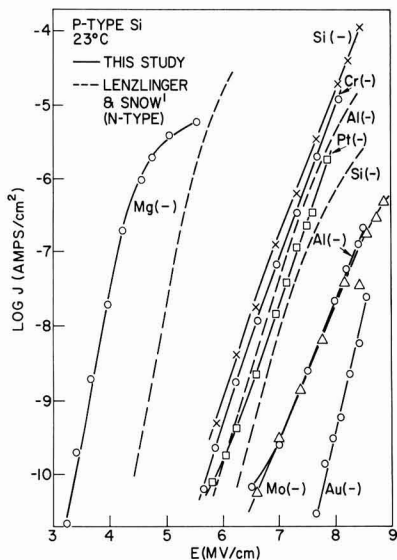


Fig. 3. Current-voltage characteristics resulting from electron injection into the SiO₂ from various metals.

material although the current levels may be considerably different when it is observed.

Both the Fowler-Nordheim and the Schottky conduction mechanisms are highly sensitive to the barrier height at the injecting electrode, and hence to the metal as observed in Fig. 3. The distinction between Fowler-Nordheim and Schottky emission are best seen with the energy level diagram of Fig. 5a. The energy difference between the metal Fermi level and the oxide conduction band presents a barrier (ϕ) for the electrons in the electrode to enter the oxide which is tri-

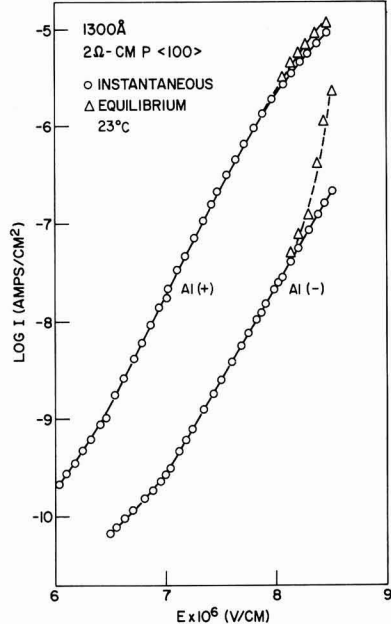


Fig. 4. Instability in I-V characteristics

angular-shaped when an electric field is applied. Electrons can tunnel through the barrier from the metal Fermi level (Fowler-Nordheim) or can be emitted over the barrier by thermal emission (Schottky). The intermediate conduction mechanism is thermally assisted electrode tunneling whereby thermally excited electrons tunnel through the upper portion of the energy barrier. The actual barrier is not a sharp tri-

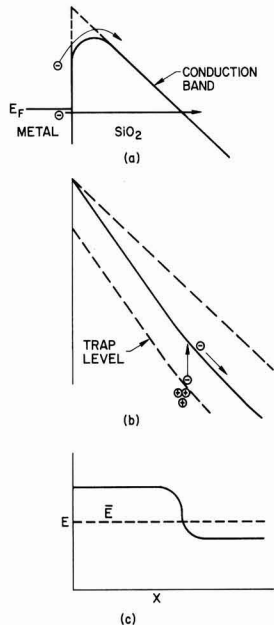


Fig. 5. Energy and field distribution near metal-silicon dioxide interface. (a) Under applied field showing image force lowering; (b) after collision ionization leaves relatively immobile positive charge (image force lowering neglected); (c) field distribution showing high-field region near interface and low-field region in bulk.

angle but is curved and has a height less than ϕ because of image-force lowering. The image-force lowering term arises from the potential redistribution in the oxide as a result of image charge induced in the metal from charge in the oxide.

The Fowler-Nordheim tunneling current J_{FN} into a solid with a barrier height of ϕ with image-force lowering is given by (1)

$$J_{FN} = (q^3 E^2 m^* / 8 \pi h \phi m^*) [1/t^2(y)] [\pi k T / \sin(\pi k T)] \quad [1]$$

$$X \exp \{ - [4(2m^*)^{1/2} \phi^{3/2} / 3 h q E] v(y) \} \quad [1]$$

where m^* is the electron effective mass in the SiO_2 , E is the applied field, q , m , h , k are the electronic charge, electron mass, Planck's constant, and Boltzmann's constant, respectively, and

$$C = 2(2m^* \phi)^{1/2} t(y) / h q E \quad [2]$$

$$y = 1/\phi (q^3 E / 4 \pi \epsilon_r \epsilon_0)^{1/2} \quad [3]$$

with ϵ_r being the relative dielectric constant of SiO_2 and ϵ_0 the permittivity of free space. The correction for image-force lowering appears in the elliptic integrals $t(y)$ and $v(y)$ and are tabulated elsewhere (21).

The Schottky current J_S is given by (13, 20)

$$J_S = (4 \pi m q k^2 / h^3) T^2 \times \exp \{ - [\phi - \sqrt{E} (q^3 / 4 \pi \epsilon_r \epsilon_0)^{1/2} / k T] \} \quad [4]$$

This Schottky conduction mechanism can be rejected for several reasons: (i) It predicts an exponentially activated temperature dependence which is not observed in Fig. 6 and 7. (ii) The slope $d \log J_S / d \sqrt{E}$, at room temperature gives a dielectric constant of only 0.35, well below even the optical value of 2.2. (iii) Temperature-field plots (13) giving regions for Fowler-Nordheim tunneling, thermally assisted tunneling, and Schottky emission show that Fowler-Nordheim conduction is expected for the conditions in this work with the possible exception of the highest temperature ($\sim 300^\circ\text{C}$) at lower fields where conduction does appear to vary exponentially with reciprocal temperature. The intermediate mechanism of thermally

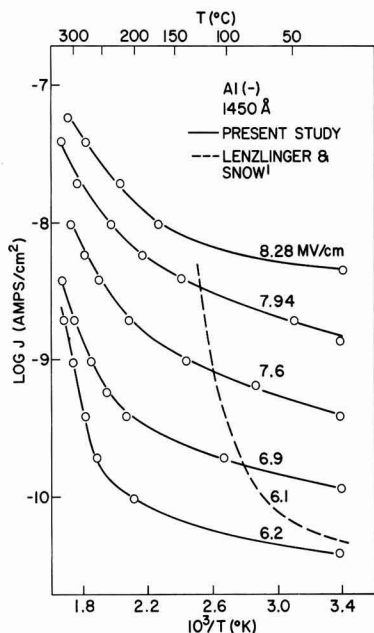


Fig. 6. Temperature dependence of conduction for electron injection from aluminum.

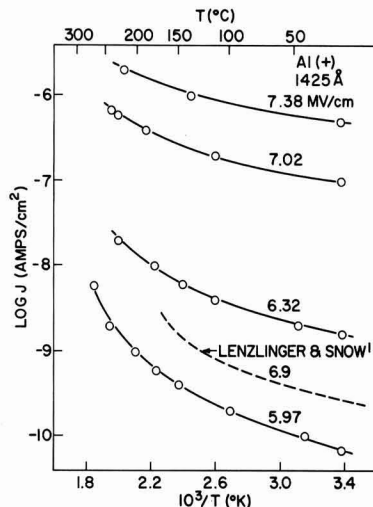


Fig. 7. Temperature dependence of conduction for electron injection from silicon.

assisted tunneling can also be ruled out since that current should vary roughly exponentially with $1/T$.

For a given field, the currents observed in this study were one-to-three orders of magnitude greater than those reported by Lenzlinger and Snow, with the exception of aluminum injection where it was two orders less (see Fig. 3). It should be noted that a layer of phosphosilicate glass (100Å, 5% P_2O_5) under the aluminum contact did not change the normally observed current. Within the limits of experimental error, the present data would fit Eq. [1]; furthermore, Lenzlinger and Snow's observation of the absolute magnitude of the current being one order of magnitude low can be explained by only a few per cent error in barrier height, effective mass, or even oxide thickness which seems very reasonable in view of their discrepancies in effective mass.

Due to the dominant exponential term in Eq. [1], it was not possible to independently determine the barrier height and the effective mass from the data but only their product. Lenzlinger and Snow used additional barrier height measurements to determine the effective mass; they found a best fit for a mass ratio of about 0.43, but this ratio varied by over 10% depending on the metal electrode, and it was not sufficient to explain their observed temperature dependence.

Table I gives the slope of the J/E^2 vs. $1/E$ plot for injection from various metals in column 2; column 3 gives the barrier height if one assumes $m^*/m = 0.5$ with the standard deviation for the least squares fit

Table I. Conduction and breakdown strengths for injection from various metals

Metal	$\phi^{3/2} \cdot \sqrt{\frac{m^*}{m}} \cdot v(y)$	Barrier height, eV		Breakdown strength E_{max} (mV/cm)
		This study†	Literature	
Mg	1.7	1.9 [0.3]	2.4 (1)	8.3
Si (bulk)	3.6	3.1 [0.1]	2.25-2.5 (2)	8.9
			3.25 (1)	
			3.15 (18, 22), 3.29 (23)	
Cr	3.6	3.1 [0.3]	3.2 (22)	8.0
Pt	3.7	3.2 [1.1]	—	8.8
Mo	4.0	3.4 [0.2]	—	9.2
Al (23°C)	4.2	3.5 [0.3]	3.2 (1, 21)	9.2
(100°C)	3.6	3.1 [0.5]	—	—
(200°C)	3.4	3.0 [0.3]	—	—
Au	7.8	5.2 [0.6]	4.2 (1)	8.0
			4.0-4.1 (21)	

† Assuming $m^*/m = 0.5$.

given in brackets [the correction for image-force lowering, from $v(y)$, is about 7% using the optical dielectric constant of 2.2]. The barrier heights are within 10% of those reported (1, 18, 22-24) elsewhere for Si, Cr, Mg, and Al; the agreement for the Au barrier heights is not as good where the experimental error is large. Despite the high work function of Pt, the Pt-SiO₂ barrier was only 3.2 eV high, as determined by I-V measurements. Quite possibly this unexpectedly low value as well as differences in conduction levels between this work and that of Lenzlinger and Snow can be explained in terms of impurities at the M/SiO₂ interface altering work functions. As shown by the measured barrier heights in Table I, there is a reasonable spread in the values from one study to another.

The most obvious temperature-dependent term in the Fowler-Nordheim conduction equation is $(\pi CkT)/\sin(\pi CkT)$. By adjusting the effective electron mass, Lenzlinger and Snow could fit their data to that functional form for one given field strength but then show that such a mass adjustment is unwarranted. They subsequently calculated the temperature dependence of the barrier height that would give such results. An examination of the temperature dependence of the conduction in Fig. 6 and 7 for several different field strengths show: (i) the temperature dependence is smaller for higher fields; (ii) the Si(-) polarity condition gives a more pronounced variation with temperature than the Al(-) one; and (iii) at lower fields, the current at higher temperatures begins to increase very rapidly. On the basis of these observations, it seems that more than one term in Eq. [1] is temperature dependent. Although the $\pi CkT/\sin(\pi CkT)$ term does give a more pronounced temperature dependence at low fields since $C \propto 1/E$, it does not quantitatively describe the variation of temperature dependence with field. In the exponential term, m^* , ϕ , and the dielectric constant in $v(y)$ could vary with temperature; a variation in barrier height seems most likely to explain the second observation. Table I also gives the least squares slope of the conduction for a few temperatures and shows that the exponential term in Eq. [1] decreases with increasing temperature. The rapid increase in current at high temperature and low field can be accounted for by either the $\pi CkT/\sin(\pi CkT)$ term which becomes infinite at $CkT \rightarrow 1$ or by a change of conduction mechanism to one that is activated such as Schottky emission or even bulk conduction; Faradaic currents are probably too small to make any contribution at these temperatures (25). Higher temperature measurements will be necessary to resolve this conduction mechanism. Although the temperature and field dependence of the current are more complex than originally reported (1), the magnitude of the variation is smaller particularly with Al(-). This may be attributed in part to a transient species that required special precautions to insure steady-state results as discussed earlier. Often a very large temperature dependence of conduction was observed on initial thermal cycling. These data were not repeatable however, and the final reproducible data showed much less variation with temperature.

Annealing of the SiO₂ films after metalization had a very important effect as shown in Fig. 8 by markedly reducing the current resulting from a given applied field for electron injection from both the Al and the Si contacts. Additional heat treatment (5 min or more at 500°C) did not further shift the 10 min, 500°C curves by more than a few per cent. Analysis of the data reveals that the Fowler-Nordheim slopes of the unannealed specimens give barrier heights for both electrodes that are 1.5 eV lower than those of annealed specimens. It seems unlikely that this is a true barrier height lowering due to impurities or surface states at the injecting interface since the apparent barrier lowering is the same for the Si/SiO₂ interface as for the Al/SiO₂ one. Instead two alternate models are proposed. First there is a trap level 1.5 eV below the con-

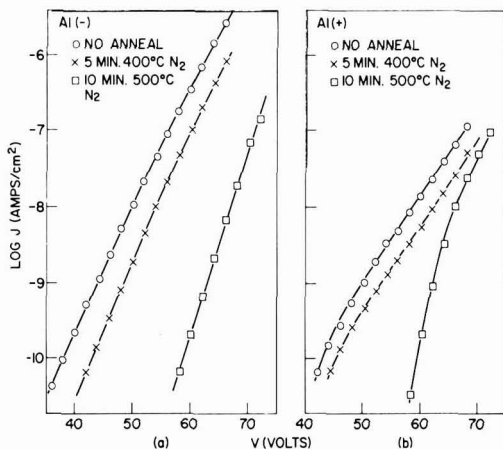


Fig. 8. Effect of postmetalization annealing on the I-V characteristics of an Al-SiO₂-Si capacitor. (a) Electron injection from aluminum electrode; (b) electron injection from silicon.

duction band in SiO₂ that can be annealed out; electrons are injected into this level with the unannealed samples and have sufficient mobility to travel along this trap level through the sample. It should be noted that trap levels (18) 2.0 eV below the conduction band have been reported and that irradiation has changed barrier heights at Si-SiO₂ and Cr-SiO₂ interfaces (23). In the second model, unannealed charge trapped in the bulk varies the potential distribution within the oxide resulting in a nonlinear potential *vs.* distance profile thereby altering the shape of the tunneling barrier. If the trapped charge is somewhat uniformly distributed throughout the oxide, the tunneling barriers at both interfaces will be equally reduced. Flatband voltage shifts during the anneal show relatively small changes in charge ($\sim 10^{12}/\text{cm}^2$) compared to the amount of charge necessary to Schottky lower the barrier by 1.5 eV ($\approx 2 \times 10^{13}/\text{cm}^2$); nevertheless, localized charges are not detected by the flatband voltage measurement. Without additional measurements it is not possible to determine which model is more correct. Since samples metalized from a tungsten filament instead of with an electron gun did not show as large an effect of annealing, the traps or oxide charge are presumed to be induced during metalization rather than present in as-grown oxide films.

Dielectric breakdown.—The high-field current instability is of particular interest in the study of dielectric breakdown. Figure 9 shows a typical current *vs.* time plot in this region of instability. The time constant associated with this current buildup appears to decrease slightly as the applied voltage increases. This instability is observed over only a small upper field region with a width of about 5% of the applied field making it somewhat difficult to observe experimentally. As Fig. 4 shows, there is a voltage at which the steady-state I-V curve becomes vertical and results in breakdown. The instability in Fig. 9 also occurs at a comparable rate when the sample is immersed in liquid nitrogen making a thermal breakdown mechanism unlikely. Likewise, any redistribution of space charge by motion of ionic carriers seems unreasonable particularly since the low-field I-V characteristics are reproducible after the conduction has been unstable. When the field is reduced after a period of time in the unstable region, the current relaxes to its original low value at that field; the time constants for this relaxation are about the same at -196° and 23°C. Capacitance-voltage flatband measurements made immediately after the instability had occurred showed at least 0.2V shift for the M(-) instability and $\approx 1V$ for the M(+) one. This C-V shift apparently indicates posi-

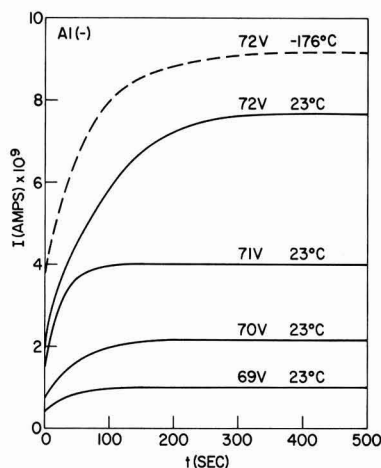


Fig. 9. Time dependence of current instability for various applied voltages.

tive charge in the oxide near the injecting electrode as a result of the high-field instability.

This onset of this instability correlates very well with the maximum breakdown strength [measured with a voltage ramp (10)] in both thickness and temperature dependence. Figure 10 shows the onset current increasing markedly with decreasing oxide thickness for films less than 800 Å thick and remaining constant for thicker films. Data showing the increasing dielectric strength with decreasing thickness below 800 Å are included for reference (10). The current region over which stable Fowler-Nordheim tunneling occurs is merely extended for thin oxides. The temperature dependence of the maximum breakdown strength (10) is plotted in Fig. 11 along with that of the onset of the instability. The scale is greatly expanded, and both the breakdown field and the instability field increase by a few per cent with increasing temperature. The observation that the instability occurs at a fixed field regardless of the barrier height of the injecting electrode is further substantiated by breakdown measurements included in Table I showing the maximum breakdown strength is constant to within 10% for the different metals tested.

The relative temperature and barrier height independence of the current instability are evidence that the instability is field-controlled. In this regard, it is possible to associate the instability with the onset of nondestructive avalanching in the oxide in a region, probably close to the injecting electrode. After injected electrons drift under the influence of the applied field,

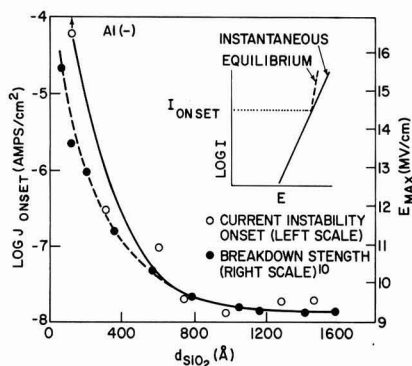


Fig. 10. Oxide thickness dependence of current instability and breakdown strength.

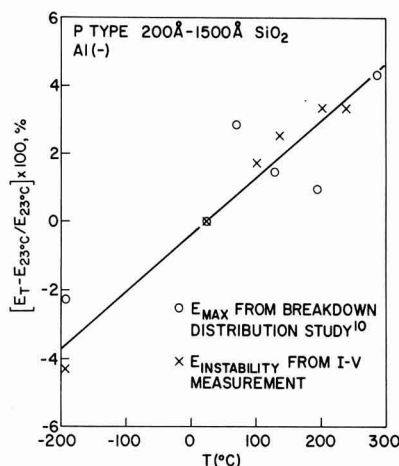


Fig. 11. Temperature dependence of current instability and breakdown strength.

additional carriers are created by collision ionization forming a space charge region which can modify the shape of the previously triangular tunneling barrier. The process is diagrammed in Fig. 5b and c, wherein, under the application of a field \bar{E} , injected electrons with mean free path λ gain energy $\bar{E}\lambda$; above a critical field this energy becomes enough to excite carriers from an energy level within the bandgap upon collision. The excited electrons are rapidly swept to the collecting electrode leaving positive charge a distance of λ from the injecting electrode. This charge modifies the potential and field distribution as seen in Fig. 5b and c with the effect of increasing the field in a narrow region around the injecting constant and reducing the field in the rest of the bulk. The reduced field prevents further collision ionization in the bulk that could lead to complete breakdown. Ionization at the interface continues until all the available traps are excited or until recombination and ionization rates equalize resulting in a steady-state condition after a few minutes (see Fig. 9). The current enhancement is due to the reduction in the size of the tunneling barrier (Fig. 5b); calculations with a 4 eV high barrier demonstrate over a 30% reduction in barrier area with 10^{13} charges/cm² (0.01 of a monolayer) located 100 Å from the interface. With a 34 Å mean free path (26) and an 8 MV/cm nominal field, the injected carriers should be able to excite traps 2.7 eV below the conduction band. Certainly a sophisticated treatment of the process would consider the energy distribution of traps and the variance of the mean free path. It is surprising, however, that an electronic process should have such a long time constant (viz., 100-500 sec).

Recently, O'Dwyer (27-28) has made theoretical calculations of high-field conduction for a dielectric material in which collision ionization processes are taken into account. His I-V curves for both Fowler-Nordheim and Schottky cathode emission show a negative resistance instability which he associates with breakdown in very much the same way that the instability observed here can be associated with breakdown. The dielectric thickness coefficient (γ) of breakdown as computed in $E_{\max} \propto d^{-\gamma}$ using his model is generally less than one half which is usually associated with electronic breakdown and one quarter which has been predicted under certain conditions (29). Samples similar to those used there (10) showed $E_{\max} \propto d^{-0.21}$. This work then provides qualitative experimental support for O'Dwyer's model. More precise quantitative comparisons will need to be based on physically determined properties such as ionization coefficients and

carrier mobilities; these data, unfortunately, are not yet available.

Summary

The initial conduction in thermal SiO_2 films is seen to decrease with time. The decay can be characterized by at least two different exponential time constants. The fast decay is nearly temperature dependent while the magnitude and temperature dependence of the slow component agrees with data (17) on release of mobile ions from traps. Due to the lack of an appreciable flatband voltage change during decay, only a small component of the transient current can be attributed to mobile ion motion or polarization. A steady-state conduction is observed after several hours under high-field (7 MV/cm) stressing. The data equally well fit $\log J$ vs. $E^{1/2}$ and $\log J/E^2$ vs. $1/E$ plots indicative of Schottky and Fowler-Nordheim emission processes, respectively. The former mechanism seems unlikely because it predicts a dielectric constant value for SiO_2 which is much less than the experimentally observed one and the temperature dependence of J is not exponentially activated, as expected. The data fit the Fowler-Nordheim conduction equation, although both the effective mass and the barrier height could not be independently computed because the results were not sufficiently accurate. However, assuming a reasonable effective mass, the calculated barrier heights give good agreement (to within 10-20%) to previously measured values.

The temperature dependence of the conduction is more complex than previously reported (1) since it was found to decrease with increasing applied field, vary with electrode material, and become exponentially activated at low fields. The results cannot be explained in terms of the usual temperature dependence of Fowler-Nordheim conduction; rather, one is forced to consider a temperature-dependent barrier height or effective mass. It is not known whether the activated region represents Schottky or bulk conduction.

The postmetalization anneal reduced the current level by up to three orders of magnitude for both polarities. The mechanism proposed involves charged defects or traps in the unannealed oxide film. It was not possible to determine if tunneling and conduction were via these trap levels rather than the oxide conduction band or if the charged defects modified the internal potential distribution so as to reduce the size of the tunneling barrier.

A high-field current instability was observed that could lead to dielectric breakdown; the onset field of this instability was about 8 MV/cm and was independent of the electrode material. Likewise maximum breakdown strengths were not significantly influenced by the choice of the electrode metal. The onset of the instability increases with decreasing oxide thickness and increasing temperature in much the same way as dielectric strength. The observation of this instability at low temperatures points to an electronic mechanism. The results qualitatively fit O'Dwyer's (27-28)

model where the instability is due to collision ionization. Further calculations with this model must await additional data on ionization and drift kinetics in SiO_2 .

Acknowledgments

The authors would like to express their gratitude to Dr. J. Eldridge and Dr. N. Chou for stimulating discussions and reviewing this work and to Dr. S. Raider and Dr. T. Hickmott for helpful discussions and exchange of ideas. They are also indebted to D. Ormond for the preparation of samples.

Manuscript submitted Sept. 1, 1971; revised manuscript received Dec. 10, 1971.

Any discussion of this paper will appear in a Discussion Section to be published in the December 1972 JOURNAL.

REFERENCES

1. M. Lenzlinger and E. H. Snow, *J. Appl. Phys.*, **40**, 278 (1969).
2. E. H. Snow, *Solid State Commun.*, **5**, 813 (1967).
3. E. H. Snow, A. S. Grove, B. E. Deal, and C. T. Sah, *J. Appl. Phys.*, **36**, 1664 (1965).
4. M. Yamin, *IEEE Trans. Electron Devices*, **ED-12**, 88 (1965).
5. S. R. Hofstein, *Appl. Phys. Letters*, **10**, 291 (1967).
6. R. W. Brander, D. R. Lamb, and P. C. Rundle, *Brit. J. Appl. Phys.*, **18**, 23 (1967).
7. A. G. Revesz, *Phys. Status Solidi*, **24**, 115 (1967).
8. D. R. Lamb and P. C. Rundle, *Brit. J. Appl. Phys.*, **18**, 29 (1967).
9. V. F. Korzo, *Fiz. Tverd. Tela*, **11**, 1758 (1969).
10. C. M. Osburn and D. W. Ormond, To be published.
11. D. R. Lamb, "Electrical Conduction Mechanisms in Thin Insulating Films," Methuen and Co., London (1967).
12. A. K. Jonscher, *Thin Solid Films*, **1**, 213 (1967).
13. R. M. Hill, *ibid.*, **1**, 39 (1967).
14. P. Balk, *This Journal*, **112**, 185C (1965).
15. N. Klein, *IEEE Trans. Electron Devices*, **ED-13**, 788 (1966).
16. W. A. Pliskin, D. R. Kerr, and J. A. Ferri, "Physics of Thin Films," Vol. 4, pp. 257-324, Academic Press, Inc., New York (1967).
17. S. R. Hofstein, *IEEE Trans. Electron Devices*, **ED-14**, 749 (1967).
18. R. Williams, *Phys. Rev.*, **140**, A569 (1965).
19. R. H. Waiden and R. J. Strain, 8th Annual Proc. Reliability Physics, Las Vegas, Nevada, April 7-10, pp. 23-28 (1970).
20. M. A. Lampert and P. Mark, "Current Injection in Solids," pp. 113-139, 187, Academic Press, New York (1970).
21. R. E. Burgess, H. Kroemer, and J. M. Houston, *Phys. Rev.*, **90**, 515 (1953).
22. B. E. Deal, E. H. Snow, and C. A. Mead, *J. Phys. Chem. Solids*, **27**, 1873 (1966).
23. J. L. Peel, R. A. Kjar, and R. C. Eden, *Appl. Phys. Letters*, **17**, 3 (1970).
24. A. M. Goodman, *Phys. Rev.*, **152**, 785 (1966).
25. N. J. Chou, *This Journal*, **118**, 601 (1971).
26. C. N. Berglund and R. J. Powell, *Appl. Phys.*, **42**, 573 (1971).
27. J. J. O'Dwyer, *J. Appl. Phys.*, **40**, 3887 (1969).
28. J. J. O'Dwyer, *ibid.*, **39**, 4356 (1968).
29. F. Forlani and N. Minnaja, *Phys. Status Solidi*, **4**, 311 (1964).

Preparation of (Y,Yb,Er)F₃ Phosphors for Green-Light Emission

Sidney G. Parker* and Rowland E. Johnson

Texas Instruments Incorporated, Dallas, Texas 75222

ABSTRACT

A coprecipitation method has been used to prepare (Y,Yb,Er)F₃ phosphor powders for conversion of infrared to visible light. The coprecipitated material was treated in a stream of HF at 800°-900°C to dehydrate the powder and convert oxyfluorides to the fluorides. An interesting example of crystal growth occurred which gave a stable phosphor of the desired particle size. The phosphor converted up to 3% of the infrared radiation of GaAs:Si diodes to green light at 5400Å.

(Y,Yb,Er)F₃ has been used for conversion of infrared light of 9300-9600Å to green light having a wavelength of 5400Å (1). The phosphor has previously been prepared by melting the fluorides of Y, Yb, and Er together or by heating the fluorides together in a flux such as BeF₂, then leaching out the flux (1,2). The material obtained by melting the fluorides was uniform in composition, but the particles were too large for an application which required a particle size ≤ 20 μ m. When ground to the desired particle size, the crystals were apparently damaged, seriously reducing the phosphor conversion efficiency by 50% or more. Flux-grown material also required grinding and, in addition, was nonuniform and contained a high concentration of flux even after extensive leaching. A further disadvantage is the highly toxic nature of BeF₂. In both methods, the starting material must be the anhydrous, high-purity rare-earth fluorides.

We describe a method of coprecipitation of the rare earth fluorides, washing and filtering the precipitate, and treatment with HF at 900°C to prepare the phosphors. The phosphors are uniform, of the proper particle size and show a high conversion efficiency. The starting materials are rare earth oxides which are readily available in high purity at relatively modest price levels.

Experimental

Oxides of Y, Yb, and Er of 99.999%, 99.999% and 99.9999% purity (with respect to other rare earths) were used. Approximately 10g of the oxides in the desired mole ratio were dissolved in 25 ml of hot concentrated HCl. The clear solution was diluted with 50 ml H₂O and cooled to room temperature. To this solution in a polyethylene beaker we slowly added, while stirring vigorously, a mixture of 10 ml concentrated HF and 10 ml concentrated HNO₃. The gelatinous precipitate which formed was digested at ~70°C with constant stirring for 20-24 hr during which the precipitate became more crystalline. The supernatant liquid was decanted and the precipitate washed with 10% HF-10% HNO₃ until the wash was free of chlorides. The digestion and washing with 10% HF-HNO₃ was repeated several times. The precipitate was then rinsed with methanol, filtered, and air-dried at 110°C; it was a free-flowing powder which was probably a mixed rare earth fluoride and oxyfluoride with an unknown amount of water of hydration.

The material was heated slowly to 800°C over a period of 2 hr in a stream of He or N₂. Anhydrous HF was then mixed into the gas stream and the material was heated at 900°C for 4-8 hr. The reaction chamber was a vitreous carbon tube or an iridium tube with carbon liner; the phosphor was held in a platinum or vitreous carbon boat. The final product

from this dehydration-crystal growth treatment was very stable in air and could be used as a phosphor without further processing. It is routinely stored in a desiccator or drying oven and has shown no degradation of phosphor efficiency in more than a year.

Optimum processing conditions were selected by comparing conversion efficiencies of the phosphors. We define efficiency as the ratio of green-light output to infrared power emitted by a GaAs diode; an efficiency of 3.0% was achieved with our best phosphors.

Results and Discussion

Composition and Purity

An optimum phosphor composition was Y_{0.80}Yb_{0.19}Er_{0.01}F₃ as determined by varying the Y/Yb and Yb/Er ratios independently. The source of the starting materials greatly influenced the efficiency of the resulting phosphor. For example, Y and Yb, reported to be 99.999% purity, from two different sources gave phosphors of 1.5 and 2.5% efficiency. Analysis of the rare-earth elements and their compounds is very difficult; although emission spectroscopy is frequently used, the complex spectra make detection of many impurities impossible. Table I shows emission spectrographic analysis of typical phosphors; in this series, only Batch 36 had a high efficiency, and it also had the highest purity.

Table II shows the results obtained by mass spectrographic analysis on phosphor material as coprecipitated and after the dehydration-crystal growth steps and indicates the large number of impurities present. The concentration of all impurities except carbon and gold was decreased by the dehydration-crystal growth in HF. The amount of oxygen in the material was rather high even after dehydration and suggests that the final product may still contain oxyfluoride. Carbon could come from the organic compounds used for extraction and purification of the rare-earth oxides or from the carbon tube and boat used during dehydration. The effects of various impurities on phosphor performance were not studied. Electron microprobe analysis showed the particles to be homogeneous within the accuracy of the instrument which was $\pm 2\%$.

Coprecipitation Conditions

It was necessary to exercise control over the coprecipitation conditions to give a material easy to handle,

Table I. Emission spectrographic analyses of Y_{0.80}Yb_{0.19}Er_{0.01}F₃ phosphors

Batch No.	Impurities in ppm by weight				
	Mg	Mn	Cu	Si	B
36	0.1-1	ND	0.1-1	1-10	ND
62	0.1-1	ND	0.1-1	1-10	1-10
64	0.5-5	0.1-1	0.1-1	1-10	ND

* Electrochemical Society Active Member.

Key words: phosphors, infrared conversion, rare-earth compounds, coprecipitation, crystal growth.

Table II. Mass spectrographic analyses of
Y_{0.80}Yb_{0.19}Er_{0.01}F₃ phosphors
(ppm atomic)

Impurity	Coprecipitated material	Dehydrated-sintered material
C	1200	2200
O	20,000	8000
Na	560	115
Mg	28	10
Al	430	11.3
P	10	2.8
Cr	10	1.6
Ni	6.5	—
Cu	580	13
Zn	177	4.4
Te	50	18
Ba	1.1	0.28
Au	1.3	6.1
Hg	0.89	—
Pb	4.1	3.3
Si	1800	—

as established in past work (3), as well as a material which has a high conversion efficiency. Standard procedures described for gelatinous precipitates include low temperature (25°C) precipitation, dilute solutions, and slow addition of the precipitant with stirring. Phosphors prepared from concentrated solutions or at elevated temperatures gave approximately 1/20 the conversion efficiency of the best phosphors. The poor phosphors were presumably due to occlusion of impurities or water during precipitation which could not be removed in subsequent handling.

Homogeneous precipitation (4) to produce the mixed fluoride would presumably be of value here. A method has been reported by Vecht (5) which produces fluoride ion by acid hydrolysis of fluoroborate ion, (BF₄)⁻, but we have not tested his method on this system.

Digestion and Washing

The digestion and washing conditions had a great effect on the phosphors. The best phosphors were formed by digestion for 24 hr at about 70°C with a 10% HF-10% HNO₃ solution followed by washing and additional digestion with dilute HF-HNO₃ solution. Digestion is a well-known method of obtaining particle growth and exclusion of impurities (3). Digestion of our gelatinous precipitate made it denser until it was transformed into a fine powder.

Analysis of phosphor efficiency indicated that it was necessary to use an acidic wash solution and to repeat the wash and digestion step a number of times. Digestion and washing in water alone gave phosphors with 0.1% efficiency compared with 3.0% for the best. This "water only" material could be improved to 2.5% by acid digestion and wash. Material which was digested once for only 24 hr or which was washed in water after acid digestion gave low-efficiency phosphors. Repeated digestions and washings seemed necessary to obtain breakdown of the gelatinous precipitate and to give a crystalline material containing much less water of hydration. Debye-Scherrer x-ray diffraction patterns of the material after the digestion washing in dilute acid solutions showed that the material was crystalline although the lines were rather diffuse and weak in intensity.

Dehydration—Crystal Growth

The dehydration period and temperature were also important factors in producing a good phosphor. The highest efficiency phosphors were obtained by starting a flow of N₂ or He, increasing the temperature over a period of 2 hr to 800°C and then maintaining at that temperature for 1 hr. TGA and gas chromatography showed H₂O was evolved, starting at about 500°C. After complete dehydration, anhydrous HF was added to the gas stream, the temperature raised to 900°C, and the system maintained for 4 hr. Heating at temperatures greater than 900°C gave inferior phosphors as did heating at 800°C for up to 12 hr in anhydrous HF. Bringing the temperature directly to 900°C also gave

a degraded phosphor. Heating at 900°C for periods longer than 4 hr did not improve the phosphor.

Phosphors with almost identical conversion efficiencies were formed when the dehydration-crystal growth steps were carried out in either a vitreous carbon boat or a Pt boat in a vitreous carbon tube. Mass spectrographic analysis of phosphors treated in Pt boats showed 0.2-2 ppm(wt) Pt in the final product. Using an iridium tube resulted in doping the phosphor to 500 ppm with Ir which reduced the conversion efficiency to 1/10 of its normal value. However, reaction of HF with Ir could be prevented by placing a carbon foil inside the Ir tube. There was little or no reaction of carbon foil or vitreous carbon if exposed to anhydrous HF. The phosphor was packed roughly into the boat; presumably these processes would occur more efficiently if the powder were spread in a thin layer or if gas flow could be directed through a bed of the powder.

As indicated in Table III, x-ray diffraction patterns on the freshly coprecipitated material which had been air dried at 110°C were diffuse, but after heating in HF the lines were sharp. This suggested that crystal growth occurred as well as dehydration. The diffraction pattern for the final product corresponded to that for the material produced by melting the anhydrous fluorides together in a dry HF ambient. Scanning electron micrographs of the phosphor at various stages confirmed that crystal growth occurred during heating in HF at 800°C and higher. Little if any crystal growth occurred by heating in the absence of HF. Figure 1(a) shows a scanning electron micrograph of the material after heating for 1 hr at 800°C in He; the appearance is identical to the unheated powder. Figure 1(b) shows the same powder after He treatment followed by treatment in HF at 800°C for 1 hr. It can be seen by comparison that the particles have increased in size by sintering together during the HF treatment. Continued heating in HF at 800°-900°C for 4 hr or more gave well-shaped crystals ≤20 μm in diameter, as shown by microscopic examination. Previous treatment also affected crystal growth. Thus, a fluoride precipitate which had been washed with H₂O, rather than the HF-HNO₃ mixture, showed very little crystal growth under the standard treatment and showed poor conversion efficiency as a phosphor.

Figure 2 shows photomicrographs of samples in index matching oil in transmitted light and crossed polarized light of material treated in HF at 900°C for 4 hr. It can be seen from the shape of the well-faceted

Table III. Comparison of d-spacings for Y_{0.80}Yb_{0.19}Er_{0.01}F₃ phosphors for different stages of hydration

Line No.	Co-ppt phosphor		Dehydrated phosphor		Melted phosphor	
	"d", Å	1/l ₀	"d", Å	1/l ₀	"d", Å	1/l ₀
1	3.70	Very diffuse	3.65	15	3.67	15
2	3.44	Sharp	3.56	50	3.57	50
3	3.24	Very diffuse	3.38	25	3.39	25
4	2.84	Diffuse	3.16	10	3.17	100
5	2.52	Very diffuse	2.85	30	2.86	30
6	2.31	Very diffuse	2.47	15	2.49	15
7	2.06	Very diffuse	2.39	2	2.40	2
8	1.95	Very diffuse	2.18	10	2.31	2
9	1.89	Very diffuse	2.04	20	2.19	10
10	1.85	Diffuse	1.98	30	2.05	30
11	1.72	Very diffuse	1.82	90	1.93	30
12	1.66	Very diffuse	1.80	25	1.92	90
13	1.56	Very diffuse	1.84	90	1.90	25
14			1.83	15	1.85	90
15			1.77	30	1.83	15
16			1.74	30	1.77	30
17			1.70	20	1.74	30
18			1.66	20	1.71	20
19			1.58	10	1.66	20
20			1.54	10	1.58	10
21			1.53	10	1.54	10
22			1.48	10	1.48	10
23			1.46	10	1.46	10
24			1.43	10	1.43	10
25			1.41	10	1.41	10
26			1.35	5		
27			1.33	5		
28			1.28	2		
29			1.27	5		



(a)



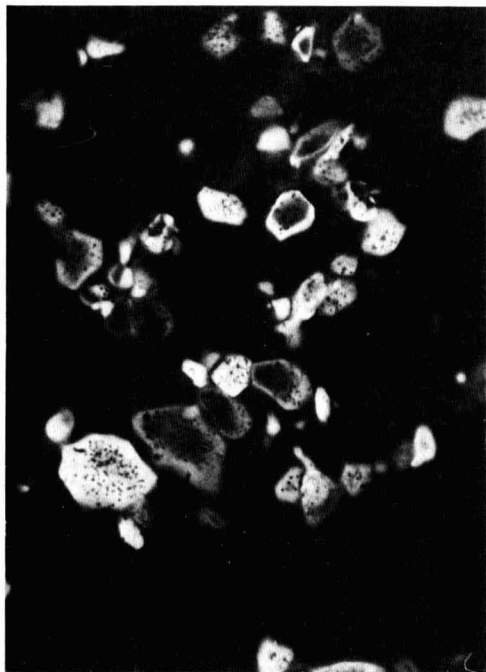
(b)

Fig. 1. Scanning electron micrographs (3000X) of (a) phosphor heated in He at 800°C for 1 hr (unheated phosphor showed identical appearance) and (b) phosphor from (a) heated in HF at 800°C for 1 hr.

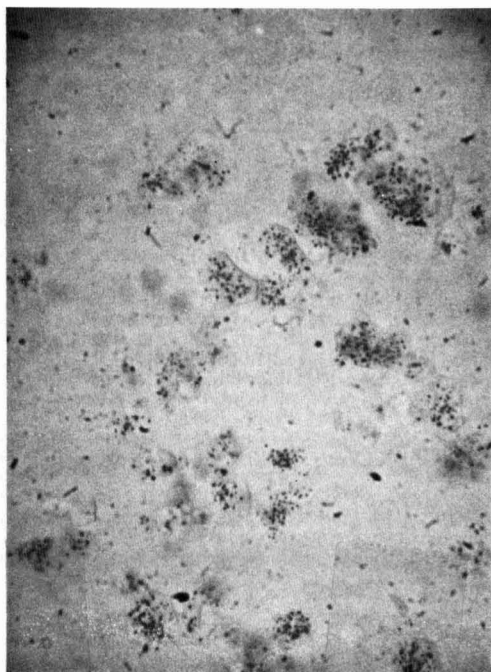
particles that crystal growth has occurred. There is some strain in the crystals as evidenced by the shading. It is also apparent that during sintering or crystal growth, occlusions were formed in the crystals, most likely due to the pores or holes between the small particles during agglomeration (6). Heating in HF at 800°C did not give the pores; however, the particles

treated at 800°C were less efficient light converters than those treated at 900°C. It was possible that the pores acted as scattering centers and increased the conversion efficiency. Prolonged sintering in anhydrous HF at 900°C did not reduce the number or size of the pores.

We conclude that dehydration, in the absence of HF, is necessary before the fluoridation step. This latter



(a)



(b)

Fig. 2. Phosphor particles in index matching oil: (a) cross-polarized light and (b) transmitted light. Magnification 360X

process converts any oxyfluoride to fluoride and induces the desired crystal growth at about 900°C. Moisture in the HF stream could degrade the phosphor by forming an excessive amount of oxyfluoride or by attacking the carbon tube or boat and dispersing carbon particles throughout the system.

Testing and Application of the Phosphor

The method for evaluating the phosphors gave a rapid relative comparison but was not optimized for maximum output. For testing, the phosphor powder was mixed with silicone oil to form a viscous slurry with about 75% phosphor by weight. The slurry was applied to a 0.072-in. diameter domed GaAs:Si diode which gave infrared of 9300-9600 Å. Slurry was applied until maximum green light output was obtained. The GaAs diode was operated at 2A at a power level of 3.36W. The diode was well heat-sunk and operated for only short periods. The green-light intensity was determined with a silicon solar cell, filtered to remove the infrared. The solar cell voltage was measured across a fixed resistor and had been calibrated to give output power. The maximum conversion of diode infrared output to green light output was 3.0% which represented a brightness of ~8000 ft-L. No effort was made to obtain the maximum in light output by use of reflective surfaces, index-matching media, or a particular particle size, although some preliminary experiments indicated that the green-light output could be doubled by use of reflective coatings. The test method was reproducible to 1% and accurate to probably $\pm 10\%$; it enabled phosphors to be checked for conversion efficiency in only a few minutes. The phosphor-oil slurry was readily removed so the same diode was used for all tests.

Evaluation devices were made from diode chips, 0.024 in. square. An epoxy was applied; then the phosphor powder was allowed to settle through the epoxy. After curing, the epoxy-phosphor layer was ~200 μ m thick and roughly 50% phosphor. Characteristics of some devices are given in Table IV. Since the phosphor emission depends on a 2- (or more) photon absorption, there is a nonlinear relation of infrared emission to green-light emission. Again, no effort was made to optimize the brightness of these devices. These green-light emitters showed little or no degradation in light output after 6 months under constant load at 50 mA but did show 10% degradation at 100 mA load. This

Table IV. Green light output at various current levels for $Y_{0.80}Yb_{0.19}Er_{0.01}F_3$ on GaAs:Si diodes

Diode No.	IR power (mW)		Brightness, ft-L			
	50 mA	100 mA	25 mA	50 mA*	100 mA**	125 mA
49	2.42	4.93	17	77	250	325
23	2.76	5.77	27	130	430	560
25	2.90	6.19	49	210	640	850

* Brightness 99% after 6 months at 50 mA.

** Brightness 90% after 6 months at 100 mA.

was caused by degradation of the diode rather than the phosphor. There appeared to be no reaction of the phosphor with the epoxy. Phosphors tested periodically over the span of one year showed no decrease in conversion activity. This suggests that the lifetime of a green-light emitter would be determined by the lifetime of the GaAs diode.

Acknowledgments

We wish to acknowledge the help of Mr. Jack E. Pinnell in the preparation of the phosphors. Dr. Kent Watts provided valuable aid in measuring the efficiencies of the phosphor, and Mr. Kent Carson obtained the scanning electron micrographs.

Manuscript received Oct. 12, 1971. This was Paper 55 presented at the Washington, D. C., Meeting of the Society, May 9-13, 1971.

Any discussion of this paper will appear in a Discussion Section to be published in the December 1972 JOURNAL.

REFERENCES

1. L. G. Van Uitert, L. Pictroski, and W. H. Grodziewicz, *Mater. Res. Bull.*, **4**, 777 (1969).
2. R. A. Hewes and J. F. Sarver, *Phys. Rev.*, **182**, 427 (1969).
3. I. M. Kolthoff and E. B. Sandell, "Textbook of Quantitative Inorganic Analysis," pp. 103-117, Macmillan, New York (1937).
4. C. N. Reilly, Editor, "Advances in Analytical Chemistry and Instrumentation," Vol. 4, p. 1, Interscience, New York (1965).
5. A. Vecht and A. Hickey, Paper 54 presented at Electrochem. Soc. Meeting, Washington, D.C., May 9-13, 1971.
6. W. D. Kingery, "Introduction to Ceramics," p. 369, John Wiley and Sons, New York (1963).

Thermodynamic Calculations for $GaAs_{1-x}P_x$ Vapor Growth

M. Bleicher

Technische Universität, Institut für Technische Elektronik, 8 München 2, Germany

ABSTRACT

The combined transport of GaAs and GaP to form $GaAs_{1-x}P_x$ mixed crystals in an open-flow system by $AsCl_3$ and PCl_3 with two separate Ga sources has been calculated, based on simple thermochemical considerations. A new approach has been taken to determine theoretically the solid composition of the $GaAs_{1-x}P_x$ mixed crystal. The influence of the seed temperature on the solid composition has been studied as well as the influence of the total concentration of the incoming gases.

Production of $GaAs_{1-x}P_x$ mixed crystals has become very important in recent years. Two ranges of composition are especially favored: first the composition of x

Key words: vapor phase deposition, thermodynamics, $GaAs_{1-x}P_x$, computer calculations.

about 0.4 for applications in the visible, and second very low-phosphorus contents to produce GaAs heterojunction lasers (1). One of the reasons for the great interest in the $GaAs_{1-x}P_x$ mixed crystals is their relatively easy and cheap production by means of epitaxial

growth from the vapor phase. A well-known system is the Ga-As-P-Cl-H open tube flow system, which uses Ga, AsCl₃, and PCl₃ as starting materials and hydrogen as a carrier gas.

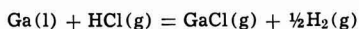
Since the early investigations (2, 3) much work has been done on the arsenic half of this system, for example by Boucher and Hollan (4), Shaw (5), and Kirwan (6). On the phosphorus half Luther and Roccasecca (7), Seki *et al.* (8, 9), and Kirwan (6) have made a new approach experimentally as well as theoretically since the early work of Oldham (10). For the whole complex system however only experimental studies of the preparation and investigation of the crystals are known.

This paper carries out thermodynamic calculations for the complex system and highlights the influence of the substrate temperature on the composition of the epitaxial deposit.

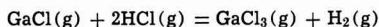
Computer Calculations

Chemical and thermodynamical background.—Calculations are made for a system containing two separate gallium sources, which are fed by PCl₃ and AsCl₃, respectively. The incoming pressures p_{PCl_3} and p_{AsCl_3} are varied from 10^{-4} up to 0.1 atm.

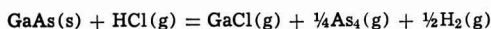
Within the reacting tube nine different vapor species are taken into account, which are assumed to govern seven dominant chemical reactions, taking place at the usual operation temperature range between 700° and 1000°C. These reactions are listed below together with their equilibrium constants.¹



$$K_1 = \frac{p_{\text{GaCl}} p_{\text{H}_2}^{1/2}}{p_{\text{HCl}}} \quad [1]$$



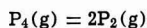
$$K_2 = \frac{p_{\text{GaCl}_3} p_{\text{H}_2}}{p_{\text{GaCl}} p_{\text{HCl}}^2} \quad [2]$$



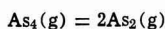
$$K_3 = \frac{p_{\text{GaCl}} p_{\text{As}_4}^{1/4} p_{\text{H}_2}^{1/2}}{p_{\text{HCl}}} \quad [3]$$



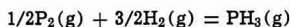
$$K_4 = \frac{p_{\text{GaCl}} p_{\text{P}_4}^{1/4} p_{\text{H}_2}^{1/2}}{p_{\text{HCl}}} \quad [4]$$



$$K_5 = \frac{p_{\text{P}_2}^2}{p_{\text{P}_4}} \quad [5]$$



$$K_6 = \frac{p_{\text{As}_2}^2}{p_{\text{As}_4}} \quad [6]$$



$$K_7 = \frac{p_{\text{PH}_3}}{p_{\text{P}_2}^{1/2} p_{\text{H}_2}^{3/2}} \quad [7]$$

Recently it has been shown by Ban (17) that the assumption for the reactions is justified especially for the deposition process (Eq. [3] and [4]). All of the itemized vapor species, except PH₃, are commonly expected to occur in systems like the one described. But, concerning PH₃, Ban (17) stated its existence in a relative high concentration experimentally.

Combinations between phosphorus and arsenic like AsP, As₂P₂, As₃P, or AsP₃ are not taken into considera-

¹ Some further possible vapor species were estimated and found to lie several magnitudes below that of the interesting ones. Over the whole range of considered temperatures and input concentrations $p_{\text{AsCl}_3} < 10^{-7}$ atm, $p_{\text{PCl}_3} < 10^{-6}$, $p_{\text{AsH}_3} < 10^{-10}$ atm, and $p_{\text{PCl}_2} < 10^{-13}$ atm; hence these species are ignored in the analysis.

Table I. Equilibrium constants, atm units

$\log_{10} K_1 = 3.67 - 0.87 \times 10^3/T - 0.16 \ln T$
$\log_{10} K_2 = -13.95 + 9.58 \times 10^3/T + 0.92 \ln T$
$\log_{10} K_3 = 6.04 - 6.99 \times 10^3/T - 0.35 \times 10^{-2} T - 0.22 \ln T$
$\log_{10} K_4 = 6.08 - 7.255 \times 10^3/T - 0.03 \ln T$
$\log_{10} K_5 = 11.5 - 1.21 \times 10^4/T - 0.5 \ln T$
$\log_{10} K_6 = 11.5 - 1.59 \times 10^4/T - 0.43 \ln T$
$\log_{10} K_7 = -4.04 + 3.58 \times 10^3/T - 0.207 \ln T$

tion because of the lack of thermodynamical data. As soon as this information becomes available, there will be no difficulty in introducing them in the given set of reactions. The values for the reaction equilibria constants, which are related to the standard free energy change of the concerned reaction in the form $-\Delta G_1 = RT \ln K_1$, are taken from a list given by Kirwan (6) for the first five equations, while the sixth is taken from Hurle and Mullin (13) and the seventh is calculated from data of the JANAF Tables (14). These values which are listed in Table I originate from a careful literature survey and have been found to be less contradictory ones.

Arsenic-saturated source reaction equilibria.—For source temperatures of the Ga boat of about 925°C it is assumed that after some time of saturation with arsenic a thin layer of GaAs will cover the liquid gallium. Therefore the reaction equations [2], [3], and [6] must be applied. Because the pressures of six different vapor species are involved at this place, three more equations are required. The latter are denoted as equations of conservation. In general, for such problems one gets for n different vapor species always $n-3$ equations from the chemical reactions and three equations of conservation, from which one describes the conservation of the total pressure of the system. For an open-flow system this is expressed as

$$\Sigma p_i = 1 \text{ atm} \quad [8]$$

The remaining two equations are given in the case regarded here by conservation of chlorine

$$p_{\text{GaCl}} + 3p_{\text{GaCl}_3} + p_{\text{HCl}} = 3p_{\text{AsCl}_3} \quad [9]$$

and conservation of arsenic

$$4p_{\text{As}_4} + 2p_{\text{As}_2} = p_{\text{AsCl}_3} \quad [10]$$

where p_{AsCl_3} denotes the partial pressure of the incoming AsCl₃.

It must be stated at this point that due to the criterion of constant pressure a volume change is induced in the system while the reactions are taking place, because mole numbers are changing. For this reason the equations of conservation Eq. [9] and [10] should be expressed in terms of moles instead of partial pressures. Since the relative volume change for the whole system has been estimated to be smaller than 3%, this error will be ignored in the calculations. Equation [10] is only true for the source region, where no deposition can occur. The etch rate ER of the gallium source in grams per minute is expressed by

$$\text{ER} = \frac{(p_{\text{GaCl}} + p_{\text{GaCl}_3}) g_{\text{Ga}}}{RT_0} \cdot V_0 \quad [11]$$

where g_{Ga} is the atomic weight of Ga, T_0 the temperature at which the reaction products are entering the tube, and V_0 is the total flow rate (cubic centimeters per minute).

Phosphorus-saturated source reaction equilibria.—The same procedure described above is now applied to this source, also containing gallium. In this case, however, Luther (7) and Seki (8) have pointed out that no skin of GaP forms. For this reason Eq. [1], [2], [5], [7], [8] and in addition

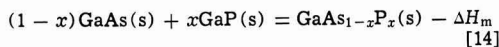
$$p_{\text{GaCl}} + 3p_{\text{GaCl}_3} + p_{\text{HCl}} = 3p_{\text{PCl}_3} \quad [12]$$

and

$$4p_{\text{P}_4} + 2p_{\text{P}_2} + p_{\text{PH}_3} = p_{\text{PCl}_3} \quad [13]$$

have to be taken into account.

Deposition reaction equilibria.—In the deposition zone of the reaction tube the incoming vapor mixture is allowed to form an equilibrium phase between all its species and solid GaAs and GaP, respectively, for all temperatures considered. This assumption is only true for low flow rates as well as for a long deposition region. Here Eq. [2] to [7] must be applied and, in addition, the heat of mixing which occurs at the reaction



The heat of mixing is given by

$$\Delta H_m = \Omega x(1-x) \quad [15]$$

Huber (15) has calculated Ω to be 1 kcal/mole, i.e., the maximum heat of mixing at $x = 0.5$ is 0.25 kcal/mole. The resulting modification in the equilibrium constants is negligible and therefore ignored in the following. Equation [8] and the conservation of chlorine is still valid

$$p_{\text{GaCl}} + 3p_{\text{GaCl}_3} + p_{\text{HCl}} = 3p_{\text{AsCl}_3} + 3p_{\text{PCl}_3} \quad [16]$$

The third equation of conservation states that the sum of arsenic and phosphorus atoms precipitating out of the vapor phase must be equal to that of the gallium atoms

$$4p_{\text{As}_4} + 2p_{\text{As}_2} + p_{\text{PH}_3} + 4p_{\text{P}_4} + 2p_{\text{P}_2} - 4p_{\text{As}_4} - 2p_{\text{As}_2} - p_{\text{PH}_3} - 4p_{\text{P}_4} - 2p_{\text{P}_2} = p_{\text{GaCl}} + p_{\text{GaCl}_3} - p_{\text{GaCl}} - p_{\text{GaCl}_3} \quad [17]$$

where the p_{ol} 's indicate the partial pressures coming from the source into the deposition zone of the reactor.

This new equilibrium yields the amount of GaAs and GaP depositing at the seed dependent only on the input partial pressures of AsCl_3 and PCl_3 , the source and the substrate temperature. The concentration x of GaP in the solid is given by the rates of precipitation similar to Eq. [17]

$$x = \frac{p_{\text{OPH}_3} + 4p_{\text{OP}_4} + 2p_{\text{OP}_2} - p_{\text{PH}_3} - 4p_{\text{P}_4} - 2p_{\text{P}_2}}{p_{\text{OGaCl}} + p_{\text{OGaCl}_3} - p_{\text{GaCl}} - p_{\text{GaCl}_3}} \quad [18]$$

On the other hand it is possible to express x in terms of vapor pressures and equilibrium constants by combining Eq. [3] and [4] in the form

$$\text{GaAs}_{1-x}\text{P}_x\text{(s)} + \text{HCl(g)} = \text{GaCl(g)} + (1-x)/4\text{As}_4\text{(g)} + x/4\text{P}_4\text{(g)} + 1/2\text{H}_2\text{(g)}$$

$$K_3^{1-x} K_4^x = \frac{p_{\text{GaCl}} p_{\text{P}_4}^{x/4} p_{\text{As}_4}^{(1-x)/4} p_{\text{H}_2}^{1/2}}{p_{\text{HCl}}} \quad [19]$$

where x becomes

$$x = \frac{\ln \left[\left(\frac{p_{\text{HCl}}}{p_{\text{GaCl}} p_{\text{H}_2}^{1/2}} \right)^4 \frac{K_3^4}{p_{\text{As}_4}} \right]}{\ln \left[\left(\frac{K_3}{K_4} \right)^4 \frac{p_{\text{P}_4}}{p_{\text{As}_4}} \right]} \quad [20]$$

Equation [20] serves to predict in what direction x will change as soon as equilibrium is no longer maintained.

Results

The model proposed here is based only on simple chemothermodynamical relations. No account is taken of the kinetic mechanisms which might control the growth of an epitaxial layer in reality. Also no regard has been paid to the fact that in practice total homogeneity is not achievable.

Figure 1 shows the equilibrium partial pressures of the different vapor species over the arsenic- and phosphorus-saturated gallium source at 1200°K over various input pressures of AsCl_3 and PCl_3 , respectively. It must be noted that in contrast to the negligible arsine pressure (8, 9), phosphine by Eq. [7] has a remarkably high vapor pressure. This plot is for a single source

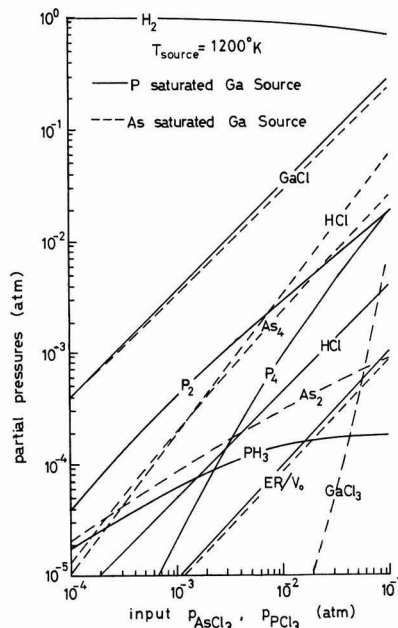


Fig. 1. Partial pressures and etch rates over a arsenic and phosphorus saturated Ga source, respectively, vs. the AsCl_3 and PCl_3 input partial pressures, respectively, for a constant 1200°K source temperature.

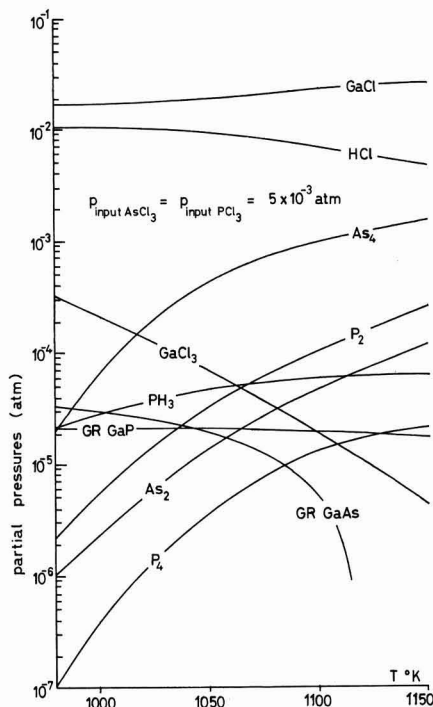


Fig. 2. Partial pressures and growth rates over a $\text{GaAs}_{1-x}\text{P}_x$ deposit vs. the deposit temperature.

temperature but above 920°C there is little influence on growth. For the Group V elements only the ratio of dimers to tetramers is varying, while their total concentration remains constant. The dominant Group III

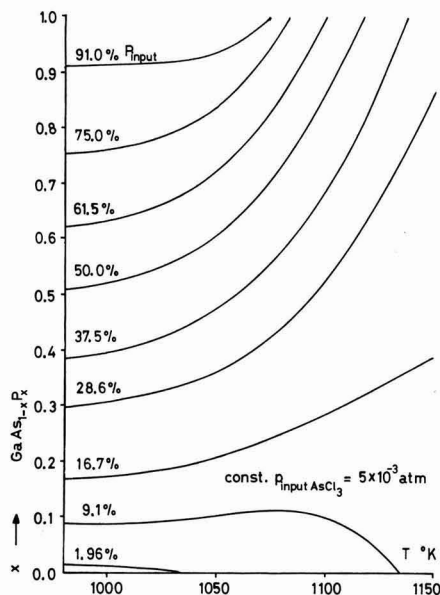


Fig. 3. $\text{GaAs}_{1-x}\text{P}_x$ deposit composition vs. the deposit temperature for several phosphorus percentages of the PCl_3 and AsCl_3 input gases.

element pressure, p_{GaCl} , is about constant too, because the HCl pressure lies more than one magnitude lower.

In Fig. 2 the equilibrium pressures in the deposition zone are plotted vs. the seed temperature for equal incoming pressures of AsCl_3 and PCl_3 . Two things are most interesting. First again the high phosphine pressure, which dominates until about 1060°K , second the behavior of the growth rates (denoted as GR GaAs and GR GaP and weighted with their molecular weight) while the growth rate of GaP stays nearly constant, the GaAs growth rate reveals a steep slope at higher temperatures. This behavior may be explained by the temperature dependence of Eq. [3]. In any case this phenomenon causes mostly the strong variation of the GaP solid concentration vs. deposition temperature shown in Fig. 3. According to this figure it should be possible to grow pure GaP crystals within a vapor containing arsenic at elevated temperatures. Further-

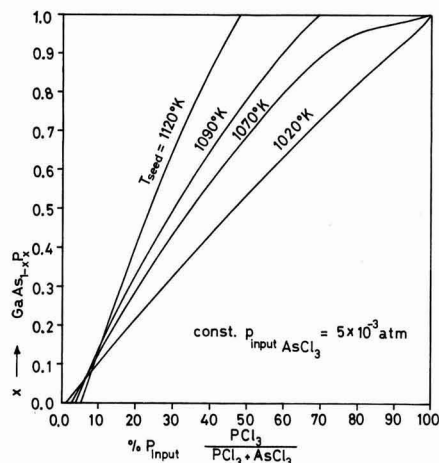


Fig. 4. $\text{GaAs}_{1-x}\text{P}_x$ deposit composition vs. the phosphorus percentage of the PCl_3 and AsCl_3 input gases.

more in this region a GaAs seed will be etched away. Figure 4 illustrates the solid composition x vs. the percentage of PCl_3 to AsCl_3 in the input gas. Once more the strong influence of the seed temperature can be seen. This is not in agreement with Finch and Mehal (11) who observed a straight relationship for temperatures between 775° and 820°C , but they used only one source, which is not comparable with the calculations done here. Stewart (16) with the AsH_3 , PH_3 , HCl/Ga system at $\sim 780^\circ\text{C}$ obtains a GaP solid concentration of 0.4 employing a P to As input vapor percentage of 28.6%, a point that fits exactly the calculations here. He also observed a composition variation by varying the HCl flow. This may be explained by Eq. [20], if the equilibrium over the source is not reached completely, i.e., the ratio p_{HCl} to p_{GaCl} changes. Finally it can be seen from Fig. 3 and 4 that for very low-phosphorus input concentrations no GaP is forming, in fact in this range all the available phosphorus is used in forming phosphine.

The great influence of the substrate temperature on the composition of the deposit diminishes with the higher concentrations of the input gases, indicated in Fig. 5. Here the solid composition approaches exactly the same value given by the ratio of the input gas concentration.

Conclusions

Applying the AsCl_3 , PCl_3 , Ga, H_2 system for growth of $\text{GaAs}_{1-x}\text{P}_x$ mixed crystals the seed temperature influences strongly the solid composition of the crystal. This dependence becomes smaller with increasing input concentrations of the trichlorides. Within the reactor a relatively high, at any case, a nonnegligible vapor pressure of phosphine exists. Above about 920°C , variation of the source temperature has little influence on the growth conditions.

Acknowledgment

The author would like to thank Professor W. G. Oldham for his encouragement, his valuable criticism of the manuscript, and his helpful discussions.

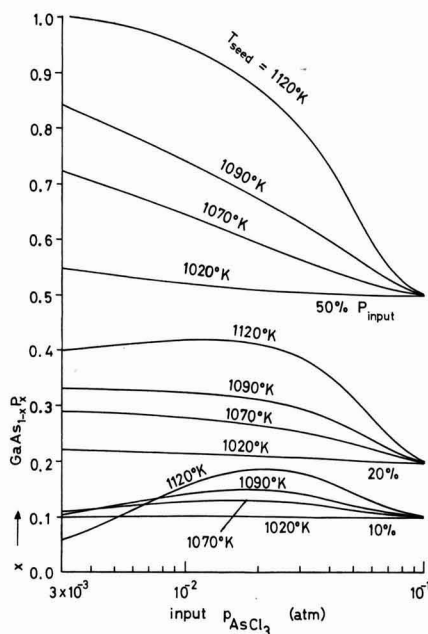


Fig. 5. $\text{GaAs}_{1-x}\text{P}_x$ deposit composition vs. the AsCl_3 input pressure for several phosphorus percentages and several deposit temperatures.

Manuscript submitted Aug. 20, 1971; revised manuscript received ca. Dec. 6, 1971.

Any discussion of this paper will appear in a Discussion Section to be published in the December 1972 JOURNAL.

REFERENCES

1. M. G. Craford, W. O. Grovesand, and M. J. Fox, *This Journal*, **118**, 355 (1971).
2. R. R. Fergusson and T. Gabor, *ibid.*, **111**, 585 (1964).
3. D. Effer, *ibid.*, **112**, 1020 (1965).
4. A. Boucher and L. Hollan, *ibid.*, **117**, 932 (1970).
5. D. W. Shaw, *ibid.*, **117**, 683 (1970).
6. D. J. Kirwan, *ibid.*, **117**, 1572 (1970).
7. L. C. Luther and D. D. Roccasecca, *ibid.*, **115**, 850 (1968).
8. H. Seki, H. Eguchi, and T. Gejo, *Jap. J. Appl. Phys.*, **10**, 39 (1971).
9. H. Seki and H. Araki, *ibid.*, **6**, 1414 (1967).
10. W. G. Oldham, *J. Appl. Phys.*, **36**, 2887 (1965).
11. W. F. Finch and E. W. Mehal, *This Journal*, **111**, 814 (1964).
12. R. W. Haisty, L. G. Baily, and R. C. Sangster, First Interim Report for Development of GaAsP Graded-Band-Gap-Base Transistor Structures, Texas Instruments Report No. 08-64-154 (1964).
13. D. T. J. Hurle and J. B. Mullin, Proc. Internat. Conf. on Crystal Growth, Boston, p. 241 (1966).
14. JANAF, "Interim Thermochemical Tables," Vol. 5, Thermal Laboratories, Dow Chemical Co.
15. D. Huber, Proc. Internat. Conf. on Heterojunctions, Budapest, I, p. 195 (1971).
16. C. E. E. Stewart, *J. Crystal Growth*, **8**, 269 (1971).
17. V. S. Ban, *This Journal*, **118**, 1473 (1971).

A Cross-Hatch Pattern in $\text{GaAs}_{1-x}\text{P}_x$ Epitaxially Grown on GaAs Substrate

Seigo Kishinô, Masahiko Ogirima, and Kazuhiro Kurata*

Central Research Laboratory, Hitachi Ltd., Kokubunji, Tokyo, Japan

ABSTRACT

A cross-hatch pattern which appears on the surface of $\text{GaAs}_{1-x}\text{P}_x$ epitaxially grown on the GaAs substrate was studied by x-ray diffraction techniques. The origin of this structure was determined by x-ray diffraction topography to be a misfit dislocation array aligned along lines perpendicular to each other in the layer of graded composition. The composition profile normal to the wafer was also determined by electron microprobe analyses. Furthermore, the growth mechanism of the aligned dislocations was proposed from the fact that aligned dislocations enable a considerable reduction in the curvature of the wafer which is due to the lattice mismatch between the $\text{GaAs}_{1-x}\text{P}_x$ epitaxial layer and the GaAs substrate. The $\text{GaAs}_{1-x}\text{P}_x$ wafer having the cross-hatch pattern was determined to be high in quality from the half width of the rocking curve.

$\text{GaAs}_{1-x}\text{P}_x$ ($x \leq 0.4$) is one of the most promising materials currently being utilized for visible injection electroluminescence. The efficiency of emission which is in the red at room temperature is high because the bandgap is direct, and the material can be made high conductivity n- or p-type. At present, $\text{GaAs}_{1-x}\text{P}_x$ has a technological advantage over $\text{Ga}_{1-x}\text{Al}_x\text{As}$ and GaP for display application because relatively large areas of $\text{GaAs}_{1-x}\text{P}_x$ wafer suitable for use in electroluminescent devices can be readily obtained by the vapor phase growth technique. An understanding of the role of the crystal defects in the growth mechanism is important in order to control and improve the efficiency.

The crystal defects such as dislocations and stacking faults which may be important in determining the properties of vapor phase epitaxially grown $\text{GaAs}_{1-x}\text{P}_x$ wafers have been described by a number of investigators (1-5).

This paper deals with the relationship between the cross-hatch pattern (6) and the dislocations and specifically with the origin of the dislocations and their effects on the perfection of epitaxially grown $\text{GaAs}_{1-x}\text{P}_x$ wafer.

Experimental

The $\text{GaAs}_{1-x}\text{P}_x$ crystals doped with Te were epitaxially grown on GaAs substrate in an open-tube system using Ga, PCl_3 , As, and H_2 (7). Hydrogen, purified by Pd diffusion, was metered into the system through two

flowmeters. One of them was connected to PCl_3 bubblers while the other controlled further dilution of the displaced PCl_3 vapors. The diluted vapors then passed over Ga feed material. The alloy composition was controlled by the temperature of arsenic source. Mechanically and chemically polished surfaces of (100) oriented seeds were used.

Typical operating conditions were: gallium temperature, 900°C; seed temperature, 810°C; PCl_3 bubbler (0°C) flow rate, 40 cc/min; dilution hydrogen flow rate, 160 cc/min; temperature gradient at the substrate, 10°C/cm; arsenic source temperature, 430°C.

To minimize strains and crystal imperfections due to lattice mismatch between $\text{GaAs}_{1-x}\text{P}_x$ and GaAs, a layer of continuously graded composition was grown before growing a thick layer of uniform composition. The layer of graded composition was grown by controlling the temperature of arsenic source in the range of 430°-530°C. The thickness of the epitaxially grown layer was usually 100 μm and the growth rate was usually 25 $\mu\text{m/hr}$. As mentioned later, the optimum thickness of the graded composition was 20-40 μm . So the temperature of arsenic source was varied from 530° to 430°C continuously for 1 hr in the initial period of epitaxial process. When the thickness of the graded composition layer was out of the range of the optimum thickness described above, the cross-hatch pattern was hardly observed.

Dislocations were observed by the Lang method, in which $\text{AgK}\alpha_1$ radiation from microfocus x-ray equipment was used, with the use of two kinds of specimens. (i) One specimen was the epitaxially grown $\text{GaAs}_{1-x}\text{P}_x$

* Electrochemical Society Active Member.

Key words: $\text{GaAs}_{1-x}\text{P}_x$, x-ray diffraction, x-ray topography, dislocation, epitaxial layer.

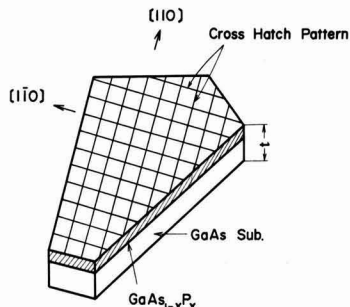


Fig. 1. The shape of specimen 1 from which x-ray topographs were taken.

wafer 50-100 μm thick including the GaAs substrate, which was reduced to 100 μm thickness by mechanical polishing with 2000 mesh carborundum and chemical etching with an etch solution of $3\text{H}_2\text{SO}_4:1\text{H}_2\text{O}:1\text{H}_2\text{O}_2$. The schematic diagram of the specimen is shown in Fig. 1. (ii) The wafer composed of the epitaxially grown $\text{GaAs}_{1-x}\text{P}_x$ layer and the GaAs substrate was angle lapped at 5° in order to reveal dislocations in the substrate, the graded composition layer, and the constant composition layer. This specimen was also etched with a similar etch solution described above after mechanical lapping. The schematic diagram of the specimen is shown in Fig. 2(a) and (b).

The composition profiles of the phosphorus content in the $\text{GaAs}_{1-x}\text{P}_x$ layer normal to the GaAs substrate were examined by electron microprobe analyses. A particular precaution was taken to detect the variation of the phosphorus content in the graded composition layer. At the same time variation of the arsenic content was observed throughout the depth of the wafer for supporting the results.

The difference in lattice parameter between the $\text{GaAs}_{1-x}\text{P}_x$ epitaxial layer and the GaAs substrate causes a pronounced curvature in the structure. This curvature was measured by an x-ray diffraction technique (8). Prior to measurement, the thickness of the GaAs substrate was kept constant because the curvature of the wafer depends on the thickness of the substrate. In this case (400) $\text{CuK}\alpha_1$ diffraction in the Bragg case was used. The x-ray beam was incident not at the $\text{GaAs}_{1-x}\text{P}_x$ epitaxial layer but at the GaAs substrate because the measured results were governed by the compositional variation when the epitaxially grown $\text{GaAs}_{1-x}\text{P}_x$ surface was used for measurement.

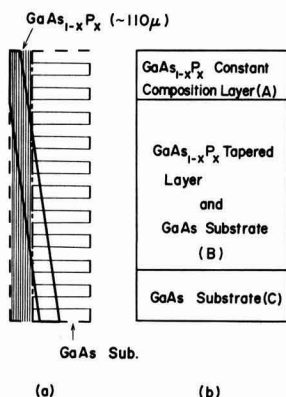


Fig. 2. The angle lapped specimen which is composed of the $\text{GaAs}_{1-x}\text{P}_x$ constant composition layer, the graded composition layer, and the GaAs substrate, respectively. (a) and (b) show the section and the plane figures, respectively.

The perfection of the epitaxially grown $\text{GaAs}_{1-x}\text{P}_x$ wafer was also examined by an x-ray diffraction technique (9) in which two different wavelengths of x-ray beams (10) were used for diffraction. X-ray radiation of two wavelengths, $\text{CuK}\alpha_1$ and $\text{CuK}\beta_1$, were used. With the use of this method the phosphorus content, assuming that Vegard's law of solid solutions holds for this GaAs-GaP system (11), was also examined. The perfection of the $\text{GaAs}_{1-x}\text{P}_x$ wafer was examined from the half width of the rocking curve which was the diffracted intensity vs. a small fraction of the incident angle $\Delta\theta$ around the Bragg angle.

The efficiency of junction luminescence was measured by silicon photocells at 10 A/cm² of diode current.

Results and Discussion

X-ray topographs were taken from the specimen whose surface revealed the cross-hatch pattern as shown in Fig. 3, and they are shown in Fig. 4(a), (b), (c), (d), and (e). The shape of the specimen in this

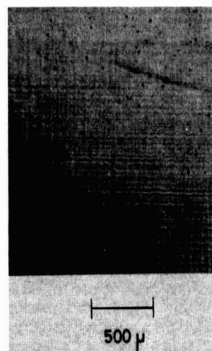


Fig. 3. The optical photograph of the surface which reveals the cross-hatch pattern.

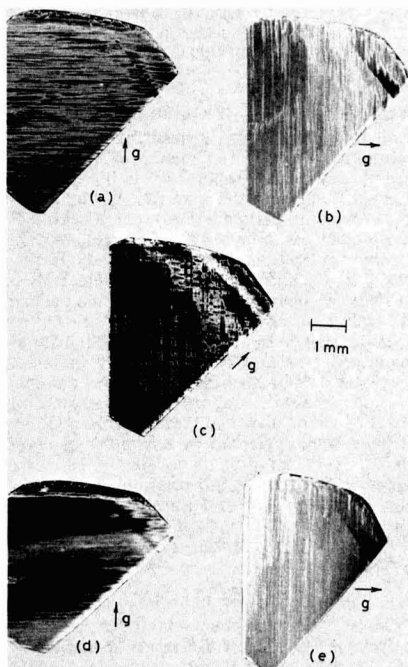


Fig. 4. X-ray topographs of the specimen 1. (a), (b), (c), (d), and (e) show topographs from (220), ($2\bar{2}0$), (040), (111), and ($1\bar{1}1$) diffractions, respectively.

case is shown in Fig. 1. The type of the dislocation observed here is similar to one observed by Ewing (2), that is, dislocation networks are aligned along $[011]$ and $[0\bar{1}1]$ directions with $\frac{1}{2}a[011]$ and $\frac{1}{2}a[0\bar{1}1]$ Burger's vectors, respectively. X-ray topographs using the diffraction vectors $[111]$ and $[1\bar{1}1]$ are also reproduced in Fig. 4(d) and (e) for determining the Burger's vector more accurately. The diffraction planes used here are shown in the pole figure, Fig. 5. From these x-ray topographs and the pole figure, Burger's vector of two kinds of the dislocations aligned along lines perpendicular to each other were determined exactly to be $\frac{1}{2}a[011]$ and $\frac{1}{2}a[0\bar{1}1]$. The image contrast criterion (12), for $[011]$ and $[0\bar{1}1]$ dislocations only, is violated in some local areas. Therefore, where contrast violations exist, dislocations may have screw component or interact each other. Detailed examinations were not established at this stage.

X-ray topographs of a similar specimen are also reproduced in Fig. 6(a) and (b), in which the shape of the specimen is shown in Fig. 2(a) and (b). From these x-ray topographs it is obvious that dislocation densities in both the GaAs substrate and the constant composition layer, are rather low, while the aligned dislocations gather in the graded composition layer of the specimen. This may be the result of the large lattice mismatch between the GaAs substrate and the $\text{GaAs}_{1-x}\text{P}_x$ layer.

An x-ray topograph was also taken from the specimen whose surface does not reveal the cross-hatch pattern as shown in Fig. 7. The shape of the specimen is similar to that shown in Fig. 1. In this case there is the irregular form in the image of dislocations because

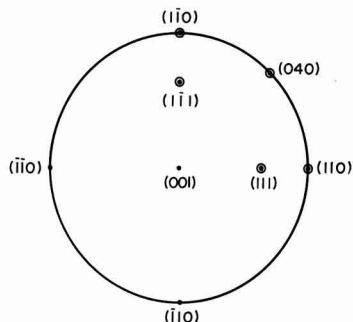


Fig. 5. The pole figure of specimen 1 from which x-ray topographs were taken.

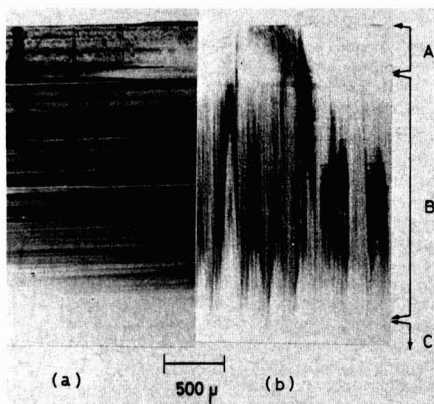


Fig. 6. X-ray topographs of specimen 2 in which signs A, B, and C correspond to those in Fig. 2(b). (a) and (b) are topographs from (220) and $(\bar{2}20)$ diffractions, respectively.

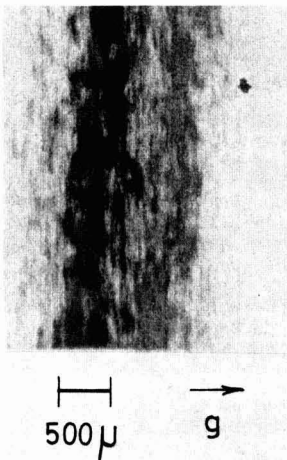


Fig. 7. X-ray topograph obtained by (220) diffraction from the $\text{GaAs}_{1-x}\text{P}_x$ wafer whose surface does not reveal the cross-hatch pattern.

dislocations could not align along the line. The lattice strain might be too large to be compensated by making the misfit-dislocations array in the graded composition layer because of the sudden change of the phosphorus content as discussed later.

Variation of the phosphorus contents in the growth layer were measured by electron microprobe analyses as shown in Fig. 8(a) and (b). Figures 8(a) and (b) are obtained from the specimens which reveal, respectively, the cross-hatch pattern clearly and obscurely on the surface of the epitaxial $\text{GaAs}_{1-x}\text{P}_x$ wafer. It is fairly obvious that the aligned dislocations were introduced in the graded composition layer when the epitaxial $\text{GaAs}_{1-x}\text{P}_x$ wafer has the graded composition layer of $40\text{ }\mu\text{m}$ width as shown in Fig. 8(a).

If the lattice mismatch between the $\text{GaAs}_{1-x}\text{P}_x$ epitaxial layer and the GaAs substrate causes the curvature and no dislocations are introduced to compensate the elastic strain, the curvature ρ can be obtained from the following equation (13-15)

$$\rho = \frac{6 \left[t_0 \sum_{j=1}^N t_j \left(\frac{d_0 - d_j}{d_0} \right) + \sum_{i=1}^N \sum_{j>i}^N t_i t_j \left(\frac{d_i - d_j}{d_0} \right) \right]}{\left[\sum_{j=0}^N t_j \right]^3} \quad [1]$$

where t_0 , $t_i(j)$, $d_i(j)$, and d_0 are the thickness of the substrate, the thickness of the $i(j)$ th epitaxial layer, the lattice parameter of the $i(j)$ th epitaxial layer, and the lattice parameter of the substrate, respectively. Figure 9 shows schematically the representative epitaxial layer which is composed of eight different layers. The result calculated by Eq. [1] is shown in Fig. 10 with a solid line. In this case the thickness of the substrate is $400\text{ }\mu\text{m}$ and the epitaxial layer is composed of eight layers each of $5\text{ }\mu\text{m}$ thickness but each layer has different phosphorus contents. The curvature of the wafers measured by an x-ray diffraction technique (8) are also shown in Fig. 10 in order to make correlation to the visibility of the cross-hatch pattern. Signs \circ , Δ , and \times show the wafers which reveal the cross-hatch pattern clearly, rather clearly, and obscurely, respectively. It is evident that the curvature of the wafer in which the cross-hatch pattern is visible clearly is always smaller than that of the wafer in which the cross-

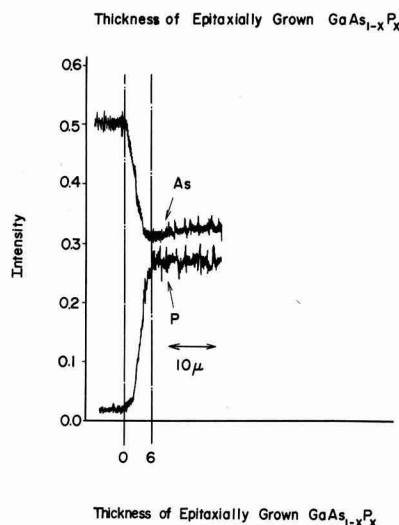
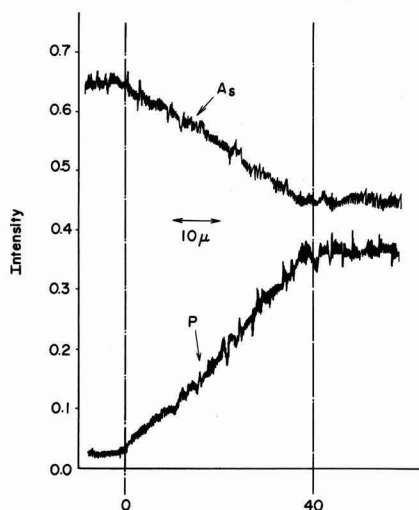


Fig. 8. Variation of the phosphorus content by electron microprobe analyses in the graded composition layer. (a, above) and (b, below) show the result from the $\text{GaAs}_{1-x}\text{P}_x$ wafer which reveals and does not reveal the cross-hatch pattern on the surface, respectively.

hatch pattern is obscure. In this experiment a convex configuration as viewed from the GaAs side was observed. It is also to be noted that the sign of the curvature is always reverse of those observed by Saul (16). From the result that a concave configuration was observed as viewed from the GaAs side, Saul determined that the thermal mismatch was larger than the lattice mismatch between the GaP epitaxial layer and the

Table I. Mole fraction of GaP (x)

Specimen No.	From the lattice parameter	From the energy gap
1	0.417	0.42
2	0.404	—
3	0.421	0.42
4	0.382	0.38
5	0.372	0.37
6	0.389	—
7	0.380	0.38
8	0.476	—
9	0.427	0.40

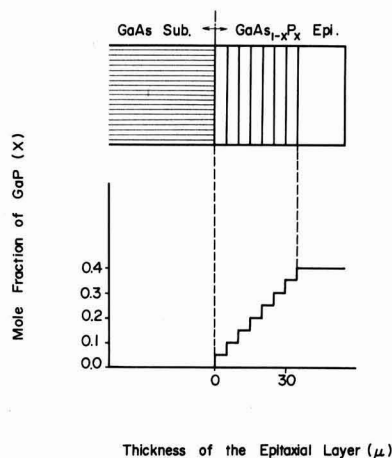


Fig. 9. The model from which the curvature of the $\text{GaAs}_{1-x}\text{P}_x$ wafer was calculated. It is postulated that the misfit dislocations are not introduced.

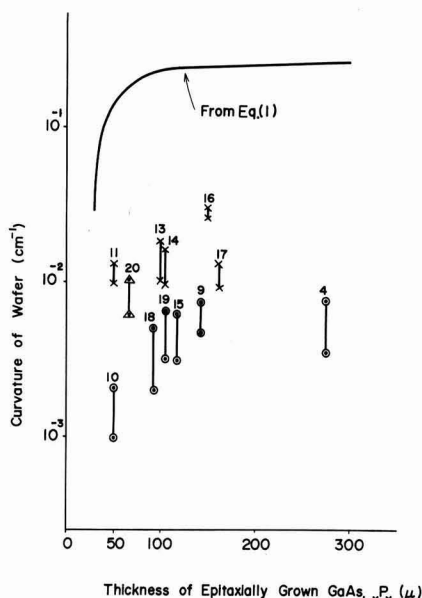


Fig. 10. Relation between the visibility of the cross-hatch pattern and the curvature. Signs \circ , Δ , and \times show the $\text{GaAs}_{1-x}\text{P}_x$ wafer which reveal the cross-hatch pattern clearly, rather clearly, and obscurely, respectively. Solid line shows the result obtained from Eq. [1].

GaAs substrate. However, the present observed sign of the curvature supports that the stress due to lattice mismatch considerably exceeds the stress due to differential thermal contraction in the $\text{GaAs}_{1-x}\text{P}_x$ -GaAs system, as Abrahams *et al.* have already reported (5).

Contrary to the result by Saul, it is reasonable to assume from our results that the wafer bends progressively during growth, if the lattice mismatch is not perfectly compensated by misfit dislocations. From the experimental results described above, a model of the formation mechanism of the misfit dislocation array in this case is proposed as shown in Fig. 11 and 12, where (a) and (b) show the plane and the section views of the wafer, respectively. Figures 11 and 12 show the model of the wafer in which the cross-hatch pattern is visible and obscure, respectively.

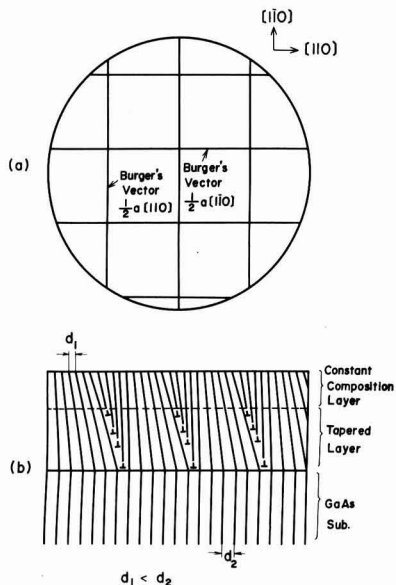


Fig. 11. The model of crystal growth in which dislocations are lined up in the graded composition layer. (a) and (b) show the plane and the section figures, respectively.

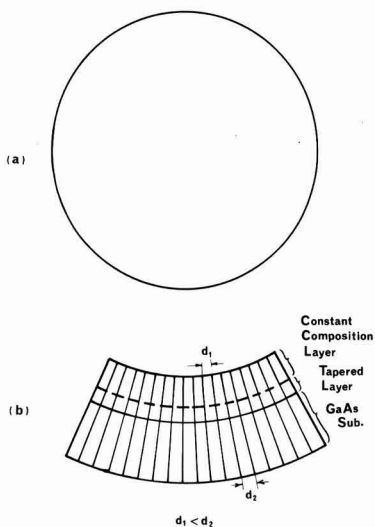


Fig. 12. The model of the crystal exhibiting curvature due to lattice mismatch between the $\text{GaAs}_{1-x}\text{P}_x$ layer and the GaAs substrate. (a) and (b) show the plane and the section figures, respectively.

When the cross-hatch pattern is visible, the aligned dislocations observed by x-ray topography may be composed of many dislocations which line up as if the small grain boundary is constructed. If the dislocations are arranged as shown in Fig. 11, the lattice mismatch at the graded composition layer can be compensated easily by the dislocations induced. The cross-hatch pattern visible on the surface, however, does not show the aligned dislocations themselves, because the aligned dislocations are existing in the graded composition layer and they are materially reduced in number on the surface as shown in Fig. 6. The cross-hatch pattern may be formed on the surface because growth rate variation of the epi-

taxial layer are initiated by: (i) the impurity concentration difference at the dislocation lines in the graded composition layer, and (ii) the screw components of some parts of the aligned dislocations which are visible in the x-ray topographs shown in Fig. 4.

If this model is used, it is easy to explain that the curvature of the wafer is small when the cross-hatch pattern is clearly visible. When the gradient of the phosphorus content is very sharp as shown in Fig. 8(b), the formation of the lattice strain during growth may be too large to be released by introducing the aligned dislocation array. In such a case dislocations may have a random distribution and consequently the cross-hatch pattern cannot be visible.

The phosphorus contents at the surfaces of the epitaxially grown $\text{GaAs}_{1-x}\text{P}_x$ wafers are shown in Table I with the results obtained from the energy gap data. The phosphorus contents were obtained from the lattice parameters which were measured from the differences of the two peak profiles obtained from (511) $\text{CuK}\alpha_1$ and (400) $\text{CuK}\beta_1$ diffractions (10, 17). The representative peak profiles are shown in Fig. 13 and 14 in which the upper and the lower profiles show (400) $\text{CuK}\beta_1$ and (511) $\text{CuK}\alpha_1$ diffractions, respectively. Figures 13 and 14 show the peak profiles obtained from the specimens where the cross-hatch pattern is clearly visible and obscure, respectively. This peak profile is a kind of the rocking curve, although the incident beam is not perfectly monochromatic. The

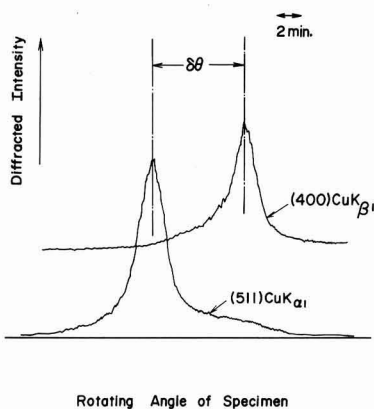


Fig. 13. Rocking curves of the $\text{GaAs}_{1-x}\text{P}_x$ wafer whose surface reveals the cross-hatch pattern clearly. In this figure $\delta\theta$ shows the lattice parameter, and the half width shows the perfection of the crystal.

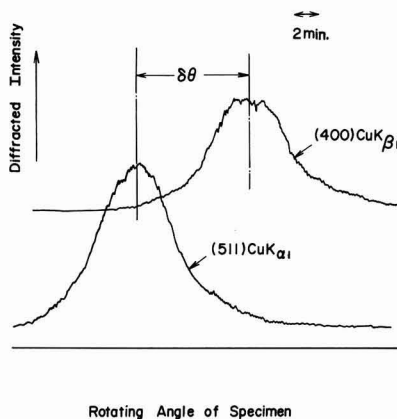


Fig. 14. Rocking curves of the $\text{GaAs}_{1-x}\text{P}_x$ wafer whose surface does not reveal the cross-hatch pattern.

perfection of the crystal, however, can be similarly estimated from the half width of the peak profile shown in Fig. 13 and 14. The half width of the peak profile of the epitaxially grown $\text{GaAs}_{1-x}\text{P}_x$ wafer, with a clearly revealed cross-hatch pattern, is comparable to that of the GaAs substrate in which dislocation density is lower than 10^4 cm^{-2} . The half width of the peak profile is broader, as shown in Fig. 14, when the wafer does not reveal the cross-hatch pattern. This high quality of the epitaxially grown $\text{GaAs}_{1-x}\text{P}_x$ wafer could be also expected from the model shown in Fig. 11 because the aligned dislocations need not be introduced at the surface.

When light emitting diodes are fabricated from the wafer which reveals the cross-hatch pattern clearly, the electroluminescent efficiency is higher by about 50% than that of the wafer with no cross-hatch pattern.

Conclusions

1. A cross-hatch pattern on the surface of $\text{GaAs}_{1-x}\text{P}_x$ layer appears when the graded composition layer of $20 \sim 40 \mu\text{m}$ width is formed in the initial period of epitaxial process.

2. The origin of the cross-hatch pattern was determined by x-ray topography to be a misfit dislocation array aligned along lines perpendicular to each other in the graded composition layer.

3. The curvature of the $\text{GaAs}_{1-x}\text{P}_x$ wafer is small or large depending on whether the cross-hatch pattern is clear or obscure on the surface.

4. When the cross-hatch pattern is visible on the surface, the $\text{GaAs}_{1-x}\text{P}_x$ wafer is high in quality on the surface because the half width of the rocking curve is as narrow as that of the GaAs substrate.

5. These results support the proposed model with regard to the growth mechanism of the aligned dislocation array.

Acknowledgment

The authors wish to express their appreciation to Dr. H. Kusumoto for his encouragement, to Mr. Y. Taguchi for making electron microprobe analyses, and also to Messrs. Y. Ono, K. Homma, and Y. Kekoin for their helpful support. The authors gratefully acknowledge the assistance of Mr. S. Aoki in carrying out part of the experimental portion of this study.

Manuscript submitted Aug. 13, 1971; revised manuscript received Nov. 22, 1971.

Any discussion of this paper will appear in a Discussion Section to be published in the December 1972 JOURNAL.

REFERENCES

1. C. M. Wolfe, C. J. Nuese, and N. Holonyak, Jr., *J. Appl. Phys.*, **36**, 3790 (1965).
2. R. E. Ewing and D. K. Smith, *ibid.*, **39**, 5943 (1968).
3. G. B. Stringfellow and P. E. Greene, *ibid.*, **40**, 502 (1969).
4. M. S. Abrahams, L. R. Weisberg, C. J. Buiocchi, and J. Blanc, *J. Mater. Sci.*, **4**, 223 (1969).
5. M. S. Abrahams, L. R. Weisberg, and J. J. Tietjen, *J. Appl. Phys.*, **40**, 3754 (1969).
6. R. A. Burmeister, Jr., G. P. Pighini, and P. E. Greene, *Trans. TMS-AIME*, **245**, 587 (1969).
7. M. Ogirima and K. Kurata, *Japan J. Appl. Phys.*, **10**, 1474 (1971).
8. T. Tokuyama, Y. Fujii, Y. Sugita, and S. Kishino, *ibid.*, **6**, 1252 (1967).
9. J. K. Howard and R. D. Dobrott, *This Journal*, **113**, 567 (1966).
10. S. Kishino, *Japan J. Appl. Phys.*, **10**, 1113 (1971).
11. M. Rubenstein, *This Journal*, **112**, 426 (1965).
12. A. R. Lang, *J. Appl. Phys.*, **30**, 1748 (1959).
13. S. Timoshenko, *J. Opt. Soc. Am.*, **11**, 23 (1925).
14. R. H. Saul, *J. Appl. Phys.*, **40**, 3273 (1969).
15. T. Mitsuishi, S. Kishino, and A. Noda, *Japan J. Appl. Phys.*, **10**, 1734 (1971).
16. R. H. Saul, *This Journal*, **115**, 1184 (1968).
17. S. Kishino, To be published.

The Equilibrium Pressure of N_2 over GaN

C. D. Thurmond* and R. A. Logan

Bell Telephone Laboratories, Incorporated, Murray Hill, New Jersey 07974

ABSTRACT

The equilibrium pressures of N_2 over GaN and Ga are not known. Values of the heat and entropy of formation of GaN are proposed that give equilibrium N_2 pressures as a function of temperature. Experiments reported in the literature lead to consistent upper and lower bounds to the calculated curve but do not define its position very well. We report the results of three different types of experiments, using NH_3 in H_2 , which tighten the bounds to the equilibrium curve: the NH_3 pressures at which GaN could be seen to form from Ga were upper limits; the pressure of NH_3 in the exiting gas stream after reaction with Ga gives a qualified upper limit; and of greatest importance, we believe, are the measurements of the NH_3 pressures generated when H_2 is passed over GaN. These latter pressures are lower limits to the equilibrium curve and are believed to lie close to it. The experimental results are in agreement with the calculated equilibrium pressures of N_2 over GaN and Ga obtained using the heat of formation of GaN based on the measurements of Hahn and Juzo, and Mah and the assumption that the entropy and heat capacity of GaN are the same as those of ZnO.

The temperature and nitrogen pressure ranges over which GaN is stable are not known. It is believed that very high pressures of nitrogen are required to form GaN from Ga(l) at temperatures above 1000°C (1). At lower temperatures a skin forms on the Ga(l), presumably GaN, impeding further reaction (1). NH_3 at a pressure 1 atm reacts with Ga(l) above 1050°C

(2), any reaction below this temperature also is impeded by a thin GaN film.

It has been suggested (3) that the decomposition of GaN(s) may lead to polymeric nitride molecules, $(\text{GaN})_x$. Transport experiments offered some support for the existence of such species (4) but no evidence of polymeric nitride molecules was obtained from mass-spectrometer studies (5, 6).

It is the purpose of this paper to calculate the equilibrium pressure of N_2 over GaN and Ga as a function

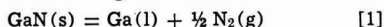
* Electrochemical Society Active Member.

Key words: gallium nitride, equilibrium, decomposition pressure, heat of formation, entropy.

of temperature from a heat of formation in the literature and an estimated entropy and heat capacity of GaN. It will then be shown that this curve is consistent with previously reported experimental results which, however, do not define the position of the curve very well, and is in good agreement with our experimental results which do define the position much more sharply.

Equilibrium Pressure Curve

The equilibrium between GaN, liquid Ga, and N₂ is described by the following reaction



The equilibrium N₂ pressure is related to the standard free energy change of reaction [1] by the expression

$$\frac{1}{2} RT \ln P_{\text{N}_2} = -\Delta G^\circ_1 \quad [2]$$

It has been assumed that GaN has a narrow non-stoichiometry range and that the solubility of GaN in Ga is negligible. The standard free energy change, in turn, is related to the free energy of formation of GaN, and the heat and entropy of formation by

$$-\Delta G^\circ_1 = \Delta G^\circ_{\text{GaN}} = (\Delta H^\circ_{\text{GaN}} - T\Delta S^\circ_{\text{GaN}}) \quad [3]$$

The heat of formation of GaN at 298°K given in the NBS tables (7), is -26.4 kcal. It is based on the heat of combustion of GaN measured by Hahn and Juza (2) and the heat of combustion of Ga measured by Mah (8). The entropy of formation of GaN has not been measured, but following a suggestion by Sime and Margrave (4), we have estimated the entropy of GaN by assuming it is the same as that of ZnO which is the same crystal structure (wurtzite), is isoelectronic, and is of nearly the same molecular weight. The entropy of ZnO at 298°C is 10.43 eu (9). In addition, we have assumed that the heat capacity of GaN is the same as that of ZnO (10). With the available thermodynamic information on liquid Ga (11) and on N₂ (12), the heat and entropy of formation of GaN can be obtained, from which the equilibrium N₂ pressure can be calculated.

The equilibrium N₂ pressure, estimated as described above, has been plotted in Fig. 1. At temperatures higher than 800°C, the calculated N₂ pressure is greater than 1 atm; at 1200°C, the pressure is 1000 atm, reaching 100,000 atm at about 1700°C.

Comparison with Available Experimental Data

The calculated N₂ pressures can be compared to related observations reported by a number of workers.

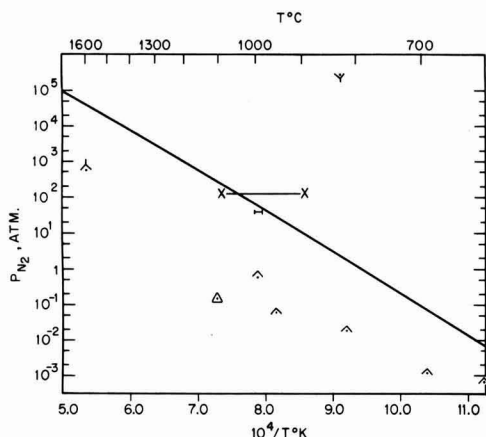
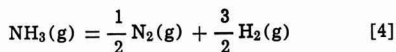


Fig. 1. Pressure of N₂ over GaN(s)-Ga(l), ($\log P_{\text{N}_2}$ vs. $10^4/T$). The solid line is calculated. Lower limits to the equilibrium curve: Δ MacChesney and co-workers (13), ∇ Juza and Hahn (2), \circ Lorenz and Binkowski (14). Upper limits to the equilibrium curve: \times Maruska and Tietjen (16), \times Logan and co-workers (17), --- Lorimer and co-workers (18).

The most direct information comes from a measurement by MacChesney and co-workers (13) who found that at 1600°C, under a pressure of about 700 atm of N₂, GaN decomposed. This observation gives a lower limit to the equilibrium curve and, as plotted in Fig. 1, is consistent with the calculated curve. Lorenz and Binkowski (14) studied the rate of decomposition of GaN over the temperature range from 600° to 1000°C. They noted the highest N₂ pressures reached at the time the rate measurements were discontinued. These pressures also represent lower limits to the equilibrium curve and are plotted in Fig. 1. The five points are consistent with the estimated curve. Juza and Hahn (15) provide one point obtained by the same method.

The three sets of measurements just cited represent all of the information found in the literature that could be used to give lower limits to the equilibrium curve. There are three reports, however, on the reaction of NH₃ with Ga that can also be used to give upper limits to the equilibrium curve.

The first of these is by Maruska and Tietjen (16) who prepared GaN by passing GaCl and NH₃ in H₂ over a sapphire substrate at 825°C and at atmospheric pressure. The fact that GaN was formed in the presence of 0.14 atm of NH₃ and 0.86 atm of H₂ permits an upper limit to the equilibrium N₂ pressure over GaN and liquid Ga to be calculated. It is equal to the N₂ pressure corresponding to equilibrium with the NH₃ and H₂ pressures used in growing the GaN layers. This equilibrium is described by the equation



which leads to the following expression relating the partial pressures to the equilibrium constant, K_4

$$P_{\text{N}_2}^{1/2} = K_4 \frac{P_{\text{NH}_3}}{P_{\text{H}_2}^{3/2}} \quad [5]$$

The value of K_4 obtained from the JANAF Tables (12) is about 3×10^3 at 825°C, leading to a value for the N₂ pressure of 3×10^5 atm. This point is plotted in Fig. 1 and lies far above the calculated equilibrium curve. It is, of course, consistent with this curve but does not help appreciably to define it.

Recently, two additional observations related to the reaction of NH₃ with Ga provide upper limits to the equilibrium N₂ pressure curve. Logan and co-workers (17) have added N to GaP by passing NH₃ in H₂ over liquid Ga containing dissolved phosphorus from which GaP was grown by cooling. It was found that the N concentration in GaP was proportional to the NH₃ pressure and there was an NH₃ pressure above which good crystal growth of GaP was not possible. Lorimer and co-workers (18), in applying Logan's technique to the addition of N to GaP, observed that the concentration of N saturated. That is, crystal growth could be obtained with some difficulty at higher NH₃ pressures but no further increase in N concentration was found. They observed altered crystal growth and reported that GaN was formed.

The NH₃ pressures in H₂, at which GaN was formed from Ga in the studies of N doping of GaP, were in the range of 10^{-3} atm at temperatures of approximately 1000°C. Equivalent N₂ pressure can be calculated from the conditions used and have been plotted in Fig. 1. It is seen that Logan's point straddles the calculated curve, while Lorimer's point lies slightly below the curve. The temperature range of each of these points corresponds to the range over which GaP epitaxial layers were grown.

It is concluded that the equilibrium N₂ pressure curve lies on or below the curve plotted in Fig. 1 but not lower than 1 to 2 decades below it.

We have attempted to obtain improved upper limits to the equilibrium N₂ pressures by finding the mini-

mum NH_3 pressures at which GaN can be formed from Ga. Additional information has been obtained from the NH_3 pressure leaving the tube after reaction with Ga. The discovery that high pressures of NH_3 , relatively speaking, are generated by the reaction of H_2 with GaN, has led to greatly improved lower limits to the equilibrium curve.

Experimental

Most of the GaN used in these studies was grown by reacting a partial pressure of NH_3 in H_2 with Ga at 1150°C in a furnace system that was previously used (17) to grow epitaxial layers of N-doped GaP. The furnace was modified so that an easily replaceable quartz liner was used inside the main quartz furnace tube. The NH_3 pressure ranged from 10^{-3} to 5×10^{-2} atm in H_2 , with gas flow rates of 70 to 280 cc/min and a tube ID of 2.1 cm. The GaN formed was in the form of small, black, irregularly shaped crystals with dimensions ranging from 75 to 500 μm . The other GaN studied was composed of smaller crystals, gray in color, grown by Zetterstrom (19) by reacting Ga with 1 atm of NH_3 at 1100°C in a similar furnace. To separate out the very small crystals formed in this growth, the batch was repeatedly rinsed with agitation and the larger crystals retained. They ranged in size from 20 to 100 μm . In all cases, the GaN was separated from the Ga growth melt by digestion in aqua regia.

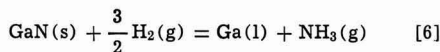
P_{NH_3} was determined by causing the NH_3 - H_2 furnace exhaust gas to bubble through a 4 cm high column of HCl solution of known column and normality, and containing methyl red indicator. The normality of the HCl solution was adjusted to give a convenient titration time of 5 to 10 min so that the uncertainty (a few seconds) in the determination of the time of the indicator color change was negligible. The contribution of the indicator to the normality of the solution became significant ($\sim 10\%$) only at the lowest normality used ($2 \times 10^{-5}\text{N}$). Since the furnace gas flowed at constant rate rather than at constant pressure, the gas flow rate was unaffected by the small change in gas pressure due to the titration. The NH_3 dissolution into the HCl solution was complete as evidenced by doubling the column height of the HCl solution by the addition of H_2O , without changing the titration time for a given gas mixture. P_{NH_3} is determined from the gas flow rate and the titration time of the solution of known volume and normality.

The system was routinely monitored for evidence of dissociation of NH_3 in the furnace. A clear indication of dissociation was the variation of P_{NH_3} with furnace temperature. Dissociation could be made negligible by use of new quartz furnace liner which was cleaned in deionized H_2O and alcohol prior to use. No bake-out was necessary. The main quartz furnace tube caused NH_3 dissociation after continual use for one to three months. The dissociation correlated with devitrification of the tube and was rectified by replacement with a new quartz tube. It was observed that the low oxygen (and water vapor) level in the furnace ambient was essential to achieve negligible NH_3 dissociation. The pyrolytic graphite crucibles used both in the formation and dissociation studies of GaN did not cause NH_3 decomposition and the crucible weight loss during an experiment was less than 1 mg.

The NH_3 pressure from the reaction of H_2 with GaN was determined by inserting 1-13g of GaN crystals, contained in a pyrolytic graphite crucible, into the furnace, at uniform temperature and with a pure H_2 ambient. The NH_3 pressure in the exit gas was monitored continuously and increased to a constant value in about 60 min. This is about the time required to achieve a constant value of the NH_3 pressure when H_2 and NH_3 are mixed and passed through the empty tube. Typically, about 25 w/o (weight per cent) of the GaN dissociated, leaving Ga, in heating times which ranged from 16 hr at 925°C to 4 hr at 1175°C .

Results and Discussion

In the work reported here, the reaction of NH_3 with Ga has been used to give upper limits to the N_2 equilibrium pressure over GaN and Ga. The reaction H_2 with GaN has been used to give lower limits to the N_2 equilibrium pressure. Both of these reactions can be described by the following equation



The equilibrium constant relates the equilibrium pressures of NH_3 and H_2 in the equation

$$\frac{P_{\text{NH}_3}}{P_{\text{H}_2}^{3/2}} = K_6 \quad [7]$$

It has again been assumed that the nonstoichiometry range of GaN is small and that the solubility of GaN in Ga is negligible. The pressure ratio $P_{\text{NH}_3}/P_{\text{H}_2}^{3/2}$ is also given in Eq. [5] from which the following equations can be written

$$\frac{P_{\text{NH}_3}}{P_{\text{H}_2}^{3/2}} = K_6 = \frac{P_{\text{N}_2}^{1/2}}{K_4} \quad [8]$$

Since K_4 can be obtained from the JANAF Tables (12), the values of $P_{\text{NH}_3}/P_{\text{H}_2}^{3/2}$ can be calculated for the equilibrium N_2 pressures given in Fig. 1. They are plotted in Fig. 2 as $\log P_{\text{NH}_3}$ vs. $10^4/T$ and give the solid line. This is the reverse of the calculations made in the section on Comparison with Available Experimental Data to obtain upper limits to the equilibrium N_2 line from NH_3 and H_2 pressures at which GaN formed.

The minimum NH_3 pressures in H_2 at which GaN was seen to form when passed over liquid Ga, have been plotted in Fig. 2 and are upper limits to the equilibrium NH_3 pressure. Measurements made independently by Ilegems (20) are included.

An independent upper limit to the equilibrium curve is obtained from the pressure of NH_3 leaving the reaction tube. This pressure is always less than that entering. Measurements of the NH_3 pressure after NH_3 in H_2 was passed through clean empty tubes showed that negligible decomposition occurred. However, it cannot be ruled out that some decomposition of NH_3 to H_2 and N_2 occurred during the reaction with liquid

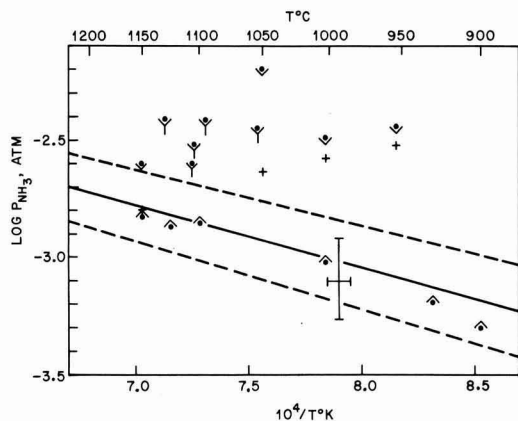


Fig. 2. Pressure of NH_3 in H_2 over GaN(s)-Ga(l), ($\log P_{\text{NH}_3}$ vs. $10^4/T$). The solid line is equivalent to the calculated line of Fig. 1. The dashed lines represent a ± 1 kcal uncertainty in the free energy of formation of GaN. ∇ Minimum NH_3 pressures at which GaN was seen to form from Ga. \triangle NH_3 pressures in exiting gas stream. ∇ Independent measurements by M. Ilegems of minimum input NH_3 pressures at which GaN was seen to form from Ga. \triangle NH_3 pressures from the reaction of H_2 with GaN. —|— Lorimer and co-workers (18).

Ga. At lower NH₃ pressures where GaN is not formed, the NH₃ pressure decreased about 10% in passing through the reaction zone. We have taken this to be an estimate of the extent of dissociation of NH₃ in these experiments. The lowest observed exit pressures at several temperatures where GaN was formed are plotted in Fig. 2. These points may be too low by as much as 10%.

All of the upper limit points plotted in Fig. 2 are consistent with the calculated equilibrium line except for one point at the highest temperature which, however, agrees within the 10% estimated uncertainty.

We have found that impressively high pressures of NH₃ are generated when H₂ is passed over GaN. The measured pressures set lower limits to the equilibrium curve. The points plotted in Fig. 2 are the highest pressures measured at each temperature and are steady-state values achieved after about 1 hr of heating. They all are consistent with the estimated line and fall well within the band resulting from the 1 kcal uncertainty in the heat of formation of GaN.

The dependence of the NH₃ pressure on flow rate and sample area suggested that equilibrium was near. The observed NH₃ pressure increased ~20% as the flow rate decreased from 280 to 70 cc/min and a similar small increase was observed when the GaN area increased by a factor of 5. The GaN area was varied by changing the weight of crystals of a given mesh size. The points plotted in Fig. 2 are the highest NH₃ pressures measured at each temperature, obtained with the largest GaN area and smallest flow rate used at each temperature. It is possible, however, that equilibrium pressures were not attained because appreciable catalytic decomposition of NH₃ may have taken place in the hot tube down stream from the GaN. This possibility restrains us from accepting these as equilibrium measurements. They are, however, completely acceptable lower limits to the equilibrium curve.

On the basis of the lower and upper limiting points that we have obtained, we conclude that the equilibrium pressure of NH₃, given by the calculated line of Fig. 2, is consistent with all of the experimental information available as is true also for the pressure of N₂ given by the line of Fig. 1. The data of Lorimor *et al.* (18), plotted in Fig. 1 in terms of N₂ pressure, is plotted in Fig. 2 in terms of NH₃ pressure and provides an upper limit, with the indicated uncertainty in the NH₃ pressure. The data of Fig. 2 are summarized in Table I.

These results, then, are consistent with a heat of formation of GaN of -26.4 ± 1.0 kcal (2, 7, 8) and an entropy and heat capacity the same as those of ZnO

Table I. Pressure of NH₃ in H₂ over GaN(s)-Ga(l) vs. T°C (data of Fig. 2)

Experimental conditions	T°C	P _{NH₃} (10 ⁻³ atm)
(✓) Minimum input NH ₃ pressure at which GaN was seen to form from Ga	1150 1050 1000 950	2.5 7.0 3.2 3.5
(+) NH ₃ pressures in exiting gas stream	1150 1050 1000 950	1.58 2.30 2.60 3.00
(Ÿ) Independent measurements of M. Ilegems of minimum input NH ₃ pressures at which GaN was seen to form from Ga	1130 1105 1100 1095 1055	3.85 3.04 2.51 3.81 3.49
(—) Lorimor and co-workers (18)	1000-985	1.48
(^) NH ₃ pressures from the reaction of H ₂ with GaN	1149 1125 1100 1002 929 899	1.48 1.34 1.39 0.905 0.645 0.501

Table II. Heat and free energy of formation of GaN(s)

T, °K	Ga(s,l) + ½N ₂ (g) = GaN(s)	ΔG°, kcal
298	26.40 ± 1.0	-33.04 ± 1.0
900	26.94	-4.06
1000	26.74	-1.54
1100	26.52	-0.97
1200	26.29	+3.46
1300	26.04	+5.93
1400	25.78	+8.39
1500	25.52	+10.81
1600	25.24	+13.21

(9, 10). The heats of formation and free energies of formation used to calculate the curve of Fig. 1 are given in Table II.

Two criteria have been used to determine limits to equilibrium conditions: GaN must decompose or it must form. The fact that GaN may appear not to decompose under certain conditions does not give useful information since the rate of decomposition may be too slow to be observed. Similarly, Ga may appear not to react with N₂ or NH₃ and H₂ when, in fact, the reaction may be impeded by a thin surface nitride film. Conclusions can be drawn when changes occur; they cannot be drawn when changes do not occur.

We have taken advantage of two slow kinetic processes in order to closely approximate the equilibrium properties of GaN: the slow rate of decomposition of GaN to form Ga and N₂, and the slow rate of decomposition of NH₃ to N₂ and H₂. The iron-nitrogen system has been studied under somewhat related circumstances and equilibrium nitrogen pressures up to hundreds of thousands of atmospheres have been deduced from the much lower NH₃ pressures in H₂ used to control the nitrogen chemical potential (21).

Summary

The equilibrium pressure of N₂ over GaN and liquid Ga has been calculated from available thermodynamic functions with the assumption that the entropy and heat capacity of GaN are the same as those of ZnO. The calculated equilibrium pressure curve was found to be consistent with a number of reported experiments although the spread between upper and lower bounds was rather broad. NH₃ pressures in H₂, which were found to be the maximum pressures at which GaP, doped with N, could be grown (17, 18), gave equivalent nitrogen pressures in agreement with those calculated.

Three different experimental methods are reported here which were used to narrow the gap between upper and lower limits to the equilibrium pressure curve. In one method the minimum NH₃ pressure at which GaN could be seen to form on the surface of Ga was measured. Another consisted of measuring the NH₃ partial pressure in H₂ after passing over liquid Ga. Of importance is the last method, which appears to give results near equilibrium, where measurement was made of the NH₃ pressure generated by the reaction of H₂ with GaN. All measurements were consistent with the calculated equilibrium curve.

Acknowledgments

We are indebted to H. G. White for his assistance in performing these experiments. We thank M. Ilegems for helpful comments and for the experimental data used in Fig. 2 and R. B. Zetterstrom for providing the GaN crystals grown by reacting Ga with 1 atm of NH₃.

Manuscript submitted Sept. 22, 1971; revised manuscript received Dec. 27, 1971.

Any discussion of this paper will appear in a Discussion Section to be published in the December 1972 JOURNAL.

REFERENCES

1. A. Rabenau, "Compound Semiconductors," Vol. 1, p. 174, R. K. Willardson and H. L. Goering, Eds.

- tors, Reinhold Publishing Corp., New York (1962).
2. H. Hahn and R. Juza, *Z. Anorg. u. allgem. Chem.*, **244**, 111 (1940).
3. J. L. Margrave and P. Sthapitanonda, *J. Phys. Chem.*, **59**, 1231 (1955).
4. R. J. Sime and J. L. Margrave, *ibid.*, **60**, 810 (1970).
5. Z. A. Munir and A. W. Searcy, *J. Chem. Phys.*, **42**, 4223 (1965).
6. R. C. Schoonmaker, A. Buhl, and J. Lemley, *J. Phys. Chem.*, **69**, 3455 (1965).
7. D. D. Wagman, W. H. Evans, V. B. Parker, I. Halow, S. M. Bailey, and R. H. Schumm, *Nat. Bur. Std., Tech. Note* 270-3 (1968).
8. A. D. Mah, *Nat. Bur. Mines. Rept.* 5965 (1962).
9. K. K. Kelley, *Bur. Mines. Bull.* 477 (1950).
10. K. K. Kelley, *Bur. Mines. Bull.* 548 (1960).
11. D. R. Stull and G. C. Sinke, "Thermodynamic Properties of the Elements," *Am. Chem. Soc.* (1956).
12. D. R. Stull, Project Director, "JANAF Thermochemical Tables," (1967).
13. J. B. MacChesney, P. M. Bridenbaugh, and P. B. O'Conner, *Mater. Res. Bull.*, **5**, 783 (1970).
14. M. R. Lorenz and B. B. Binkowski, *This Journal*, **109**, 24 (1962).
15. R. Juza and H. Hahn, *Z. Anorg. u. allgem. Chem.*, **244**, 133 (1940).
16. H. P. Maruska and J. J. Tietjen, *Appl. Phys. Letters*, **15**, 327 (1969).
17. R. A. Logan, H. G. White, and W. Wiegmann, *Solid State Electron.*, **14**, 55 (1971).
18. O. G. Lorimer and L. R. Dawson, *This Journal*, **118**, 292C (1971).
19. R. B. Zetterstrom, *J. Mater. Sci.*, **5**, 1102 (1970).
20. M. Ilegems, Private communication.
21. L. S. Darken and R. W. Gurry, "Physical Chemistry of Metals," p. 378, McGraw Hill Publishing Co., New York (1953).

Kinetics of Manganeseo-Wustite Scale Formation on Iron-Manganese Alloys

P. Mayer* and W. W. Smeltzer**

Department of Metallurgy and Materials Science, McMaster University, Hamilton, Ontario, Canada

ABSTRACT

The oxidation kinetics of Fe-Mn alloys containing up to 59 w/o (weight per cent) Mn exposed to carbon dioxide-carbon monoxide atmospheres at 1000°C have been determined by a thermogravimetric technique. The experimental conditions were chosen in order that the reaction would lead to formation of a single-phase manganeseo-wustite [(Fe Mn)O] scale. The rate of parabolic oxidation decreased and the manganese content in wustite increased with increasing manganese content in the alloy. A diffusion model, which is based on equations derived by Wagner for metal diffusion through the scale under chemical activity gradients, leads to a description of the scaling kinetics, and to evaluations for the self-diffusion coefficients of iron and manganese and the nonstoichiometry as a function of the manganese content in wustite.

A major objective of this investigation was to contribute to the understanding of the oxidation mechanism of binary alloys when a single-phase superficial oxide scale is formed as the major reaction product with only a relatively small degree of oxide precipitation in an internal oxidation zone. In recent papers, Wagner (1), and Coates and Dalvi (2) have advanced methods for calculating the distribution of cations in a metal-conducting scale growing by parabolic kinetics. The Fe-Mn-O system could meet these requirements since Foster and Welch (3) have demonstrated that wustite and manganous oxide form a continuous solid solution.

In the present work, the oxidation kinetics, morphological development, and composition of the wustite scale on Fe-Mn alloys exposed to CO₂-CO atmospheres at 1000°C were investigated under conditions to insure formation of (FeMn)O scale by parabolic kinetics. These results are used in combination with diffusional and thermodynamic properties of this ternary system and the above-mentioned theoretical considerations to gain an insight into the mechanism of scale growth and the metal transport properties of the oxide solid solution.

Experimental

The alloys were prepared from electrolytic iron, 99.96 w/o (weight per cent) pure, and manganese, 99.99 w/o

pure. Approximately 300g of material were placed in the melting chamber of a nonconsumable arc furnace with a tungsten electrode operating under argon. In order to prevent any long range segregation, each charge was melted, inverted, and then remelted until a total of four melting operations had been completed. It was then sealed in a quartz tube filled with argon and annealed for five days at 1000°C. The compositions of the alloys are given in Table I.

Alloy buttons were hot-rolled at 800°C to a thickness of 4 mm. The surface of each sheet was cleaned by pickling in dilute hydrochloric acid and by abrasion using 600 grit silicon carbide paper. The sheets were then cold-rolled to a thickness of approximately 2.5 mm. Test specimens, 10 × 10 × 2 mm, were prepared from these sheets by mounting plates in Bakelite and metallographically polishing all surfaces to 1μ diamond abrasive using kerosene as lubricant. After removal from the Bakelite mountings, specimens were washed with petroleum ether and stored in dried acetone.

Table I. Chemical analyses of Fe-Mn alloys based on manganese determinations

Alloy number in text	Nominal composition of alloys, w/o Mn	w/o Mn in alloys
1	0	0.0
2	1	0.93
3	12	12.33
4	27	27.35
5	32	31.83
6	59	58.94

* Electrochemical Society Student Associate.

** Electrochemical Society Active Member.

Key words: Fe-Mn alloys, parabolic oxidation, manganeseo-wustite scale.

An Ainsworth, Type RV, continuous recording microbalance was used to determine the weight change of a specimen exposed to a reaction atmosphere. The thermogravimetric assembly has been described previously (4); the temperature of the reaction zone in the furnace was controlled to $\pm 2^\circ\text{C}$. A specimen was lowered into the reaction atmosphere which was maintained at a flow rate of 0.6 cm/sec to prevent thermal segregation of the gases. Carbon dioxide, 99.95 v/o (volume per cent) pure, was dried by passage through columns containing magnesium perchlorate, reduced copper oxide, and activated alumina. Carbon monoxide, minimum purity of 99.6 v/o, was purified by passage through columns containing magnesium perchlorate and ascarite.

Oxidized specimens were mounted in epoxy, cold, self-setting resin, the final polishing being done with 1μ diamond abrasive and kerosene as lubricant. Chemical analyses were carried out by means of a Cameca electron-probe microanalyzer operating at 15 keV and a specimen current 50-80 nanoA. This instrument was calibrated as described previously (5). Standards for checking the calibration curves for the alloys were alloys of several known compositions. The calibration procedure for the wustite phase could be verified only for pure wustite. The Debye-Scherrer method of x-ray analysis using Co K α radiation was used to determine oxide crystallographic structures.

Results

The dependences of the oxidation kinetics on the compositions of the exposed alloys and on the CO_2/CO ratios in the reaction atmospheres are illustrated by the parabolic plots [(oxygen weight gain/unit area) 2 vs. (time)] in Fig. 1 and 2. These curves, which were reproducible within $\pm 15\%$, are of the same shape as those obtained for pure iron due to a relatively smaller reaction rate before onset of parabolic kinetics (6, 7). The plots in Fig. 3 illustrate that the values of the

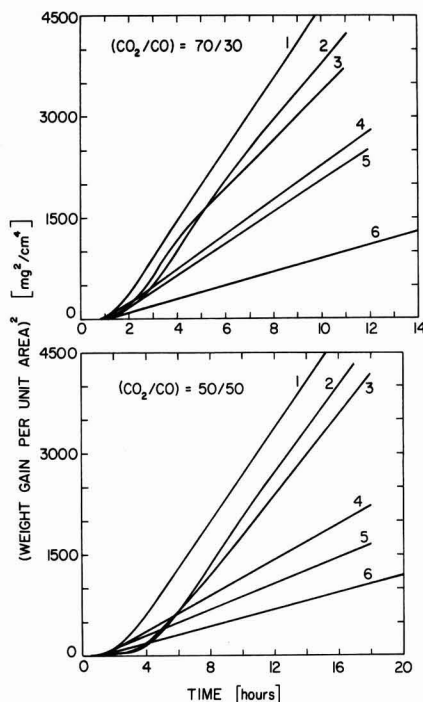


Fig. 2. Parabolic plots for the oxidation kinetics of Fe-Mn alloys in 70/30 and 50/50 CO_2 -CO atmospheres at 1000°C . The numbers on curves correspond to the alloy composition designations in Table I.

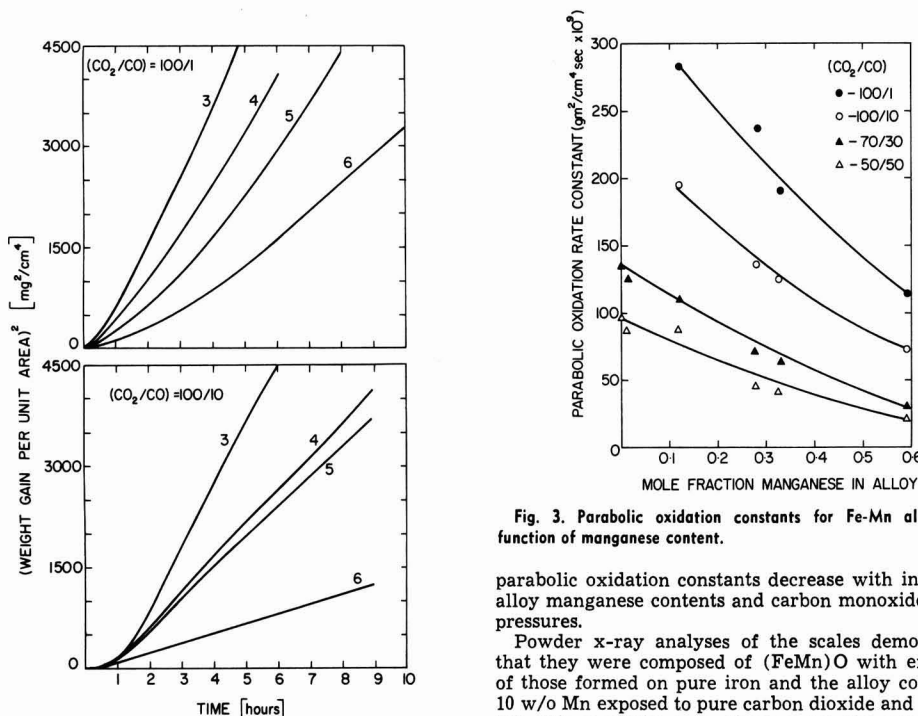


Fig. 3. Parabolic oxidation constants for Fe-Mn alloys as a function of manganese content.

Fig. 1. Parabolic plots for the oxidation kinetics of Fe-Mn alloys in 100/1 and 100/10 CO_2 -CO atmospheres at 1000°C . The numbers on curves correspond to the alloy composition designations in Table I.

parabolic oxidation constants decrease with increasing alloy manganese contents and carbon monoxide partial pressures.

Powder x-ray analyses of the scales demonstrated that they were composed of $(\text{FeMn})\text{O}$ with exception of those formed on pure iron and the alloy containing 10 w/o Mn exposed to pure carbon dioxide and a 100/10 CO_2 -CO atmosphere. In these cases, the presence of magnetite was identified. The mean lattice parameter of the single-phase scales, Fig. 4, exhibited a variation linearly related to the MnO content of the oxide solid solution.

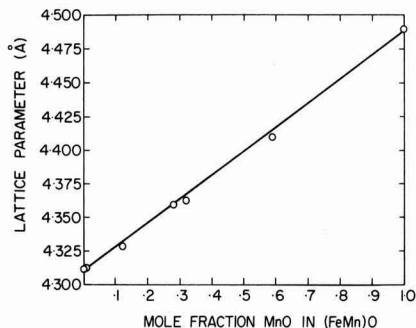


Fig. 4. Mean lattice parameter of the (FeMn)O solid solution scales.

A scale was essentially compact and uniformly thick during its growth. There was a small degree of internal oxidation but the penetration depth of its zone was negligible compared to the thickness of the scale. These features are illustrated by the micrographs in Fig. 5 and 6. Internal oxidation for the Fe-1% Mn alloy was so small that its penetration distance could not be determined at the comparatively high magnification of 1000X. In the alloy of highest manganese content, 59 w/o Mn, the penetration depth of oxide never exceeded 10% of the scale thickness. The only oxide identified in both the scales and internal zones was (FeMn)O.

Manganese concentration profiles in the scales and alloy substrates of specimens exposed to the various atmospheres for different intervals in the regions of parabolic oxidation were determined by the electron microprobe technique. The profiles shown in Fig. 7 and 8 for the alloy specimens containing 1 and 59 w/o Mn illustrate typical distributions for the alloying element between the metal and scale. The manganese concentrations were determined to within $\pm 0.5\%$ of

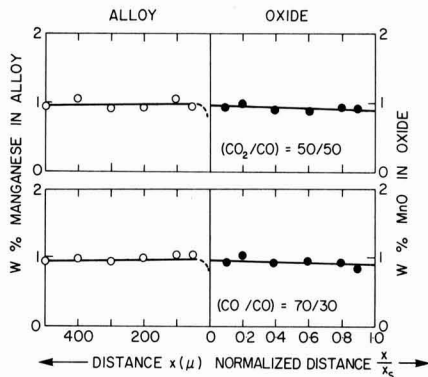


Fig. 7. Manganese concentration profiles in the metal and (FeMn)O scale of an Fe-1 w/o Mn alloy oxidized at 1000°C. The scale thickness has been standardized to $y = x/x_s$.

the determined values. Manganese depletion from an alloy was small, the depletion distance never extending inward more than 50μ from the alloy interface. The change of manganese concentration across a scale was small but the decrease in its concentration toward the outer surface gave rise to a linear manganese gradient. These gradients in the scales formed on the different alloys under various atmospheric conditions are recorded in Table II. Values are also tabulated for the MnO concentration at the outer scale surfaces as determined by extrapolation of the linear profiles.

Discussion

Oxidation of the alloys gave rise predominately to a scale consisting of a solid solution of the divalent oxides. An oxidation curve exhibited a region of slow reaction before onset of parabolic kinetics due to interfacial control at the scale/gas boundary. Oxidation in all atmospheres, nevertheless, proceeded at significant

Fig. 5. The metallographic cross-sections and the interfaces between the scales formed on Fe-1 w/o Mn and Fe-12 w/o Mn alloys exposed to a 70/30 CO_2 -CO atmosphere at 1000°C (X130).

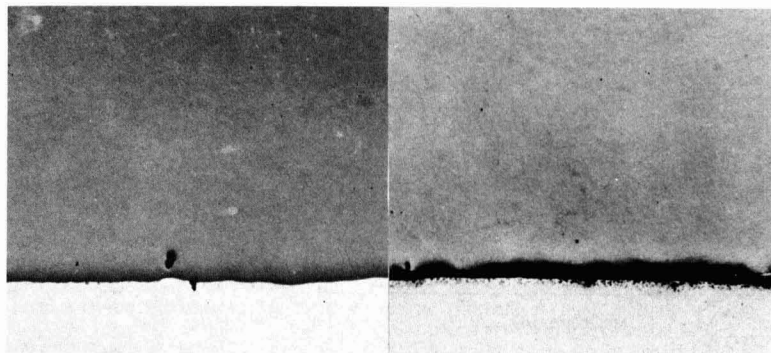
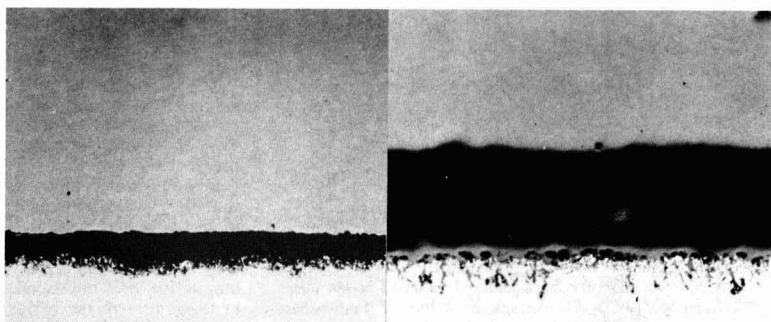


Fig. 6. The metallographic cross sections and the interfaces between the scales formed on Fe-32 w/o Mn and Fe-59 w/o Mn alloys exposed to a 70/30 CO_2 -CO atmosphere at 1000°C (X130).



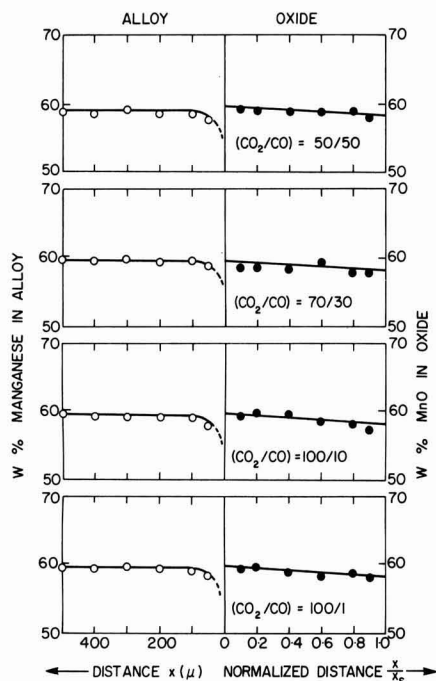


Fig. 8. Manganese concentration profiles in the metal and (Fe,Mn)O scale of an Fe-59 w/o Mn alloy oxidized at 1000°C. The scale thickness has been standardized to $y = x/x_s$.

rates because of rapid metal diffusion within the oxide layer of large nonstoichiometry. The metal ratio in the scale was only slightly different from that in the alloy inasmuch as manganese, the less noble metal, entered the scale preferentially. Further, the ratio of manganese to iron in the scale decreased with distance from the alloy interface due to manganese exhibiting a smaller mobility than iron in the oxide solid solution. The metal gradients, nevertheless, attained a steady-state value during the stages of parabolic oxidation kinetics (Fig. 7 and 8).

The occurrence of parabolic kinetics governing growth of a relatively uniform scale with steady-state gradients in the oxide solid solution and the absence of an appreciable degree of internal oxidation meet the requirements of the theoretical analysis carried out by Wagner (1) for the distribution of cations in a metal conducting scale. Accordingly, the equations that he has deduced may be utilized with the present experimental results to calculate the metal diffusion coefficients in (Fe,Mn)O and the dependence of its nonstoichiometry on the MnO content. His formalism is used and the reader is referred to the original paper for mathematical details.

The equations for the flux of metal cations through the scale are

$$j_{Fe}(eq) = -D_{Fe} \frac{1-\xi}{V} \frac{\partial \ln a_{Fe}}{\partial x} \quad [1]$$

$$j_{Mn}(eq) = -D_{Mn} \frac{\xi}{V} \frac{\partial \ln a_{Mn}}{\partial x} \quad [2]$$

when correlation effects are disregarded. In these equations, D is a metal self-diffusion coefficient, ξ/V is the local concentration of manganese in equivalents per unit volume, and a is a local activity. Since the parabolic scaling rate is supposed to be controlled by diffusion, the above relationships yield Equation 11 from Ref. (1) for the parabolic oxidation rate constant

$$D_{Fe} (1-\xi) \left(-\frac{\partial \ln a_{FeO}}{\partial \xi} \frac{d\xi}{dy} + \frac{z_{Fe}}{z_o} \frac{d \ln a_o}{dy} \right) + D_{Mn} \xi \left(-\frac{\partial \ln a_{MnO}}{\partial \xi} \frac{d\xi}{dy} + \frac{z_{Mn}}{z_o} \frac{d \ln a_o}{dy} \right) = k \quad [3]$$

where ξ is the mole fraction of MnO in the oxide and $y = x/x_s$ is the normalized scale thickness.

The Gibbs-Duhem equation for the oxide solid solution may be expressed as

$$(1-\xi) d \ln a_{FeO} + \xi d \ln a_{MnO} = 0 \quad [4]$$

Since the (Fe,Mn)O solid solution may be considered as nearly ideal (3)

$$\frac{d \ln a_{MnO}}{d \ln \xi} = 1 \quad [5]$$

Utilizing the equalities of the absolute valences, $z_{Fe} = z_{Mn} = z_o = 2$, we can express Eq. [3] upon substitution of [4] and [5] as

$$(1-p) \frac{d\xi}{dy} + \frac{d \ln a_o}{dy} [(1-\xi) + p\xi] = k^* \quad [6]$$

where

$$k^* = k/D_{Fe} \quad \text{and} \quad p = D_{Mn}/D_{Fe} \quad [7]$$

The metal profiles in the oxide scales which were stationary and very flat under conditions for parabolic oxidation could be approximated to a linear gradient

$$\xi = a + by \quad [8]$$

where, $a = \xi'$ is the mole fraction of MnO in the scale at its inner interface and b is the gradient across the oxide. On substitution of Eq. [7] and [8] into [6]

$$\frac{d \ln a_o}{dy} = \frac{k^* + (p-1)b}{1 + (p-1)\xi} \quad [9]$$

The second equation that may be utilized in this calculation from Wagner's analysis is the algebraic expression 39 in Ref. (1) for material balance at the outer interface for manganese

$$- \left[D_{Mn} \xi \left(\frac{d \ln a_{MnO}}{d \xi} \cdot \frac{d \xi}{dy} - \frac{d \ln a_o}{dy} \right) \right]_{y=1} = \xi'' k \quad [10]$$

On applying the same simplifications as in the previous case, the resulting expression is

Table II. The values for the linear gradient, b , and the concentration at the outer oxide interface, ξ'' , of MnO in scales on alloys exposed to CO₂-CO atmospheres. The values of b and ξ'' from Eq. [8] are expressed as MnO mole fractions

Oxidation atmosphere, v/o [CO ₂ /CO]	Alloy composition, w/o Mn									
	0.93		12.33		27.35		31.83		59.04	
	$b \times 10^4$	ξ''	$b \times 10^4$	ξ''	$b \times 10^4$	ξ''	$b \times 10^4$	ξ''	$b \times 10^4$	ξ''
50/50	-0.9	0.0092	-12.3	0.121	-27.0	0.271	-31.4	0.314	-59.2	0.584
70/30	-0.9	0.0091	-12.2	0.122	-27.8	0.270	-31.8	0.313	-53.3	0.584
100/10	—	—	-12.2	0.120	-27.8	0.269	-31.2	0.315	-59.1	0.586
100/1	—	—	-12.3	0.121	-27.7	0.271	-31.6	0.315	-59.0	0.584

$$k^* = p \frac{d \ln a_o}{dy} - \frac{pb}{\xi''} \quad [11]$$

Substitution of Eq [9] into [11] yields

$$k^* = \frac{pb}{(p-1)(1-\xi'')\xi''} \quad [12]$$

These equations allow one to express the cation self-diffusivities in the following forms

$$D_{Fe} = \frac{k\xi''(p-1)(1-\xi'')}{pb} \quad [13]$$

$$D_{Mn} = \frac{k\xi''(p-1)(1-\xi'')}{b} \quad [14]$$

where the parabolic rate constant k is related to the experimental rate constant k_p by the relation

$$k \left(\frac{\text{cm}^2}{\text{sec}} \right) = \frac{k_p}{2} \left(\frac{V}{16} \right)^2 \quad [15]$$

In order to carry out calculations for metal self-diffusion coefficients and oxide nonstoichiometry, certain assumptions and approximations must be made to evaluate the constant p . The manganese concentration in the scale at its outer surface for an alloy of given composition was not measurably dependent on the oxygen potential of the atmosphere over the CO_2/CO ratios examined (Table II). This result and in view of previous findings that the $(\text{FeMn})\text{O}$ solid solution is nearly ideal allows one to invoke the assumption by Wagner that the enrichment of a metal toward the outer surface in a scale (in this case iron) results from its larger mobility. Since there is general agreement that the transport of iron and manganese in FeO and MnO takes place by a vacancy mechanism (8, 10), we may approximate the self-diffusion coefficients to

$$D_{Mn} = D^{\circ}_{Mn} \frac{x_{\square}}{(x^{\circ}_{\square})_{\text{MnO}}}; \quad D_{Fe} = D^{\circ}_{Fe} \frac{x_{\square}}{(x^{\circ}_{\square})_{\text{FeO}}} \quad [16]$$

Here D° and x°_{\square} refer to the self-diffusivities and vacancy concentrations for the pure oxides, and x_{\square} refers to the vacancy concentration in $(\text{FeMn})\text{O}$. The ratio for the diffusivities in the oxide solid solution

$$\frac{D_{Mn}}{D_{Fe}} = \frac{D^{\circ}_{Mn}}{(x^{\circ}_{\square})_{\text{MnO}}} \bigg/ \frac{D^{\circ}_{Fe}}{(x^{\circ}_{\square})_{\text{FeO}}} \quad [17]$$

therefore essentially corresponds to the ratio of the jump frequencies for manganese and iron into an adjacent cation vacancy. Hence, the factor for manganese depletion across the scale may be regarded as corresponding to the mobility ratio of manganese to iron. That is

$$p = \frac{D_{Mn}}{D_{Fe}} = \frac{\xi''}{\xi'} \quad [18]$$

where from Eq. [8], $\xi''/\xi' = 1 + (b/a)$. A value of $p = 0.99 \pm 0.004$ is obtained using the results given in Table II.

The metal self-diffusivities are therefore related as follows

$$D_{Fe} = 1.01 D_{Mn} \quad [19]$$

The self-diffusion coefficient of iron may now be determined by substituting the value for p and the experimental values for the oxidation parameters in Eq. [12]. These results are presented in Fig. 9. Addition of MnO to FeO decreased the diffusion rate of both cations. The values for the self-diffusion coefficient of iron in wustite for oxygen potentials corresponding to 50/50

and 70/30 $\text{CO}_2\text{-CO}$ atmospheres may be evaluated from published results (8, 9). It is seen that the plots determined for this diffusivity in $(\text{FeMn})\text{O}$ under these conditions extrapolate to these limiting values.

Wustite and manganous oxide exhibit metal deficiencies associated with occurrence of cation vacancies (8, 10). The former oxide shows by far the largest range of nonstoichiometry at 1000°C and the magnitude of the self-diffusion coefficient for iron is directly proportional to nonstoichiometry (8, 9). We therefore express the dependence of the diffusivity on nonstoichiometry for the ternary oxide solid solution as

$$D_{Fe} = D^{\circ}_{Fe} \frac{x_{\square}}{(x^{\circ}_{\square})_{\text{FeO}}} = D^{\circ}_{Fe} \frac{(X-1)X^{\circ}}{(X^{\circ}-1)X} \quad [20]$$

and where X° and X are the ratios of the atomic fractions of oxygen to metal in pure wustite and the ternary oxide. Consequently, we may utilize diffusion evaluations from this investigation to determine the variation of $(\text{FeMn})\text{O}$ nonstoichiometry with increasing manganese content.

The results of these calculations using Eq. [20] are shown in Fig. 10. A comparison is also given between the calculated values and those determined by Voetzel

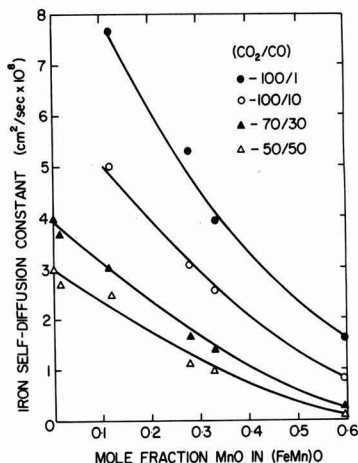


Fig. 9. Self-diffusion coefficient of iron in the $(\text{FeMn})\text{O}$ solid solution at 1000°C.

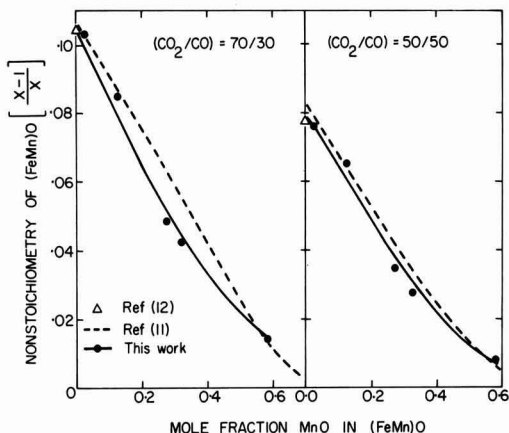


Fig. 10. Nonstoichiometry of the $(\text{FeMn})\text{O}$ solid solution at 1000°C. The dashed curve represents values obtained at 1100°C by Voetzel and Manenc (11) on equilibration of $(\text{FeMn})\text{O}$ in atmospheres undergoing the water-gas reaction. The values for pure FeO are those determined at 1000°C by Swaroop and Wagner (12).

and Manenc (11) and Swaroop and Wagner (12). The determinations from the first investigation are those obtained at 1100°C, but the investigators report that the nonstoichiometry was practically identical within the experimental precision at 1100° and 1000°C in atmospheres of constant CO₂/CO ratio (11). A very small variation in nonstoichiometry of pure wustite only occurs over the temperature range 1000°-1100°C, the nonstoichiometry at 1000°C being 2-3% smaller than that at 1100°C for atmospheres of constant CO₂/CO ratio. Within these limitations, it can be seen from Fig. 10 that there is good agreement between values obtained in this investigation and those in the literature. This consideration offers additional substantiation to the diffusion model and analysis adopted to describe the parabolic oxidation kinetics of the Fe-Mn alloys in CO₂-CO atmospheres.

Summary

The parabolic kinetics were determined for the formation of the manganese-wustite scale on Fe-Mn alloys exposed to CO₂-CO atmospheres at 1000°C. The morphological development and manganese gradients in the scale and metal demonstrated that the reaction proceeded under steady-state conditions. A model based on a diffusion analysis was shown to account for this kinetic behavior. It was possible by this analysis to evaluate the self-diffusion coefficients for iron and manganese and the nonstoichiometry of wustite as a function of manganese content. All of these parameters were found to decrease with increasing amounts of manganese dissolved in the (FeMn)O solid solution.

Acknowledgments

This research was carried out under the auspices of the National Research Council of Canada. The paper is based on the thesis submitted by P. Mayer to McMaster University in partial fulfillment of the requirements for the M. Eng. degree.

Manuscript submitted Sept. 16, 1971; revised manuscript received Jan. 12, 1972.

Any discussion of this paper will appear in a Discussion Section to be published in the December 1972 JOURNAL.

REFERENCES

1. C. Wagner, *Corrosion Sci.*, **9**, 91 (1969).
2. D. E. Coates and A. D. Dalvi, *J. Oxidation Metals*, **2**, 331 (1970).
3. P. K. Foster and A. J. E. Welch, *Trans. Faraday Soc.*, **52**, 1626 (1956).
4. R. Logani and W. W. Smeltzer, *J. Oxidation Metals*, **1**, 3 (1969).
5. A. D. Dalvi and W. W. Smeltzer, *This Journal*, **117**, 1431 (1970).
6. W. W. Smeltzer, *Acta Met.*, **8**, 377 (1960).
7. F. S. Pettit and J. B. Wagner, Jr., *ibid.*, **12**, 35 (1964).
8. L. Himmel, R. F. Mehl, and C. E. Birchenell, *Trans. AIME*, **197**, 827 (1953).
9. P. Hembree and J. B. Wagner, Jr., *ibid.*, **245**, 1547 (1969).
10. I. Bransky and N. M. Tallan, *This Journal*, **118**, 788 (1971).
11. J. Voeltzel and J. Manenc, *Mem. Sc. Rev. Metallurg.*, **64**, 8 (1967).
12. B. Swaroop and J. B. Wagner, Jr., *Trans. AIME*, **239**, 1215 (1967).

Electrical and Structural Properties of Metal Sulfides in Chloride Melts

The Systems Cu₂S-CuCl and FeS-FeCl₂

A. K. Garbee¹ and S. N. Flengas*

Department of Metallurgy and Materials Science, University of Toronto, Toronto, Ontario, Canada

ABSTRACT

The phase diagrams of the systems Cu₂S-CuCl and FeS-FeCl₂ and the densities of the liquid solutions have been measured over the permissible concentration and temperature ranges. Specific conductivities of the liquid mixtures have also been determined. The results indicate that the Cu₂S-CuCl solutions, for concentrations up to about 30 m/o (mole per cent) Cu₂S and temperatures below 1000°C, are essentially ionic conductors. Electronic conductance becomes evident for the more concentrated solutions. In the FeS-FeCl₂ solutions, ionic conductivity appears to be restricted to concentrations below 10 m/o FeS.

The thermodynamic calculations from the Cu₂S-CuCl phase diagram and the structural interpretation of the density measurements indicate that (Cu₂S)₂ dimers are present in dilute solutions. Further association occurs at higher concentrations and the formation of a continuous sulfide network appears to be related to the onset of electronic conduction. The solubility of copper metal in cuprous chloride is very low, and the conductivity of cuprous chloride, and of cuprous chloride-rich melts with cuprous sulfide, appears unaffected by the presence of copper metal. The addition of excess copper metal to molten cuprous sulfide, however, greatly increases its electrical conductivity.

Because the electrical conductivities of cuprous and ferrous sulfides are predominantly electronic in nature electrodeposition from the molten sulfides is not feasible. Electrolysis of solutions of Cu₂S in CuCl in the composition and temperature ranges of ionic behavior yielded copper metal at the cathode with high current efficiencies. Copper metal was also recovered selectively from solutions of a synthetic Cu-Fe-S matte dissolved in molten CuCl. It is also shown that FeS may be extracted from a synthetic FeS-Cu₂S matte by solvent extraction using molten CuCl at the appropriate temperatures. The extraction is attributed to an exchange reaction which converts the FeS component into the soluble ionic form of FeCl₂.

of metal sulfides in their corresponding metal chlorides exhibit interesting thermodynamic and electrical properties. Within specific temperature and composition ranges such solutions, rather dilute in metal sulfide, behave like ionic conductors. As the sulfide con-

Previous work in this laboratory (1-4) and elsewhere (5-9) has indicated that the molten solutions

* Electrochemical Society Active Member.

¹ Present address: Armco Steel Corporation, Middletown, Ohio 45042.

Key words: electrical conductivities, metal sulfides, metal chlorides, electrical properties of mattes, densities of metal sulfides.

tent and the temperature are increased electronic conductivity sets in, and the concentrated solutions behave more like the electronically conducting "pure" molten metal sulfide. It is evident that in the range of ionic behavior the recovery of metals from their sulfide ores by fused salt electrolysis should be feasible. In addition to this practical aspect, the factors determining the ionic to electronic transitions as well as the thermodynamic and structural properties of such high-temperature liquid semiconductors are of theoretical interest.

The sulfide solutions investigated previously in this laboratory include $\text{Ag}_2\text{S}-\text{AgCl}$ (1-2) and the $\text{PbS}-\text{PbCl}_2$ (3-4) binary systems. The present paper describes work on the thermodynamic and structural properties of the molten salt solutions of Cu_2S and of FeS in CuCl and FeCl_2 , respectively. The investigation includes the determination of the liquidus curves of the binary systems $\text{Cu}_2\text{S}-\text{CuCl}$ and $\text{FeS}-\text{FeCl}_2$, and measurements of densities and electrical conductivities in these systems. Finally, copper metal has been recovered by electrolysis of the $\text{Cu}_2\text{S}-\text{CuCl}$ solutions and from a synthetic matte containing Cu-Fe-S dissolved in molten CuCl .

Experimental

Preparation of materials.—Anhydrous CuCl was prepared from an aqueous solution of cupric chloride by reduction with sulfurous acid. The precipitated CuCl was washed with anhydrous alcohol and was dehydrated by treatment under vacuum for several hours, followed by melting and sublimation in a stream of dry hydrogen chloride gas. Chemical analysis of the product indicated a purity of better than 99.7% by weight.

Anhydrous FeCl_2 was prepared from reagent-grade hydrated FeCl_2 dried in a vacuum oven at 110°C for several days. This partly dehydrated solid was finely ground in a dry box filled with purified argon and then was treated with dry hydrogen chloride gas at about 500°C . The chemical analysis of this product corresponded to a 99.7% FeCl_2 content.

Pure Cu_2S was prepared by direct reaction between stoichiometric amounts of hydrogen-reduced copper metal powder and sulfur which had been previously purified by sublimation. The reactants were charged to quartz ampoules which were then flame-sealed under vacuum. The reaction was completed by heating at about 600°C for at least three days.

The chemical analysis of the reaction product indicated a Cu_2S compound in the composition range $\text{Cu}_{1.97}\text{S}$ to $\text{Cu}_{2.00}\text{S}$. The x-ray analysis was in excellent agreement with the established diffraction patterns for Cu_2S .

Stoichiometric FeS was also prepared by reacting equivalent quantities of hydrogen-reduced iron metal powder (99.999% by weight) with sublimed sulfur in double-wall glass ampoules which were sealed under vacuum. This type of reaction cell was found necessary as, during heating, volume changes within the reacting mixtures tended to crack the inner compartment. The reaction between iron and sulfur was highly exothermic and could be initiated simply by touching the walls of the reaction site with a gas flame. When this initial violent reaction had subsided, the reaction cell was transferred to a furnace and heated to 600°C for a period of six days. The chemical analysis of the reaction product indicated an FeS composition between $\text{FeS}_{1.00}$ and $\text{FeS}_{1.01}$. X-ray analysis was in excellent agreement with the established diffraction patterns for FeS .

All other chemicals used in the course of this investigation (NaCl , KCl , and BaCl_2) were of reagent grade and were dried in a vacuum oven at 110°C prior to use.

Materials handling and transfer were always conducted in a dry box filled with purified argon gas, fitted with an air-lock.

Thermal stability of systems investigated.—Because of the pronounced dependence of the electrical properties of Cu_2S and FeS on stoichiometry the thermal stability of Cu_2S , FeS , and of their solutions with CuCl and FeCl_2 , respectively, was investigated. This information was a prerequisite for designing appropriate freezing-point depression apparatus, the density measuring apparatus, and the cells for measuring the electrical conductivities. The arbitrary temperature of 750°C was selected for comparison, simply on the basis of its being about half-way between the melting points of Cu_2S and CuCl . For this measurement, about 4g of material was added to a thin-walled quartz basket which was suspended from a quartz spring thermobalance in a closed all-silica-glass system. After the entire system had been evacuated argon gas was introduced and a movable furnace kept at 750°C was raised until the part of the quartz tubing containing the basket was in the hot zone of the furnace. The observed loss of weight was then recorded as a function of time over a period of 18 hr.

Weight losses in pure Cu_2S and FeS were not detected. However, a solution containing 11 m/o (mole per cent) Cu_2S lost about 8% by weight due to vaporization of CuCl . With pure CuCl and FeCl_2 the weight losses due to vaporization were alarmingly high. Both samples lost about 20% by weight after 18 hr of exposure. A sample of Cu_2S of 4.642g was also studied thermogravimetrically at a temperature of 1150°C . The complete heating and holding at 1150°C for 1 hr resulted in a loss of weight of 17 mg due to sulfur evolution which is equivalent to 0.36% of the original weight. When cooled to room temperature the solidified melt had acquired star-shaped copper metal crystallites which were visible around the circumference.

Hence, at the higher temperatures in an open experimental apparatus some unavoidable desulfurization should be expected to occur. For this reason it was decided to conduct the experiments in closed systems, where possible, or otherwise to measure a given property over the shortest possible period of time which would be compatible with the establishment of equilibrium and the reproducibility of the measurement.

Experimental.—Liquidus temperatures in the $\text{Cu}_2\text{S}-\text{CuCl}$ system were determined using a previously described technique (1, 3) and existing apparatus. Cooling rates were varied between 0.57° and $1.5^\circ\text{C}/\text{min}$. For these measurements the heart-shaped quartz cells fitted with a thermocouple well and containing about 15g of salt mixture were sealed under vacuum. Temperatures below 800°C were recorded using a 1 mV full-scale recorder and 24-gauge Chromel-Alumel thermocouples. For higher temperatures the thermocouples were platinum-13% platinum-rhodium. The sensitivity of the recorder was about 0.25°C , but the accuracy of the melting points should be taken as to the nearest degree. For chloride-rich compositions supercooling was not noticeable. However, supercooling did occur in the sulfide-rich melts and was minimized by vibrating the cells.

For the $\text{FeS}-\text{FeCl}_2$ mixtures, the steepness of the liquidus curve and the limited solubilities did not permit accurate cryoscopic measurements by this method. Only the melting point of pure FeCl_2 and the eutectic temperature could be detected. Hence, a decantation technique was employed. The measurements involved the equilibration at a given temperature of the sulfide-chloride mixtures placed in decantation quartz cells fitted with two side arms as described elsewhere (10).

At the beginning of a run, the cell with the salt mixture was sealed under vacuum and placed inside a graphite cylinder also containing the thermocouple wells and radiation baffles. The assembled system could be lowered into the hot zone of a cylindrical tilting furnace. The temperature along the 4-in. long graphite block was maintained constant to within $\pm 3^\circ\text{C}$. When heated to the desired temperature the liquid phase

saturated with FeS was decanted into the second side arm of the cell by tilting the entire furnace. Prior to decantation the solutions were allowed to remain for several hours at temperature to ensure equilibration. After cooling, the cell was opened and the decanted phase was analyzed by extracting the water-soluble FeCl_2 with distilled water. The accuracy of the method was established from separate blank experiments during which both fused samples and mechanically mixed FeS and FeCl_2 were used. The former method yielded consistently slightly lower FeS contents by less than 0.5%. Thus, even for the smallest sulfide composition studied, 2.34% by weight FeS, the absolute error was only 0.012%. The only significant uncertainty in this type of measurement originated from the difficulty in maintaining a temperature control over the 4-in. long decantation cell of better than $\pm 3^\circ\text{C}$.

The densities of the molten solutions in the Cu_2S - CuCl and FeS - FeCl_2 systems were determined by measuring the apparent loss of weight of a density sinker dipping into a melt at given compositions and temperatures. The density sinker was made by encapsulating a tungsten rod in quartz glass. For the oxygen-free melts quartz was found to be an excellent container material. All measurements were conducted in an atmosphere of purified argon using the quartz spring thermobalance apparatus and the cathetometer described previously (1, 3).

For the present measurements the quartz spring under a load of 5g had a total extension of 65 cm, allowing the detection of weight changes of the order of ± 0.2 mg. The results were corrected for the slight increase in weight due to condensation of the salt on the quartz fiber supporting the density sinker.

The densities for pure Cu_2S could not be measured by this method because of the high viscosity and high surface tension of the melts.

Electrical conductivities in the systems Cu_2S - CuCl and FeS - FeCl_2 were measured as functions of melt composition and temperature, using the U-tube quartz capillary cells of 2 mm diameter described previously (2, 4). All measurements were taken under an atmosphere of oxygen-free argon gas. Cell constants varied between 500 and 900 cm^{-1} . Calibrations were made using a 1.0 demal KCl solution (11). The electrical conductivities were measured using an a-c conductivity bridge equipped with a Wagner ground and an oscilloscope detector. The bridge was operated at a frequency of 3000 Hz and resistances could be measured to within ± 0.02 ohms. All values were corrected for lead

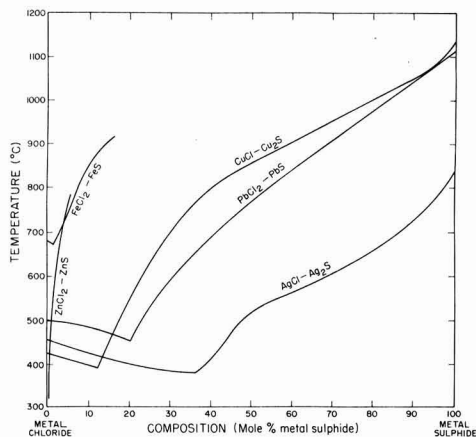


Fig. 2. Comparison between the phase diagrams of the systems: Cu_2S - CuCl , FeS - FeCl_2 , PbS - PbCl_2 , Ag_2S - AgCl , and ZnS - ZnCl_2 .

and electrode resistances. For the lower temperatures the temperature control throughout the length of the cell was better than $\pm 1.5^\circ\text{C}$, but between 1100° and 1200°C , it was only $\pm 3^\circ\text{C}$.

Finally, the electrolysis experiments were conducted in the quartz cells shown in Fig. 1. Electrode materials were copper for the cathode and graphite for the anode. These cells were also operated under an atmosphere of purified argon.

Experimental Results

Phase diagram determination.—The liquidus curves for the system Cu_2S - CuCl and part of that for the system FeS - FeCl_2 are given in Fig. 2, where they are compared with those for similar systems.

The Cu_2S - CuCl system is of the simple eutectic type. The characteristic points are the melting points of CuCl and Cu_2S given as $422.9^\circ \pm 1.0^\circ\text{C}$ and $1127.9^\circ \pm 2.0^\circ\text{C}$, respectively, and the eutectic temperature at $389.5^\circ \pm 1.5^\circ\text{C}$. The eutectic occurs at 12.1 m/o Cu_2S . The detailed data of the measured liquidus and eutectic temperatures are given in Table I.

Table I. Phase diagram measurements

Composition $X_{\text{Cu}_2\text{S}}$	Liquidus temperature ($^{\circ}\text{C}$)	Eutectic temperature ($^{\circ}\text{C}$)
Cu ₂ S-CuCl system		
1.0 (Pure Cu ₂ S)	1128 (m.p.)	—
0.950	1083	—
0.900	1047	—
0.850	1027	—
0.800	994.2	—
0.734	963.3	388.0
0.635	942.2	386.3
0.499	880.8	389.5
0.417	846.9	391.0
0.346	793.2	389.6
0.254	—	390.6
0.231	—	391.8
0.183	—	390.0
0.145	—	389.0
0.109	382.8	389.2
0.075	401.0	389.5
0.041	410.2	389.5
0 (Pure CuCl)	422.9 (m.p.)	—
Temperature ($^{\circ}\text{C}$)	Solubility X_{FeS}	
FeS-FeCl ₂ system		
697	0.032	
730	0.057	
735	0.058	
800	0.072	
857	0.108	
868	0.100	
890	0.120	
898	0.138	

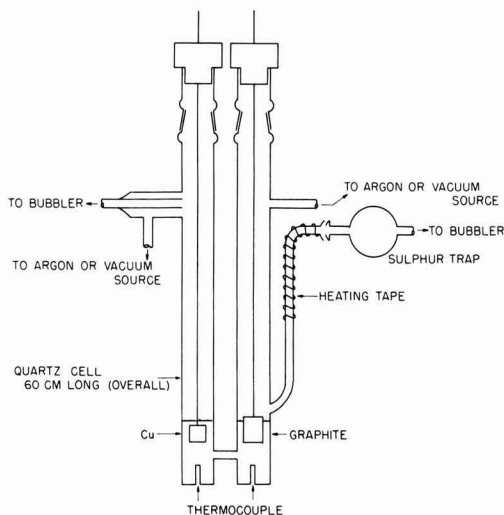


Fig. 1. Electrolysis cell

The present data should be compared with previous measurements by Urazov and Schleide (12) and by Truthe (13). The agreement is generally poor on the Cu_2S side of the eutectic where there is a 36°C spread in the reported values for the melting point of "pure" Cu_2S . In the composition range between 70-90 m/o Cu_2S , Truthe's (13) measurements differ by about 60°C from the present results. Urazov and Schleide (12) did not report any measurements beyond 48 m/o Cu_2S .

X-ray studies on material cooled from the eutectic, on both the sulfide and the chloride-rich sides, did not show any peak shift or line broadening. Therefore, solid solubility in this system is slight, if it occurs at all.

The cooling curves for pure CuCl and for compositions rich in CuCl indicate an exothermic reaction at 406°C which should be associated with the phase transformation of CuCl (14) from α -wüstite to the β -zinc blende type structure.

Cooling curves for the system FeS-FeCl_2 for compositions up to 40 m/o FeS showed only one inflection at a eutectic temperature of 674°C . In nine determinations FeCl_2 was found to melt at $679.4^\circ \pm 0.7^\circ\text{C}$. The solubility of FeS in FeCl_2 is limited and was measured by the decantation technique. The results are given in Fig. 2 and in Table I.

In Fig. 2, the liquidus curves of the systems FeS-FeCl_2 and $\text{Cu}_2\text{S-CuCl}$ are compared with those for Pb-PbCl_2 (3), $\text{Ag}_2\text{S-AgCl}$ (1), and ZnS-ZnCl_2 (15).

It may be seen that at corresponding temperatures the solubility of the sulfides in the chloride melt decreases in the order: $\text{Ag}_2\text{S-PbS-Cu}_2\text{S-FeS-ZnS}$, which is in the same order as the cation-ionic radius, or in the approximate order of the melting points of the pure metal sulfides. Work in this laboratory (10) on the reciprocal systems, PbS-NaCl , PbS-KCl , PbS-RbCl , and PbS-CsCl has indicated solubilities of the order of only 2 to 5 m/o sulfide which increased from the NaCl-PbS to the CsCl-PbS systems. Thus, the solubility trends in common cation and in reciprocal systems are entirely different.

Cryoscopic calculations.—In order to clarify the transformation for CuCl , and also for the purpose of obtaining information regarding the nature and the activities of the ionic species present in these solutions and of their degree of dissociation, freezing point depression measurements were also made on the systems CuCl-NaCl , CuCl-KCl , and CuCl-BaCl_2 .

From the results for the Cu_2S -rich liquidus curve, the activities of Cu_2S have been calculated using the simplified form of the van't Hoff equation

$$\ln a_{\text{solvent}} = \frac{-\Delta H_F}{R} \left[\frac{1}{T_L} - \frac{1}{T_F} \right] \quad [1]$$

where, T_L and T_F are, respectively, the liquidus and the fusion temperature of pure Cu_2S , and ΔH_F is the heat of fusion of Cu_2S given (16) as 2600 ± 500 cal. The results of the calculations are presented in Table II and indicate positive deviations from ideality.

Activity calculations were also made for CuCl for compositions along the CuCl liquidus. For this calculation the new heat of fusion for CuCl , determined calorimetrically in this laboratory (16), was used. The calorimetric measurements have shown that the solid transformation for CuCl at 406°C is accompanied by a heat effect of 1550 ± 50 cal/mole. Fusion occurs at 422.9°C and has a heat effect of only 1800 ± 50 cal/mole. It should be noted that the solid transformation is not mentioned in compilations of thermodynamic data and the heat of fusion is reported as having such widely different values as 2430 cal/mole (17) and 3879 cal/mole (18).

For the calculation of the activities of CuCl at temperatures below the transformation temperature, the

Table II. Activity calculations

System	x_{CuCl}	T_L (Liquidus temp, $^\circ\text{C}$)	a_{CuCl}	γ_{CuCl}
$\text{CuCl} + \text{BaCl}_2$	1.000	422.9	—	—
	0.990	417.0	0.989	0.989
	0.987	414.9	0.985	0.988
	0.981	411.6	0.979	0.998
	0.976	408.0	0.972	0.996
$\text{CuCl} + \text{KCl}$	0.992	418.1	0.990	0.999
	0.988	415.9	0.987	0.998
	0.978	410.2	0.976	0.997
	0.969	405.2	0.965	0.995
	0.966	403.4	0.959	0.992
$\text{CuCl} + \text{NaCl}$	0.956	398.7	0.941	0.984
	0.952	396.6	0.935	0.982
	0.931	386.2	0.808	0.865
	0.922	418.9	0.992	1.000
	0.983	414.5	0.984	1.001
$\text{CuCl} + \text{Cu}_2\text{S}$	0.974	410.3	0.976	1.001
	0.965	405.5	0.966	1.001
	0.958	403.5	0.959	1.000
	0.953	401.5	0.952	0.999
	0.934	394.5	0.928	0.988
$\text{Cu}_2\text{S-CuCl}$	0.890	379.6	0.875	0.984
	0.995	421.1	0.996	1.001
	0.988	419.0	0.992	1.005
	0.978	416.6	0.988	1.010
	0.974	414.6	0.984	1.010
$\text{Cu}_2\text{S-BaCl}_2$	0.965	412.2	0.960	1.015
	0.958	409.5	0.975	1.017
	0.951	407.5	0.971	1.020
	0.936	403.5	0.959	1.024
	0.923	400.2	0.947	1.027
$\text{Cu}_2\text{S-CuCl}$	0.917	399.0	0.943	1.028
	0.907	396.5	0.934	1.030
	0.898	394.4	0.927	1.032
	0.891	392.8	0.921	1.034
$\text{Cu}_2\text{S-CuCl}$	$x_{\text{Cu}_2\text{S}}$		$a_{\text{Cu}_2\text{S}}$	$\gamma_{\text{Cu}_2\text{S}}$
	1.000	1128	—	—
	0.9765	1101	0.9865	1.0102
	0.9612	1092	0.9757	1.0151
	0.9500	1083	0.9695	1.0205
$\text{Cu}_2\text{S-BaCl}_2$	0.9000	1047	0.9443	1.0492
	0.9748	1108	0.9867	1.0511
	0.9432	1118	—	—

van't Hoff equation was used in the form

$$\ln \frac{a_{TL}}{a_{TF}} = - \frac{(\Delta H_F + \Delta H_T)}{R} \left[\frac{1}{T_L} - \frac{1}{T_T} \right] \quad [2]$$

where, a_{TL} and a_{TF} are the activities at the liquidus and the transformation temperatures, respectively. ΔH_F is the heat of fusion of (β)- CuCl , and ΔH_T is the heat for the $\alpha \rightarrow \beta$ transformation.

All activity calculations are referred to pure super-cooled CuCl as the state of reference. Table II also includes the activities of CuCl in the binary systems CuCl-BaCl_2 , CuCl-KCl , and CuCl-NaCl , calculated from the cryoscopic results. It is readily seen that in these systems the deviations from ideality are slightly negative, while in the $\text{Cu}_2\text{S-CuCl}$ system the deviations are positive. The positive deviations from ideality in the $\text{CuCl-Cu}_2\text{S}$ system may be considered as evidence that Cu_2S is present in the liquid solutions as associated species.

Solute association may be evaluated quantitatively by applying the limiting law to the van't Hoff relationship. For the very dilute solutions, Eq. [1] may be written as

$$\Delta T = -n \frac{RT_F^2}{\Delta H_F} \cdot \frac{M_{\text{CuCl}}}{1000} \cdot m \quad [3]$$

where, ΔT , is the measured freezing point depression, m is the molality of Cu_2S , and n has the significance of the number of foreign particles produced from one molecule of solute.

Using Eq. [3], n has been calculated from the experimental ΔT values, and the calculations are summarized in Table III.

For a molten salt system with a common ion, $n = 1$ if the solute salt is totally dissociated. Inspection of the data in Table III shows that n is essentially unity for the systems NaCl-CuCl , KCl-CuCl , and CuCl-BaCl_2 . For the system $\text{CuCl-Cu}_2\text{S}$, n is about 0.6, indicating that Cu_2S exists as an associated species.

If it is assumed that Cu_2S in solution is present as

Table III. Cryoscopic calculations of the number of foreign particles in CuCl solutions

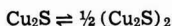
Solute	m* solute, molality	n
Cu ₂ S	0.04964	0.6850
	0.12569	0.5851
	0.22564	0.5274
	0.26857	0.5838
	0.36853	0.5484
	0.44405	0.5700
	0.51487	0.5650
KCl	0.08444	1.0742
	0.12455	1.0616
	0.22395	1.0712
	0.08156	0.9265
NaCl	0.17625	0.9003
	0.26527	0.8972
BaCl ₂	0.10326	1.0975
	0.13906	1.1003
	0.19569	1.1004
	0.25092	1.1292

* For dilute solutions

$$X_{\text{solute}} = \frac{M_{\text{CuCl}}}{1000} \cdot m$$

where, M_{CuCl} is the molecular weight and X is the mole fraction.

the dimer $(\text{Cu}_2\text{S})_2$, the following association reaction should be expected to have occurred



The equilibrium constant for this reaction may be written as

$$K = \frac{\frac{\alpha}{2} X}{(1-n)X} \quad [4]$$

where, α represents the fraction of Cu_2S which forms the associated species and X is the solute mole fraction.

From a mass balance calculation it is readily shown that

$$n = 1 - \frac{\alpha}{2} \quad [5]$$

From Eq. [4] and [5]

$$K = \frac{(1-n)X}{(2n-1)} \quad [6]$$

Using the n values determined by cryoscopy for the dilute solutions containing up to 5 m/o Cu_2S , K is found to be practically constant for all compositions and to have the average value of $K = 1.3$.

From the α values obtained from Eq. [5] it is seen that about 80% of Cu_2S is present in the dilute solutions in the form of $(\text{Cu}_2\text{S})_2$ dimers.

The behavior of Cu_2S in the Cu_2S -CuCl system bears close resemblance with that of PbS in the PbS-PbCl₂ system previously investigated (3), which also showed positive deviations from ideality. However, in the Ag_2S -AgCl (1) system the dilute solutions of Ag_2S were shown to obey Temkin's rule, thus indicating that Ag_2S could be present either as a dissociated compound or as a monomer (Ag_2S).

Similar calculations have not been performed on the FeS-FeCl₂ system owing to the limited solubilities observed and also because of the lack of reliable data for the heat of fusion. It is evident, however, from the low solubilities that this system should also be characterized by large positive deviations from ideality.

Density measurements.—Densities were measured as functions of composition from pure CuCl to solutions containing 69.4 m/o Cu_2S . Because of the volatilization of CuCl at high temperatures, most of the measurements with melts rich in CuCl were conducted at temperatures below 750°C.

Similar measurements for the FeS-FeCl₂ system could only be obtained over the narrow composition range permitted by the phase diagram. Reproducibility for all these measurements was better than $\pm 0.3\%$. The density data for each composition were fitted by

Table IV. Density measurements ($d = a + bt$) (°C) $\text{g}\cdot\text{cm}^{-3}$

X_{CuCl}	a	b $\times 10^4$	Stand. dev.	Temp range (°C)
System Cu ₂ S-CuCl				
1.000	4.0829	-7.9298	0.007	465-838
0.964	4.2173	-8.4622	0.005	411-862
0.952	4.2535	-8.6774	0.003	492-639
0.943	4.2478	-8.3080	0.002	452-749
0.934	4.2888	-8.2019	0.002	464-794
0.903	4.3635	-8.4947	0.003	426-697
0.864	4.4708	-7.3269	0.005	539-699
0.825	4.4236	-8.1457	0.004	509-787
0.790	4.6189	-8.2951	0.003	613-795
0.746	4.5462	-6.0143	0.003	672-689
0.698	4.5840	-4.7938	0.003	842-1018
0.633	4.7182	-5.5801	0.001	902-1000
0.551	4.7514	-5.0319	0.002	902-1054
0.450	4.7159	-3.4010	0.002	908-1074
0.306	4.9236	-3.5308	0.001	1043-1150
X _{FeCl₂}				
System FeS-FeCl ₂				
1.000	2.7237	-5.5488	0.003	685-884
0.946	2.7378	-5.5913	0.002	727-884
0.916	2.7430	-5.5758	0.001	830-851

the least squares method to linear equations of the type

$$d = a + bt$$

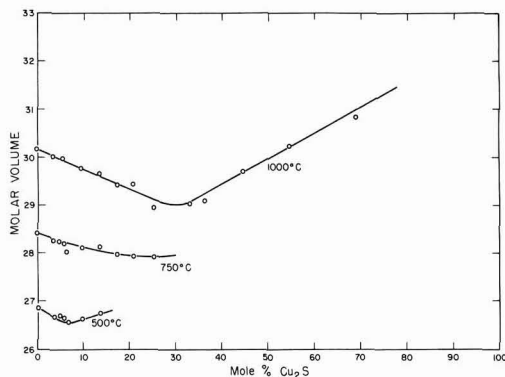
where a and b are constants, and t is the temperature in °C. The equations for the two systems, Cu_2S -CuCl and FeS-FeCl₂ are given in Table IV, together with the corresponding standard deviations.

Densities for pure CuCl have also been measured by Klemm (19) and are in agreement with the present results to within $\pm 0.5\%$.

From the results shown in Table IV molar volume isotherms for the Cu_2S -CuCl system were calculated at the selected temperatures of 500°, 750°, and 1000°C, and are shown in Fig. 3.

The dominant feature of the molar volume isotherms is a pronounced minimum occurring at about 30 m/o Cu_2S at 1000°C. The minimum is shifted to lower Cu_2S contents as the temperature is decreased.

The isotherm at 1000°C indicates negative deviations from apparent additivity. The approximate partial molar volumes that may be obtained from the isotherm at 1000°C by the method of tangents indicate two distinct trends. Below about 30 m/o sulfide, CuCl in solution should have about the same packing as in pure CuCl. Molten CuCl in this sense appears to be an associated liquid and to have a loosely packed structure. Cu_2S enters these solutions at a substantially decreased partial molar volume of about 25.9 cm³/mole. For compositions containing more than 30 m/o Cu_2S the trend is reversed and CuCl appears to enter an essentially unaltered Cu_2S structure at the smaller

Fig. 3. Molar volume isotherms in the Cu_2S -CuCl system

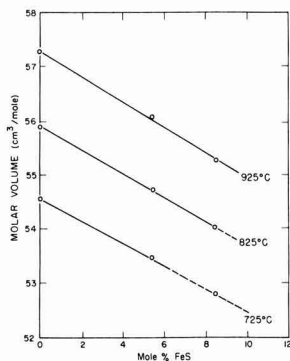


Fig. 4. Molar volume isotherms in the FeS-FeCl₂ system

partial molar volume of about 27.2 cm³/mole. The partial molar volume of Cu₂S in this range appears to be approximately the same as for pure Cu₂S.

These effects may be understood if it is considered that in concentrated solutions Cu₂S exists as a heavily associated structure of rather poor packing where CuCl can be easily accommodated. The decrease of the partial molar volume of Cu₂S for compositions below 30 m/o Cu₂S is indicative of the more efficient accommodation of the sulfide within the open CuCl structure because of dissociation of the polymeric Cu₂S to simpler species. This interpretation is in agreement with the cryoscopic calculations which indicated the presence of Cu₂S dimers in dilute solutions.

The shift with decreasing temperature of the minimum in the volume isotherms toward lower sulfide concentrations indicates the possible increase in the covalency of the melts at the lower temperatures.

The transition toward increased association at about 30 m/o Cu₂S at 1000°C roughly corresponds to the composition at which, as it will be shown shortly, significant electronic conduction appears to be setting in.

For the few compositions studied, molar volume isotherms have been calculated for the FeS-FeCl₂ system and are given in Fig. 4. It is seen that the molar volume decreases linearly with increasing FeS content. The initial decrease of the molar volume on addi-

Table V. Specific conductivity in the Cu₂S-CuCl system

Composition X _{Cu₂S}	Specific conductivity (mhos/cm)					
	500°C	600°C	700°C	800°C	900°C	1000°C
CuCl	3.55	3.78	3.89	3.96	3.99	3.96
0.035	3.39	3.59	3.73	3.81	3.80	—
0.077	3.00	3.50	3.67	(3.82)	—	—
0.093	3.30	3.45	3.48	—	—	—
0.125	3.28	3.46	3.65	—	—	—
0.162	3.25	3.45	3.67	3.87	—	—
0.192	—	3.43	3.72	4.00	4.18	—
0.260	—	—	3.75	4.04	4.33	4.46
0.267	—	—	—	4.04	4.41	4.52
0.304	—	—	—	4.13	4.40	4.72
0.360	—	—	—	4.21	4.88	5.48
0.506	—	—	—	—	5.17	6.06
0.652	—	—	—	—	(7.47)	10.45
0.752	—	—	—	—	—	12.20
0.853	—	—	—	—	—	(12.9)

Parentheses indicate extrapolated values.

tion of FeS appears to follow the same trend as with the copper system.

Electrical conductivity measurements.—Cu₂S-CuCl system.—Specific conductivities for pure molten CuCl were determined at temperatures between 450° and 970°C, and are given in Fig. 5 and in Table V.

The system has also been investigated by Grantham and Yosim (20) in the temperature range 475°–1157°C, and by Sakai (21) in temperature of 475°C to about 600°C. The present results are in excellent agreement with the former. It is of interest to note the nonlinear increase of the electrical conductivity of CuCl with temperature. At about 900°C the conductivity curve reaches a maximum and then the conductivity acquires a negative temperature coefficient. This abnormal behavior has also been detected by Grantham and Yosim (20) and has been explained as indicating increased covalency in CuCl at the high temperatures. Nevertheless, the magnitude of the conductance is typical of that encountered with ionic melts. Additional evidence for the ionic behavior of molten CuCl is provided from electrolysis experiments which have been reported to proceed with 100% current efficiency (8).

The specific conductivity of pure molten Cu₂S has also been measured in the temperature range 1130°–1195°C and is represented by the equation

$$K \text{ mho} \cdot \text{cm}^{-1} = 19.5010 + 0.1235 (t - 1000^\circ) \text{ in } ^\circ\text{C} \quad [7]$$

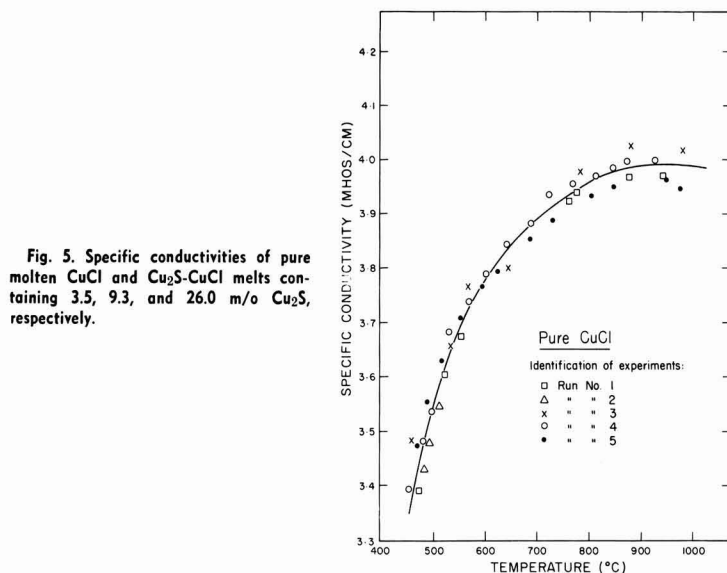
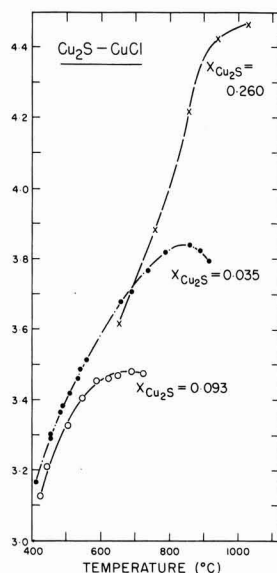


Fig. 5. Specific conductivities of pure molten CuCl and Cu₂S-CuCl melts containing 3.5, 9.3, and 26.0 m/o Cu₂S, respectively.



The standard deviation is 0.365 mho/cm. Molten Cu_2S may be described as a liquid semiconductor having conductivities which increase from 35 mho/cm at 1130°C to 44 mho/cm at 1195°C. At temperatures higher than 1200°C significant desulfurization of the molten sulfide was evident and measurements were not taken.

The specific conductivities of nonstoichiometric molten Cu_2S containing excess copper were also measured at 1150°C and the results are given in Fig. 6. For these measurements the nonstoichiometric Cu_2S was prepared by melting together in the conductivity cell known amounts of copper metal powder with stoichiometric sulfide. Clearly, the presence of excess copper causes a significant increase in the conductivity of molten Cu_2S .

The present results on "stoichiometric" Cu_2S are about 35% lower and less temperature dependent than the values reported by Yang, Pound, and Derge (8), although the Cu_2S used by the latter contained between 0.44 and 1.64% excess copper and should be expected to yield higher conductivities. Knacke and Strese (22) have also reported values for the conductivities of Cu_2S which change from 25 mho/cm at 1130°C to 97 mho/cm at 1480°C and are much lower than the present results.

The specific conductivities of the Cu_2S - CuCl solutions were also measured as functions of melt composition and temperature and the results are summarized in Table V. The specific conductance curves for melts containing 3.5, 9.3, and 26 m/o Cu_2S are also given in Fig. 5.

The conductivities for the latter were not linear functions of temperature and could not be represented by linear equations. The transition from a positive to a negative temperature coefficient which was observed with pure CuCl also characterized the Cu_2S - CuCl melts containing up to about 27 m/o Cu_2S .

The specific conductivity isotherms in the low-temperature range up to 700°C for solutions containing up to 25 m/o Cu_2S are given in Fig. 7. It is evident that the specific conductivity of the solutions decreases initially on addition of sulfide. For the isotherm at 700°C, the conductivities reach a minimum at about 10 m/o Cu_2S and then increase up to the liquidus composition. These solutions should be considered as ionic as their conductivities are still lower than the conductivities of pure CuCl at the same temperatures.

The initial decrease of the conductivity on addition of sulfide should be attributed to the lower mobility of the divalent sulfide anion and to its anchoring effect on the surrounding cations. The thermodynamic cal-

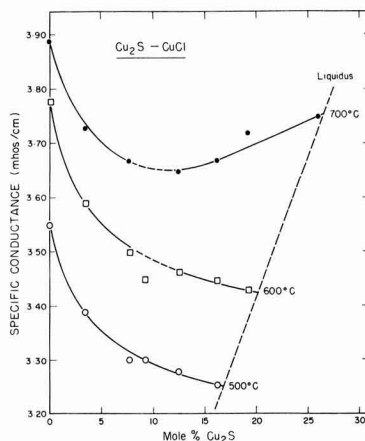


Fig. 7. Specific conductivity isotherms of dilute solutions of Cu_2S in CuCl .

culations have indicated the presence of associated $(\text{Cu}_2\text{S})_2$ dimers and such nonionic groups are not expected to contribute to the ionic conductivity. The conductance minima shift toward higher sulfide concentrations at lower temperatures.

The specific conductivity data at 1000°C given in Table V have been converted to molar conductivities and are presented in Fig. 8. A significant increase in the specific conductance is observed at higher temperatures when the sulfide content exceeds about 30 m/o. Thus, the molar conductivity of a solution containing 30 m/o Cu_2S is about 30% higher than that of pure CuCl . As the associated Cu_2S in solution is not expected to contribute to the conductance, as shown by the initial decrease in conductance on the addition of Cu_2S , it follows that the increase in conductance must be attributed to electronic contributions.

When the present results are compared with the measurements by Yang, Pound, and Derge (8), there is disagreement with regard to the sulfide content at which electronic conductivity sets in. At 1200°C

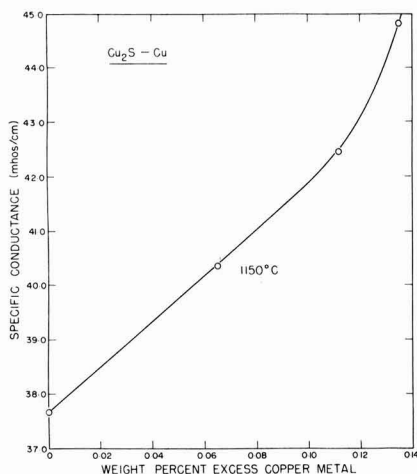


Fig. 6. Conductivities of nonstoichiometric Cu-rich cuprous sulfide at 1150°C.

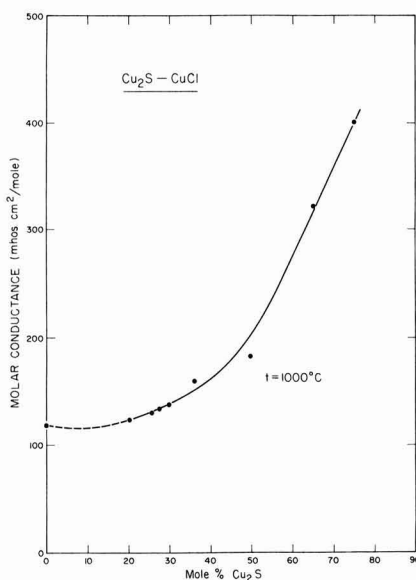


Fig. 8. Molar conductivity isotherm at 1000°C of the Cu_2S - CuCl system.

the specific conductivities measured by these authors remained almost constant at 5 mho/cm, from pure CuCl to about 50 m/o Cu₂S, and then increased to about 77 mho/cm for "pure" molten Cu₂S. Hence, melts containing up to 50 m/o Cu₂S were considered to be ionic conductors. In the present study even at 1000°C electronic conductivity sets in at about 30 m/o Cu₂S, and at 1200°C it should be expected that the onset of electronic conductance would occur at even lower Cu₂S contents.

Considering the effect of dissolved copper on the specific conductivities of the Cu₂S-CuCl melts, measurements were also obtained with conductivity cells fitted with copper electrodes immersed in melts containing pure CuCl and a Cu₂S-CuCl solution (15 m/o Cu₂S), respectively, at a temperature of 700°C. Both these solutions had previously been equilibrated with Cu metal. The resistance of these cells was monitored as a function of time. After 72 hr of operation the resistance change was only 0.5%, indicating that for all practical purposes the presence of dissolved copper in these melts, if any, does not introduce electronic contributions.

FeS-FeCl₂ system.—The specific conductivity for pure FeCl₂ was also measured as a function of temperature and may be expressed by the equation

$$K_{\text{FeCl}_2} (\text{mho} \cdot \text{cm}^{-1}) = 0.00149 + 1.889 \times 10^{-3} t \quad (\text{in } ^\circ\text{C}) \quad [8]$$

with a standard deviation of 0.004. Other data for this system are not available in the literature.

As was the case with the density measurements with the FeS-FeCl₂ melts the specific conductivity measurements presented in Fig. 9 are restricted to a narrow range of compositions. The dotted lines represent extrapolated values obtained from measurements at higher temperature where the system is miscible. It is evident that in this system a conductivity minimum does not occur.

From the conductivity isotherm at 925°C it is seen that the FeS-FeCl₂ solutions probably remain essentially ionic up to a composition of 10 m/o FeS, and that the more rapid increase in conductance at higher concentrations could indicate possible electronic contributions.

Accuracy of results.—With regard to the accuracy and reproducibility of the results, the reproducibility of the specific conductivities for CuCl between runs was of the order of ± 0.03 mho/cm, or within $\pm 0.9\%$. For FeCl₂ the reproducibility was of the order of ± 0.01 mho/cm, or better than $\pm 0.8\%$. The electrical con-

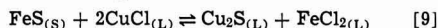
ductivity of cuprous sulfide could be reproduced within ± 0.15 mho/cm, or better than $\pm 0.4\%$. Reproducibilities of the conductivities of the solutions were of comparable magnitude. However, taking into account the additional factors of calibrating procedure and temperature uncertainty, the accuracy of the conductivity measurements reported herein is given with 1% confidence.

Electrolysis experiments.—For the binary mixtures Cu₂S-CuCl the electrolyte contained 10 to 20 m/o Cu₂S and the temperature was varied between 450° and 600°C. Electrolysis of Cu₂S dissolved in molten CuCl, and of a synthetic Cu₂S + FeS matte dissolved in molten CuCl, produced copper metal at the cathode and sulfur gas at the anode. The choice of electrolyte composition was made so as to obtain the highest sulfide content in the ionic composition range indicated by the conductivity results. Also, it was desirable that the solutions should remain liquid at low enough temperatures. The boiling point of sulfur (444.6°C) was used as the lower temperature limit for the experiments, and therefore, the anodic reaction product was always a vapor which could be swept out of the anode compartment by the argon carrier gas.

The current efficiencies were obtained by weighing the cathodic deposits and were found to vary. Low values for the current efficiencies for small amounts of deposits could be attributed to the fragile structure of the dendritic deposits and to the resulting breakage of the dendrites while the cathodes were being removed from the melts. Continuous electrolysis produced large well-shaped copper crystals. The structure of the deposits was not uniform throughout deposition. At the initial stage of electrolysis the deposits were generally coarse and multipyramidal but further deposition led to the formation of rather large dendritic crystals having fine needle-like projections. In all 25 electrodeposition runs the measured deposition potentials were of the order of 0.3–0.5V, which values are lower than 0.63V representing the theoretical (17) decomposition potential of Cu₂S in an ideal solution.

Current efficiencies of about 80% were obtained in the low-temperature range 450°–500°C with low apparent current densities up to 15 mA/cm², and with Cu₂S concentrations not exceeding 30 m/o. An electrolyte containing 6.6 m/o Cu₂S, at a cathodic current density of 0.3 mA/cm², yielded a current efficiency of 97.3%. Apparent current densities of the order 20–40 mA/cm² usually yielded poorly defined deposits and low current efficiencies of about 50%. At 650°C, a solution containing 46.4 m/o Cu₂S yielded a small amount of spongy deposit mixed with electrolyte with practically zero current efficiency, because of the electronic conductance at such high Cu₂S concentrations.

With the ternary solutions, FeS-Cu₂S-CuCl, which are the equivalent of dissolving the synthetic matte in a CuCl solvent, electrolysis produced copper metal at the cathode and chlorine-contaminated sulfur gas at the anode. Deposition of iron metal appeared to be totally absent. This behavior should be understood in terms of the exchange reaction



which is thermodynamically favored and has a standard free energy of –9800 kcal/mole at 1100°C. The implications are that in the molten salt mixture of the synthetic matte Cu₂S-FeS dissolved in excess CuCl, the stable components are FeCl₂ and Cu₂S. Considering 1 g-mole of solution having the initial composition: X₁ g-moles CuCl, X₂ g-moles Cu₂S, and X₃ g-moles FeS, where X₃ \leq X₁ and X₂, the final composition after the exchange reaction has taken place is readily calculated as

$$X_{\text{CuCl}} = \frac{2X_1 - X_3}{2X_1 + 2X_2 + 3X_3}, \quad X_{\text{Cu}_2\text{S}} = \frac{2X_2 + 2X_3}{2X_1 + 2X_2 + 3X_3}$$

$$X_{\text{FeCl}_2} = \frac{2X_3}{2X_1 + 2X_2}, \quad \text{and } X_{\text{FeS}} = 0 \quad [10]$$

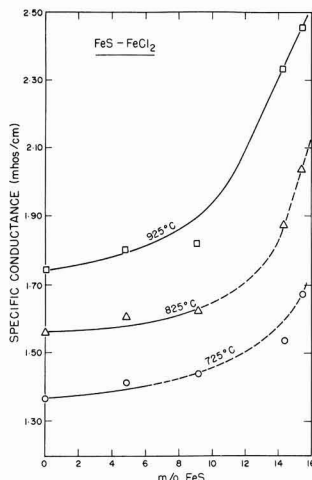


Fig. 9. Specific conductivity isotherms in the FeS-FeCl₂ system

Table VIII. Electrical conductance of molten sulfides near their melting points

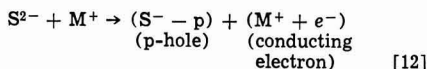
Compound	Temperature (°C)	Specific conductance (mho/cm)	Temperature coefficient of conductance (mho/cm · °C)	Reference
Cu ₂ S	1130	36	+0.12	Present study
PbS	1120	116	+0.30	Bell and Flengas (4)
Ag ₂ S	840	202.5	Nil	Bell and Flengas (2)
FeS	1200	400	-0.5	Argyriades et al. (24)
CoS	1182	1410	-10.0	Velikhanov (25)
NiS	797	4055	-11.0	Velikhanov (25)
Sb ₂ S ₃	550	0.17	+0.00275	Velikhanov (25)
TiS	375	0.10	+0.0133	Stoneburner (26)
Ti ₂ S ₃	216	0.017	+0.0026	Stoneburner (26)
GeS	664	1.33	+0.0209	Handfield et al. (27)
SnS	895	24	+0.0065	Boutin and Bourgon (28)

For the dilute solutions of the metal sulfides in their chlorides the thermodynamic calculations and the interpretation of the molar volumes for these systems are in substantial agreement in indicating the dissociation of the sulfides into monomeric- or dimeric-type species. These solutions appear to be ionic conductors.

The electronic conductivity in the sulfide-rich melts appears to be related to the association of the sulfide species and to the creation of a continuous sulfide network acting as a suitable path for electron transfer. This was particularly evident in the Ag₂S-AgCl and Cu₂S-CuCl melts where the abnormally high partial molar volumes of the metal sulfides for the sulfide-rich compositions indicated the presence of the associated sulfide network of rather poor packing capacity. The breakdown of the electronic conductivity on the addition of the metal chloride is at least partially due to the dissociation of the structure into monomeric or dimeric species and to their subsequent isolation by the chloride solvent. The electronic conductivity in molten metal sulfides may be understood in terms of a modified "band model."

In a perfect covalently bonded material the electrons are generally restricted in their directional bonds and cannot contribute to the conductance. The appearance of electronic conductivity requires the promotion of electrons from their valence band to a conducting energy level. At high temperatures such transitions are probable and in addition impurity-type mechanisms may arise as the result of the thermal decomposition of the sulfides which is expected to create some nonstoichiometry. Also, in polar crystals the electrons of the negative ions may be excited to a conduction band of positive ions creating positive holes which offer a convenient path for p-type semiconductivity. Electrons excited to a conduction band may contribute to the electronic conductivity by moving from one positive ion to the next.

Thus, the conductivity mechanism for monovalent molten sulfides may be described by exchange reactions of the type



followed by



for n-type conductivity and by



for p-type conductivity. In addition, electron trapping should not be excluded and the melts could become predominantly p- or n-type semiconductors.

The excitation of electrons from the valence band of S²⁻ species to the conduction band of the M⁺ species requires a certain energy E_g , and in an electronically conducting liquid the concept of the band model must be modified to account for the lack of long-range order. However, the degree of directional long-range order which appears to exist in these polymeric sulfides should be helpful for the purpose of understand-

ing the conductivity path for electron transfer. In addition, collisions between polymeric chains and chain rearrangements should present instantaneous energetically favorable conditions for electron transfer from chain to chain. Apparently, the presence of the ionic component MCl in a binary system MCl-MS has the effect of decreasing the size of the polymeric M-S chains through the normal route of dissociation and the over-all energy gap for the transfer process increases with increasing MCl content until the solutions become ionic.

The measured activation energies (4) in the PbS-PbCl₂ system support this interpretation. The activation energy for electronic conduction which is about 8 kcal in "pure" molten PbS increases to 18, 22, 25, and 38 kcal/mole as the concentration of PbS in the binary PbS-PbCl₂ systems decreases to 80, -6, 45, and 40 m/o, respectively. The number of thermally activated carriers for electronic conductivity, if nonstoichiometry effects are ignored, should also be a function of temperature and increase as the temperature increases.

The addition of excess dissolved metal increases the total electronic conductivity because the added M atoms act as electron donors according to reaction [4]



However, it should also be expected that such electrons are donated at a conduction band level and accordingly the activation energy for conduction should not be affected to any large extent. The behavior of the previously investigated Pb-PbS-PbCl₂ (4) ternary system supports this interpretation. For solubilities of Pb in PbS ($X = 0.45$) - PbCl₂ melts varying between 0.01 and 1.13 m/o Pb the activation energy for conduction remains constant at about 25 kcal/mole. This activation energy is about the same for the binary PbS-PbCl₂ melt containing 45 m/o PbS which do not contain any dissolved "excess" lead.

It appears, however, that the ionization reaction [16] does not proceed to completion and that only a fraction of the "excess" metal atoms present are capable of providing conducting electrons. For example, a Cu₂S-Cu melt containing 0.012 w/o (weight per cent) dissolved copper has a conductivity which is only 4 mhos/cm higher than that of pure molten Cu₂S. Similarly, in the case of the PbS-PbCl₂-Pb system (4) it has been calculated that if all the added metal atoms were ionized giving free electrons in the conduction band, then a concentration of 0.014 m/o excess Pb should have increased the melt conductivity by about 1000 times.

Thus, it is evident that excess metal solubility should be accounted for by both "ionized" and "nonionized" species, the latter being the most numerous. The excess metal solubility in the corresponding pure metal sulfides at comparable temperatures appears to decrease in the order Cu₂S-PbS-Ag₂S. However, the magnitude of the electronic conductivity in these liquids does not appear to be directly related to the metal solubility.

Acknowledgments

The financial support of the National Research Council of Canada is gratefully acknowledged. The authors wish to thank Dr. W. T. Thompson for helpful discussions.

Manuscript submitted April 30, 1971; revised manuscript received Dec. 1, 1971.

Any discussion of this paper will appear in a Discussion Section to be published in the December 1972 JOURNAL.

REFERENCES

1. M. C. Bell and S. N. Flengas, *This Journal*, **111**, 569 (1964).
2. M. C. Bell and S. N. Flengas, *ibid.*, **111**, 575 (1964).
3. M. C. Bell and S. N. Flengas, *ibid.*, **113**, 27 (1966).
4. M. C. Bell and S. N. Flengas, *ibid.*, **113**, 31 (1966).

5. I. Gul'din, A. Buzhinskaya, V. Borseg'yan, and V. Ruppel, *Zh. Prikl. Khim.*, **33**, 378 (1960), *English translation, Soviet Electrochemistry*, **3**, 100 (1961), Consultants Bureau, New York.
6. H. Sawamoto and T. Saito, *Nippon Kogyo Kaishi*, **68**, 555 (1952).
7. V. Winterhager and R. Kammel, *Z. Erzbergbau Metallhüttenw.*, **9**, (3), 97 (1956).
8. L. Yang, G. Pound, and G. Derge, *Trans. AIME*, **206**, 783 (1956).
9. T. Hoar and R. Ward, *Trans. Inst. Min. & Met.*, **67**, 393 (1958).
10. A. D. Pelton and S. N. Flengas, *Can. J. Chem.*, **48**, 2016 (1970).
11. M. C. Bell, Ph.D. Thesis, p. 37, 1964, Dept. Metallurgy and Materials Science, University of Toronto, Toronto, Ontario, Canada.
12. G. Urazov and L. Tschleide, *Akad. Nauk SSSR Izvestia, Phys. Chem. Section, Analysis*, **13**, 263 (1941).
13. W. Truthe, *Z. Anorg. Chem.*, **76**, 161 (1912).
14. M. Lorenz and J. Prener, *Acta Cryst.*, **9**, 538 (1956).
15. G. Gashurov and A. Levine, *J. Chem. Eng. Data*, **5**, 517 (1960).
16. W. T. Thompson and S. N. Flengas, *Can. J. Chem.*, **49**, 1550 (1971).
17. O. Kubaschewski, L. E. Evans, and C. B. Alcock, "Metallurgical Thermochemistry," pp. 366-389, Pergamon Press, Toronto (1967).
18. J. Lumsden, "Thermodynamics of Molten Salt Mixtures," p. 313, Academic Press, New York (1966).
19. W. Klemm, *Zh. Anorg. Chem.*, **152**, 235 (1926).
20. L. Grantham and S. Yosim, *J. Chem. Phys.*, **45**, 1192 (1966).
21. K. Sakai, *J. Chem. Soc. Japan*, **75**, 182 (1954).
22. O. Knacke and G. Strese, *Z. Erzbergbau Metallhüttenw.*, **10**, 207 (1957).
23. H. Kellogg, *Trans. AIME*, **188**, 862 (1950).
24. D. Argyriades, G. Derge, and G. Pound, *Trans. AIME*, **215**, 909 (1959).
25. A. A. Velikanov, Proc. of the All-Union Conf. on Phys. Chem. of Molten Salts and Slags, 1960. U.S. AEC Translation No. 5948, 1963.
26. D. Stoneburner, *Trans. AIME*, **233**, 153 (1965).
27. G. Hanfield, M. D'Amboise, and M. Bourgon, *Can. J. Chem.*, **44**, 853 (1966).
28. D. Boutin and M. Bourgon, *Can. J. Chem.*, **39**, 915 (1961).

On the Transition from Internal to External Oxidation in Ternary Alloys

Howard W. Pickering*

Edgar C. Bain Laboratory, United States Steel Corporation, Research Center, Monroeville, Pennsylvania 15146

ABSTRACT

Addition of certain metals to binary A-B alloys can markedly improve oxidation resistance through formation of a dense layer of BO_x on the surface, e.g., the addition of Cr to Fe-Al alloys with the formation of a dense layer of Al_2O_3 . The reason for the improved oxidation resistance is the subject of this paper. Experiments are described for the model alloy system, Ag-Zn-Al. A Ag-3 atomic per cent (a/o) Al alloy exhibits internal oxidation without formation of an Al_2O_3 layer on the surface. Upon addition of 21 or 25 a/o Zn, internal oxidation is completely suppressed and a dense, highly protective Al_2O_3 layer is formed. These data support the mechanism originally advanced by Wagner whereby Zn functions as a secondary getter for oxygen atoms. Other aspects of the results pertaining to the occurrence of exclusive internal oxidation in the alloys of low solute content and to the complex transient behavior exhibited by alloys of intermediate solute content are also discussed.

Oxidation resistant alloys for industrial use at elevated temperatures are usually ternary or multicomponent alloys rather than binary alloys. The low oxidation rate of Fe-Cr-Al alloys, for example, is well known (1-6). The good performance of these alloys results from the formation of a dense Al_2O_3 layer over the surface. The presence of Cr in the alloy in relatively large amounts is essential for the formation of this layer at feasible Al contents. Yet, Cr does not appear to enter the Al_2O_3 layer to an appreciable extent. Addition of other elements to Fe-Al alloys (in place of Cr) are in certain instances even more beneficial for the formation of an Al_2O_3 layer (7).

Wagner (8) has tentatively outlined the basic principles underlying the oxidation resistance of such alloys. In essence he suggested that one or more of the components functions as a getter for oxygen along with the component of highest affinity for oxygen. The action of the secondary getters supposedly decreases the diffusion of oxygen inward when the dissolved primary getter is depleted in the surface layers. In discussing the Cu-Zn-Al system Wagner points out that the oxygen concentration in the alloy next to the ZnO layer, determined by equilibrium between ZnO

and Zn in the alloy, may be as small as 10^{-6} of that determined by the coexistence of Cu and Cu_2O , as in the case of a copper alloy containing 1 or 2 a/o Al but no Zn. Hence virtually no oxygen diffusion into the alloy is to be expected when Zn is present in rather large amounts. As a result Al atoms may diffuse to the depleted surface region without being intercepted by oxygen atoms. They may then react with oxygen and also with the Cu_2O and ZnO which are formed at the beginning of oxidation (along with nuclei of Al_2O_3) to form more Al_2O_3 by a displacement reaction.

Wagner (8) specifically explained in this manner the excellent oxidation resistance of the Fe-Cr-Al alloys as well as that of the Cu-Zn-Al alloys as reported by Dunn (9) already four decades ago. The possibility of forming a dense Al_2O_3 layer by addition to the alloy of other metals has considerable technological importance since the ternary alloys with low Al content not only give excellent oxidation resistance but at the same time exhibit good mechanical behavior—quite the contrary of their counterpart binary alloys which have poor mechanical properties as a result of the high Al contents required for the formation of a protective Al_2O_3 layer.

Pfeiffer's (5) x-ray and electron diffraction data of the oxide scales which form on Fe-20% Cr-5% Al at 1073°-1473°K in air may be an indication that the

* Electrochemical Society Active Member.
Key words: alloys, elevated temperature properties, mechanism, oxidation, silver.

Table I. Composition of alloys—mean and standard deviation
Number of samples analyzed for each determination are given in parenthesis

Alloy	a/o Zn	a/o Al	Alloy	a/o Zn	a/o Al
Ag3Al	0	3.0 ± 0.1 (7)	Ag5Zn3Al	5.2 ± 0.4 (2)	3.1 ± 0.1 (4)
Ag6Al	0	6.1 ± 0.2 (9)	Ag10Zn3Al	10.0 ± 0.1 (4)	3.2 ± 0.2 (4)
Ag10Al	0	9.5 ± 0.4 (3)	Ag12Zn3Al	12.2 ± 0.3 (7)	3.1 ± 0.1 (3)
Ag14Al	0	14.0 ± 0.3 (3)	Ag21Zn3Al	20.6 ± 0.5 (2)	3.0 ± 0.1 (3)
Ag5Zn	4.7 ± 0.2 (2)	0	Ag24Zn3Al	24.1 ± 0.2 (3)	2.6 ± 0.3 (3)
Ag9Zn	9.3 ± 0.1 (3)	0	Ag5Zn6Al	5.1 ± 0.2 (3)	5.9 ± 0.2 (2)
Ag15Zn	14.8 ± 0.1 (2)	0	Ag10Zn6Al	9.5 ± 0.4 (4)	6.0
Ag21Zn	20.9 ± 0.8 (5)	0	Ag15Zn6Al	14.8 ± 1.1 (4)	6.0 ± 0.2 (2)
			Ag20Zn6Al	20.2 ± 0.6 (4)	6.1 ± 0.3 (2)

Wagner mechanism operates in this system. At early stages of oxidation, corresponding to the formation of $\sim 3 \times 10^{-6}$ cm-thick scales, Al_2O_3 , FeAl_2O_4 , and Cr_2O_3 were identified, whereas at longer times ($\sim \mu\text{m}$ -thick scales) only Al_2O_3 could be found.

It is the purpose of the present work to obtain a more definite validation of Wagner's tentative proposal by systematically investigating the oxidation behavior of a series of binary and ternary alloys. For ease of interpretation and experimentation Ag was chosen as the principal component since it does not form a stable oxide above 460°K at one atmosphere of oxygen, and Zn and Al were chosen as the secondary getter and the protective scale former, respectively, in accord with their relative tendencies to form stable oxides. The system Ag-Zn-Al is thus a model system in which the complexities of multiphase and multilayer surface oxides are not encountered.

As a result of prior investigations on Ag-In (10,11) and other alloys (12-17), in the present study one may expect that Ag-Al and Ag-Zn alloys with low Al and Zn contents would show internal oxidation, whereas those of higher (> 15 a/o) Al and Zn contents would show external oxidation. The ternary Ag alloys of low Al and Zn contents also may show internal oxidation whereas if the Wagner hypothesis holds, ternary alloys of low Al but high Zn content should exhibit external oxidation and a low rate of oxidation through formation of an Al_2O_3 surface layer.

Experimental Procedure

Alloy samples were exposed to 1 atm of oxygen at 823°K (550°C) and in a few cases at 923°K (650°C). Except where specifically stated, data are for 823°K. The alloys, Table I, were prepared from 99.9999% Ag, 99.9999% Al, and 99.999% Zn by zone leveling in a high-purity graphite boat under an atmosphere of Pd-purified hydrogen; the Ag and Zn metals were deoxidized prior to alloying by melting under the same atmosphere. This melting procedure was found to be the best of several tried; appreciable Zn loss was encountered in the melting of the high Zn alloys but since the loss per zone leveling pass was fairly reproducible, sufficiently close estimates of the required Zn content in the initial charge could be made. The zone-leveling homogenization was determined to be satisfactory by chemical analysis. Subsequent electron microprobe examination of the specimens detected no microsegregation in the alloys. The alloys are all well within the composition range of the terminal fcc phase of the binary Ag alloys so that metallic-metallic phase transformations are not likely during oxidation. A section of each ingot was cleaned of oxide by grinding and was cold-rolled to 0.05 cm. Specimens 1.3 cm on edge were cut from the strip and a small hole drilled at one corner for suspension. The specimens were then cleaned in chloroform, rinsed in alcohol, and dried prior to a recrystallization anneal at 873°K in an evacuated silica capsule for 7.2 ksec (20 hr). Grain size of several of the alloys was measured and found to be in the range of 0.05 to 0.2 μm . Immediately prior to a run the specimen was electrolytically etched in 1N HNO_3 at 0.06 A cm^{-2} for 30 sec, as suggested by Rapp (11). This procedure gave sufficiently reproduc-

ible results in the oxidation runs. A 3-winding, vertical-silica) tube furnace (18, 19) with a 4-cm uniform-temperature zone of $\pm 0.2^\circ\text{K}$ was used for the oxidation experiments.

Before a run a specimen was weighed by a balance precise to 0.05 mg and then suspended in the cold zone above the furnace by a silica hook and stainless steel chain. With the reaction zone at 823°K (or 923°K) and a steady upward oxygen flow of approximately 2 $\text{cm}^3 \text{sec}^{-1}$ the specimen was lowered into the reaction zone, held there for a prescribed time, and then raised to the cold zone. After cooling the specimen was removed and weighed. Weight gain data as a function of oxidation time were obtained by oxidizing several specimens of a given alloy for different times in this manner. Each specimen was then examined by cross-section metallography and other methods. In a few experiments continuous weightings were made using another furnace of similar design and a thermobalance; this produced complete weight gain-time data with one specimen. Results were essentially the same with both weighing methods; unless otherwise stated, data in this paper were obtained by the discontinuous weighing method. Cross-section metallographic examination and electron microprobe analysis after completion of a run helped ascertain the structure and composition of the oxidation zone.

Results

The data are presented and analyzed in separate sections, first those pertaining directly to the Wagner hypothesis and subsequently two other sections, one on the Ag alloys of low solute content which undergo exclusive internal oxidation and the other on the alloys of intermediate solute content which eventually exhibit a low oxidation rate after an initial period of high oxygen uptake.

Transition in ternary alloys (Wagner hypothesis).—Weight-gain, m , and thickness, ξ , of the zone of internal oxidation, for reaction of Ag-Al and Ag-Zn specimens with oxygen at 1 atm and 823°K (550°C), are shown in Fig. 1-3. Ag3Al (Ag-3 a/o Al) was found to oxidize at a very high rate, and according to the parabolic law for the duration of the test of 61.2 ksec (17 hr) except for a relatively short initial period. This, along with other information to be presented, established that the Ag3Al alloy undergoes essentially exclusive internal oxidation, and, hence, is suitable for investigating the role of Zn additions. In contrast the rate of oxidation of Ag10Al and Ag14Al is very low (Fig. 1) as a result of the formation of a dense, protective Al_2O_3 layer. The addition of Zn by itself to Ag is not as effective as Al additions in reducing the oxidation rate (Fig. 3), e.g., the Ag21Zn alloy oxidizes at a rate nearly matching that of Ag3Al.

The weight-gain at 823°K for ternary Ag-Zn-Al alloys containing 3 a/o Al and various amounts of Zn are shown in Fig. 4. Additions of 21 or 25 a/o Zn to the Ag3Al alloy are sufficient to reduce the rate of oxidation to a very low value, similar to that of the Ag14Al alloy. Actually the rate attained after an initial period is even lower than that indicated by the total weight gain of 150 μg since extrapolation of the data to zero time gives a nonzero intercept (100 to 150 μg), i.e., there is an initial, though brief, higher rate

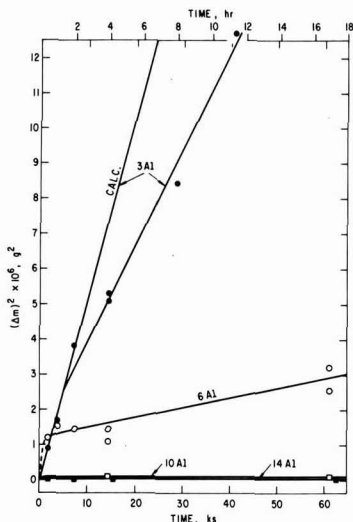


Fig. 1. Weight gain-time data for Ag3Al(●), Ag6Al(○), Ag10Al(□), and Ag14Al(■) specimens at 823°K. Calculated weight gain for exclusive internal oxidation (Eq. [7]) are given for comparison.

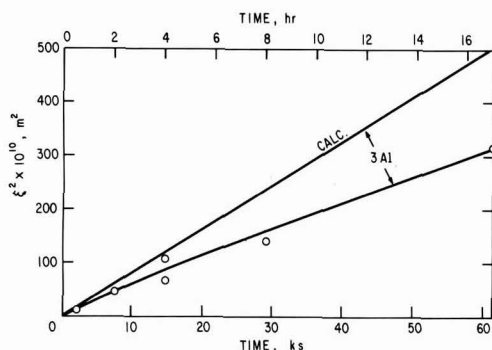


Fig. 2. Measured thickness-time data of the zone of internal oxidation on Ag3Al(○) specimens. Each point represents the mean value of 16 or more measurements on each specimen; the largest standard deviation was only 2.2×10^{-5} m for the mean value at 61.2 ksec. Calculated thicknesses (Eq. [5]) of the internal oxidation zones are given for comparison.

of oxidation. Similarly there was found an initial higher rate of oxidation for the binary Ag10Al and Ag14Al alloys. The exceedingly low rate of oxidation attained in the second period is essentially the same for the alloys, Ag10Al, Ag14Al, Ag21Zn3Al, and Ag25Zn3Al, in agreement with the formation of a dense, protective Al_2O_3 layer on each of the alloys.

Similar oxidation results were obtained for the ternary alloys containing 6 a/o Al and varying amounts of Zn. These data, though, are less instructive since according to Fig. 1, the Ag6Al alloy already exhibits partial formation of a protective Al_2O_3 layer.

Cross-section metallographic observations of the specimens are in agreement with the above interpretation of the kinetic data. Oxidized Ag3Al specimens show a zone of internal oxidation (Fig. 5).

In contrast the Ag10Al, Ag14Al, Ag21Zn3Al, and Ag25Zn3Al specimens form only a thin oxidized region along the surface (Fig. 6 and 7). The detailed morphology of this region is the same for all four alloys, and is more complicated than the formation merely of a dense Al_2O_3 layer at the surface. Proceeding outward

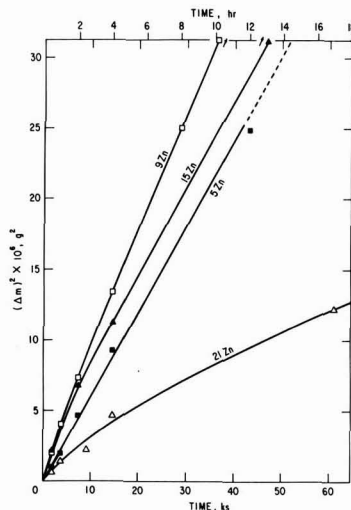


Fig. 3. Weight gain-time data for Ag5Zn(■), Ag9Zn(□), Ag15Zn(▲), and Ag21Zn(△) specimens.

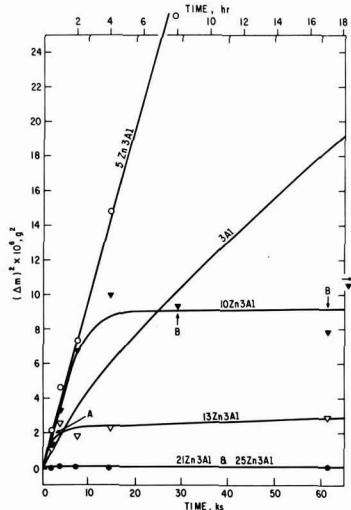


Fig. 4. Weight gain-time data for Ag5Zn3Al(○), Ag10Zn3Al(▼), Ag13Zn3Al(▽), Ag21Zn3Al(●), and Ag25Zn3Al(●) specimens, and for Ag3Al from Fig. 1.



Fig. 5. Cross-section micrograph showing a zone of internal oxidation (Z.I.O.) in a Ag3Al sample which was oxidized for 29 ksec at 823°K. Etched.

from the alloy there is often a discontinuous porous layer, then a dense layer, and finally patches of a white, metallic-appearing material. A porous region appears as a cavity or gap unless precautions are taken to avoid pullout during metallographic preparation as in the middle micrograph of Fig. 6.

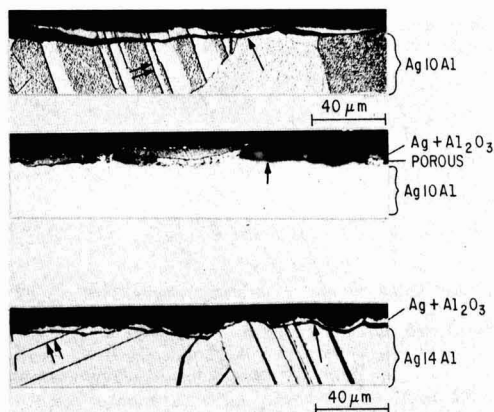


Fig. 6. Cross-section micrographs of oxidized Ag10Al and Ag14Al samples. The top and bottom micrographs are etched. ↑ indicates gap. ↑↑ indicates twin boundary.

The patches of white material were identified as Ag by electron microprobe examination. Silver was seen on the surfaces of many specimens, and particularly those containing higher amounts of solute as in Fig. 7. Wriedt and Darken (20) also observed Ag patches on the surface of internally oxidized Ag-Al alloys, and found that the amount increased with time of oxidation. They identified them by x-ray diffraction. Two sets of Ag lines were observed: one from the Ag patches on the surface and the other from an expanded and distorted Ag matrix within the internal oxidation zone.

The dense layer contains the alloy microstructure (Fig. 6 and 7), i.e., grain and twin boundaries, characteristic of a zone of internal oxidation. Yet, for the ternary alloys in particular, these layers reflect light rather poorly, much as oxide layers do. Furthermore, in the case of the ternary alloys the dense layer is decidedly enriched in Zn and approximately unchanged in Al relative to the bulk alloy according to electron microprobe examination; this indicates a high volume per cent of oxide, mainly ZnO, in the layer. The Ag content in the layer on the other hand is lower than in the alloy, in agreement with the presence of Ag on the surface.

Electron microprobe examination was not made for Ag10Al and Ag14Al alloys. Presumably the dense layer has a higher ratio of Ag/Al₂O₃ than in the ternary alloys, since the (alloy) microstructure was more readily revealed by etching and the amount of Ag on the surface was less.

The occurrence of some, albeit very little, "internal" oxidation during exposure of the oxidation-resistant

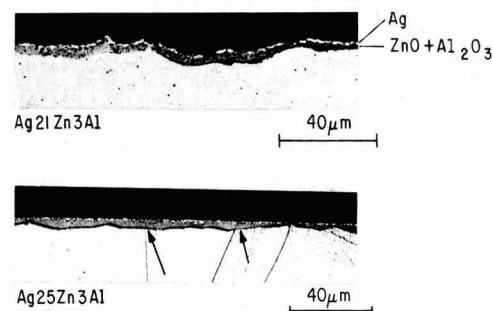
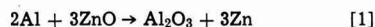


Fig. 7. Cross-section micrographs of oxidized Ag21Zn3Al and Ag25Zn3Al specimens. The bottom micrograph is etched. ↑ points to twin boundaries in the oxidized region.

binary and ternary alloys to oxygen agrees with the brief, higher oxidation rate prior to the establishment of the exceedingly low oxidation rate shown for these alloys in Fig. 1 and 4. The dense Al₂O₃ layer which ultimately forms and reduces the oxidation rate to virtually nil is probably very thin and is not resolved by optical microscopy.

Discussion.—These data show that the addition of Zn to a Ag alloy containing a relatively small amount of Al results in the formation of a dense, protective Al₂O₃ layer. The beneficial effect of Zn in the formation of this layer is illustrated in Fig. 8. These data support the Wagner hypothesis (8, 21, 22) for the transition from internal to external oxidation in ternary alloys and, along with other data to be described, give some clue as to further details. On the basis of the data the transition is visualized as follows: When the surface of a Ag21Zn3Al alloy is initially bare, ZnO and Al₂O₃ are nucleated at the beginning of oxidation. The relatively large amount of Zn provides for the formation of sufficient oxide in the surface region to effectively block the diffusion of oxygen. Much of the initial silver in this region is "extruded" (20) or migrates to the surface; the latter may occur if the activity of Ag in the zone of internal oxidation is greater than unity as a result of strain. The presence of a ZnO layer ensures that the activity of oxygen in the alloy is very low, since it is determined by the coexistence of ZnO and Zn. As a result, the diffusion of oxygen into the alloy is negligible. In view of the depletion of Al in the alloy next to the surface, Al atoms migrate towards the surface without being converted to Al₂O₃ on their way. Hence, the supply of Al atoms diffusing toward the surface is sufficient for preferential reaction of the oxygen with Al. In addition, the initially formed nuclei of ZnO may be converted at least in part to Al₂O₃ by the displacement reaction



Once a dense Al₂O₃ layer is formed between the outer Zn-rich oxide layer and the bulk alloy the oxidation rate falls to the very low value determined by transport through Al₂O₃.

Hagel (23) offers an alternative explanation of the role that a third component plays in the formation of a protective layer; it is based on the degree of protection afforded by an α -Al₂O₃ vs. a γ -Al₂O₃ layer. He suggests that transformation from γ -Al₂O₃ to a more protective α -Al₂O₃ layer is enhanced by the presence of certain alloying elements. This mechanism, however,

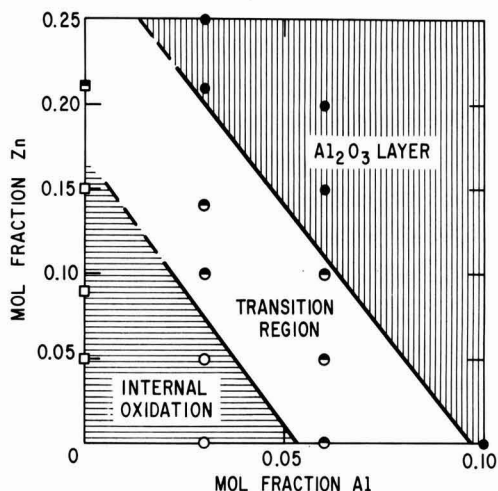


Fig. 8. Chart illustrating the beneficial effect of Zn in Ag-Zn-Al alloys for promoting the formation of a protective Al₂O₃ layer.

cannot be responsible for the transition to low oxygen uptake upon the addition of Zn to Ag-Al alloys since Ag₃Al without Zn additions does not form any Al₂O₃ layer.

Hence it seems reasonable to proceed on the basis that some, and perhaps many, of the multicomponent industrial alloys rely for their superior oxidation resistance on the "gettering action" of certain components which themselves may not be a constituent of the final protective oxide layer. It follows that the basic principles advanced by Wagner (8) may be used in the development of new alloys. Certain complications, however, must be avoided. Wood (24) points out that, depending on the kinetics of growth of the solvent metal oxide and on the alloy interdiffusion coefficient, the solvent metal oxide may engulf (overgrow) the nuclei of the solute metal oxide in accord with the earlier theoretical consideration of Wagner (21) and thereby preclude the formation of a protective solute metal oxide layer. He shows for Fe-Cr-Al alloys of relatively low chromium and aluminum contents that it is possible for the iron oxides to overgrow and undercut the Cr₂O₃ and spinel nuclei. This seemingly is not a problem with the higher alloyed Fe-Cr-Al alloys where a protective layer is well known to form at low total oxygen uptake (1-6), nor with certain other oxidation-resistant, Fe-base alloys, according to recent data of Boggs (7).

Exclusive internal oxidation.—For diffusion control and fixed boundary conditions the depth, ξ , of the zone of internal oxidation is given as a parabolic function of the time, t ,

$$\xi = 2\gamma (D_0 t)^{1/2} \quad [2]$$

where D_0 is the diffusivity of oxygen in the two phase (solvent metal + solute oxide) zone of internal oxidation, and γ is a dimensionless parameter. Darken (25),

Wagner (26), Rhines *et al.* (27), and Meijering and Druyvesteyn (28) have solved the relevant diffusion equation. For the special case that movement of the front is completely determined by diffusion of oxygen in the metal one has the conditions (26)

$$\gamma \ll 1 \quad [3]$$

and

$$\gamma D_0/D_M \gg 1 \quad [4]$$

in which case Eq. [2] becomes

$$\xi \cong \left[\frac{2N_0^{(s)} D_0 t}{\nu N_M^{(o)}} \right]^{1/2} \quad [5]$$

where $N_0^{(s)}$ is the solubility of oxygen in the external interface of the solvent metal, ν is the atomic ratio of oxygen to metal in the internal oxide and $N_M^{(o)}$ is the mol fraction of the metal M in the bulk alloy. The solubility product of the internal oxide is here assumed to be negligibly small. The conditions of Eq. [3] and [4] were found to be satisfied for the alloys in the present investigation which contain low amounts of Al and Zn. For example, after internal oxidation of Ag₃Al for 14.4 ksec (4 hr) the measured ξ is 8.7×10^{-3} cm (Fig. 2), and $\gamma = 0.03$ which satisfies conditions in Eq. [3] and also Eq. [4] since D_0/D_M is very large.

Modification of Eq. [5] gives a relation for the weight gain, Δm , of the specimen

$$\frac{\Delta m}{A} \cong \xi \frac{N_M^{(o)}}{V_m} \cdot \nu W_O \quad [6]$$

where V_m is the molar volume of the alloy and W_O is the atomic weight of oxygen. Substituting Eq. [5] into Eq. [6] one has

$$\frac{\Delta m}{A} \cong \frac{W_O}{V_m} [2\nu N_M^{(o)} N_0^{(s)} D_0 t]^{1/2} \quad [7]$$

Values for $N_0^{(s)}$ and D_0 in Eq. [5-7] were assumed to be the solubility and diffusivity, respectively, of pure Ag as reported by Eichenauer and Müller (29), ν was assumed to be 1.5 and 1.0 corresponding to the

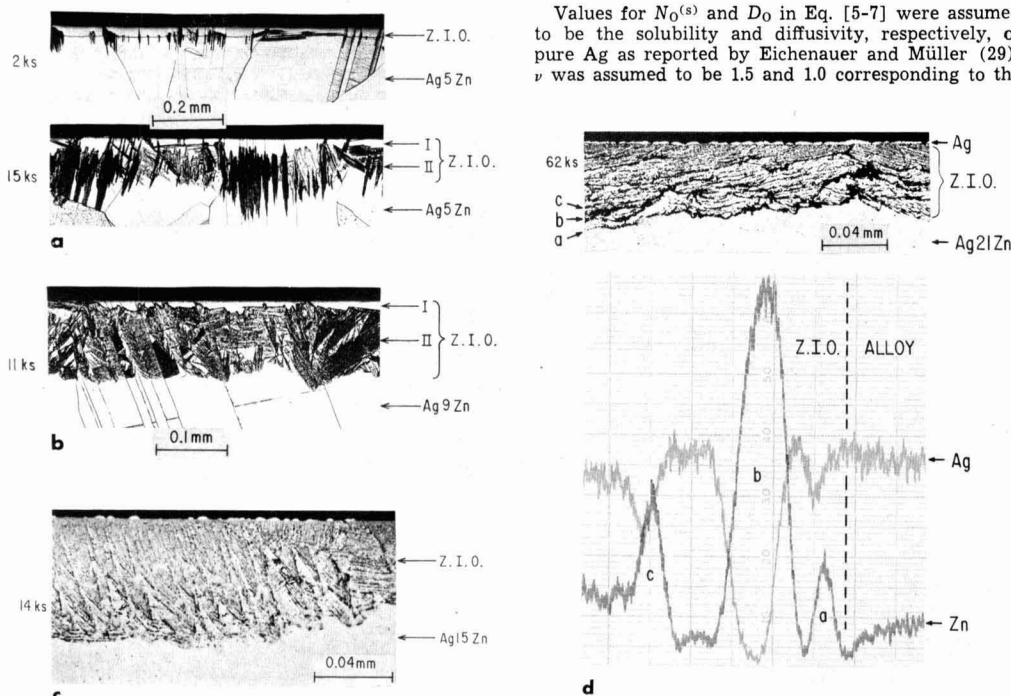


Fig. 9. Cross-section micrograph showing morphologically different zones of internal oxidation in Ag-Zn specimens, and an electron microprobe analysis which shows that the black "lines" within the zone of internal oxidation (Z.I.O.) of the Ag₂₁Zn specimen are Zn-rich. Ag trace lags the Zn trace by 1.2 μ m; probe traverse was from right to left. Specimens in (a) and (b) were etched.

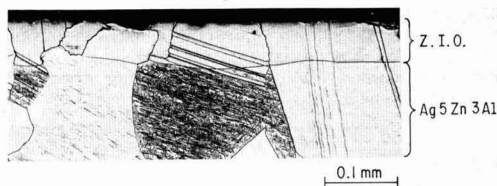


Fig. 10. Cross-section micrograph of a Ag5Zn3Al sample after 7.2 ksec at 823°K showing a zone of internal oxidation. Etched.

formation of stoichiometric Al_2O_3 and ZnO , respectively, $V_M = 10 \text{ cm}^3 \text{ mol}^{-1}$ and $A = 3.5 \text{ cm}^2$. Data in Fig. 1-4 indicate that the alloys Ag3Al, Ag5Zn, Ag9Zn, and Ag5Zn3Al undergo exclusive internal oxidation. On the other hand definite departures occur for all other alloys, e.g., the weight gain for Ag15Zn (Fig. 3) is lower than that for Ag9Zn and significantly lower than the calculated value from Eq. [7]. Still, Ag15Zn and some of the other alloys of intermediate solute content undergo appreciable internal oxidation and are discussed later in the section on transition alloys.

Cross-section metallographic examination shows a zone of internal oxidation for the Ag3Al (Fig. 5), Ag5Zn, Ag9Zn (Fig. 9a and 9b), and Ag5Zn3Al alloys (Fig. 10). Internal oxidation of the Ag-Zn alloys is complex. Examination of oxidized Ag5Zn specimens after polishing and etching reveals what appears as a "normal" zone of internal oxidation next to the surface and a second morphology (of internal oxidation) next to it which is comprised of acicular segments aligned mostly perpendicular to the surface (Fig. 9a). The acicular segments begin to develop after about 2 ksec oxidation as seen in the top micrograph, and to line up along twin boundaries or other planes which presumably are unresolved (micro) twin boundaries. At higher magnification the acicular segments are seen to be comprised of fine, parallel-arranged rows of material; this material may be porous as indicated by the fact that pull-out occurs during metallographic polishing. After etching, this structure is readily revealed as gaps or cavities in the scanning electron microscope (Fig. 11). The change from the normal to the acicular morphology occurs in the absence of a noticeable change in the kinetics of oxidation (Fig. 3).

Two morphologies of internal oxidation are also observed for Ag9Zn (Fig. 9b). The second morphology for Ag9Zn forms at an earlier stage and appears less acicular and less aligned perpendicular to the surface. In the higher Zn, binary alloys, on the other hand, only the second morphology, in further modified form, is observed. In the most Zn-rich alloy (Ag21Zn) the rows of material lie mainly parallel to the surface. It is shown in the next section that the formation of layers parallel to the surface is characteristic of alloys of intermediate solute content, i.e., those which often exhibit a two-stage kinetic behavior, and a total oxygen uptake between that for exclusive internal oxidation and that for formation of a dense, protective oxide layer at the surface.

Electron microprobe examination of the cross-sectioned Ag3Al and Ag5Zn specimens showed that the contents of the component metals within the zones of internal oxidation were essentially the same as in the original (unoxidized) alloys. Individual internal oxide precipitates are not resolved since the area analyzed by the beam is large relative to the precipitate size. The absence of solute enrichment within the zone of internal oxidation is additional justification for the assumption that for these alloys the kinetics of the internal oxidation process are controlled by the diffusion of oxygen within the zone of internal oxidation and, hence, of the applicability of Eq. [5].

Discussion.—The internal oxidation of Ag3Al appears to be uncomplicated in comparison to that of Ag5Zn and other alloys of higher solute content. The somewhat lower-than-calculated values of ξ and Δm for Ag3Al may be the result of a slightly reduced oxygen flux as a result of incipient "blocking" by the Al_2O_3 precipitates, or the solubility of oxygen may be lower as a result of strain (30).

For the other alloys, in which the thickness of the zone of internal oxidation was irregular the "average" observed ξ for each alloy is in accord with Eq. [5] and values of $N_0^{(s)}D_0$ in the literature. However, the maximum ξ observed at only a few locations yields a significantly larger $N_0^{(s)}D_0$ product, e.g., $N_0^{(s)}D_0(\text{max})$ for Ag5Zn equals $9 \times 10^{-10} \text{ cm}^2 \text{ sec}^{-1}$ vs. $1.85 \times 10^{-10} \text{ cm}^2 \text{ sec}^{-1}$ for pure Ag (29). This may be explained by significant interface diffusion or gas phase transport through pores of the acicular structure.

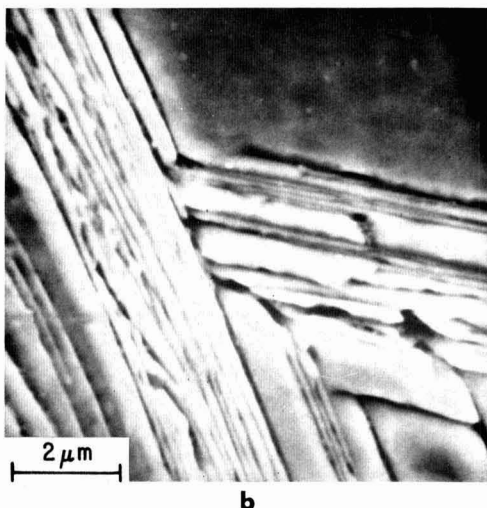
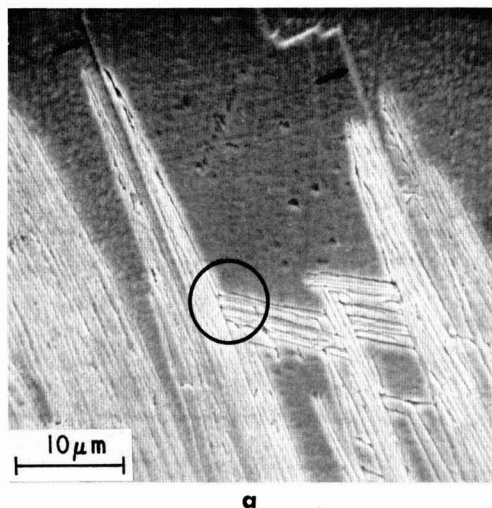


Fig. 11. Cross-section, scanning electron micrographs of an oxidized Ag5Zn specimen showing the acicular structure as gaps or cavities after pullout during mechanical polishing and subsequent etching. Micrograph in (b) is enlargement of circled region in (a). \uparrow indicates twin boundary.

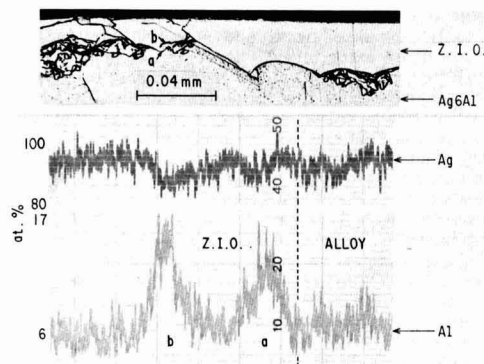


Fig. 12. Cross-section micrograph of an etched Ag6Al sample after 62 ksec of oxidation at 823°K, and an electron microprobe analysis which shows that the black "lines" in the region of the boundary between the alloy and the zone of internal oxidation (Z.I.O.) are Al-rich. Ag trace lags Al trace by 1.2 μ m; probe traverse was from right to left.

Transition region in binary and ternary alloys.—Data in Fig. 1-4 show that an induction period of large oxygen uptake precedes a falloff in the oxidation rate for the alloys of intermediate solute content, i.e., Ag6Al, Ag21Zn, Ag10Zn3Al¹, and Ag13Zn3Al. In a sense, the oxidation resistant alloys, Ag10Al, Ag14Al, Ag21Zn3Al, and Ag25Zn3Al also belong in this group since they, too, exhibited an, albeit very short, induction period.

Cross-section optical metallographic examination of oxidized specimens of the Ag6Al, Ag21Zn, Ag10Zn3Al, and Ag13Zn3Al alloys always shows a zone of internal oxidation containing what appears as black, ragged lines usually aligned roughly parallel to the surface (Fig. 9d and 12). These "lines," sometimes referred to in the literature as films, have been observed in Cu-Si (12), Ag alloys (31, 32, 11), Fe-Al (33), Ni-Al (34), and other alloys. Meijering (32) found that their frequency and thickness increased with solute content and that alloys which contain them oxidize at a lower rate. Elongated shapes and alignment of internal oxide precipitates including needles, plates, and dendrites have also been observed by electron microscopy for

¹Continuous weighing measurements give a weight-time curve similar to that shown and indicate that the unusually large scatter of points from the discontinuous weighing measurements for Ag10Zn3Al is not significant.

various systems by Kahlweit and co-workers (35, 36) and others (33).

The material appearing as black lines in Fig. 9d and 12 is shown to be porous by the fact that pullout readily occurs during metallographic preparation. After appreciable pullout, gaps or cavities remain which are revealed by scanning electron microscopy (Fig. 13). Microhardness measurements show that these regions are softer than the neighboring two-phase material (Ag + oxide), in agreement with their porous structure.

Electron microprobe analysis shows that the layers even after appreciable pullout are rich in the solute metal, undoubtedly in the form of oxide (Fig. 9d and 12). The traces give average values, i.e., the magnitudes of the local departures from the alloy composition are probably greater than indicated in the microprobe traces. The layers within the zone of internal oxidation for Ag10Zn3Al consist of oxides of both Al and Zn, according to electron microprobe analyses.

The top micrograph of Fig. 14 is of the Ag10Zn3Al alloy after 1.8 ksec (30 min) of oxidation and corresponds to the initial period of the high rate of oxidation (point A in Fig. 4). At these early stages of oxidation porous oxide layers are, for the most part, absent within the zone of internal oxidation. They are first observed along grain boundaries between the surface and the internal oxidation front and then along the front itself. The middle and bottom micrographs of Fig. 14 are of other specimens of the same alloy, but correspond to the later, very low rate of oxidation (point B in Fig. 4). In the bottom micrograph the specimen was etched to reveal the twin and grain boundaries. At these longer oxidation times the layers are common features within and at the front of the zone of internal oxidation, as they are after comparable oxidation times for Ag21Zn and Ag6Al (Fig. 9 and 12).

The thickness of the zone of internal oxidation varies appreciably for these alloys, in contrast to the alloys of lower solute content which do not form protective oxide layers. Some regions, usually amounting to less than 5% of the surface, are observed in cross-section to be free from internal oxidation. Presumably in these regions a protective oxide layer forms immediately upon contact of the specimen with the oxidizing environment. Such behavior has previously been observed by Rapp (11) and others.

A slight drop of the Zn content in the unoxidized portion of the Ag21Zn specimen at the internal oxidation front in Fig. 9d indicates enrichment of Zn in the zone of internal oxidation. Diffusion of solute metal and, in addition, of oxygen along grain boundaries in the alloy ahead of the internal oxidation front were

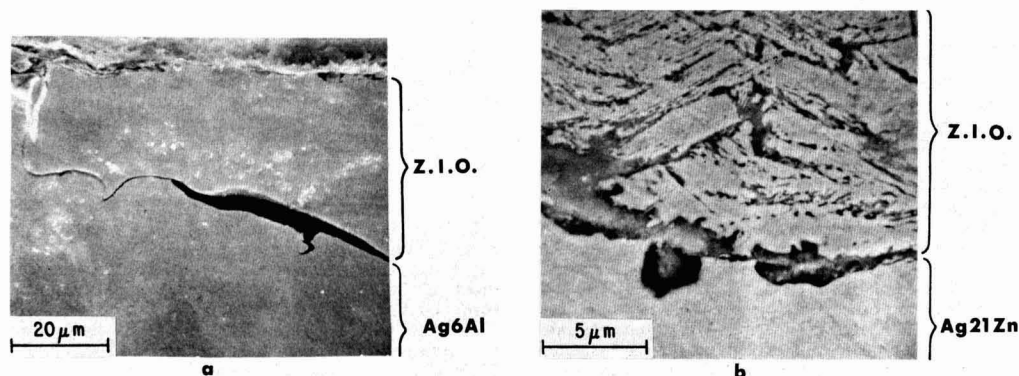


Fig. 13. Cross-section, scanning electron micrographs showing a gap(s) along the boundary between the alloy and the zone of internal oxidation (a) for an oxidized (923°K) Ag6Al specimen, mechanically polished and etched, and (b) for an oxidized Ag21Zn specimen, mechanically polished. Different phases are not distinguishable.

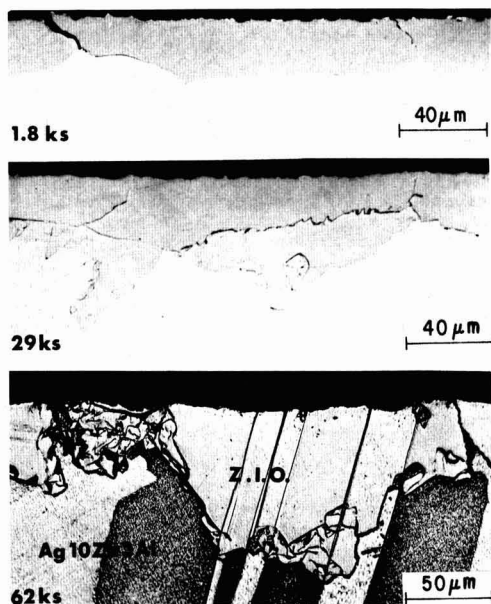


Fig. 14. Cross-section micrographs of oxidized Ag10Zn3Al specimens illustrating black "lines," identified as Al- and Zn-rich regions, within the zone of internal oxidation. The bottom micrograph is etched.

indicated also for Ag6Al and the ternary alloys which oxidize according to the kinetics of the transition region. Subsequent deformation of these specimens revealed that grain boundaries within the nominally unoxidized portion of the specimens had become embrittled.

Discussion.—Transition from internal to external oxidation does not take place at a definite concentration in these alloys but rather over a fairly wide composition range (Fig. 8). This occurs for specimens of identical thermal and mechanical history and surface preparation. Rapp has already showed that the boundary of the transition region depends to some extent on the prior surface preparation.

The data in the present paper show further that for alloys in the transition region the attainment of a low rate of oxidation is preceded by an induction period during which the oxidation rate is much higher and a zone of internal oxidation forms. The occurrence of an induction period is not surprising in view of early considerations by Wagner (21, 22). Chattopadhyay and Wood (37) have recently emphasized the occurrence of transient behavior during initial external scale formation accompanied by internal oxidation.

The main question for binary and ternary alloys in the transition region (and seemingly general to all of the alloys which attain a low oxidation rate) is where and how a dense oxide layer of the solute metal is formed once internal oxidation has transpired. Time invariant diffusion behavior is usually assumed in analyses of oxidation processes, except initially when diffusion control would require an infinite rate. Applying the concept generally means that for a given set of experimental conditions (p_{O_2} , solute content, etc.) a single oxidation process, e.g., internal oxidation, occurs for the duration of the experiment and a single rate constant is obtained. When exceptions to such behavior are observed during internal oxidation they can sometimes be traced to the initial period (prior to the establishment of diffusion control) when starting conditions allow oxidation to occur heterogeneously over the surface. One specific explanation of the transient

behavior is that patches of dense oxide which form initially spread sideways and eventually impinge to give a dense oxide layer at the external surface (38). Then one has the end of inward transport of oxygen, i.e., the extremely low oxidation rate which is observed after an initial period of a high rate of oxygen uptake. For this mechanism to operate it is necessary that Al can diffuse to the surface after internal oxidation begins. This would appear to be possible along segments of unoxidized alloy which extend to the surface. A surface scale is sometimes observed on the Ag6Al specimens; portions of one are barely visible in Fig. 12.

Another factor which may account for a change in the diffusion kinetics at some stage of the oxidation process is void formation during the internal oxidation process; voids may block the diffusion of an important species and thereby be a precursor to the formation of a dense Al_2O_3 layer along the boundary between the zone of internal oxidation and the alloy.

There is some reason to suspect that voids do form at temperature as part of the internal oxidation process. The easy pullout of material within the zone of internal oxidation indicates porosity which is developed either as a result of internal oxidation or of cooling after the oxidation run. Features usually associated with nonuniform contraction during cooling, however, such as matching surfaces, are not very evident.

Conclusions

Weight gain data and cross-sectional metallographic examination show that whereas a Ag3Al alloy exhibits internal oxidation without formation of a dense Al_2O_3 layer, upon addition of 21 or 25 at/o Zn internal oxidation is completely suppressed and a dense highly protective Al_2O_3 layer is formed. These data support the hypothesis advanced by Wagner (8) that Zn may be considered as a secondary getter for oxygen atoms so that virtually no oxygen atoms diffuse into the alloy and, therefore, aluminum atoms can diffuse to the surface without being intercepted by oxygen atoms. Newly arriving Al atoms may then form additional Al_2O_3 by a displacement reaction with initially formed nuclei of ZnO. Other metals such as chromium and silicon in base metal alloys containing aluminum as the least noble constituent, e.g., Fe-Cr-Al, may be expected to behave similarly in the formation of a highly protective layer of Al_2O_3 .

For Ag5Zn and Ag9Zn the internal oxidation process changes at a certain depth to one which is strongly influenced by the microstructure. The front of internal oxidation is irregular. At points of greater penetration the $N_0^{(62)}D_0$ product is significantly larger than that for pure Ag.

For the "transition" alloys the formation of a protective Al_2O_3 layer is preceded by an induction period during which internal oxidation occurs. Rows of aluminum oxide and/or zinc oxide form in alignment roughly parallel to the surface within the zone of internal oxidation. It is not clear though if these layer-like regions are instrumental in the eventual attainment of a lower rate of oxidation or are simply a consequence of a reduced inward flux of oxygen caused by the eventual formation of a continuous, dense Al_2O_3 layer at the surface.

Acknowledgments

It is a pleasure to acknowledge the considerable contribution of C. Wagner of the Max Planck Institut für Physikalische Chemie who outlined the experiments in this paper and made many helpful comments throughout the course of this investigation. Valuable discussions with several colleagues are also gratefully acknowledged, especially those with L. S. Darken and W. E. Boggs. Considerable assistance was provided on the oxidation experiments by H. A. Hughes, in the metallographic examinations by R. M. Lytle, P. J. Byrne, C. E. Brickner, and W. Gundaker, and on alloy preparation by B. B. Rice. The author is also grateful

to B. F. Oliver of the University of Tennessee for advice on preparation of the various alloys.

Manuscript submitted June 25, 1971; revised manuscript received ca. Oct. 5, 1971. This was Paper 116 presented at the Atlantic City Meeting of the Society, Oct. 4-8, 1970.

Any discussion of this paper will appear in a Discussion Section to be published in the December 1972 JOURNAL.

REFERENCES

1. A. Portevin, E. Pretet, and H. Jolivet, *Rev. Met.*, **31**, 101, 186, 219 (1934).
2. E. Scheil and E. H. Schulz, *Arch. Eisenhuettenw.*, **6**, 155 (1932/33).
3. E. Scheil and K. Kiwit, *ibid.*, **9**, 405 (1935/36).
4. E. A. Gulbransen and K. F. Andrew, *This Journal*, **106**, 294 (1959).
5. I. Pfeiffer, *Z. Metallk.*, **53**, 309 (1962).
6. G. C. Wood and M. G. Hobby, *Proc. Intern. Congr. Met. Corr.*, 3rd Moscow, Vol. 3, 102 (1966).
7. W. E. Boggs, Applied Research Laboratory, U.S. Steel Corp., Monroeville, Pa., Private communication (1970).
8. C. Wagner, *Corrosion Sci.*, **5**, 751 (1965).
9. J. S. Dunn, *J. Inst. Metals*, **46**, 25 (1931).
10. I. Dietrich and L. Koch, *Z. Metallk.*, **50**, 31 (1959).
11. R. A. Rapp, *Acta Met.*, **9**, 730 (1961).
12. K. W. Fröhlich, *Z. Metallk.*, **28**, 368 (1936).
13. J. P. Dennison and A. Preece, *J. Inst. Metals*, **81**, 229 (1952/53).
14. L. E. Price and G. J. Thomas, *ibid.*, **63**, 21 (1938).
15. F. N. Rhines and B. J. Nelson, *Trans. Am. Inst. Min. Met. Eng.*, **156**, 171 (1944).
16. F. Maak, *Z. Metallk.*, **52**, 538, 545 (1961).
17. W. E. Boggs, *This Journal*, **118**, 906 (1971).
18. L. S. Darken, *Trans. AIME*, **180**, 430 (1949).
19. R. P. Smith, *Acta Met.*, **1**, 578 (1953).
20. D. R. Wriedt and L. S. Darken, summarized in part by L. S. Darken, *Trans. Am. Soc. Metals*, **54**, 600 (1961).
21. C. Wagner, *This Journal*, **103**, 627 (1956).
22. C. Wagner, *ibid.*, **99**, 369 (1952).
23. W. C. Hagel, *Corrosion*, **21**, 316 (1965).
24. G. C. Wood, *Oxid. Metals*, **2**, 11 (1970).
25. L. S. Darken, *Trans. AIME*, **150**, 157 (1942).
26. C. Wagner, *Z. Elektrochem.*, **63**, 772 (1959).
27. F. N. Rhines, W. A. Johnson, and W. A. Anderson, *Trans. AIME*, **147**, 205 (1942).
28. J. L. Meijering and M. J. Druyvesteyn, *Philips Res. Rept.*, **2**, 81, 260 (1947).
29. W. Eichenauer and G. Müller, *Z. Metallk.*, **53**, 321, 700 (1962).
30. J. C. M. Li, R. A. Oriani, and L. S. Darken, *Z. Physikalische Chemie Neue Folge*, **49**, 271 (1966).
31. F. N. Rhines and A. H. Grobe, *Trans. AIME*, **147**, 318 (1942).
32. J. L. Meijering, *Pgh. Internat. Conf. on Surface Reactions*, (1948), p. 101.
33. R. P. Smith, formerly with E. C. Bain Laboratory for Fundamental Research, U.S. Steel Corp., Monroeville, Pa., Private communication (1958).
34. F. S. Pettit, *Trans. AIME*, **239**, 1296 (1967).
35. G. Böhm and M. Kahlweit, *Acta Met.*, **12**, 641 (1964).
36. P. Bolsaitis and M. Kahlweit, *ibid.*, **15**, 765 (1967).
37. B. Chattopadhyay and G. C. Wood, *Oxid. Metals*, **2**, 373 (1970).
38. C. Wagner, Private communication (1970).

Technical Notes



Electrical Switching in Anodic Oxide Films on Zircaloy-2

N. Ramasubramanian

Chalk River Nuclear Laboratories, Atomic Energy of Canada Limited, Chalk River, Ontario, Canada

The advantage of using the Widmanstätten morphology for locating weak spots in anodic oxide films on Zircaloy-2 was reported by us (1). It was shown that the initial electrical breakdowns were centered on the α -platelet boundaries where the intermetallic precipitates and second phase impurities have segregated during cooling the alloy in vacuum from the β phase. These breakdowns were always preceded by switchings to a high conductivity state; the occurrence of one or the other was governed by the load resistance in the circuit. The results obtained on such switching phenomena are presented here.

Experimental

The details regarding material, heat treatment, surface preparation, anodization, and current-voltage measurements have been described elsewhere (1). Zircaloy-2/anodic oxide/metal sandwiches were prepared by evaporation of gold or silver contacts through masks to a thickness of 1000-1500 Å (monitored by a quartz crystal). Silver counterelectrodes were also formed utilizing the Eccobond Solder 56C supplied by Emerson and Cuming Inc. and G. C. Electronics' silver paint. The Eccobond contact was cured at 70°C for 2

hr, and the paint was air-dried. The voltage sources were an Electro Pulse Inc. Model 2140A pulse generator, d.c. from dry cells and a.c. from a Variac. The series resistance was 10 kohm during switch ON operation (high to low impedance state) and varied from 3 to 1 ohm during the low to high impedance, switch OFF operation. Impedance measurements were made using a GR-1680A automatic capacitance bridge.

Results

The electrical switching characteristics of the anodic oxide films on Zircaloy-2 could be classified into three types: (a) the most commonly observed one, associated with the delayed type of breakdown, (b) a nondestructive bistable switching, and (c) transitory switching observed in thin films, 250 to 750 Å thick. Out of a total of thirty tested (as-received material), each carrying four or more diodes, all the specimens exhibited the type (a) and about 15% of the diodes the type (b) switching behavior. All the thin films tested showed the transitory switchings.

Bistable switching, type (a).—The current-voltage characteristics of the diode were traced first at 80° and 190°K; only the leakage currents were measured for potentials of both polarities up to ~60% of the anodizing voltage. Time of holding at various applied volt-

ages was varied from a few seconds to ~ 5 min, with no detectable change in conductivity. Similarly at room temperature a positive bias on the alloy in the same range of voltages did not produce any change in conductivity. However, when a negative potential was applied at room temperature, current bursts were observed at ~ 15 V and holding the alloy at the voltage for a few minutes brought about a switch to the ON state. In this initial ON condition the $i \times V$ relation was ohmic, and the temperature coefficient of resistance was positive.

Considering the case of a 50V film as a typical example, -16.5 V on the alloy for $\frac{1}{2}$ min duration at room temperature turned the diode ON; in the ON state the resistances were 63 and 54 ohm at 300° and 80°K , respectively. A current of 100 mA (60 Hz from a Variac) turned the diode OFF. In the case of diodes carrying evaporated electrodes this initial switch OFF operation resulted in the "single-hole" type of breakdowns (1). When Eccobond solder or silver paint formed the counterelectrode, it was noticed that after the initial switching OFF operation the diode could be turned ON by a positive or a negative bias on the alloy.

A number of ON \rightleftharpoons OFF operations were carried out and the behavior was quite varied: switch ON voltages were in the range of 5 to 27 V; OFF currents varied from 75 to 150 mA and the $i \times V$ relation was either ohmic or nonohmic with a positive or negative temperature coefficient of resistance, respectively.

Bistable switching, type (b).—A few of the diodes exhibited the type (b) switching which occurred in the temperature range of 80° to 300°K when the applied bias exceeded ± 6 V. As the d-c voltage across the oxide film was gradually increased, a sharp increase followed by a rapid decrease in current was observed at ~ 6 V. More such current transients were observed when the applied voltage was increased to ~ 10 V. Then at some stage, when lowering the applied bias, the current suddenly increased by more than two orders of magnitude at around 4 V i.e., a switch to the low impedance ON state. The current-voltage curves showed the following characteristics in the ON state: an initial ohmic portion, a zero temperature coefficient of resistance, a zero differential resistance region, and multiple conduction levels. Any systematic variation of the minimum voltage required for the onset of current bursts with the oxide thickness was not found.

A typical example of the conductivity changes is illustrated in Fig. 1 and 2 for a 2100Å film carrying an evaporated gold contact and tested at liquid nitrogen temperature. In the low impedance ON state a slight instability in current was observed and the $i \times V$ curves were nearly symmetrical for positive and negative bias on the alloy, curves c and d. On warming the sample to room temperature no changes in the $i \times V$ relation were noticed, and the same curves c, d were traced. From the ohmic portion of the curves a resistance of 18.5 kohm can be calculated.

Then the impedance of the diode was measured at 1 kHz, and it was found that this act had effected an ON to OFF switching. The curves shown in Fig. 2 were traced subsequently. At ~ 3 V current transients were noticed and the diode switched ON at 3.2 V, (curve a_2 in the figure). Curves a_3 and a_4 were traced in the ON state; a_4 was found to be symmetrical with a_3 until the current through the diode exceeded 90 μA , the maximum passed immediately after OFF \rightarrow ON switching (curve a_3). When the current through the diode was increased beyond this maximum value, a zero differential resistance portion a_5 was traced, with the increases in applied voltage going almost entirely across the series resistor. Finally the curves a_6 and a_7 were traced. A similar type of behavior was observed when the alloy was biased negative following another impedance measurement, curves b_1 to b_7 in the figure. Switching times for OFF \rightarrow ON transitions (curves a_2

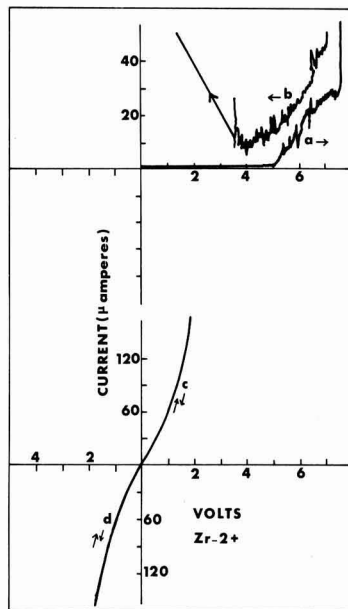


Fig. 1. Tracing of x-y recorder plots of the establishment of conductivity and switching in Zircaloy-2/2100Å anodic oxide film/gold (0.27 cm^2) at 80°K .

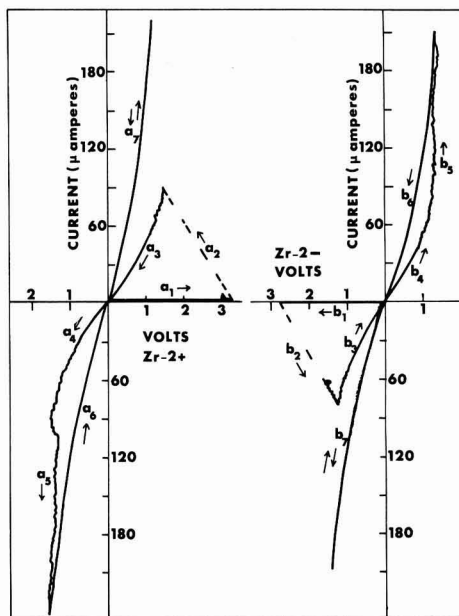


Fig. 2. Switching, zero differential resistance regions and multiple conduction levels; tracing of x-y recorder plots obtained during the tests at 80°K on the diode referred to in Fig. 1.

and b_2 in the figure) were less than 10^{-8} sec, and attempts to trace these current-time curves were unsuccessful.

A number of ON \rightleftharpoons OFF operations similar to that in Fig. 2 were carried out and the $i \times V$ tracings recorded for various maximum currents through the diode in the low impedance state. Switch ON voltages were all around ± 2.5 V. The zero differential resistance region on both the positive and negative sides was seen to cover a current range from ~ 30 to >240

μA . The curves were similar in shape and symmetrical about the origin; the resistances of the ohmic portions varied from 30 to 10 kohm and the switch off currents varied from 500 to 750 μA . No surface changes were noticed on the evaporated counterelectrodes.

Transitory switchings in thin films.—A set of $i \times V$ curves, selected from those obtained at room temperature on a 25V ($\sim 700\text{\AA}$) film, is shown in Fig. 3. At 8.7V negative bias on the alloy the current through the diode increased abruptly, a_1 in the figure followed by a zero differential resistance portion a_2 . Instability in the current flow was noticed when the diode tended to switch OFF and then ON as shown by the loop a_3 , a_4 and a_5 in the $i \times V$ characteristics. When the current through the diode was decreased, slight instability was still noticed and the portion a_7 was traced which passed through the origin. In tracing a_7 the current was gradually reduced to zero, over a period of 15 sec.

Immediately after tracing a_7 the diode was found in the high-impedance state. Then a number of $i \times V$ tracings were made; in each instance the diode was highly resistive to start, was turned to the ON state at about $\pm 1.4\text{V}$ and the $i \times V$ curve in the ON state passed through the origin. In the ON state, during the transitory switching, the $i \times V$ curves were almost linear and the resistance varied in the range of 5 to 8 kohm. Then the diode settled to bistable switching, and the ON state was characterized by an ohmic $i \times V$ relation and zero temperature coefficient of resistance.

Some of the diodes were tested at 80° and 190°K before the room temperature experiments. For voltages up to $\sim 50\%$ of the anodizing voltage, at lower temperatures only the leakage current flow was noticed. At room temperature transitory switching occurred, the easy direction for the first one to be initiated being Zircaloy-2 negative. The number of transitory operations prior to the onset of bistable mode varied among the various specimens and also on a single specimen carrying a number of diodes.

Vacuum-cooled material.—The oxide thickness varied from 1200 to 2500Å and a total of 50 diodes carrying evaporated gold electrodes were tested. All these were characterized by the type (a) bistable switching. The switch ON voltage did not vary with the oxide thickness and was $18 \pm 2\text{V}$. The initial switch OFF operation led to a few isolated single-hole breakdowns centered on the boundaries between the α platelets (1). Subsequent to this initial switch OFF operation, a second set of breakdowns were produced in some of the diodes by having a low series resistance in the circuit and by applying a negative potential of $20 \pm 2\text{V}$ on the alloy. These breakdowns

were more in number than the initial ones and their density averaged to $\sim 10^2/\text{cm}^2$. The diodes were highly conducting following this step; Park and Basavaiah have reported a similar type of behavior in oxide films on evaporated zirconium (2). The scanning electron micrographs of a second set of breakdowns are shown in Fig. 4. Almost all such breakdown spots were also found to be located on the α -platelet boundaries.

Discussion

When Zircaloy-2 is cooled in vacuum from the β phase, second phase intermetallic (Zr-Fe-Cr and Zr-Fe-Ni) particles are precipitated along the α -platelet boundaries. Second phase impurity particles (Zr and C, P, or Si present in ppm quantities) are probably the nucleation sites for the growth of the α -platelets (3). The initial and the subsequent breakdowns, in oxide films on the vacuum-cooled material, were all located on the α -platelet boundaries; the delayed type of bistable switching in these films is in the majority observed in oxide films grown on the alloy in the as-received condition. Therefore, it is reasonable to conclude that the second phase particles in the as-received alloy are the sites of such switching and the associated breakdowns.

Park and Basavaiah identified the conducting filament with the rim around the breakdown spots (2). In our experiments, however, the switch ON operation did not result in a breakdown when the series resist-

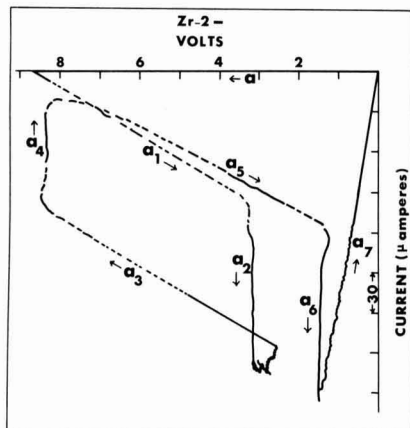


Fig. 3. Zircaloy-2/25 V anodic oxide film/silver (Eccobond, 0.12 cm^2) tested at atmospheric conditions; x-y recorder plots of the transitory switchings.

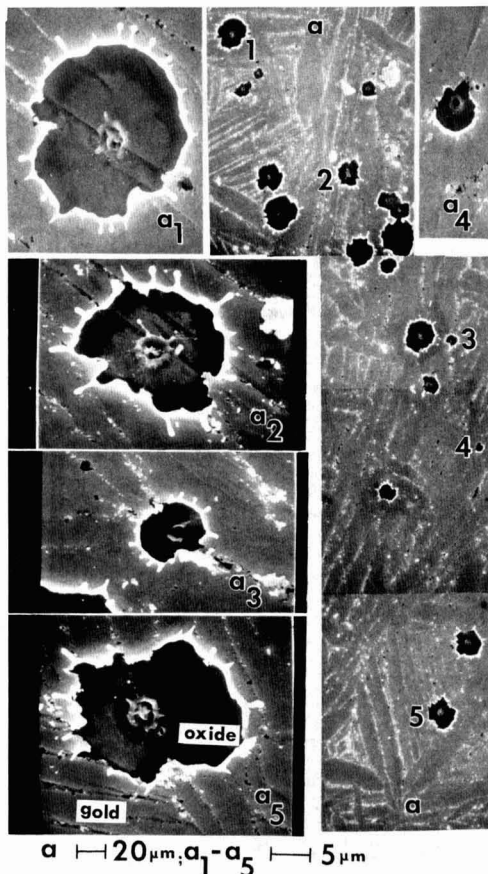


Fig. 4. Scanning electron micrographs of the second set of breakdowns in anodic oxide (2100Å thick) grown on the vacuum-cooled Zircaloy-2.

ance in the circuit was sufficiently high; also, the initial switch OFF operation resulted most often in single breakdown spots and the diode subsequently was highly resistive. Therefore, Park and Basavaiah's observation might represent an intermediate state and the current carrying filament present prior to breakdown is likely to be very different from that produced after the breakdown. The breakdown spots generally were 3 to 4 μm in diameter (cf. Fig. 4); however, the original current carrying filament is likely to have been much smaller in dimensions. Moreover, the oxide grown on the second phase particles has been shown to be highly heterogeneous and porous (1). Therefore, calculation of the resistivity of the filament based on the diameter of the breakdown spot and the anodic oxide (zirconia matrix) thickness would be meaningless. Though a positive temperature coefficient of resistance was found in the ON state, the nature of the filament material thus remains unknown.

At this stage, any attempt to interpret the mechanism of the initial switching would be highly speculative because the composition of the second phase particles, their behavior during wet anodization, the type of oxide grown on them, etc., remain unknown. In this connection, a study of the oxide growth on the inter-

metallics of zirconium and iron, chromium or nickel and their electrical properties might be helpful.

Conclusions

In anodic oxide films on Zircaloy-2, the second phase particles are the sites where a majority of the bistable switchings and the associated breakdowns occur.

Acknowledgments

The author remains indebted to Dr. B. Cox for several profitable discussions. He is most grateful to Mr. T. Trotter who assisted in carrying out the experiments.

Manuscript submitted Feb. 22, 1971; revised manuscript received ca. Jan. 12, 1972. This was Paper 152 presented at the Atlantic City Meeting of the Society, Oct. 4-8, 1970.

Any discussion of this paper will appear in a Discussion Section to be published in the December 1972 JOURNAL.

REFERENCES

1. N. Ramasubramanian and T. Trotter, *This Journal*, **118**, 1797 (1971).
2. K. C. Park and S. Basavaiah, *J. Non-Crystalline Solids*, **2**, 284 (1970).
3. R. A. Holt, *J. Nucl. Mater.*, **35**, 322 (1970).

The Composition of $\text{Ga}_{1-x}\text{Al}_x\text{As}$ Grown from Ga-Rich Solutions as a Function of Growth Temperature and Solution Composition

W. G. Rado, W. J. Johnson, and R. L. Crawley

Scientific Research Staff, Ford Motor Company, Dearborn, Michigan 48121

It has been shown that efficient visible light emitting diodes can be fabricated from liquid phase epitaxially (LPE) grown layers of $\text{Ga}_{1-x}\text{Al}_x\text{As}$ (1). The maximum direct energy gap obtainable is 1.9 eV corresponding to a composition of $x = 0.37$ (2). The work of Panish and Sumski (3) and Ilegems and Pearson (4) on the Ga-Al-As ternary system indicates that $\text{Ga}_{1-x}\text{Al}_x\text{As}$ in the range of $0 < x < 0.37$ can be grown by LPE at or below 1000°C from solutions containing less than about 0.007 atom fraction Al. This communication presents experimental data for $\text{Ga}_{1-x}\text{Al}_x\text{As}$ grown in the temperature range of 800°-950°C from Ga-Al-As solutions containing 0.002-0.014 atom fraction Al.

The $\text{Ga}_{1-x}\text{Al}_x\text{As}$ was grown by LPE on (111)-Ga and As faces of single crystal GaAs substrates that were doped with Te or Se in the range of 0.5 to 2.5×10^{18} electron/cm³. The growth apparatus was similar to that of Hayashi et al. (5) in that the solution was pushed over the substrate. Our apparatus also employed a special provision to shear the solution during its push in order to expose a fresh, unoxidized surface. The solution typically contained 4g of six nines pure Ga and the appropriate amounts of six nines pure Al and polycrystalline undoped GaAs. For each run, the saturation temperature, T_s , the temperature at which the Ga-Al solution is just saturated with the specific amount of GaAs used, was determined by using the ternary phase diagram of Ilegems and Pearson (4).

The substrates were lapped with 1 μm alumina, etched in 10 HNO₃:1 HF:5 H₂O for 10 sec, rinsed and dried before being loaded into the boat. The GaAs source material was heavily etched, rinsed, dried, and then wetted with Ga before placement in the solution.

During loading, the solution was heated to 50°C to insure that the Al was dissolved properly. After positioning in the furnace, the system was flushed overnight with H₂ purified by Pd. The system was then heated to an equilibration temperature, T_e , either equal to T_s or exceeding T_s by about 40°C. After at least one hour at T_e , cooling at 40°C per hour was initiated. The solution was pushed over the substrate at 3°-5°C below T_s and allowed to cool to room temperature. Typical grown layers were 30 to 200 μm thick.

The x-ray emission produced from the layers by the electron beam of an ARL model EMX electron microprobe was analyzed to yield the alloy composition. Measurements were made as a function of position along the growth direction in 2-20 μm steps. The composition at the onset of growth was then obtained by interpolation to zero thickness. The error was estimated at $\pm 2\%$. The variation of the initial solid composition with atom fraction Al in the solution, $X_{\text{Al}}(1)$, and saturation temperature, T_s , is shown in Fig. 1.

Within the experimental uncertainties, the measured concentration of AlAs in the solid did not depend on substrate orientation, the physical properties of the substrate (doping level, dopant, etchpits density, etc.) or on the equilibration temperature, T_e . Examination of the metallurgical interface between the substrates and the grown layers indicated that no etchback of more than a few micrometers took place. Post-growth inspection of the solution revealed no undissolved GaAs source material. From these observations we concluded that a condition close to equilibrium existed in the solution before the initiation of growth.

In Fig. 2, our experimental values are compared to the calculations of Ilegems and Pearson (4). Our data are in moderately good agreement with the calculated

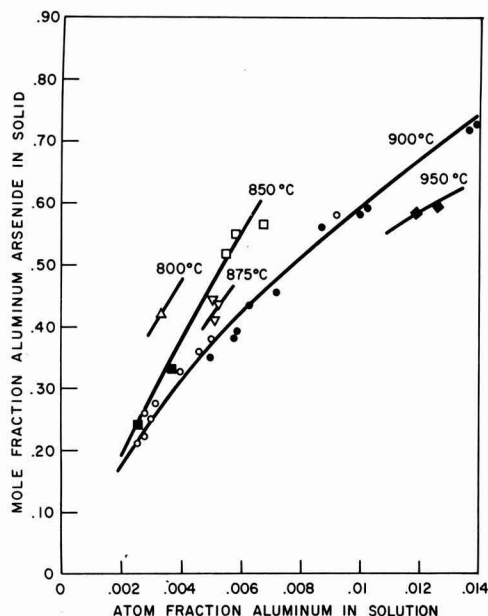


Fig. 1. Initial AlAs concentration in solid $\text{Ga}_{1-x}\text{Al}_x\text{As}$ vs. Al atom fraction in Ga-Al-As solution for specific values of T_s . For $T_s = T_e$, \triangle 800°-805°C, \square 850°-855°C, ∇ 875°C, \circ 895°-905°C. For $T_s = T_e - 40^\circ\text{C}$, \blacksquare 850°-855°C, \bullet 895°-905°C, \blacklozenge 945°-950°C.

isotherms, but deviations as high as 30% are found for Al solution compositions in the 0.003-0.006 atom fraction range. A much better agreement is found between our data and the experimental values of Alferov *et al.* (6).

In conclusion, experimental data are presented establishing the relationship between the AlAs concentration in solid $\text{Ga}_{1-x}\text{Al}_x\text{As}$ and the Al concentration in the solution for crystal growth by LPE in the 800°-950°C range. These data should prove useful in the growth of direct energy gap $\text{Ga}_{1-x}\text{Al}_x\text{As}$ for use in efficient light emitting diodes.

Manuscript submitted Nov. 11, 1971; revised manuscript received ca. Jan. 28, 1972.

Any discussion of this paper will appear in a Discussion Section to be published in the December 1972 JOURNAL.

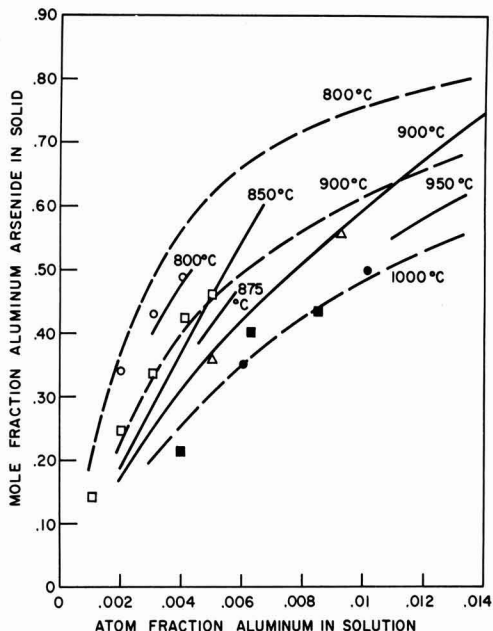


Fig. 2. Experimental isotherms from Fig. 1 (solid lines) and those calculated by Ilegems and Pearson (4) (dashed lines). For comparison purposes, the following data points are also included: \bullet 1000°C Ref. (3), \blacksquare 1000°C Ref. (4), \circ 802°C, \square 852°C and \triangle 900°C Ref. (6).

REFERENCES

1. H. C. Casey, Jr. and F. A. Trumbore, *Mater. Sci. Eng.*, **6**, 69 (1970).
2. H. C. Casey, Jr. and M. B. Panish, *J. Appl. Phys.*, **40**, 4910 (1969).
3. M. B. Panish and S. Sumski, *J. Phys. Chem. Solids*, **30**, 129 (1969).
4. M. Ilegems and G. L. Pearson, "1968 Symposium on GaAs," pp. 3-10, Institute of Physics and The Physical Society, London (1969).
5. I. Hayashi, M. B. Panish, P. W. Foy, and S. Sumski, *Appl. Phys. Letters*, **17**, 109 (1970).
6. Zh. I. Alferov, V. M. Andreyev, S. G. Konnikov, V. G. Nikitin, and D. N. Tret'yakov, *Proc. Internat. Conf. on Heterojunctions I*, p. 93, Academy of Sciences, Budapest, 1971.

Erratum

Regarding the paper "Electroplating of Osmium" by A. J. Appleby which appeared on p. 1610 in the December 1970 JOURNAL, Vol. 117, No. 12, it has recently been brought to the author's attention that a practical aqueous bath for obtaining bright osmium electrodeposits was described by L. Greenspan [*Engelhard Ind. Tech. Bull.* **10**, 48 (1969)] as the above paper was in final preparation. As stated by Mr. Greenspan: "This bath contains osmium in alkaline solution as an anionic complex formed by reacting osmium tetroxide

with sulfamic acid. Using this bath at a temperature of 65°-75°C, and with current densities of 2-10 A/ft², deposits at a rate of about 100 $\mu\text{in.}/\text{hr}$ are obtained with current efficiencies of the order of 40-80%. Deposits of about 50 $\mu\text{in.}$ are from lustrous to bright; those of 100 $\mu\text{in.}$ and above are dull but smooth. This bath appears more suited for practical electrodeposition of osmium than the cyanide bath and is commercially available." The author is indebted to Mr. Greenspan for bringing this omission to his attention.

CALL FOR PAPERS



SECOND INTERNATIONAL SYMPOSIUM ON SILICON MATERIALS SCIENCE AND TECHNOLOGY MAY 13-18, 1973

The Second International Symposium on Silicon Materials Science and Technology, co-sponsored by the Electronics and the Electrothermics & Metallurgy Divisions of The Electrochemical Society, is scheduled for the May 1973 meeting in Chicago. The interdependence of silicon material preparation and properties, device manufacturing processes, and electrical characteristics of the final device will be stressed with particular emphasis on the practical aspects of material processing and device manufacturing. Authors will be encouraged to relate the process history of the materials to the subsequent interpretation of device performance.

Authors must submit a 500-word abstract in English, double spaced, indicating title, authors, and affiliation. In addition, each author is requested to submit an informal summary of no more than three type-written pages, including diagrams, describing his work in more detail. This summary will be used to assist the reviewers in evaluating the suitability of the paper for oral presentation at the Symposium. All abstracts and summaries must be submitted in quadruplicate before **September 1, 1972**, to either of the Symposium Co-Chairmen: Howard R. Huff, Texas Instruments, Inc., P. O. Box 5936, M/S 144, Dallas, Texas 75222; or Ronald R. Burgess, Motorola Semiconductor Products Division, Phoenix, Arizona 85008.

Detailed instructions concerning manuscript preparation for publication will be forwarded to each author upon acceptance of his paper for oral presentation. Manuscripts will be required in quadruplicate by **January 1, 1973**, to allow time for the Symposium proceedings to be published and available for distribution at the meeting.

Initial plans call for about one-half of the papers to be comprehensive reviews with the other half to be a selection of papers submitted in the areas listed below.

MATERIAL PREPARATION AND CHARACTERIZATION

Silicon Wafer Quality Advancements (Co-Chairmen—E. Sirtl and F. Padovani):

Crystal Growth (striations and swirls in dislocation-free silicon; doping, compensation, and recombination level control; carbon, oxygen). Annealing Kinetics (fast-diffusing impurities; surface and bulk defect characterization). Wafer Preparation (production handling; saw; polish; surface cleanliness; orientation-dependent etchants).

Deposition and Growth of Silicon and Insulating Films (Co-Chairmen—E. Kooi and K. Bean):

Epitaxy (homo- and hetero-nucleation; impurity distribution; thin- and multiple-layer; selective growth; low temperature). Insulating Films (silicon oxide and nitride; composite masking; strain effects; polysilicon). Interface Phenomena (surface passivation; electrical instabilities; impurity segregation).

Diagnostic Techniques and In-Process Measurements (Co-Chairmen—W. M. Bullis and G. H. Schwuttke):

Measurements and Instrumentation (minority-carrier lifetime; micro-resistivity fluctuations; thin epitaxy layers; small-area measurements; activation analysis; electron diffraction; lasers; microprobe; SEM; TEM; LEED; Auger; Hall; C-V). Nondestructive Techniques (ellipsometry; x-ray topography; ion back-scattering). Chemical Analysis (ppb).

DEVICE MANUFACTURING SCIENCE

Material Processing Phenomena and Device Performance (Co-Chairmen—J. Lawrence and S. Dash):

Correlation between process parameters and device characteristics; physical mechanism of interaction between process-induced and grown-crystal defects—influence on device characteristics. Role of ambient and cool-down procedures during high-temperature processes in promoting impurity precipitation, diffusion anomalies, and plastic deformation.

Process Modeling and Device Parameter Control (Co-Chairmen—P. Wang and M. L. Joshi):

Role of process-control devices to discriminate influence of process parameters and predict performance of integrated circuits. Comparative analysis of advantages and disadvantages of processes for achieving specific device performance levels. Computer-aided design and simulation analysis. Equipment design innovations.

Innovative Device Manufacturing Process Technologies (Co-Chairmen—B. T. Murphy and U. Davidsohn):

New device and integrated structures exploiting advanced technologies; (ion implantation; electron beam; dielectrics for isolation and gate structures).



DIVISION NEWS

Electro-Organic Division

Notice of Vote to Change Bylaws

The Executive Committee of the Electro-Organic Division has evolved the idea of increasing the scope of their Division and changing the Divisional name. They have now agreed to submit these changes to the membership of the Division in the form of proposed changes to the bylaws of the Division.

The new name of the Division would be the Organic and Bioelectrochemistry Division, and Article II, Purpose, would be changed to reflect the increase in the scope of the Division.

The proposed changes in the bylaws of the Division will be voted upon at the Divisional luncheon business meeting to be held Wednesday, May 10, 1972, in the Columbia Room of the Shamrock-Hilton Hotel, Houston, Texas.

Industrial Electrolytic Division

The appointed Nominating Committee for the May 1972 election of officers in the Industrial Electrolytic Division, R. G. Milner, J. R. Anton, and M. P. Grotheer, Chairman, proposes the following slate of candidates:

Chairman—N. E. Richards

Vice-Chairman—D. N. Goens

Secretary-Treasurer—T. C. Jeffrey, E. H. Cook, L. L. Dunn, and J. Parker.

Each of the candidates has been contacted personally. All have consented to be nominated and to serve in the respective offices if elected.

Additional nominations may be made from the floor by active members of the division at the May 1972 Business Meeting to be held in Houston.

Notice of Vote to Amend Bylaws

The Executive Committee of the Industrial Electrolytic Division has agreed on the draft of proposed changes in the bylaws of the Division. The proposed changes will be voted upon at the Divisional luncheon business meeting to be held May 8, 1972, in the Nile Rooms of the Shamrock Hilton Hotel, Houston, Texas. The proposed changes are additions to the existing bylaws and are as follows:

Article VIII—Duties of Officers.

Section 1. The chairman shall have the following duties: (k) To appoint, soon after his election, one member to the Program Planning Committee. (l) To appoint each year an author for the Report of the Electrolytic Industries to

MCKINLEY AND BECK TAKE OFFICE IN HOUSTON, TEXAS



Theodore D. McKinley

As a result of the recent annual elections, in which the voting was by mail ballot, Theodore D. McKinley has been elected the new President of The Electrochemical Society (1972-1973) and Theodore R. Beck has been elected Vice-President (1972-1975). They will take office on May 12, 1972.

Mr. McKinley, research supervisor at the DuPont Experimental Station, Wilmington, Delaware, replaces Cecil V. King who will continue as Past-President on the Board of Directors.



Theodore R. Beck

Dr. Beck, who joined Flow Research, Inc., Kent, Washington, on May 1, 1972, and who has been appointed Affiliate Professor, Department of Engineering, at the University of Washington in Seattle, begins the first of his three-year term as Vice-President.

Other offices not affected by this election are those of the two other Vice-Presidents, N. Bruce Hannay and D. A. Vermilyea; that of the Secretary, Dennis R. Turner; and that of the Treasurer, R. Homer Cherry.

serve for a period of two years. By this procedure, two authors will be appointed for each report.

Section 2. It shall be the duty of the Vice Chairman: (a) To actively assist the Chairman in all of his duties and to perform the duties of Chairman in his absence; (b) To be a member of and act as Chairman of the Program Planning Committee.

Article XI—Standing Committees.

Section 1. The Industrial Electrolytic Division shall maintain a Program Planning Committee which will select program and symposium topics and program chairmen for national meetings of The Electrochemical Society. The Program Planning Committee shall consist of the Chairman (the Vice-Chairman of the Industrial Electrolytic Division) and three additional members appointed for six-year terms. The three appointed members should represent a broad spectrum of Division technological activities, both theoretical and applied.

Article XII—Report of the Electrolytic Industries.

Section 1. The Division shall issue a report on the production volume, economics, and new technology of the electrolytic industries.

(Cont. on p. 150C)

New Officers	149C
Division News	149C-150C
Section News	150C-153C
New Members	155C
People	155C
ECS Membership Statistics	150C
Obituary	154C
New Products	154C
Book Reviews	156C-157C
Position Available	158C
Positions Wanted	158C

ECS Membership Statistics

The following three tables give a breakdown of membership as of January 1, 1972. In Table I it should be noted that the totals appearing in the right-hand column are not the sum of the figures in that line since members belong to more than one Division. The totals listed are the total membership in each section.

Table I. ECS Membership By Sections and Divisions

Section	Division											Total as of 1/1/71	Total as of 1/1/72
	Battery	Corrosion	Dielectrics & Insulation	Electro- deposition	Electronics	Electro- Organic	Electrothermics & Metallurgy	Industrial Electrolytic	Physical Electrochemistry	No Division			
Chicago	52	37	16	36	46	18	16	14	31	3	182	171	
Cleveland	52	27	3	31	34	15	21	27	44	6	167	161	
Detroit	43	43	10	62	25	19	14	9	50	4	140	134	
Midland	3	3	1	2	9	3	6	11	4		34	30	
New York													
Metropolitan	158	111	58	145	274	51	83	58	140	24	666	666	
Niagara Falls	7	7	11	14	30	5	16	29	16	3	119	95	
Pacific N.W.	13	8	3	13	5	5	6	13	20	1	53	48	
Philadelphia	70	34	15	43	66	16	25	17	56	11	224	224	
Pittsburgh	12	48	12	30	57	4	34	26	41	3	175	155	
San Francisco	26	21	28	27	130	10	19	9	40	1	224	216	
National Capital													
Area	49	32	14	24	35	9	10	4	43	1	153	143	
Ontario-Quebec	16	28	18	27	38	3	43	32	41		149	147	
Boston	50	46	15	42	112	17	32	11	64	6	262	255	
S. Calif.-Nevada	55	40	16	47	134	17	33	22	66	4	285	260	
Columbus	15	25	8	16	18	3	24	6	18	1	81	75	
Indianapolis	8	10	11	8	26	4	11	3	13		56	55	
North Texas	14	12	11	14	100	4	9	3	13	4	131	131	
South Texas	3	10	3	1	10	4	3	10	15	1	47	42	
Non-Section	157	138	62	138	198	68	91	111	203	67	929	924	
<hr/>													
TOTAL as of Jan. 1, 1971	828	688	306	739	1414	267	511	427	918	163	4077		
TOTAL as of Jan. 1, 1972	803	680	315	720	1347	275	496	415	918	140		3932	

Table II. ECS Membership By Grade

	Total as of 1/1/71	Total as of 1/1/72
Active	3625	3482
Life	25	30
Emeritus	100	102
Honorary	9	9
Associate	24	17
Student	180	183
Representatives of Patron and Sustaining Members	114	109
Total	4077	3932
Delinquent	177	230
Total	4254	4162

Table III. ECS Patron and Sustaining Membership

	Total as of 1/1/71	Total as of 1/1/72
Patron Member Companies	6	6
Sustaining Member Companies	115	103

(Division News Cont.)

Article XIII—Dissolution.

If the Industrial Electrolytic Division of the Society can no longer function advantageously as a unit of the Society it may request the Board of Directors for permission to dissolve. If such permission is granted, all funds which have been accumulated by the Industrial Electrolytic Division, including money in banking and other accounts and investments of all types, shall be transferred to The Electrochemical Society, Inc. If the Industrial Electrolytic Division has underwritten any continuing awards for which invested funds provide an adequate income, the Society shall undertake to continue such awards at the discretion of the Board of Directors.

SECTION NEWS

Columbus Section

The Annual Banquet Meeting was held in December of 1971, and Columbus Section members had the opportunity to hear Dr. N. B. Hannay, Vice-President of the national Society, describe national Society affairs which affected the members-at-large. The technical portion of the meeting gave Dr. Hannay an opportunity to discuss his experience with electronic materials of the past, and trends for the future.

In January, Dr. T. E. Leontis, of the Magnesium Research Center at Battelle-Columbus, talked about magnesium as a primary energy source. He said that magnesium possesses electrochemical properties that make it an ideal material as a primary energy source. Although its theoretical potential ($E^\circ = -2.37V$) is not realized in practice, the observed value ($-1.4V$) is still 0.64V more anodic than zinc. Further, magnesium has a very favorable electrochemical equivalent: 1000 A-hr/lb as compared to 372 A-hr/lb for zinc. These characteristics of magnesium have been put to good use in sacrificial anodes to protect steel, and in reserve-type and dry cell batteries. Over 300,000,000 lb of magnesium anodes have been used since 1950 to protect pipelines, underground storage tanks, sea-going vessels, and hot water heaters. Present consumption for these applications is at a rate of 15,000,000 lb/yr. Reserve-type cells are used to power torpedos, sonobuoys, firing squibs, etc.; and rapid advances have been made in magnesium dry cells in recent years. Magnesium dry cells are superior to zinc dry cells (Leclanché-type) in several respects. They have a higher voltage, higher capacity over wide ranges of discharge rate, better voltage maintenance, broader operating temperature range, and exceptional storageability. Magnesium batteries are replacing zinc batteries in military applications, and commercial batteries can be expected in a few years.

Eric W. Brooman
Secretary-Treasurer

Cleveland Section

The Cleveland Section's speaker for the month of February was Dr. David E. L. Dyke of Battelle Columbus Laboratories. The subject of Dr. Dyke's talk was "Electrodeposition of Paint." His work involving deposits of films that may contain up to nine components indicates a fascinating challenge to electrochemists.

The speaker for the month of March will be Professor R. W. Staehle of Ohio State University. Professor Staehle will speak on "Fundamental Studies of Stress-Corrosion Cracking."

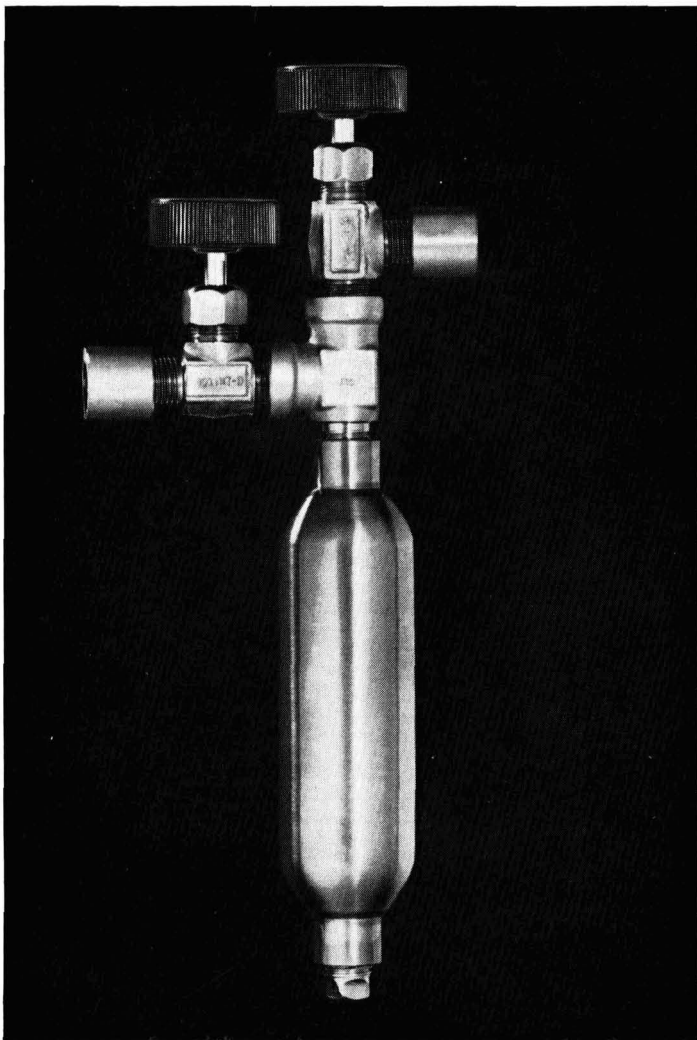
The following announcement was made by James W. Sprague and Alvin J. Salkind in the Bulletin of ICS-MnO₂ (International Common Samples of MnO₂).

The concept of International Common Samples was proposed informally during the Centennial Symposium on Leclanché Cells in 1966 at Philadelphia, Pennsylvania, U.S.A. By having available on a world-wide basis common samples of manganese dioxide, the value of fundamental research on manganese dioxide would be promoted and progress in dry cell technology would be facilitated.

The Cleveland local Section is pleased to announce that a Distribution Center for Common Samples of Manganese Dioxide has been established. The Distribution Center is sponsored jointly by our local Section and the Battery Division of The Electrochemical Society. Dr. Akiya Kozawa, well-known for his research interests in manganese dioxide and an active member of both the Cleveland local Section and the Battery Division, has been appointed Chairman of the Distribution Center. Through the cooperation of various manganese dioxide suppliers and academic and industrial research advisors, he now has quantities of ten common samples ready for distribution.

The ultimate value of each common sample will be the information developed by the researchers who use the sample. We hope that this experiment in international cooperation will be useful and successful. The first Bulletin of ICS-MnO₂ was issued on December 1, 1971. In that Bulletin, the purpose of the common samples was described by Dr. R. A. Powers and Dr. A. Kozawa in the following manner.

Manganese dioxide has been used in the Leclanché cells since 1866; but despite a number of research papers published, the physical and chemical properties of manganese dioxide required or desirable for the battery cathode have not been well established. The electrochemical behavior of manganese dioxide in the battery is influenced by crystal structure, surface area, pore size distribution, shape and size of the particle, electrical conductivity, surface condition, chemical composition, various impurities (H₂O and foreign elements) in the structure, and various defects in the structure. Reproduction of identical manganese dioxide sam-



Super Pack! Brings you 99.999+% pure TMG.

This stainless steel package—with optional dip tube—contains our new electronic-grade trimethylgallium for semi-conductor film. So pure you can switch from hard-to-control high vacuum-temperature techniques to the chemical vapor deposition process. Provides greater flexibility in use of dopants and a wider selection of substrate materials. Makes diode manufacturing simpler, easier. Use with arsine or phosphine to make epitaxial films of gallium arsenide or gallium phosphite.

A real breakthrough...but not surprising for a company so involved in organometallics for the electronics industry. Our experience—with alkyls of

aluminum, zinc, boron, magnesium, gallium, and other elements—is broad and deep. And based on the most demanding quality control procedures in the business.

For more information on new TMG write Texas Alkyls, Inc., c/o Stauffer Chemical Company.

Exclusive Sales Agent:
Stauffer Chemical Company,
Specialty Chemical Division,
Westport, Connecticut 06880



plenum
PUBLISHING CORPORATION

JOURNAL OF SOLUTION CHEMISTRY

Editor: **Robert L. Kay**, *Mellon Institute, Carnegie-Mellon Univ., Pittsburgh, Pa.*

Editorial Board: B. E. Conway (Canada), D. F. Evans (USA), Henry S. Frank (USA), Felix Franks (England), Harold Friedman (USA), Raymond M. Fuoss (USA), E. Grunwald (USA), Loren G. Hepler (Canada), H. G. Hertz (Germany), George Janz (USA), Jean-Claude Justice (France), Henry V. Kehiaian (Poland), S. Lindenbaum (USA), Rufus Lumry (USA), George Nancollas (USA), Lars Onsager (USA), R. A. Robinson (USA), George J. Safford (USA), and R. H. Stokes (Australia).

Designed as a forum for research on liquid solutions—theoretical and experimental papers in which solvent properties are of dominant importance—this new bimonthly journal will offer papers on dielectric, spectroscopic, thermodynamic, transport, and relaxation properties of both electrolytes and non-electrolytes in liquid solutions. Articles will offer a molecular interpretation of presented data; but in special cases, involving particularly important data, a purely experimental paper will be published.

SAMPLE COPIES AVAILABLE UPON REQUEST

CONTENTS OF VOLUME 1:

F. Franks, J. R. Ravenhill, and D. S. Reid: Thermodynamic Studies of Dilute Aqueous Solutions of Cyclic Ethers and Simple Carbohydrates • **Wen-Yang Wen and H. G. Hertz:** Chemical Shifts of Aqueous Nonelectrolyte Solutions—Influence of the Polar and Nonpolar Groups on the Water Proton Shifts at 0°C • **P. G. N. Moseley and M. Spiro:** Transference Numbers of Potassium Picrate in Water at 25°C and the Dimerization of Picrate Ions • **Chia-tsun Liu and W. T. Lindsay, Jr.:** Thermodynamics of Sodium Chloride Solutions at High Temperatures • **R. A. Robinson:** Excess Gibbs Energy of Mixing of the Systems H_2O - $LiCl$ - Na_2SO_4 and H_2O - $CsCl$ - Na_2SO_4 at 25°C • **J. F. Coetzee and W. R. Sharpe:** Solute-Solvent Interactions—Proton Magnetic Resonance and Infrared Study of Ion Solvation in Dipolar Aprotic Solvents.

SUBSCRIPTION: VOLUME 1, 1972 (6 ISSUES) \$34.00
PERSONAL SUBSCRIPTION* \$18.50
(PLEASE ADD \$2.70 FOR POSTAGE OUTSIDE U.S. AND CANADA)

* Personal subscriptions at a reduced rate are available on orders placed directly with the Publishers certifying that the subscription is paid for by the subscriber and is for his personal use.

plenum press / consultants bureau

Divisions of Plenum Publishing Corporation
227 W. 17th ST., NEW YORK, N. Y. 10011

ples does not appear to be a simple task even though the conditions of the preparation are thoroughly specified in a written form. At the present status of our knowledge, it is impossible to reach unanimous agreement on standard samples of MnO_2 for electrochemical activity. Under these circumstances, it seems necessary to have international common samples as a control or a reference in order to study, evaluate and compare various manganese dioxides for battery use.

Technical people in battery manufacturing and in manganese dioxide production need to compare the electrochemical behavior and the physical and chemical properties of various manganese dioxides. Data obtained by one laboratory (or data described in one paper) can be reasonably compared to those obtained by another laboratory (or to those described in another paper) if the common samples are included in these two sets of data.

Once research results (publications) on various manganese dioxides are accumulated for comparison with data on the common samples, this knowledge will be more useful and valuable than information published without reference to such common samples. Therefore, all people who are doing research on manganese dioxide have a need for such common samples, not only for confirmation of their analytical methods for determining the chemical and physical properties, but also as a

Table I. List of MnO_2 samples available (Sept. 1, 1971)

Samples	Nature of Sample	Source	Sample/bottle
I.C. No. 1	Electrolytic MnO_2 made by Ti anode	Japan	about 1 kg
I.C. No. 2	Electrolytic MnO_2 made by Pb anode	Japan	about 1 kg
I.C. No. 3	Electrolytic MnO_2 made by C anode	Japan	about 1 kg
I.C. No. 4	Electrolytic MnO_2	LaPile Leclanché (France)	about 1 kg
I.C. No. 5	Chemically prepared MnO_2	Japan Metals & Chemicals Co.	about 1 kg
(I.C. No. 6	Natural Ore	Not ready for distribution)	
I.C. No. 7	Natural MnO_2 ore	Ghana Ore	about 1 kg
I.C. No. 8	Chemically prepared MnO_2	Sedema, Belgium	about 1 kg
I.C. No. 9	Electrolytic MnO_2 (coarse grade)	Kerr-McGee Corp., U.S.A.	about 1 kg
I.C. No. 10	Electrolytic MnO_2	Kerr-McGee Corp., U.S.A.	about 1 kg
I.C. No. 11	Chemical MnO_2 made by chlorate process	Kerr-McGee Corp., U.S.A.	about 100g

Price: No. 1 to 10, \$8.00 each bottle containing 1 kg; No. 11, \$4.00 each bottle containing 100g. Shipping charge including the postage: by air mail, \$5.00 each bottle; by surface mail, \$1.50 each bottle.

reference sample for the measurement of unknown properties such as electrochemical activity for battery cathodes.

The number of common samples is not limited. Hopefully, if an appropriate new type of manganese dioxide is introduced to the market, the supplier will offer it to the International Common Sample Office. The new material will be added to the list and the subscribers to the Bulletin of ICS- MnO_2 (Bulletin of The International Common Samples of Manganese Dioxide) will be notified.

The samples now available from the Distribution Center for the I.C. Samples are shown in Table I. Extra copies of the Bulletin are also available from the I.C. Sample Office.

To order samples available as listed in Table I, send your order with your check to: the I.C. Sample Office, Attention: Dr. A. Kozawa, P.O. Box 6116, Cleveland, Ohio 44101. Advance payment is required. Checks should be made payable to the I.C. Sample Office. The amount of the check should include the price of the sample and the shipping charge.

Detroit Section

The Detroit Section held its monthly meeting on March 16, 1972, at Greenfield's Northland Restaurant. The speaker was David. A. Vermilyea, a Vice-President of the Society and a research staff member of General Electric Corporate Research and Development.

Dr. Vermilyea gave a brief report of current Society matters followed by a technical presentation of some unusual corrosion problems that have occurred in water cooled nuclear reactors. At 300°C intergranular stress corrosion cracking of sensitized or cold worked stainless steels was found to be dependent on the chromium content of the alloy and pH. Construction and operation of reference electrodes and related equipment, to obtain polarization curves and corrosion rates in aqueous solutions at high temperatures, were described.

National Capital Area Section

Dr. N. B. Hannay, Bell Telephone Laboratories, Murray Hill, N.J., discussed "Electronic Materials-Present and Future" at the February meeting of the National Capital Area Section. After pointing out that progress in electronics is becoming increasingly dependent upon progress in materials, the speaker described recent developments in electroluminescent semiconductors, materials for phosphors and lasers, acousto-optic and electro-optic crystals (including a device which can convert light of one color into another with practically 100% efficiency), ferroelectric materials for holographic memories, and "bubble-domain" magnetic materials. The latter hold great promise in memory devices because of the high concentration bits which can be stored in them. Following the lecture, Dr. Hannay, who is also a Vice-President of the Society, reported on and answered questions about Society matters.

The March meeting of the section was on the topic "Modification of the Lead-Acid Battery for Hybrid Vehicles" by Dr. H. P. Silverman, TRW Systems Group, Redondo Beach, Calif. The speaker briefly reviewed some of the proposals for low-pollution vehicles: external combustion engines, modified internal combustion engines, and hybrid vehicles. The last seems particularly promising for meeting the rapidly approaching deadlines for a low-emission vehicle.

Using a conventional automobile, a velocity-acceleration chart was plotted which showed that there were heavy concentrations of points at two areas on the graph, corresponding to urban and freeway driving conditions; and that, although the power required for freeway driving was somewhat larger than for urban driving, the additional power for acceleration was about the same for both.

Thus the hybrid vehicle concept depends on designing a conventional internal combustion engine to operate at

a relatively constant power output, permitting optimum performance, with excess power at low demand levels being used to drive a generator and charge a battery. When peak power is needed for acceleration, it would be drawn from the battery through a traction motor without additional demands on the engine.

After reviewing the various types of batteries that might be used, the lead-acid type was selected because of its low cost and high reliability. Conventional designs are not suitable, however, because their power density is too low; and they are not designed to withstand the high charge-discharge rate demands of the hybrid vehicle. Thus a program was instituted to redesign the lead acid battery to lower its internal resistance and reduce its weight. A new, more conductive alloy was used for the plates, which were also made thinner, and with an altered cross section to improve conductivity in the direction of current flow to and from the tabs. Improved separator plates were used to permit more plates in a given volume, with a corresponding reduction in electrolyte volume.

These changes resulted in a battery which was 23% lower in internal resistance and 13% lighter than conventional batteries, yet can deliver 140-160 w/lb and about 3 whr/lb, both about double the capabilities of present designs. A mock-up of the hybrid vehicle has been built, using off-the-shelf components (including batteries); and tests indicate that the concept is sound, with engine emissions within those specified in the Muskie bill, intended to apply to 1976 engines.

James Barclay
Secretary

Pittsburgh Section

1972 Spring Meeting

The Spring Meeting commemorating the 60th anniversary of the Pittsburgh Section of The Electrochemical Society will be held on Friday, May 19, at 9:00 a.m. at the Alcoa Technical Center, Pittsburgh, Pennsylvania. The meeting will be followed by a tour of the newly completed Alcoa Research Laboratories. The program includes the following papers:

"The Electrochemistry of Polymer Deposition," by Z. K. Kovac, PPG Industries.

"The Oxidation of Vapor Deposited Aluminum in Air at 23°C," by D. L. Kinosh, Alcoa Technical Center.

"The Passivation of Iron and Its Alloys," by R. P. Frankenthal, U.S. Steel Research Laboratories.

"Selective Ion Electrodes," by A. Staeb, U.S. Steel Research Laboratories.

"The High Temperature Combustion of Zirconium and Hafnium," by R. L. Tallman, Westinghouse Research Laboratories.



ISO PROBE
Measures

ELECTROSTATIC POTENTIAL

Without Physical Contact

The Easy Way

For Research or Production Line

APPLICATIONS

Accurate surface potential measurement of small area
Measurement of Electrets
Illumination effects on charged surface
Surface charge leakage measurement
Electrostatic field measurement
Electrostatic monitoring systems for:

Hazardous industrial areas
Hospitals Film Processors
Flammable fuel storage and transfer areas
Aircraft
Plastic Manufacturing
Textile Manufacturing

FEATURES

- Simple Operation - No Time Consuming Set-ups or Special Shielding Required
- Drift Free Performance
- Absolute Calibration
- Accuracy Essentially Independent of Probe-to-Surface Spacing
- Inherent error less than 0.1%
- Millivolt to kilovolt ranges
- Surface resolution better than 0.03" circle
- New **TRANSPARENT PROBE** Uses no mirrors or Coated Glass - Permits Direct Illumination of Charged Areas

ALSO AVAILABLE:

Portable Instruments
D.C. Fieldmeters
Special Purpose Electrometers

Write today for catalog



MONROE ELECTRONICS, INC.

100 HOUSEL AVENUE
LYNDONVILLE, NEW YORK 14098

OBITUARY

Edward B. Saubestre

Edward B. Saubestre, Technical Director at Ethone, Inc. since 1958, died on March 24, 1972.

An active member of The Electrochemical Society, Dr. Saubestre was a Divisional Editor of the Electrodeposition Division for the *Journal*. He had been a Divisional Editor of the Electrodeposition Division for a number of years and had been elected Division Chairman in October 1971. He was a member of the Honors and Awards Committee and on the Board of Directors of the Society.

Dr. Saubestre was also very active in the American Electroplaters Society and the American Society for Testing and Materials. His other memberships included the American Chemical Society, the American Society for Metals, the Institute of Metal Finishing (London), and the American Association for the Advancement of Science. He was a fellow of the American Institute of Chemists.

Dr. Saubestre was educated at Columbia University where he received his B.S. degree in 1945, his M.S. in 1948, and his Ph.D. in 1952. Before joining Ethone as Technical Director he was with the Central Research Laboratories of Sylvania Electric Company.

As an author, Dr. Saubestre published numerous papers relating to the metal finishing industry and contributed regularly to various technical publications. He lectured frequently both in this country and abroad on aspects of the metal finishing industry. He authored a number of patents including processes for plating on plastics, electroless plating, blackening processes for metals, metal strippers, and processes for plating on aluminum.

NEW PRODUCT

New Mercury Removal Process—A new process, available from Koertrol Corporation, permits the removal or reclamation of mercury from liquids by using a powerful reducing agent, sodium borohydride. The technique, known as the Ventron process, successfully removes in excess of 99.5% of the mercury from plant effluents. With a typical waste water system, the first step is to adjust the pH of the Hg containing effluent to a predetermined level; sodium borohydride is then metered into the effluent to reduce the mercuric compounds to the metallic state. Organic Hg must be pre-treated and converted into the inorganic form. With the aid of a floccu-

lant, the precipitated Hg metal is removed by clarification and filtration. Resultant Hg sludge is suitable for distillation without further processing. The Koertrol Corporation is located at 3427 Industrial Drive, Durham, N.C. 27704.

New Mercury Cell Accessory—Mercury content in nanogram quantities can be estimated with a mercury cell ac-

1973 Palladium Medal Award, ECS

The eleventh Palladium Medal of The Electrochemical Society will be awarded at the Fall Meeting of the Society to be held in Boston, Massachusetts, October 7-11, 1973. The medal was established in 1951 by the Corrosion Division.

The recipient shall be distinguished for contributions to the field of Electrochemical Science and Corrosion. The recipient need not be a member of the Society, nor shall there be any restrictions or reservations regarding age, sex, race, citizenship, or place of origin or residence.

The award consists of a Palladium medal and a nickel replica thereof, both bearing the recipient's name, and the sum of one thousand five hundred dollars.

The recipient shall receive the award in person at the designated meeting of the Society and shall at that meeting deliver a general address to the Society on a subject related to the contributions for which the award is being presented. Expenses involved in the acceptance of the award shall be assumed by the recipient.

In addition to the above, with regard to the selection, the rules have the following provisions:

1. The selection of the recipient is the responsibility of the Palladium Medal Award Subcommittee of the Honors and Awards Committee consisting of six members of the Society who shall be knowledgeable in the field of the award and, ex officio, the Chairman of the Honors and Awards Committee. After due deliberations the Subcommittee shall determine whether the list of nominees includes any suitably qualified candidates for the award and, from those so qualified, shall select one candidate to be recommended to the Honors and Awards Committee as the award recipient. The Honors and Awards Committee will then make its recommendation to the Board of Directors. On approval of the recommendation for the granting of the award by the Board of Directors, the President of the Society shall inform the intended recipient of the action and shall determine whether the requirements governing acceptance of the award will be met. If there is agreement by the intended recipient with the requirements governing acceptance, the recipient of the award shall be announced in the *Journal*.

2. Nominations for the award shall be solicited by the Chairman of the Award Subcommittee by announcement in the *Journal of The Electrochemical Society* and communications to the Officers, and Division and Local Section Chairmen of the Society. Nominations shall be considered closed at the beginning of the Fall Meeting of the Society (Miami Beach, Florida, 1972) but nominations once made, shall be considered in effect for two consecutive award periods.

3. All nominations, whether made by a member of the Subcommittee or by any other member of the Society, must be accompanied by a full record of qualifications of the nominee for the award.

4. The nominator must assume the responsibility of providing the Chairman with six copies of the supporting documents. If the nominator does not have facilities to readily provide the Chairman with the six copies, the material shall be supplied to the National Office of the Society, which shall then prepare the necessary six copies for the Chairman. These copies must be in the hands of the Chairman no later than October 6, 1972.

Previous medalists have been:

Carl Wagner—1951	Herbert H. Uhlig—1961
Nathaniel H. Furman—1953	Norman Hackerman—1965
Ulick R. Evans—1955	Paul Delahay—1967
Carl F. Bonhoeffer—1957	Thomas P. Hoar—1969
Aleksandr N. Frumkin—1959	Leo Brewer—1971

Please address all nominations to the Chairman of the Palladium Medal Award Subcommittee, Dr. Manfred Breiter, General Electric R & D Center, P.O. Box 8, Schenectady, New York 12301.

cessory introduced for Corning's Model 240 atomic absorption spectrophotometer. This accessory presents a flameless detection technique at 253.7 nm that exploits the absorption of monatomic mercury vapor in accordance with the well accepted Hatch and Ott procedure. For further information contact: Corning Scientific Instruments, Corning Glass Works, Medfield, Mass. 02052.

NEW MEMBERS

It is a pleasure to announce the following new members of The Electrochemical Society as recommended by the Admissions Committee and approved by the Board of Directors in March 1972.

Active Members

Davidson, R. B., University, Al.
Downey, B. J., Villanova, Pa.
Gill, R. B., East Windsor, N. J.
Hoover, T. R., Athens, Ga.
Müller, B., Berlin, Germany
Perry, J. Jr., New Shrewsbury, N. J.
Slattum, C., Dallas, Tx.
Watts, C. R., Huntington Beach, Ca.

Associate

Melnicki, L. S., Niagara Falls, N. Y.
Palermo, H. W., Springfield, N. J.

Student

Jackson, J. M., Santa Monica, Ca.
Klinedinst, K. A., Stanford, Ca.
Shallwani, M. A., Swansea, Wales, U. K.

Transfer

Bogar, F. D., Springfield, Va.
Dalvi, A. D., Mississauga, Ont., Canada
Shippey, F. L., Penfield, N. Y.

PEOPLE

Ivan C. Blake has been appointed Vice President of Manufacturing for the Yardney Electric Division, Pawcatuck, Connecticut. A member of The Electrochemical Society, Mr. Blake has authored several technical papers which have been published in the **Journal** and in trade publications. He holds U.S. and foreign patents on electrochemical devices and components.

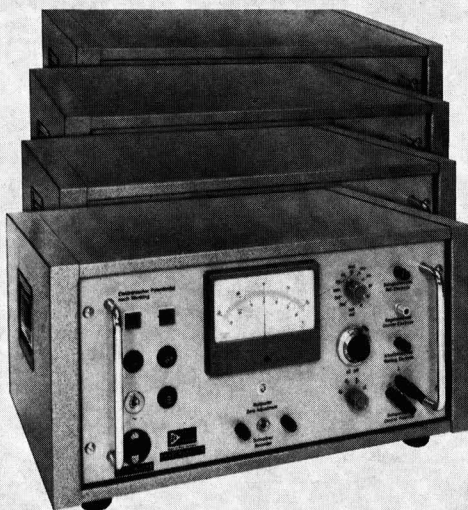
Otto Kardos, a pioneer in developing modern bright plating processes and the holder of basic patents in this field, is retiring from his position as senior research associate with M&T Chemicals, Inc., Detroit, Michigan.

Dr. Kardos obtained his Ph.D. in Chemistry from the University of Vienna in 1932 and first came to this country in 1942. In 1944 he joined the Hanson-Van Winkle-Munning Company, which later became a part of M&T Chemicals, as a research electrochemist.

Dr. Kardos specialized in the development of bright plating processes for nickel, copper, silver, zinc, cadmium, and cobalt; and he is the inventor or co-inventor of thirty U.S. patents along with corresponding foreign patents. Among these is a basic pioneering patent on which most modern bright leveling nickel plating processes are based. He developed, in cooperation with Dr. D. G. Foulke, a now generally accepted theory on the mechanism of leveling and microthrowing power during electrodeposition on small-scale profiles.

Among his professional affiliations, Dr. Kardos is a member of The Electrochemical Society. He is the author of many technical papers.

Which of our electronic potentiostats is for you?



A newly expanded line of Wenking Electronic Potentiostats for various electrochemical investigations is now available.

Choose from four basic series: 'fast rise' and/or high output voltage models (with output swing of ± 100 V); a 'high current' model (output current to ± 10 amps); several standard models, and an inexpensive laboratory model for routine requirements. Accessory systems, including a high precision voltmeter and motor potentiometers, are also available.

Which Wenking is for you? Complete literature describing all Wenking models, the world's most widely used electronic potentiostats, is available free on request to help you decide. Just write: Wenking Division, Brinkmann Instruments, Cantiague Road, Westbury, N.Y. 11590. In Canada write: Brinkmann Instruments (Canada) Ltd., 50 Galaxy Boulevard, Rexdale (Toronto), Ontario.

Wenking Potentiostats

A DIVISION OF



BOOK REVIEWS

"Thick-Film Microelectronics: Fabrication, Design, and Applications," by Morton L. Topfer. Published by Van Nostrand Reinhold Co., New York (1971). 210 pages; \$10.95

If technical books are divided into two categories, those designed to help experts and those for the person who wishes to become an expert, "Thick-Film Microelectronics" falls clearly into the latter group. As an introduction to thick-film hybrid circuitry it is surprisingly complete, covering subjects as disparate as screen-printer set-up and partitioning of circuits into individual modules. In each case the topic is covered with sufficient detail to develop most of the important criteria involved. Photographs, diagrams, and tables are used to good effect throughout the text.

The Introduction objectively reviews the triple technologies, monolithic, thin-film, and thick-film, covering areas of mutual compatibility and trade-offs. Design rules-of-thumb and the capabilities of available materials and compounds are surveyed in the second chapter. The approach is conservative; the capabilities of the technology are not oversold. The chapters dealing with artwork, screens, printing, firing, etc., have a fair "do-it-yourself" flavor and contain numerous useful pieces of common sense. They assume that the reader will avail himself of as much commercially available material and equipment as possible. No effort, for instance, is expended on the technology of ink manufacture; however, the required adjustments to optimize prints from a given ink are examined in appropriate detail.

The chapters on assembly and packaging techniques are well stocked with discussion useful to entrants into the field. The discussion of bonding techniques, although somewhat dated because of recent innovations, presents the basics well. We should note here that the preparation of any book summarizing technology in such a rapidly moving field as hybrid circuits is always a difficult undertaking; however, Mr. Topfer has been more successful than usual because he has concentrated on what you need to know to start participating rather than what are the latest developments.

The later chapters of the book address partitioning, reliability, and numerous applications which serve well in demonstrating where thick-film hybrids are finding application. Appropriate recognition is given to IBM's pioneering thick-film work for its 360 computer systems. Hybrid circuits for consumer electronic equipment now becoming important, unfortunately, only receive brief comment. Hermetic, military styles are well covered.

Two topics of major importance to anyone planning to use the technology presented in the book, manufacturing economics and process yields, receive only superficial comment. Perhaps rightly, they are apparently considered beyond the scope of the text.

For those newly facing the technical problems and opportunities of thick-film hybrid design and manufacture, this book should prove very helpful. Mr. Topfer has performed a significant service to the technical community by providing such a concise and readable distillation of otherwise available but disorganized spoken and written information.

John Piper
Union Carbide Corporation
Greenville, S. C.

"Optical Processes in Semiconductors," by Jacques I. Pankove. Published by Prentice-Hall, Inc., Englewood Cliffs, New Jersey (1971). 407 pages; \$21.00.

"Optical Processes in Semiconductors" is a graduate level text that provides an excellent overview of this field. Such an introduction has not previously been offered in any one book.

The text is lucid and terse with many citations of original work in the areas discussed. Quite a few figures from important experimental papers are reproduced and generally aid the exposition. In a number of instances these figures are inadequately integrated with the author's text and the reader is left to figure out the significance of some of the legends appearing in the figures. Usually these are sample identification numbers, but sometimes the omissions are more serious.

The principal shortcoming of this book is that the author has tried too hard to keep it short and the clarity of the argument has suffered for it. Several important and fairly subtle topics, such as plasma resonance phenomena in optical absorption, are alluded to only briefly. More significantly, the entire subject of photoconductivity, aside from effects in p-n junctions, is barely mentioned. Rather than devote a section of the book to bulk photoconductors, the author has instead chosen to refer the reader to several well-known texts on the subject.

Aside from the disregard of photoconductivity, this book is, on the whole, very well done. It achieves the author's goal of providing a clear, concise, and comprehensive introduction to the field on the graduate level. In addition, the inclusion of a wealth of carefully selected experimental data and copious references to original papers make it a valuable reference text.

David A. Kiewit
Hughes Research Laboratories
Malibu, Calif.

"Electroplating Engineering Handbook" (third edition), edited by A. Kenneth Graham. Published by Van Nostrand Reinhold Co., New York (1971). 845 pages; \$29.95.

This is a standard handbook which has no competitor and should be on the workbook shelf of every electroplating engineer. There is no other convenient single source of information on plant and processes and process control, unless one considers the expensive three-volume "Dettner/Elze Handbook" in German, or the inexpensive "Metal Finishing Guidebook."

The book is divided into two parts: Part I on General Processing Data, and Part II on Engineering Fundamentals and Practice. The successive editions have appeared at rather frequent intervals (1955, 1962, 1971) and without intensive editing and extensive additions, so owners of the first and second editions would be well advised to keep them on their active shelves. With the exception of a chapter on costs the entire first edition is essentially reprinted in the second and third editions. Why the chapter on costs should have been omitted from the second and third editions is a mystery.

The number of chapters in the first edition was 36, in the second, 38, and in the third, 40. Thus the main additions in the second edition related to Electroless Plating, Current Distribution, and Electroforming at the end of Part I. The principal additions to the third edition were chapters on Electrochemical Machining and Electrophoresis at the end of Part II.

A strange economy of space in the new third edition is a piling down of the index by about one-third or more over the second edition. Thus owners of the second edition may wish to retain it for its more detailed index, and users looking for information on a specific detail would do well to check the index in the second edition.

Another strange feature of the new third edition is the handling of material contributed by the rather numerous deceased authors. This material is now reprinted under new authorship with a rather inconspicuous footnote stating that the deceased author contributed to the first edition, and no recognition of contributions to the second edition is made. An outstanding example of this is Chapter 9, on Analysis of Plating Baths, which was contributed to the first and second editions by Myron Diggin and now appears under the authorship of the editor-in-chief, A. Kenneth Graham.

On the critical side, the weakest point in the book appeared to be the relatively brief and generalized description of semi- and fully automatic plating machines. This hardly seemed adequate to give the reader any clue to the existence of the huge fully automated machines to be found in the

Just Published!

EDWARD GOODRICH ACHESON

By
RAYMOND SZYMANOWITZ

Here is a completely documented, absorbing biography of the man who gave the world such indispensable products as Carborundum and man-made graphite—Edward Acheson, famed inventor, scientist and industrialist. An amazing success story replete with human drama and adventure. Illus. \$10.00

At bookstores or postpaid from:

VANTAGE PRESS, INC.

516 West 34th St., New York, N. Y. 10001

larger plants, handling a number of processing cycles and covering an area as large as several city blocks.

All quibbling over details aside, this handbook is a monumental contribution to the electroplating profession which defies adequate description here. There is no other comparable single source where one can count on finding dependable information on such practical matters as plating room floors, tanks, power supply, heating, ventilation, filtration, circulation, rinsing, drying, waste disposal, hygiene and safety measures, barrels, conveyors, and other automatic equipment. This is combined with descriptions of baths and processes in common use, analysis and control, metallurgy and preparation of the basis metal or non-metal as the case may be, design for plating, definitions, specifications, methods of thickness determination and corrosion testing, and tables of useful data.

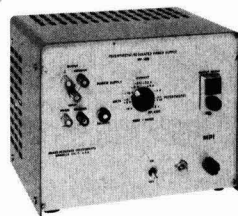
All in all, it is a reference that no one intimately concerned with electroplating can afford to be without.

George Dubernell
M&T Chemicals, Inc.
1700 East Nine Mile Road
Ferndale, Mich. 48220

ADVERTISER'S INDEX

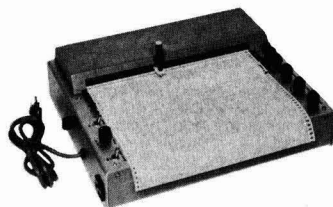
Airco Speer Carbon-Graphite	147C
Brinkmann Instruments, Inc.	155C
Great Lakes Carbon Corp., Graphite Products Division	143C
McKee-Pedersen Instruments	157C
Monroe Electronics, Inc.	153C
Plenum Publishing Corp.	152C
POWER Applications, Inc.	158C
Stauffer Chemical Company, Texas Alkyls, Inc.	151C
Texas Instruments, Inc.	158C
Vantage Press, Inc.	157C
John Wiley & Sons, Inc.	148C

MPI MODULAR SYSTEMS



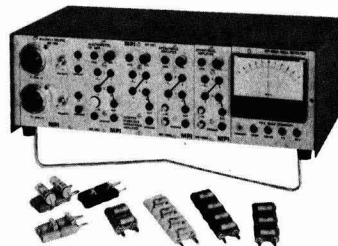
MP-1026 Power Operational Amplifier/ Potentiostat/ Regulated Power Supply

50 watt solid-state electronics provide $\pm 0-10v$ and $\pm 0-5a$ with $\pm 0.02\%$ regulation. Potentiostat mode provides $\pm 0-5v$. Operational amplifier mode has open loop gain $> 10^5$ and rise time faster than $1v/\mu sec$. Linearity of potentiometer is $\pm 0.25\%$ with $\pm 0.03\%$ resolution. \$480.00



MP-1027 Chart Recorder

10" potentiometric strip chart recorder with 6 switch-selected speeds and all solid-state electronics. Switched synchronizing outlet. Calibrated full scale ranges from 1 mv to 1v with accuracy of $\pm 0.25\%$ F.S. Pen response 0.6 second F.S. Chart speeds from 0.1 in./min. to 2.0 in./min. standard, other speeds available. \$515.00 - \$660.00



MP-1704 Operational Amplifier Manifold

Table-top or rack mounting cabinet with 8 plug-in spaces. Includes dual millivolt source, $\pm 0-4000$ mv with 0.5% linearity. Four op. amps.: two differential; chopper-stabilized; and electrometer with input impedances to 10^{13} ohms. Outputs of ± 15 volts and up to 100 ma. Other plug-ins such as bridges and integrators available. \$963.00

McKee-Pedersen Instruments
Phone 415-937-3630
Box 322, Danville, CA 94526 USA

ELECTROCHEMICAL AND BATTERY TECHNOLOGY

- • • Consultants
- • • Engineers
- • • Marketing
Specialists

For further information
contact:



POWER Applications, Inc.
41-06 Bell Blvd.
(P. O. Box 305)
Bayside, New York 11361
212-631-7784

POSITION AVAILABLE

Please address replies to the box number shown, c/o The Electrochemical Society, Inc., P. O. Box 2071, Princeton, N. J. 08540.

Battery Engineer—Modern lead acid battery manufacturing plant on the West Coast requires Battery Engineer with minimum of 2 years experience in battery development, testing, and engineering. Analytical chemical background desirable. Qualified candidates interested in joining a dynamic group write in confidence, including salary history, to Box B-60.

Positions Wanted

Society members of any class may, at no cost and for the purposes of professional employment, place not more than three identical insertions per calendar year, not to exceed 8 lines each. Count 43 characters per line, including box number, which the Society will assign.



Member of Technical Staff

CENTRAL RESEARCH LABORATORIES

This is a unique opportunity to join a truly outstanding Research and Development group in an organization where future growth is tied to continued technological leadership.

The Physical Sciences Research Laboratory of Texas Instruments needs a Ph.D. in Chemistry or Materials Science with 5-10 years experience in synthesis of III-V compound semiconductors. Should have experience with Czochralski and Bridgman methods, zone refining, and epitaxial growth including vapor phase and liquid phase techniques.

Send confidential resume, including current salary, to:

Staffing Manager
Corporate Research and Engineering
P.O. Box 5474 Dallas, Texas 75222
Mail Station 217

TEXAS INSTRUMENTS
INCORPORATED

AN EQUAL OPPORTUNITY
EMPLOYER

POSITIONS WANTED

Please address replies to the box number shown, c/o The Electrochemical Society, Inc., P. O. Box 2071, Princeton, N. J. 08540.

Physical Electrochemist—Ph.D. 15 years supervisory experience. Seeks R&D position, metal electroplating, electroless plating, metal finishing and finishes, corrosion protection and control, surface chemistry and metallurgy, anodizing, organic coatings. Patents and publications. Will relocate. Reply Box C-95.

MOS Process Engineer—M.S. 1966. 4 years experience in R&D lab. Strong background in solid-state diffusion, epitaxy, and deposition of pyrolytic oxides. Last 3 years spent in Silicon gate MOS development, including both p- and n-channel as well as complementary devices. Seeking responsible position in development or production. Will relocate. Reply Box C-96.

R&D Manager-New Product Development—Young chemist and chemical engineer, Ph.D., multilingual, experienced in leading scientific personnel, coordinating and interfacing R&D efforts with sales, and marketing and production. Technical accomplishments in corrosion and protective coatings, test methods development and electrodeposition. Reply Box C-97.

Staff Technologist—Ph.D. Inorganic chemist with industrial experience in electrochemistry, electrodeposition, metal reduction, alloy formation, coatings, and refractory materials synthesis. Highly competent in technical communications, both written and oral. Seeking industrial R&D position. Some liaison with production, marketing, and management desired. Reply Box C-98.

Materials Engineer—B.Sc. Experience in design and development of electrochemical equipment and instrumentation used in synthesis and evaluation of novel electronic materials such as phosphors, liquid crystals, and other electro-optic materials. Performed growth of single crystals. Familiar with high temperature and vacuum technology of refractory metals and ceramics. Interested in R&D or production. Reply Box C-99.

Inorganic Chemist—M.S. Research in lead-acid battery production has led to improved understanding of plate composition and battery life. Also background in areas of electroanalysis and instrumentation. Productive, enterprising, and communicative. Seek responsible position in Engineering or R&D related to inorganic and electrochemistry. No agencies. Reply Box C-100.

Electrochemist—B.S. and M.A. Chemistry. Twelve years electrochemical experience. Research on battery technology and plating processes. Process control continuous plating line. Two years adjunct college instructor. Seeking challenging and rewarding position with industrial firm or educational institution. Reply Box C-101.

Solid-State Chemist—Ph.D. 1971, M.S. 1952. 19 yrs. exp. all aspects solid-state; R&D, pilot plant, & prod. background; inorganic, analytical & phys. chem. Synthesis of materials & phosphors my specialty. 36 new products and processes developed for lighting industry. 41 patents issued, 38 papers. Supervisory, management exp. Economic evaluation from conception to plant construction. Reply Box C-102.

Electrochemist—Ph.D. 1944. Seeks challenging industrial research or development position or academic position. R&D background includes electrode kinetics, batteries, electrodeposition, corrosion, and stress corrosion. 47 publications, administrative experience. Location open. Reply Box C-103.

THE ELECTROCHEMICAL SOCIETY PATRON MEMBERS

Dow Chemical Co.

Inorganic Chemicals Dept., Midland, Mich.

General Electric Co.

Battery Business Section, Gainesville, Fla.

Chemical Laboratory, Knolls Atomic Power Laboratory,
Schenectady, N. Y.

Electronic Capacitor & Battery Dept., Irmo, S. C.

Lamp Div., Cleveland, Ohio

Materials & Process Laboratory, Large Steam
Turbine-Generator Dept., Schenectady, N.Y.

Nucleonics Laboratory, Pleasanton, Calif.

Research and Development Center,
Physical Chemistry Laboratory,
Solid State Physics Laboratory,
Schenectady, N.Y.

The International Nickel Co., Inc., New York, N. Y.

Olin Corporation

Chemicals Div., Research Dept.,
New Haven, Conn.

Westinghouse Electric Corp.

Electronic Tube Div., Elmira, N.Y.

Lamp Div., Bloomfield, N.J.

Semiconductor Div., Youngwood, Pa.

Research Laboratories, Pittsburgh, Pa.

K. W. Battery Co., Westinghouse Subsidiary,
Skokie, Ill.

THE ELECTROCHEMICAL SOCIETY SUSTAINING MEMBERS

Airco Speer Carbon-Graphite
St. Marys, Pa.

Allen-Bradley Co.,
Milwaukee, Wis.

Allied Chemical Corp.,
Industrial Chemicals Division,
Solvay, N. Y.

Aluminum Co. of America,
New Kensington, Pa.

Aluminum Co. of Canada, Ltd.
Montreal, Que., Canada

American Cyanamid Co.,
Stamford Research Laboratories,
Stamford, Conn.

American Gas & Chemicals, Inc.,
New York, N. Y.

American Metal Climax, Inc.,
New York, N. Y.

American Smelting and Refining Co.,
South Plainfield, N. J.

The M. Ames Chemical Works, Inc.,
Glens Falls, N. Y.

Ampex Corp.,
Redwood City, Calif.

Analog Devices, Inc.
Norwood, Mass.

Applied Electrochemistry Inc.
Sunnyvale, California

BASF Wyandotte Corporation,
Wyandotte, Mich.

Beckman Instruments, Inc.,
Fullerton, Calif.

Bell Telephone Laboratories, Inc.,
Murray Hill, N. J. (2 memberships)

Boeing Co.,
Seattle, Wash.

Canadian Industries Ltd.,
Montreal, Que., Canada

Carborundum Co.,
Niagara Falls, N. Y.

Chrysler Corp.,
Detroit, Mich.

Cominco Ltd.,
Trail, B. C., Canada

The Detroit Edison Co.,
Detroit, Mich.

Diamond Shamrock Corp.,
Painesville, Ohio

E. I. du Pont de Nemours & Co., Inc.,
Wilmington, Del.

Eastman Kodak Co.,
Rochester, N. Y.

Electrode Corporation
Chardon, Ohio

Eltra Corp.,
Prestolite Div., Toledo, Ohio
C&D Batteries, Conshohocken, Pa.

Engelhard Industries, Inc.,
Newark, N. J.

The Eppley Laboratory, Inc.,
Newport, R. I.

ESB Inc.,
Philadelphia, Pa. (2 memberships)

Esso Research and Engineering Co.,
Engineering Technology Div.,
Florham Park, N. J.

SUSTAINING MEMBERS (CONTINUED)

Fairchild Camera & Instrument Corp.,
Research and Development Laboratory,
Palo Alto, Calif.

Falconbridge Nickel Mines Ltd.,
Thornhill, Ont., Canada

FMC Corp.,
Inorganic Chemicals Div.
Buffalo, N. Y.

Foot Mineral Co.,
Exton, Pa.

Ford Motor Co.,
Dearborn, Mich.

General Motors Corp.,
AC Electronics Div., Milwaukee, Wis.
Allison Div., Indianapolis, Ind.
Delco-Remy Div., Anderson, Ind.
Research Laboratories Div., Warren,
Mich.

**General Telephone & Electronics Labora-
tories, Inc.,** Bayside, N. Y.

Globe-Union, Inc.,
Milwaukee, Wis.

B. F. Goodrich Chemical Co.,
Cleveland, Ohio

Gould, Inc.
Energy Technology Laboratories
St. Paul, Minn.

Great Lakes Carbon Corp.,
New York, N. Y.

Gulf Oil Canada Limited
Shawinigan Chemicals Div.,
Montreal, Que., Canada

Harshaw Chemical Co.,
Cleveland, Ohio (2 memberships)

Hill Cross Co., Inc.,
West New York, N. J.

Hooker Chemical Corp.,
Niagara Falls, N. Y. (2 memberships)

HP Associates,
Palo Alto, Calif.

**Hughes Research Laboratories, Div. of
Hughes Aircraft Co.,** Malibu, Calif.

International Business Machines Corp.,
New York, N. Y.

Jones & Laughlin Steel Corp.,
Pittsburgh, Pa.

K. W. Battery Co.,
Skokie, Ill.

Kaweci Berylco Industries, Inc.
Boyetown, Pa.

Kennecott Copper Corp.,
New York, N. Y.

Kerr-McGee Corporation,
Technical Center,
Oklahoma City, Okla.

Arthur D. Little, Inc.,
Cambridge, Mass.

Mallory Battery Company
Tarrytown, N. Y. (2 memberships)

Marathon Battery Co.,
Cold Spring, N. Y.

Molybdenum Corporation of America,
New York, N. Y.

Monsanto Company
St. Louis, Mo.

Motorola Inc.,
Phoenix, Ariz.

M&T Chemicals Inc.,
Detroit, Mich.

National Cash Register Co.,
Dayton, Ohio

National Lead Co.,
New York, N. Y.

National Steel Corp.,
Weirton, W. Va.

Nortec Electronics Corp.,
Santa Clara, Calif.

North American Rockwell Corp.,
El Segundo, Calif.

Northern Electric Co.,
Montreal, Que., Canada

Owens-Illinois Glass Co.,
Toledo, Ohio

Park Electrochemical Corp.,
Great Neck, N. Y.

Phelps Dodge Refining Corp.,
Maspeth, N. Y.

Philips Laboratories, Inc.,
Briarcliff Manor, N. Y.

PPG Industries, Inc.,
Chemical Div.,
Pittsburgh, Pa.

Radio Corp. of America,
Electronic Components and Devices,
Lancaster, Pa.

**Republic Rail
National Aluminum
A Unit of
National Steel Corp.**
Danbury, Conn.

Sabin Chlor-Alkali, Inc.,
Orrington, Maine

Sprague Electric Co.,
North Adams, Mass.

Stackpole Carbon Co.,
St. Marys, Pa.

Stauffer Chemical Co.,
Dobbs Ferry, N. Y.

Teletype Corp.
Skokie, Ill.

Texas Instruments Inc.,
Dallas, Texas

3 M Company
St. Paul, Minn.

Udylite Corp.,
Detroit, Mich. (4 memberships)

Union Carbide Corporation,
Consumer Products Division,
New York, N. Y. (3 memberships)

United States Steel Corp.,
Pittsburgh, Pa.

Varian Associates,
Palo Alto, Calif.

Western Electric Co., Inc.,
Greensboro, N. C.

Yardney Electric Division
Pawcatuck, Conn.

Zenith Radio Corp.,
Chicago, Ill.